OTTO VON GUERICKE UNIVERSITÄT MAGDEBURG

EIT FAKULTÄT FÜR ELEKTROTECHNIK UND INFORMATIONSTECHNIK

Improved cardiac gating and patient monitoring in high field magnetic resonance imaging by means of electrocardiogram signal processing

Dissertation

zur Erlangung des akademischen Grades

Doktoringenieur
(Dr.-Ing.)

von Dipl.-Ing. Johannes W. Krug
geb. am 23.05.1983 in Leipzig
genehmigt durch die Fakultät für Elektrotechnik und Informationstechnik
der Otto-von-Guericke-Universität Magdeburg

Gutachter: Prof. Dr. rer. nat. Georg Rose (Otto-von-Guericke-Universität Magdeburg)
Prof. Dr. rer. nat. Jacques Felblinger (Université de Lorraine)
Julien Oster, PhD (University of Oxford)

Promotionskolloquium am 28.05.2015

Abstract

The electrocardiogram (ECG) represents the heart electrical activity, and it is widely used in clinical practice, e. g. for the detection of cardiac arrhythmias. An ECG is also often used during magnetic resonance imaging (MRI) examinations. In cardiac MRI, the ECG is used to compensate the motion of the heart muscle. This is achieved by synchronising the acquisition of the MRI data with heart motion, which can be obtained from the ECG signal by QRS detection (gating). If sedation is used during an MRI exam or if the patient suffers from a cardiovascular disease, the ECG is also required to monitor the heart rate and heart rhythm (monitoring).

The static magnetic field and the switched gradient magnetic fields of an MRI machine severely distort the ECG signals acquired inside the bore of the scanner. This thesis starts with an investigation of the magnetohydrodynamic (MHD) effect, which is caused by the flow of blood in the presence of the static magnetic field. Due to its origin inside the body, the MHD signal is transferred to the surface of the torso and is picked up by the ECG electrodes. Since the MHD signal superimposes to the ECG signal, the diagnostic value of the ECG in clinical MRI scanners (magnetic field strengths up to $3\,\mathrm{T}$) is limited. Diagnostic information contained in the ST-segment or T-wave of the ECG cannot be accessed during an MRI examination. At higher magnetic field strengths of $7\,\mathrm{T}$ and above the MHD effect also hampers QRS detection, which limits the usage of the ECG for gating applications. The aim of this thesis is to develop denoising techniques, which would enable a reliable QRS detection at $7\,\mathrm{T}$ and allow a more detailed diagnostic analysis based on the ECG at $3\,\mathrm{T}$.

Real and simulated ECG signals were used for the development and evaluation of different denoising techniques. The influence of the MHD effect (at $7\,\mathrm{T}$) on an existing QRS detector dedicated for gating applications in MRI was firstly investigated. Based on these investigations, an existing method was optimised in order to improve the QRS detection quality. Additionally, a new technique for QRS detection at $7\,\mathrm{T}$, based on independent component analysis (ICA), was developed and evaluated using real ECG records. It was shown that the ICA-based technique could enable a reliable QRS detection at $7\,\mathrm{T}$. To obtain diagnostic information from the ECG at $3\,\mathrm{T}$, several denoising techniques were developed and evaluated using simulated ECG signals containing pathological variations. Simulated MHD signals and physiological noise (muscle artefacts) were superimposed to the simulated (pathological) ECGs. Since the ground-truth of the simulated signals was known, a detailed quantitative evaluation of the different filtering techniques was possible. Different techniques were evaluated for denoising purposes and for the extraction of diagnostic information. Based on an extensive evaluation, the simulated ECG signals filtered by the extended Kalman filter (EKF) allowed for the most precise estimation of different diagnostic parameters. This observation was confirmed qualitatively when the EKF was applied to real ECG signals.

Within this thesis, innovative techniques were introduced and should provide for both, ECG-based triggering at ultra-high fields but also for the extraction of diagnostic information, e. g. during MRI-guided interventions.

Zusammenfassung

Das Elektrokardiogramm (EKG) bildet die elektrische Aktivität des Herzmuskels ab. In der kardiologischen Diagnostik findet das EKG eine breite Anwendung, da es unter anderem eine Erkennung von Arrhythmien ermöglicht. Auch bei Untersuchungen mittels der Magnetresonanztomographie (MRT) wird ein EKG häufig genutzt, um beispielsweise bei der MRT des Herzens die Herzbewegung zu kompensieren. Mithilfe des EKG werden der Aufnahmezeitpunkt der MRT-Daten und die Herzbewegung synchronisiert (Triggerung). Sind Patienten während einer MRT-Untersuchung sediert oder leiden an einer Herz-Kreislauf-Erkrankung, werden mit dem EKG auch die Herzfrequenz und der Herzrhythmus überwacht (Monitoring).

Das statische magnetische Feld sowie die geschalteten magnetischen Gradientenfelder des MRT stören das EKG-Signal jedoch erheblich. Diese Dissertation untersucht zunächst, wie sich der magnetohydrodynamische (MHD) Effekt – welcher durch den Blutfluss im statischen Magnetfeld verursacht wird – auf das EKG-Signal auswirkt. Aufgrund seiner Entstehung im Körperinneren wird das MHD-Signal über die auf der Körperoberfläche angebrachten Elektroden aufgezeichnet und überlagert so das EKG-Signal. Der MHD-Effekt limitiert den diagnostischen Wert des EKG in typischen klinischen MRT Scannern (magnetische Flussdichte $\leq 3\,\mathrm{T}$). So sind beispielsweise die ST-Strecke oder die T-Welle nicht mehr diagnostisch nutzbar. Bei höheren magnetischen Flussdichten ($\geq 7\,\mathrm{T}$), die hauptsächlich in der Forschung eingesetzt werden, erschwert der MHD-Effekt außerdem die Triggerung der Bildgebung, da der QRS-Komplex nicht mehr zuverlässig erkannt werden kann. Das Ziel der Arbeit ist es schließlich, Methoden zu entwickeln, die sowohl die QRS-Detektion als auch den diagnostischen Wert eines im MRT aufgezeichneten EKG verbessern.

Für die Entwicklung und Evaluierung der Methoden kamen reale und simulierte EKG-Signale zum Einsatz. Zunächst wurde untersucht, wie sich der MHD-Effekt bei 7 T auf das EKG-Signal sowie auf einen schon existierenden QRS-Detektor, welcher speziell für die Anwendung im MRT entwickelt wurde, auswirkt. Mit den gewonnen Erkenntnissen wurde das vorhandene Verfahren zur QRS-Detektion optimiert und zusätzlich eine neues, auf der Independent Component Analysis (ICA) basierendes Verfahren, entwickelt und implementiert. Es konnte gezeigt werden, dass das ICA-basierte Verfahren eine zuverlässige QRS-Detektion bei 7 T ermöglichen kann. Bei der Entwicklung von Methoden zur Filterung der EKG-Signale und zur nachfolgenden Gewinnung diagnostischer Informationen wurden im ersten Schritt simulierte EKG-Signale, welche pathologische Veränderungen enthielten, verwendet. Den simulierten EKGs wurden MHD-Signale sowie physiologisches Rauschen (Muskelartefakte) überlagert. Nur mit den simulierten Daten war eine quantitative Bewertung der Ergebnisse möglich, da hier das zugrunde liegende EKG-Signal bekannt war. Für die Filterung und die Extraktion diagnostischer Parameter wurden verschiedene Verfahren untersucht. Dabei zeigte sich, daß der Extended Kalman Filter die präziseste Bestimmung verschiedener diagnostischer Parameter ermöglichte. Diese Beobachtungen konnten schließlich auch an realen EKG-Signalen qualitativ bestätigt werden.

In dieser Arbeit wurden innovative Verfahren vorgestellt, die sowohl für die EKG-basierte Triggerung im Ultrahochfeld-MRT als auch für die Bestimmung diagnostischer Parameter, z. B. während einer MRT-geführten Intervention, geeignet sind.

Contents

1

Introduction

Magnetic resonance imaging (MRI) is a medical imaging technique used to study the anatomy and physiology of the body. It has been applied for a wide range of diagnostic purposes including cancer, cardiology, vascular diseases, neurology and others. Besides high-quality anatomical images, which enable the differentiation of several soft tissue types, MRI can also provide functional information about vascular blood flow (angiography), diffusion or spectroscopy. Based on these physical information one can draw inferences about the activity of the brain, the health condition of blood vessels, the existence of malignant tumours or the connection of nerve or muscle fibres. One very important application of MRI is cardiovascular magnetic resonance (CMR). CMR covers the anatomical and functional diagnose of the heart muscle and related blood vessels. Besides its application as a diagnostic modality, MRI gained popularity as a modality for guiding minimal invasive interventions, known as interventional MRI (iMRI). In these interventions, MRI is used instead of ultrasound or X-ray imaging to guide intravascular catheters in electrophysiological (EP) interventions or percutaneous needle biopsies, e. g. of the liver or the prostate.

Several of the above mentioned MRI applications – either diagnostic or therapeutic – require an electrocardiogram (ECG) of the patient. The ECG represents the electrical activity of the heart muscle or myocardium and is acquired by electrodes placed on the surface of the thorax. For MRI, a trace of the ECG can be required for:

- synchronising the acquisition of MRI data with heart motion (*gating*),
- *monitoring* the patient's vital parameters.

Gating describes the synchronization of the CMR data acquisition with cardiac motion. It is the most important application of the (clean underlying) ECG signal in MRI. ECG-based gating is robust in most cases and due to the physiological origin of the ECG, it is usually preferred over other gating methods. It is well established for clinical MR scanners with magnetic field strengths up to 3 T. However, ECG-based gating can be prone to errors at magnetic field strengths above 7 T which are used in research settings.

For cardiovascular *monitoring*, the ECG is of high importance and is often used in clinical routine. Several scenarios exist where an ECG signal is required during an MRI examination for monitoring. While the patient is inside the bore of the MR scanner, the physician or clinical staff has to rely on the patient's vital parameters since it is often difficult to visually observe the patient. Especially patients, who are in a critical or unstable condition (e. g. patients from an intensive care unit (ICU) or patients under anaesthesia), need to be adequately monitored during MRI. However, the diagnostic information of an ECG recorded within an MR scanner is very limited. With existing MR-safe ECG recording hardware it is possible to detect the QRS complexes in most cases for healthy and pathological subjects. This enables the estimation and analysis of the heart rate and of the heart rhythm. All other information contained in the ECG signal, i. e. the morphology of the P-wave, the QRS complex, the ST-segment, the T-wave or the length of the QT-interval can currently not be accessed during MRI due to different interfering signals.

The magnetohydrodynamic (MHD) effect, which is caused by the interaction of the MR scanner's static magnetic field and the patient's blood flow, is one of the main issues for gating problems at high magnetic field strengths ($\geq 7\,\mathrm{T}$). The MHD effect is also responsible for the limited diagnostic value of the ECG at all typical magnetic field strengths which are present in clinical MR scanners (up to $3\,\mathrm{T}$). This effect cannot be avoided since the static magnetic field of an MR scanner cannot be switched off during normal operation. The MHD effect superimposes the ECG since this electrical field is also picked up by the ECG electrodes.

This thesis explores different methods and techniques to cope with the consequences of the MHD effect. Based on the applications described above, two different aims were pursued within this thesis.

The *first aim* was to develop QRS detection methods, which enable a more reliable gating for CMR applications at 7 T. 12-lead ECG signals were acquired from several subjects outside and inside a 7 T MRI scanner. Currently existing QRS detection methods for MRI were investigated and new algorithms were developed using the 7 T ECG datasets. The different algorithms were evaluated quantitatively by measuring the accuracy of the QRS detection.

The *second aim* was to improve the diagnostic value of the ECG during MRI by filtering or suppressing the influence of the MHD effect. Two different signal types were used to pursue this aim. Simulated ECG and MHD signals were used to develop and test different filter algorithms. Different models were used to simulate the ECG and MHD signals, ranging from template methods to synthetic ECG models and more realistic simulations of the MHD effect. The simulated signals are required for a quantitative evaluation of the filter results. Real ECG signals do not allow a quantitative evaluation since the ground-truth of the ECG signals acquired inside the MRI scanner is not known. Based on the simulation results, the developed methods were applied to ECG signals acquired from different subjects in a $3\,\mathrm{T}$ MR scanner. The results using the real ECG signal were evaluated qualitatively only.

The thesis will be structured as follows: Chapter 2 introduces the physiological and technical basics required to follow the ideas and methods of this thesis. This chapter also explains why ECG signals are required during MRI. The reader, who is familiar with ECG signals and MRI is directly referred to Chapter 3. The theory of the MHD effect is explained together with an overview of different existing MHD simulation models. Exemplary measurements show how the MHD effect affects the ECG signals during MRI and how this limits the currently existing ECG-based gating and monitoring applications. The experimental setup used for the acquisition of the ECG signals at 3 T and 7 T will be described in chapter 4. Chapter 4 also covers a description of the models used for the simulation of the ECG and MHD signals. Algorithms for the QRS detection at 7 T will be described and evaluated in Chapter 5. Chapter 6 will investigate different methods to access diagnostic information from an ECG during MRI. A conclusion and an outlook for future research will be given in the closing Chapter 7.

2

Medical and technical foundations

2.1 Cardiovascular physiology and electrocardiography

2.1.1 Physiological background

Cardiac anatomy

The heart can be considered as a pump made up of four different chambers. It provides the mechanical driving forces for pumping blood through the body's vessel system. The *myocardium* or heart muscle forms the largest part of the heart wall. The heart is mainly divided into two different parts, which act in a double pump configuration. A schematic of the heart's anatomy is depicted in Fig. 2.1. Each of the two parts consists of an upper chamber, the atrium and a lower chamber, the ventricle. The atria are required to store blood and to fill the ventricles. The ventricles act as the main pumps, which eject the blood into the circulatory system. Deoxygenated blood is pumped by the right ventricle into the pulmonary circulation system where it is enriched with oxygen. The oxygenated blood flows into the left atrium where it is transferred into the left ventricle and is finally pumped into the systemic circulation system. [Schmidt 07]

The haemodynamic cycle of the heart is commonly separated into a diastolic and a systolic phase. The former is the relaxation period where the atria and ventricles are filled with blood from the venous system. In the atrial systole, the atria contract and additional blood is pumped into the ventricles. This phase is followed by the ventricular systole in which the ventricles contract causing an ejection of blood into the arteries [Kohl 11, p.103]. The following parts of this section describe how the mechanical contraction of the heart is controlled by propagating action potentials and how these potentials form the basis of the ECG signals which can be measured at the surface of the body.

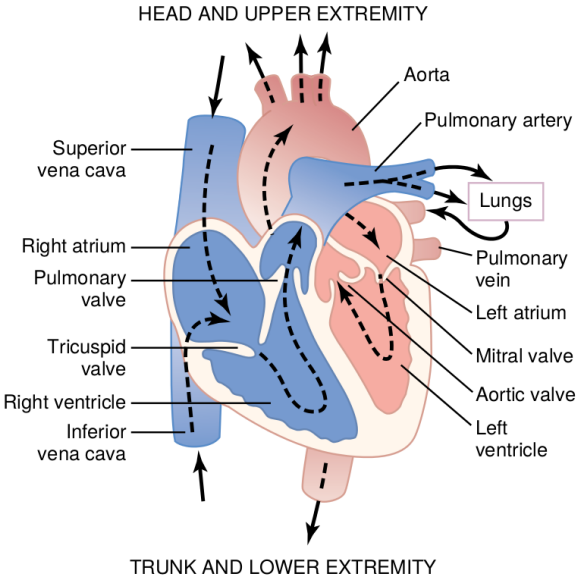

Figure 2.1.: Anatomy of the heart and surrounding blood vessels. (Image source: [Guyton 06])

Cardiac muscle cells, action potentials and body surface potentials

On the cell level, important parts of the heart are the heart muscle cells, pacemakers cells and a specialised electrical conduction system. As for nerve cells, muscle cells have excitable membranes. The membranes divide the medium into extracellular and intracellular fluids which have different ionic concentrations. Potassium (K^+), sodium (Na^+), calcium (Ca^{2+}) and chlorine (Cl^-) ions are involved in the creation of the cell potential. Active *sodium-potassium pumps*, which are located in the membrane of the cells, actively expel Na^+ from the cells and move K^+ into the cells. This active ion transport against the electrochemical gradient results in an enrichment of K^+ and a depletion of Na^+ concentration inside the cell compared to a high extracellular Na^+ and low K^+ concentration. The difference of K^+ concentration can remain because the gradients of ion concentration and of the electrical fields have equal but opposite effects. In this steady-state condition, the cell has a transmembrane potential of $-90\,\mathrm{mV}$ (intracellular potential is negative) – the so called *resting membrane potential*. [Schmidt 07]

During the *depolarisation* or excitation of a cell, its membrane permeability is modified with respect to certain ions. Firstly, the permeability to sodium (Na^+) is increased. Hence, Na^+ ions flow from the extracellular to the intracellular space. Theoretically, the influx of the Na^+ ions would cause a cell membrane potential of $60\,\mathrm{mV}$[1]. However, this voltage level is not reached since the sodium channels start to close at $-40\,\mathrm{mV}$. The cell membrane potential rises up to $30\,\mathrm{mV}$ – at this point the Na^+ channels are fully closed. Once the Na^+ are closed, Ca^{2+} channels open and Ca^{2+} ions flow slowly into the cell. This Ca^{2+} influx slightly repolarises the cell and causes the characteristic plateau phase which is depicted in Fig. 2.2. In this stage, the cell is said to be depolarised. Meanwhile, the permeability of the sodium channels returns to normal but those of the potassium channels increases about thirty-fold. Now, K^+ diffuse to the extracellular space due to the ionic concentration gradient. This brings the cell membrane potentials back to its resting level (repolarisation). The higher permeability of the K^+ channels remains. Finally, the *sodium-potassium pumps* takes over again which pumps Na^+ out of the cell and allows K^+ ions to diffuse back to the intracellular space. The time course of the different potential

[1] The cell membrane potentials can be computed by the Nernst equation which describes the relation between the electrical and chemical gradients of a single ion type [Schmidt 07, p.48].

changes due to ionic currents is known as *action potential*. Action potentials of different cell types (e. g. of muscle cells or pacemaker cells) have different temporal characteristics. The depolarisation of one cell propagates to the adjacent cells through *gap junctions* which finally depolarises the entire cardiac muscle tissue[2]. The Ca^{2+} influx causes a mechanical response: the muscle tissue contracts shortly after it was depolarised. The depolarisation lasts about 2 ms and repolarisation about 200 ms (including the plateau phase) in mammalian cardiac muscle tissue. Figure 2.2 depicts the formation of the action potential and its relation to the contraction of the muscle fibres. [Hick 06, Schmidt 07]

The activities within the cell membranes generate current densities which affect the surrounding medium, i. e. current changes in the surrounding tissue. Figure 2.3 depicts the propagation of an advancing depolarisation wavefront. An *electric dipole field* is generated from the different extracellular ion concentrations. The resulting electrical potentials can be measured on the surface of the thorax using electrodes – the measured signals form the *electrocardiogram* (ECG). The following paragraphs provide a brief description of the initial depolarisation (excitation) of the myocardium, the propagation of the depolarisation wavefront, the repolarisation of the cells and the characteristic waveforms which are induced on the surface of the thorax and are picked up by the ECG electrodes.

Origin of the ECG waveform and mechanical activation of the myocardium

In ordinary cardiac muscle cells, the resting potential can be maintained indefinitely. In specialised cells known as pacemaker cells, the transmembrane potential will increase spontaneously. Hence, the pacemaker cells are said to be *self-excitatory*. Once such a pacemaker cell depolarises, adjacent cells depolarise as well. Among others, pacemakers cells can be found in the the sinoatrial (SA) node, which is located in the right atrium of the heart. Figure 2.4 depicts a schematic of the cardiac anatomy with the most important electrophysiological sources and pathways, which together form the *cardiac conduction system*. The wavefront caused by the depolarisation of the SA node propagates concentrically through the right atrium until it reaches the left atrium and the atrioventricular (AV) node. Figure 2.5 depicts the atrial depolarisation ($t = 80$ ms). In the measured ECG signal, the atrial excitation manifests as the P-wave. The excitation of the atrium results in a mechanical contraction: blood which is located in the left and right atrium is pumped (or ejected) into the corresponding ventricles. Meanwhile, the wavefront is passing through the AV node which forms the connection between the atria

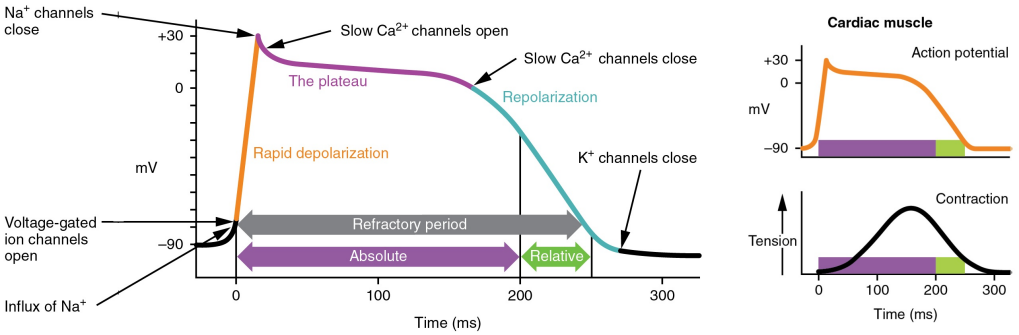

Figure 2.2.: Action potential of a cardiac muscle cell showing the depolarisation and repolarisation of the cells (left and upper right). During the absolute refractory period, the permeability of the Na^+ and Ca^{2+} channels cannot be changed. Hence, during this period it is not possible to generate a new action potential. During the relative refractory period, a strong external stimulus (e. g. due to an electric shock) can reopen the Na^+ channels causing a new action potential. The contraction of the muscle cells follows shortly after the rapid depolarisation. (Image modified according to [OSC 13])

[2]The propagation of the action potential through gap junctions does not exist in skeletal muscles.

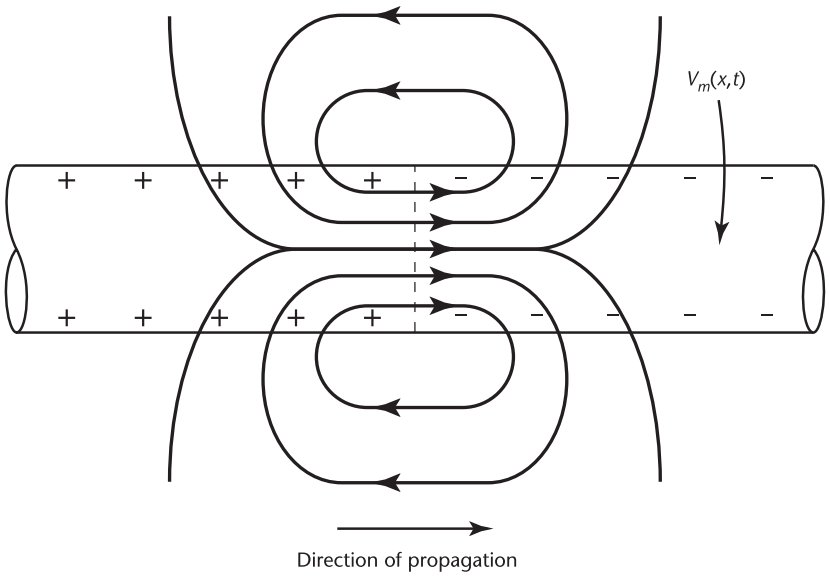

Figure 2.3.: Current flow in a myocardial cell in the direction of the propagating depolarisation wavefront. An electrical dipole field results from the different extracellular charge distributions. The transmembrane potential is given by $V_m(x,t)$. (Image source: [Clifford 06], ©MIT-OCW [Mark 04])

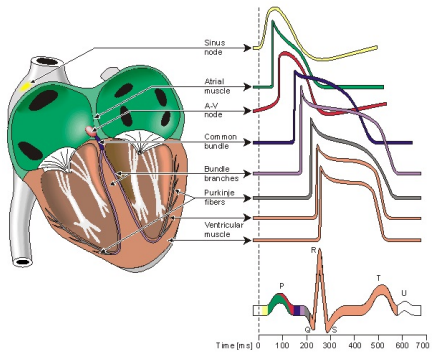

(a) Schematic anatomy of the heart showing the most important parts of the electrical conduction system. (Image source: [Malmivuo 95])

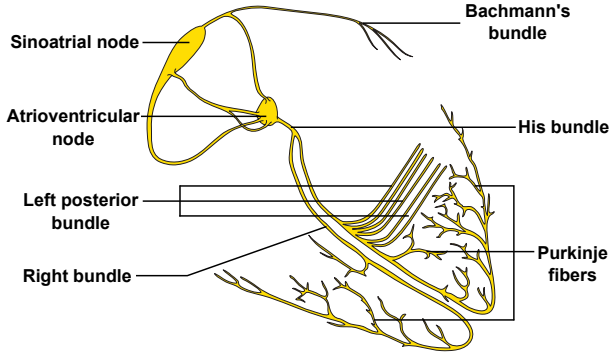

(b) Isolated cardiac conduction system. (Image source: [Commons 09])

Figure 2.4.: The anatomy of the heart, the cardiac conduction system and the formation of the ECG signal. Each part of the cardiac conduction system has a characteristic action potential. The sum of all action potentials is responsible for the formation of the body surface potentials measured by the ECG signal (a). Besides the muscle cells, additional pathways are responsible for the propagation of the action potentials throughout the heart muscle (b).

and the ventricles. Compared to the propagation velocity within the atrium or ventricles, the velocity through the AV node is relatively slow. The propagation delay prevents a simultaneous contraction of the atria and the ventricles. This enables a complete filling of the ventricles. The propagation delay caused by the AV node can be measured by the ECG's PQ-interval. Once the wavefront passed the AV node and reached the ventricles, it proceeds along the Purkinje fibres to the inner walls of the ventricles. The excitation starts from the left side of the interventricular septum followed by the activation of its right side as depicted in Fig. 2.5 at time $t = 220\,\text{ms}$. At the same time, an early apical activation is occurring. Afterwards, the left and right ventricle become excited. Finally, the basal parts of the ventricle (the 'upper' parts) depolarise. This depolarisation propagation throughout the ventricles is represented by the QRS complex of the ECG signal. When the ventricles are fully excited ($t = 350\,\text{ms}$),

a propagating wavefront or electrical sum vector does not exist any more. This phase corresponds to the ST-segment of the ECG. Hence, there is no signal measurable at that time. [Schmidt 07]

Repolarisation of the ventricles starts from the cells, which were depolarised latest (i. e. it starts from the outer sides – the epicardium – and then propagates to the inner side – the endocardium – of

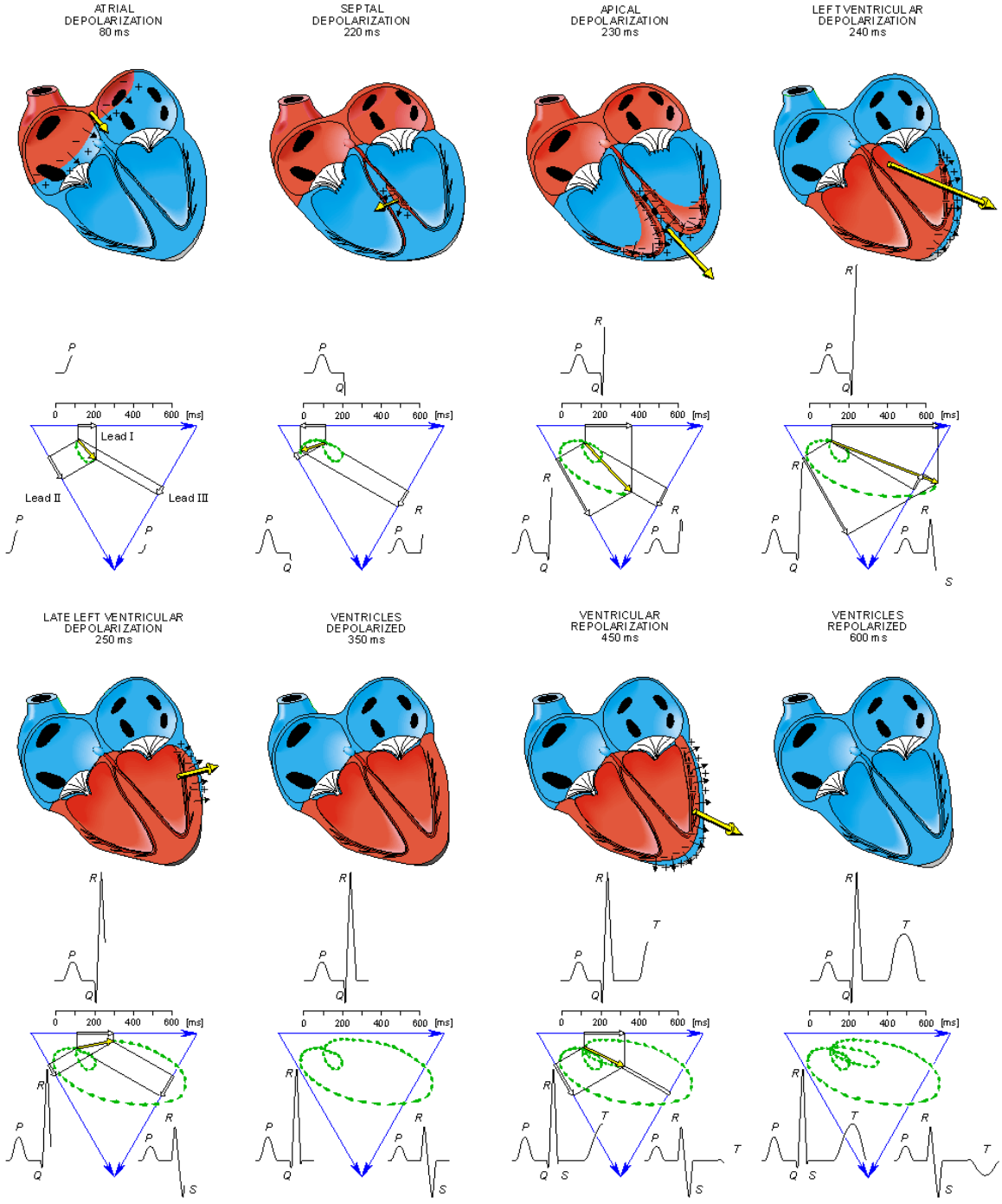

Figure 2.5.: Formation of the ECG signal at different time instances during one cardiac cycle. The ECG trace is shown for each of the three Einthoven limb leads (I, II, III) as well as the spatial propagation of the activation of the heart cells (dotted green line). (Image modified according to [Malmivuo 95])

the heart). The repolarisation of one cell does not affect neighbouring cells but it can be noticed that repolarisation generally moves from the epicardium toward the endocardium [Malmivuo 95]. In the ECG, cardiac repolarisation of the ventricle is represented by the T-wave. Compared to the QRS complex, the T-wave is much smaller and broader. This is depicted in Fig. 2.5 at the time interval between $t = 450\,\text{ms}$ and $t = 500\,\text{ms}$.

For the healthy heart depolarisation starts at the sinus node, which is the heart's primary pacemaker. If depolarisation of the sinus node fails, the AV node acts a secondary pacemaker. Its intrinsic frequency is much lower than that of the sinus node (approximately $40\,\text{bpm}$ to $60\,\text{bpm}$). The spontaneous depolarisation of the AV node is inhibited if a wavefront generated by the sinus node reaches the AV node[3]. Additionally, the Purkinje fibres (see Fig. 2.4b) can act as an even slower pacemaker (approximately $15\,\text{bpm}$ to $40\,\text{bpm}$) in case the SA or AV node do not function. [Klinge 84]

Figure 2.6 depicts a complete ECG signal with its most important fiducials and segments. As it was described above, the ECG is the representation of the cardiac's electrical activity. The Wiggers diagram depicted in Fig. 2.7 shows the relation between the electrical activity of the heart muscle cells and the corresponding mechanical activation, which is expressed by the pressures in different heart chambers and blood vessels. These relations are important in order to reduce the influence of motion artefacts in cardiac MRI as we are looking for phases in the cardiac cycle where there is no motion. The heart is in a nearly immobile position during the isovolumetric contraction/relaxation period in the systolic phase and during the mid-diastolic phase. Detailed explanations of MRI data acquisition are given in Section 2.3.1.

During physical exercise, the stroke volume is increased by approximately $20\,\%$ to $30\,\%$. A further increase of the cardiac output (ejected blood volume per time, L/min) can only be achieved by an increase of the heart rate. When heart rate increases, the duration of the diastolic phase decreases (whereas the duration of the ventricular systolic phase stays approximately constant). During rest, the cardiac output is approximately $5\,\text{l/min}$ whereas during exercise it can be $20\,\text{L/min}$ to $25\,\text{L/min}$. [Hick 06, p. 138]

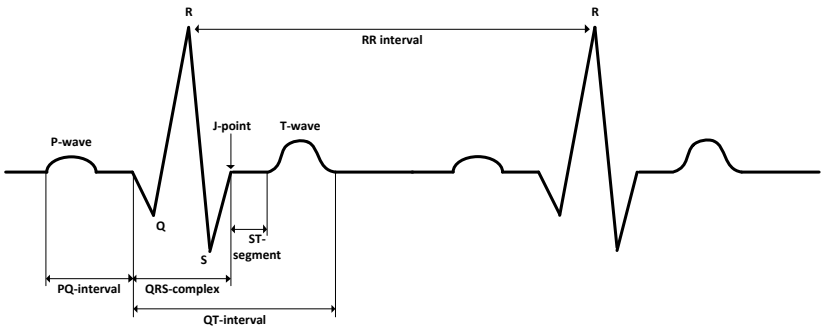

Figure 2.6.: The ECG signal with the most important fiducials and segments. The depolarisation of the atria, which is marked by the P-wave can be considered as the beginning of the cardiac cycle. The QRS complex represents the ventricular depolarisation whereas the T-wave represents the repolarisation effects. The distance between two adjacent R-peaks or QRS complexs is measured by the RR interval (RRI). (The U-wave which follows the T-wave and which can only be seen sometimes in an ECG is not shown.)

[3] This is due to the refractory period of the heart muscle cells.

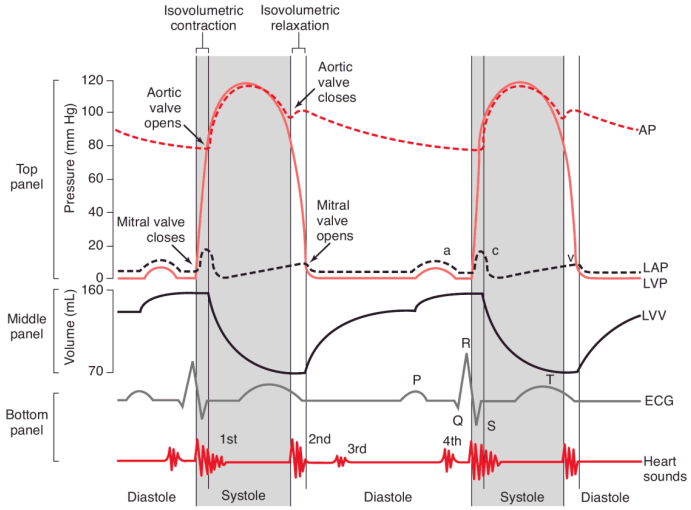

Figure 2.7.: The Wiggers diagram representing the different stages of the heart cycle with left atrial pressure (LAP), left ventricular pressure (LVP), aortic pressure (AP) and the left ventricular volume (LVV) in relation to the ECG signal and the heart sounds. An isovolumetric contraction of the myocardium occurs during the QRS complex. At the end of the QRS complex, the aortic valve opens and the blood is ejected into the aorta. The passive filling of the ventricles starts after the end of the contraction. Additional blood is actively pumped into the ventricles due to the contraction of the atria (marked by the P-wave in the ECG). (Image source: [Courneya 11])

2.1.2 The electrocardiogram (ECG) - measurement of body surface potentials

In order to measure the body surface potentials caused by the action potentials of the heart, different electrode configurations can be used. These electrode configurations are known as *ECG leads*. Figure 2.8 depicts the most common ECG lead configurations. Other configurations can be found

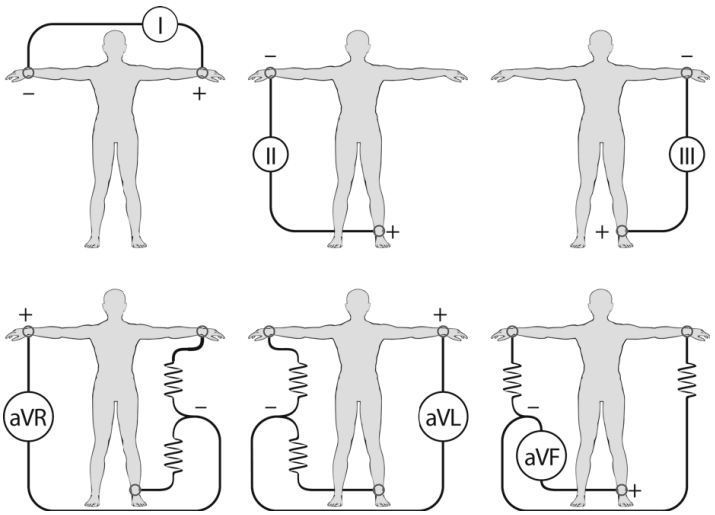

(a) Electrode positions for the frontal Einthoven (top) and Goldberger (bottom) lead schemes.

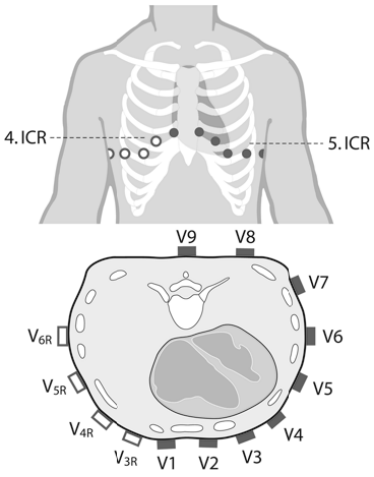

(b) Precordial leads V1-V6, additional dorsal leads V7-V9 and the right precordial leads $V_{3R} - V_{6R}$.

Figure 2.8.: Measurement of the ECG signals using different locations for the placement of the measurement electrodes. The three bipolar Einthoven leads I-III form the so called Einthoven triangle (a). The Goldberger leads can be derived from the Einthoven leads using additional electronics (a) or by vector calculus. Additional unipolar electrodes can be placed around the heart (b). Lead V1-V6 (Wilson leads) are regularly used in clinical practice. Leads I-III, aVR, aVl,aVF and V1-V6 form the 12-lead ECG. (Images modified according to [Gertsch 08])

in [Klinge 84, Gertsch 08]. The voltages of the three Einthoven leads (I,II,III) depicted in Fig. 2.8a can be defined as follows

$$\begin{aligned} I &= \Phi_{\text{LA}} - \Phi_{\text{RA}} \\ II &= \Phi_{\text{LL}} - \Phi_{\text{RA}} \\ III &= \Phi_{\text{LL}} - \Phi_{\text{LA}} \end{aligned} \tag{2.1}$$

where Φ_{LA}, Φ_{RA} and Φ_{LL} are the potentials at the electrode positions at left arm (LA), right arm (RA) and left leg (LL), respectively. Alternatively, these potentials can be measured on the thorax (left and right shoulder and lower left part of the thorax) [Sheppard 11]. Subtracting lead I from II gives

$$III = II - I. \tag{2.2}$$

Technically speaking this means that the set of measurements given in Eq. 2.1 is overdetermined.

For diagnostic purpose, additional leads are derived from the Einthoven leads: the so called augmented leads. The augmented leads are either derived by an additional electronic circuit as depicted in Fig. 2.8a or by using the following equations

$$\begin{aligned} aVR &= -\frac{I + II}{2} \\ aVL &= I - \frac{II}{2} \\ aVF &= II - \frac{I}{2}. \end{aligned} \tag{2.3}$$

Hence, only lead I and II are required to obtain all other (augmented) limb leads.

In addition to the above mentioned leads, Wilson introduced the horizontal or precordial leads [Wilson 34, Wilson 44]. The *precordial leads V1-V6* are measured against a virtual ground V_W (Wilsons's central terminal) defined by

$$V_W = \frac{1}{3}(RA + LA + LL). \tag{2.4}$$

Figure 2.8b depicts the electrode positions of the precordial leads. A 12-lead ECG can be composed by all the different ECG leads mentioned above (I, II, III, aVR, aVL, aVF, V1-V6). It is often used in clinical practice, e. g. during exercise tests, since it provides the most complete diagnostic information about the cardiac activity or pathological variations [Simonson 63, Klinge 84]. If the location of the limb electrodes are relocated from the wrist and ankles to the torso, the 12-lead ECG is also called *Mason-Likar* 12-lead ECG system [Mason 66, Drew 04].

The additional precordial leads V7-V9 shown in figure 2.8b are important for the diagnosis of a posterior myocardial infarct [van Gorselen 07]. The right precordial leads $V_{3R} - V_{7R}$ are indispensable to diagnose myocardial infarcts within the right ventricle [Andersen 89].

Technical parameters

The technical parameters or properties of the ECG signal are important for its acquisition and the further processing. ECG amplitudes are in the range of $0.1\,\text{mV}$ to $5\,\text{mV}$ whereas most of the ECG's information lies in the frequency range of $0.05\,\text{Hz}$ to $100\,\text{Hz}$. Amplification and filtering of the ECG is required before the A/D conversion. Low-pass filtering is required to remove the high frequency components before sampling and A/D conversion in order to avoid anti-aliasing effects. The DC component, which is caused by the different half-cell voltages of the electrodes, is removed by high-pass filtering. Many ECG devices acquire the filtered and amplified signals with a sampling frequency of $250\,\text{Hz}$ or above.

2.1.3 The vectorcardiogram (VCG) - a spatial representation of the ECG

Overview

The vectorcardiogram (VCG) can be used for the spatial representation of the heart's electrical activity. The VCG is defined by a 3 dimensional x-, y-, z-coordinate system. The evolution of the VCG signal over time can be seen as the fourth dimension. Figure 2.9 shows how a VCG could be obtained from a set of three dedicated electrode pairs. Each electrode pair would capture the activity of the electrical heart vector in one direction. The signals of two different electrode pairs can be plotted in one diagram (initially, this was done by using an oscilloscope in the x-y-mode). This results in a plot showing the evolution of the spatial activity over time. The plot is mainly dominated by three loops: one large loop which corresponds to the QRS complex and two smaller loops corresponding to the T-wave and the P-wave. Properties of the VCG were studied for diagnostic purposes, e. g. for the estimation of respiratory information or for the detection of acute myocardial ischemia [Leanderson 03, Romero 11]. The VCG is practically used for gating cardiac MRI sequences [Fischer 99, Chia 00, Fischer 01]. Since an improved cardiac gating is one of the thesis' aims, this section shortly introduces the synthetic VCG.

Synthetic VCG Signals

Instead of using dedicated hardware and electrode configurations to estimate a VCG, other (standard) lead configurations can be used to estimated the VCG signal. During the 1980's, Dower *et al.* investigated the relation between a standard 12-lead ECG and the VCG [Dower 88]. Based on these studies, Edenbrandt *et al.* proposed a method to obtain a VCG from a 12-lead ECG using the so called *inverse Dower matrix* [Edenbrandt 88]. A synthetic VCG can be derived from the 12-lead ECG using the inverse Dower matrix

$$\mathbf{VCG} = \mathbf{D}^{-1} \cdot \mathbf{ECG}_{\text{12-lead}} \tag{2.5}$$

where $\mathbf{D}^{-1}$ is the inverse Dower matrix defined as [Edenbrandt 88]

$$\mathbf{D}^{-1} = \begin{pmatrix} -0.172 & -0.074 & 0.122 & 0.231 & 0.239 & 0.194 & 0.156 & 0.010 \\ 0.057 & -0.019 & -0.106 & -0.022 & 0.041 & 0.048 & -0.227 & 0.887 \\ -0.229 & -0.310 & -0.246 & -0.063 & 0.055 & 0.108 & 0.022 & 0.102 \end{pmatrix} \tag{2.6}$$

and $\mathbf{ECG}_{\text{12-lead}}$ is the column vector containing the precordial leads V1-V6 and limb leads I and II in the following order

$$\mathbf{ECG}_{\text{12-lead}} = \left(V_1, V_2, V_3, V_4, V_5, V_6, I, II\right)^{\mathrm{T}}. \tag{2.7}$$

The remaining leads of the complete 12-lead ECG are not considered in this transformation since these leads (III, aVR, aVL, aVF) are linear combinations of limb leads I and II (see Section 2.1.2). By rearranging Eq. 2.5, a 12-lead ECG can be estimated from a VCG by

$$\mathbf{ECG}_{\text{12-lead}} = \mathbf{D}^T \cdot \mathbf{VCG} \tag{2.8}$$

with D being defined as

$$\mathbf{D} = \begin{pmatrix} -0.522 & 0.025 & 0.865 & 1.200 & 1.118 & 0.833 & 0.655 & 0.232 \\ 0.161 & 0.167 & 0.107 & 0.124 & 0.123 & 0.073 & -0.222 & 1.069 \\ -0.928 & -1.389 & -1.271 & -0.583 & -0.069 & 0.238 & -0.0235 & -0.143 \end{pmatrix}. \tag{2.9}$$

The initial idea of Dower *et al.* was to estimate the 12-lead ECG signal from the VCG signal in order to reduce the complexity of electrode positioning [Dower 80]. This idea could be of possible technical interest for compressing the 12-lead ECG signal to a VCG of 3 leads. However, later studies

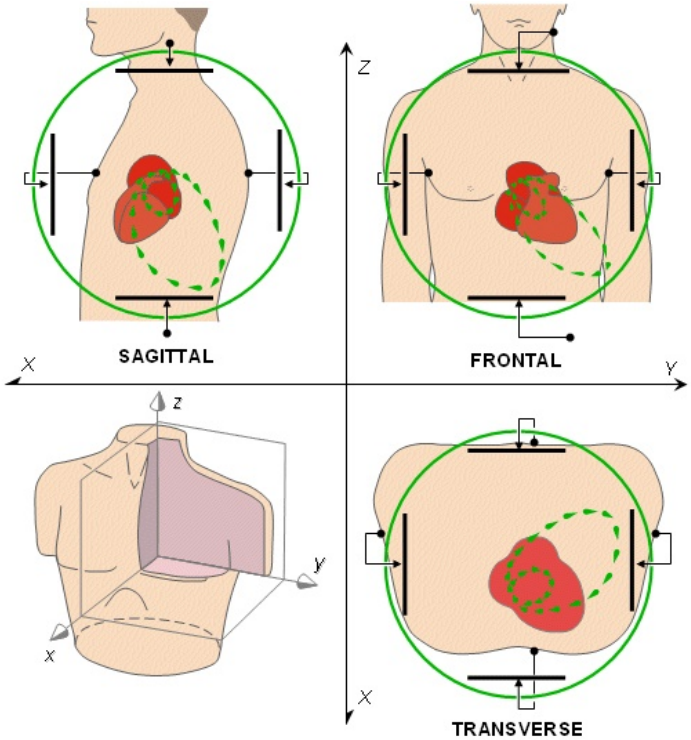

Figure 2.9.: Measurement of the vectorcardiogram (VCG) based on three dedicated electrode pairs. The measured x, y and z leads can be used for a spatial representation of the VCG (images source: [Malmivuo 95]).

revealed that the idea of reconstructing a 12-lead ECG from VCG recordings was not suitable for clinical application due to the loss of information in a VCG recording and the resulting error between an original and a reconstructed 12-lead ECG [Augustyniak 01]. Man *et al.* came up with individually calculated conversion matrices to reduce the transformation errors [Man 09]. In the context of this work, the VCG was not used for diagnostic purposes (but only for gating purposes) and hence, the standard inverse Dower matrix $\mathbf{D}^{-1}$ was applied to synthesize the VCG [Edenbrandt 88].

Two exemplary synthetic VCG signals are depicted in Fig. 2.10. The VCGs are characterized by the three loops representing the P-wave (smallest loop), by the T-wave (second largest loop) and by the QRS complex (largest loop). The outer points of the largest loop correspond to the R-peaks (black dots).

2.1.4 The pathological ECG

Figure 2.6 depicts a schematic ECG during one cardiac cycle. The origin of the different waves occurring during one (healthy, normal) cardiac cycle was described in Section 2.1.2. Pathological disorders of the myocardium manifest in the measured ECG signals. These manifold disorders can have various reasons. By analysing the P-wave, QRS complex or T-wave, inferences can be drawn about the underlying physiological variations. Only a few pathologies shall be discussed in this section - more extensive descriptions can be found in [Klinge 84, Josephson 02]. The first part of this section gives a short overview of selected *disturbances of depolarisation and repolarisation* processes. The second part names a few important *cardiac arrhythmias*.

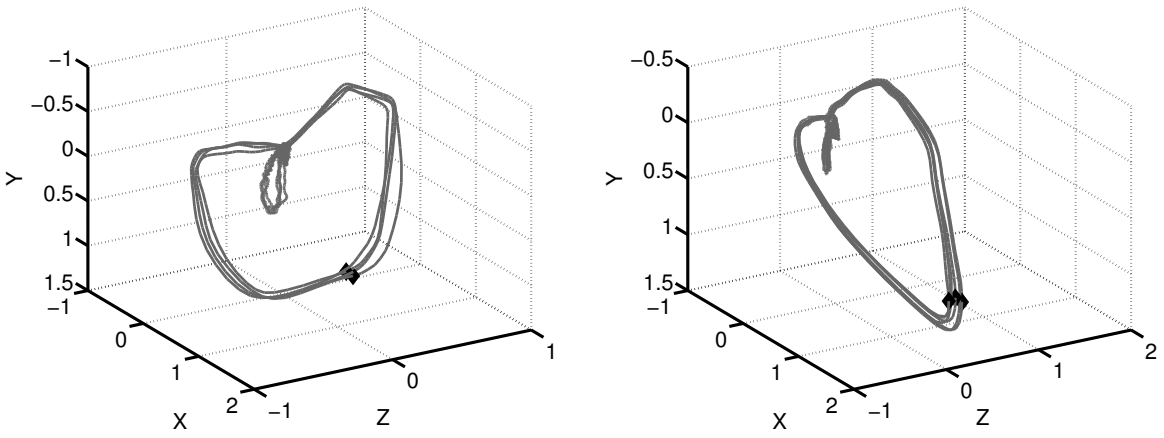

(a) Synthetic VCG, subject 1.

(b) Synthetic VCG, subject 2.

Figure 2.10.: Synthetic VCGs obtained from two subjects (a,b) based on a 12-lead ECG measurement. The black dots which are close to the turning point of the main loop mark the position of the R-peak. The two smaller loops (or 'lobes') correspond to the P-wave (smallest) and to the T-wave (second smallest). Axes values are given in [mV].

Depolarisation and repolarisation disorders

The P-wave, which marks the excitation of the atria, can be elevated and broadened when a patient suffers from a hypertrophy of the left or right atrium. A negative P-wave occurs when the heart cells are triggered by the AV node instead of the SA node: in this case, the wavefront propagates in the opposite direction (from bottom to the top). P-waves are absent when the middle AV node triggers the depolarisation or during atrial fibrillation.

The time of total depolarization of the ventricles is marked by the ST-segment. This segment is also important in cardiac diagnostics. The isoelectric level of the ST-segment can be affected by a lack of oxygen supply of the myocardium (ischemia), by a pericarditis or by an electrolyte disorder (hyperkalaemia). A horizontally elevated or depressed and downsloping ST-segment indicates a decreased coronary blood flow or myocardial ischemia[4] [Evans 09, pp.92], [Alpert 00, Hill 02, Fletcher 13]. Different ST morphologies are depicted in Fig. 2.11. Changes of the ST-segment related to a myocardial ischemia are depicted in Fig. 2.12. It can be seen that not only the amplitude of the ST-segment (revealing an elevation or depression) but also the slope (upsloping or downsloping) is of clinical relevance.

During a myocardial infarct, the Q-wave of the QRS complex can be broadened and increased in (negative) amplitude. Q-waves of very high (negative) amplitude are a sign of a hypertrophy of the septum. The whole QRS complex is broadened during a right or left bundle branch block due to a delay propagation of the wavefront within the ventricles. Hypertrophies of the right or left ventricles manifest in increased amplitudes of the QRS complex. [Klinge 84, Alpert 00]

The T-wave amplitude can increase during a hyperkalaemia or in the first phase of a myocardial infarct. Hyperkalaemia can cause a cardiac arrest and needs to be treated accordingly. A depressed

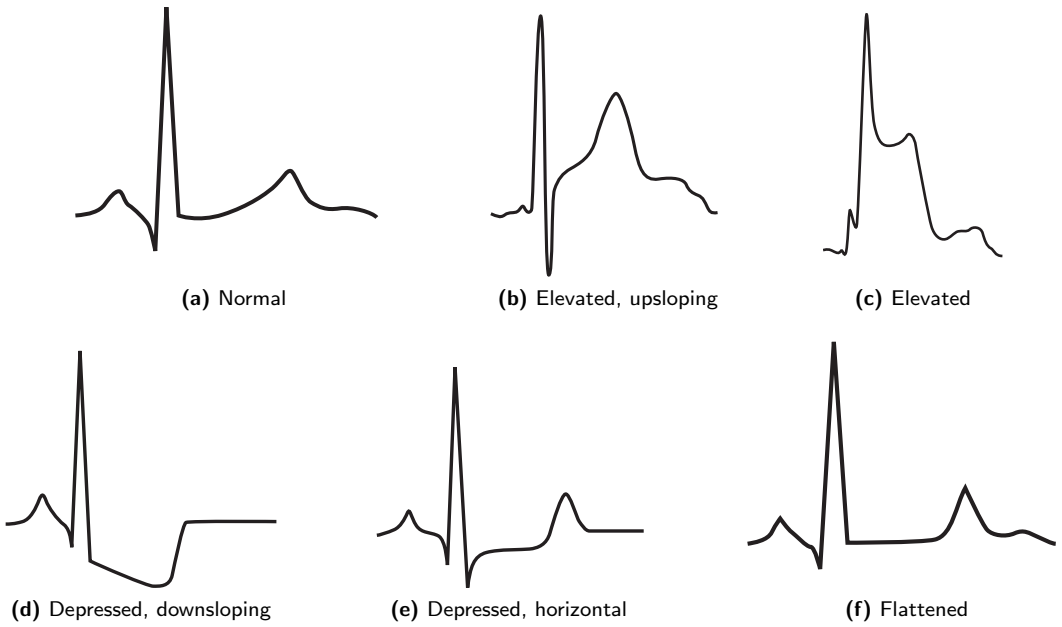

Figure 2.11.: Different morphologies of the ST-segment. (Images modified according to [Channer 02])

[4] http://lifeinthefastlane.com/ecg-library/myocardial-ischaemia/

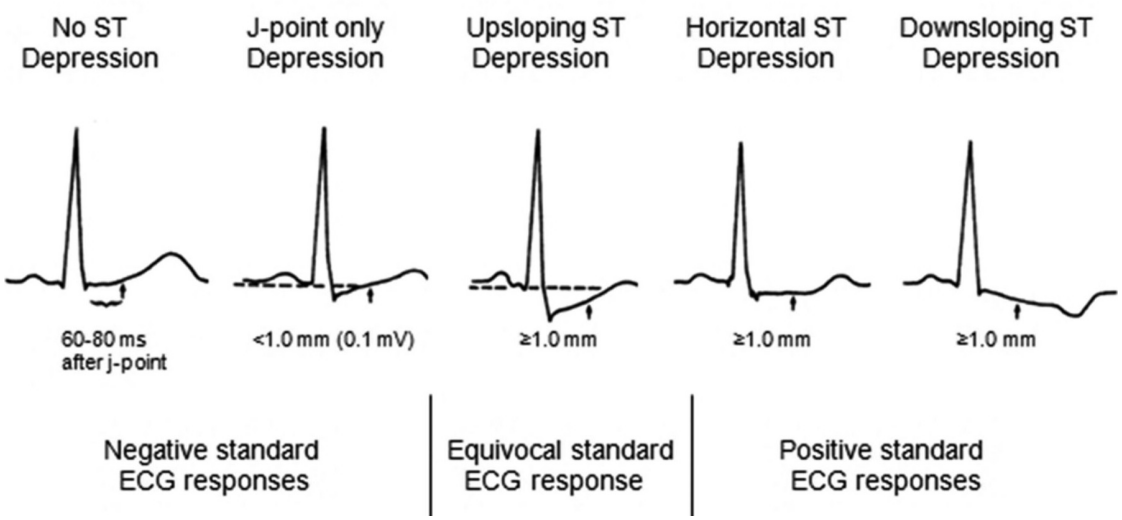

Figure 2.12.: Different morphologies of depressed ST-segments and its relation to myocardial ischemia. (Image modified according to [Fletcher 13])

T-wave can occur during a hypokalaemia or during a decreased coronary blood flow. A negative terminal T-wave indicates a specific disturbance of repolarisation: an ischemia. Figure 2.13 shows several morphological variations of the T-wave. [Klinge 84]

A delayed T-wave leads to a prolongation of the QT-interval. The QT-interval is measured between the Q-peak and the end of the T-wave (compare Fig. 2.7, p.11). Since the length of the QT-interval naturally varies with heart rate, several correction factors were proposed to compute a corrected QT-interval length, QTc [Clifford 06]. Prolonged QT-intervals in patients suffering from intraventricular conduction defects and cardiac dysfunciton are considered as an independent risk factor for sudden death due to cardiac arrest [Algra 91]. QT prolongations can also be caused by drug administration. A general threshold for the identification of a drug induced QTc prolongation does not exist. However, it should raise concerns if the QTc is prolonged by more than 30 ms [Steinberg 09].

Cardiac arrhythmias

Cardiac arrhythmias are another source for the pathological ECG [Klinge 84]. These arrhythmias can be either caused by *1)* the pacemaker system or *2)* the conduction system of the heart. As described in Section 2.1.2, several cardiac pacemakers exist (e. g. the SA node or the AV node). The corresponding arrhythmias are named after the place of origin: sinus bradycardia or the sinus tachycardia are caused by irregular behaviour of the SA node. Atrial flutter or fibrillation can be observed if the center of the pacemaker is not within the SA node but elsewhere in the atria. Both, premature atrial contractions (PACs) and premature ventricular contraction (PVCs) are described as extrasystoles. PACs or PVCs are extra beats, which occur earlier than a regular beat and can disturb the underlying cardiac rhythm. In the case of early occurrence, the ventricles are not fully filled with blood leading to a reduced cardiac output during such an extra beat. PACs or PVCs can occur in healthy and pathological subjects. The second group of arrhythmias concerns the conduction system of the heart. A very common conduction problem is caused by the AV node. The AV node is the (only) electrical connection between the atria and the ventricles. The conduction of the wavefront from the atria to the ventricles through the AV node can be delayed (prolonged PQ-intervals, *first degree AV block*), partly blocked (delay gets

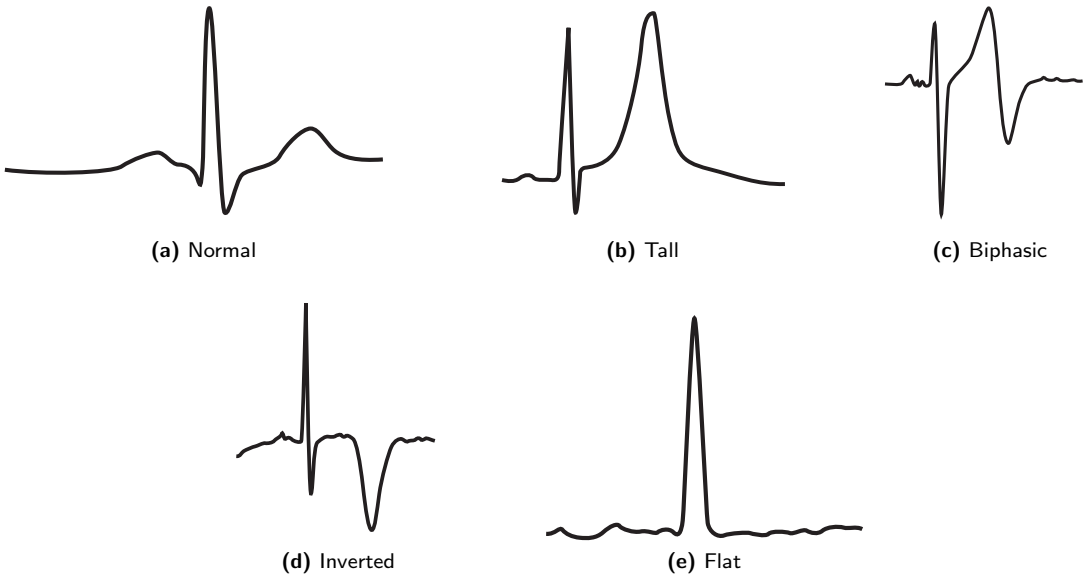

Figure 2.13.: Different morphologies of the T-wave. (Images modified according to [Channer 02])

longer and longer until conduction is completely blocked, *second degree AV block*) or is completely blocked (*third degree AV block*). A third degree AV block is one of the worst rhythmic disorders. In this case, the contraction of the ventricles either stops (due to the lack of an action potential) or a compensating but slower and asynchronous heart rhythm is generated by AV pacemakers cells or the tertiary pacemakers (bundle of His, Purkinje fibres). [Klinge 84]

Measurements during interventions in the heart catheter lab

In heart catheter labs, ECGs are not only measured at the body surface but also directly within the heart. Specialised catheters, with one or more electrodes, can be placed in dedicated locations to locally gather information about the activity of the right atrium, the coronary sinus, the bundle of His, the AV-node or other parts of the heart [Josephson 02]. The intracardiac information is combined with the information obtained from the 12-lead surface ECG to draw conclusions about an observed pathology. For example, the onset of atrial activation can be derived from the surface ECG (P-wave) whereas the His bundle electrogram (measured by an intracardiac catheter) is used to measure the activation onset of the AV-node [Khurana 06, p.269]. This measurement can be used to reveal conduction problems in the atrium. Catheter can either be used to measure the cardiac potentials or they can be used for therapeutic purposes. Therapeutic interventions can include the active stimulation of the cardiac tissue ('pacing mapping') [Haas 11, p.75], catheter ablation of pathological tissue ventricular in tachycardia [Tung 10] or during balloon dilatation. These therapeutic interventions are always combined with the measurement of surface and intracardiac ECG signals. Another measurement example in the heart catheter lab is the analysis of the QT-interval during an balloon angioplasty. Corrected QT-interval measurements (QTc) allow the detection of early transmural ischemia in patients undergoing a balloon angioplasty [Kenigsberg 07]. It was shown experimentally that during such ischemias, a prolongation of the QT-interval occurs before a changing T-wave or an elevation/depression of the ST-segment.

This section showed that the measurement of the ECG's different fiducials such as the P-wave, the QRS complex, the T-wave, the ST-segment or QT-interval are of potential interest in MRI-guided cardiac interventions, for patients undergoing stress MRI or during anaesthesia. A more detailed motivation and clinical application such as interventional MRI procedures are described in Chapter 3.

2.1.5 Heart rate variability

Heart rate is not constant but varies from beat-to-beat (except for pathological cases). These variations are mainly controlled by the autonomous nervous system (ANS) [Ravenswaaij 93, Stein 94]. The ANS is divided into a sympathetic and a parasympathetic branch. One well known variation is the respiratory sinus arrhythmia which causes an increases of the heart rate during inspiration and a decrease during expiration. Other variations of the heart rate can be caused by mental or physical stress or during different stages of sleep [Ravenswaaij 93, Stein 94]. HRV can be described by its spectral parameters. HRV analysis usually covers three frequency bands ranging from $0.003\,\text{Hz}$ to $0.04\,\text{Hz}$ (VLF band), from $0.04\,\text{Hz}$ to $0.15\,\text{Hz}$ (LF band) and from $0.15\,\text{Hz}$ to $0.4\,\text{Hz}$ (HF band). It was found that sympathetic activity is mostly represented by the LF band whereas parasympathetic activity is mostly represented by the HF band.

In the course of this thesis, HRV is important for the simulating ECG signals. The simulation of ECG signals requires a simulation of an underlying time-series representing the occurrence times of the QRS complexes. The simulation of realistic HR time-series requires its spectrum to reflect the characteristic properties of the HRV spectrum (e. g. the presence of Mayer waves or RSA).

2.2 Magnetic resonance imaging (MRI)

Physical basics

Clinical MRI is mainly based on signals generated from water (or more specifically from hydrogen protons), which is abundant in tissue. In a simplified model, the hydrogen proton (the nucleus of the hydrogen atom) can be considered as a magnet which is spinning along its axis. This proton or spin has a magnetic moment $\vec{\mu}$. Without an external magnetic field, all spins are oriented randomly in space. To align the spins in a certain direction, magnets with magnetic flux densities $\mathbf{B}_0$ of $0.3\,\text{T}$ to $9.4\,\text{T}$ are used in human MRI scanners. Such high magnetic flux densities is usually achieved by running the magnet in a superconducting state. This is achieved by cooling the coils of the magnetic close to the absolute zero point using liquid helium[5]. [Chen 89]

The spins (or their magnetic dipole direction) are aligned in parallel (low energy state) or antiparallel (high energy state) to the direction of $\mathbf{B}_0$ whereas more spins are aligned in parallel[6]. The remaining magnetisation is called the net magnetisation $\vec{\text{M}}$. This net magnetisation is used to generate an MRI signal. While the spins are aligned with $\mathbf{B}_0$, they perform a precession with the so called Larmor

[5] Most magnets use coils made of niobium-titanium (NbTi) which goes into a superconducting state at temperatures below $-263.95\,^{\circ}\text{C}$

[6] The distribution between both states follows a Boltzmann distribution which depends on the magnetic flux density $\mathbf{B}_0$ and on the temperature T.

frequency

$$f_L = \gamma' \cdot \mathbf{B}_0 \tag{2.10}$$

where γ' is the gyromagnetic ratio. For hydrogen, $\gamma' = 42.576\,\text{MHz/T}$.

To *generate an MRI signal*, the aligned spins have to be moved out of their resting state position. This is achieved by applying an external magnetic field B_1 which is perpendicular to $\mathbf{B}_0$ and hence, perpendicular to the net magnetisation vector $\vec{M}$. Since $\vec{M}$ is precessing with the Larmor frequency f_L, B_1 needs to rotate as well in order to be permanently perpendicular to the net magnetisation vector $\vec{M}$. This is achieved using dedicated radio frequency coil constructions which generate a circular polarised magnetic field B_1 rotating at the Larmor frequency. After switching off the B_1 field, the net magnetisation vector $\vec{M}$ returns to its initial orientation. Figure 2.14 depicts the excitation of the spins and the measurement of the signal used for generating an MR image.

Encoding of the MR signals is performed by applying additional gradient magnetic fields. Gradient magnetic fields are applied in x, y and z directions and vary generally linearly along these axes. These gradient fields are superimposed to the scanner's static magnetic field $\mathbf{B}_0$. With the gradients applied, the Larmor frequency of an object or patient depends on the location inside the MR scanner (see Eq. 2.10). Spatial encoding using the gradients is generally performed with in the following three steps: *1)* slice selection, *2)* phase encoding and *3)* frequency encoding. The first gradient (e. g. in z-direction) is applied at the same time as the B_1 field so that only spins in a certain slice are excited by the radio frequency magnetic field. Slice thickness can be controlled by the gradient magnitude and by the bandwidth of B_1. The second gradient (e. g. in y-direction) is applied for a short period of time. During this time, the spins will have different frequencies at the different spatial positions, which will also alter the phase relations between different spins. After switching of this gradient, all spins have the same frequency again but will have different phases along the direction of the gradient. The third gradient (e. g. in the x-direction) is similar to the second gradient. However, to avoid another phase encoding, this gradient is switched on during the readout phase of the MR signal. This enables a frequency encoding but suppresses an additional phase shift[7]. Since those signals which come from spins with different phase but with the same frequency cannot be separated, several phase encoding steps are required to form an MR image. The data collected during the different steps is written into the so called k-space matrix. By applying an inverse Fourier transform to the k-space, the final MR image is obtained. [Chen 89]

Not only spatial information can be encoded in the MRI data, but also some functional information. One important aspect in cardiovascular MRI is the measurement of blood flow. Blood flow measurements utilize the fact that blood is moving whereas the surrounding tissue is static [Siemens AG 04]. An example for the blood flow estimated using MRI is depicted in Fig. 2.15.

[7] In a practical sequence, the frequency encoding gradient also alters the phase in the frequency encoding direction. To minimize phase shift in the frequency encoding direction, an additional frequency encoding gradient is switched before but in the opposite direction (inverse polarity).

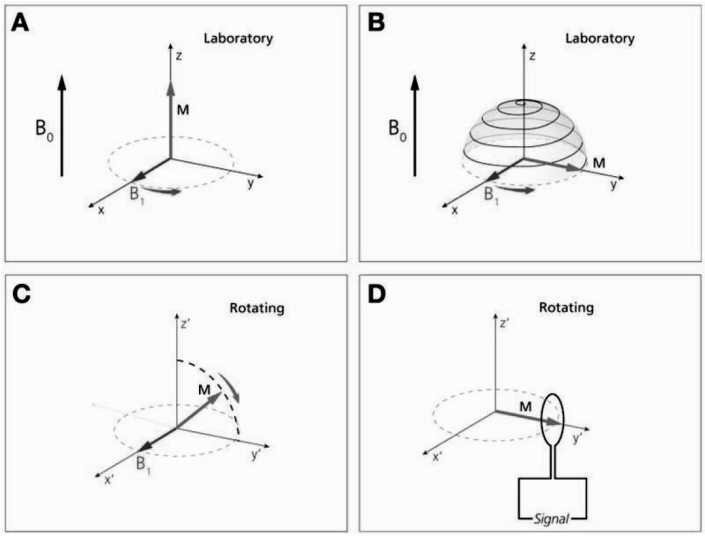

Figure 2.14.: Schematic of spin excitation and measurement of an MR signal. The laboratory reference frame utilizes a fixed coordinate system visualizing the precession of the net magnetisation vector (A,B). The rotating reference frame rotates with the Larmor frequency f_L around the z-axis (C,D). This latter representation simplifies the description of the net magnetisation vector $\vec{M}$. (image modified after [Kwong 07]).

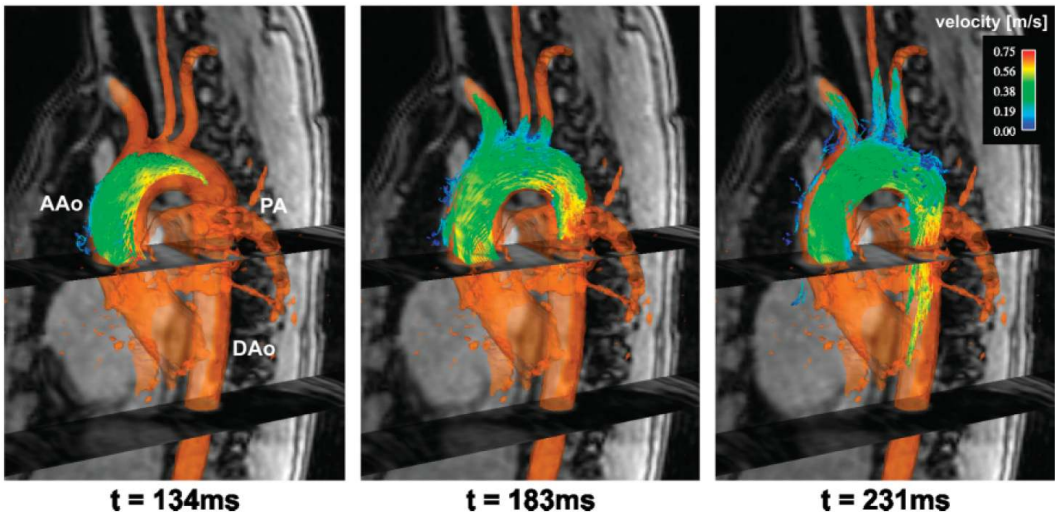

Figure 2.15.: MRI scan of the heart and surrounding vessels showing the blood flow velocity in the aorta in different phases of the sytole. (Image source: [Markl 07])

Technical parameters

MRI scanners are usually categorised by their static magnetic field strength, $\mathbf{B}_0$. Most clinical MRI scanners have magnetic strength of $1\,\mathrm{T}$, $1.5\,\mathrm{T}$ or $3\,\mathrm{T}$. Research scanners, which are not used during clinical routine, can have larger magnetic field strengths of $7\,\mathrm{T}$, $9.4\,\mathrm{T}$, $10.5\,\mathrm{T}$ or $11.7\,\mathrm{T}$. The SNR increases with the magnetic field strength, i. e. the SNR at $3\,\mathrm{T}$ is approximately twice as high as at $1.5\,\mathrm{T}$. However, the T1 relaxation time also increases with the static magnetic field strength [McRobbie 06, pp. 155-156]. As described by Eq. 2.10, the Larmor frequency depends on the magnitude of the static magnetic field. For generating clinical MR images it is important to have a homogeneous magnetic field distribution in the center of the scanner. The spatial dimension of the homogeneous magnetic field describes the actual field of view. State-of-the-art MRI scanners can have a field of view of

approximately $40\,\text{cm} \times 40\,\text{cm} \times 40\,\text{cm}$.

The gradients, which are required for the (spatial) encoding of the MR signals, have amplitudes in the range of $10\,\text{mT/m}$ to $100\,\text{mT/m}$. The slew rates of the gradients typically cover a range of $25\,\text{mT/m/ms}$ to $160\,\text{mT/m/ms}$.

High RF power is required to excite the spins and move them out of their equilibrium state. RF amplifiers provide power in the range of approximately $30\,\text{kW}$ to $50\,\text{kW}$ which is similar to the power used by FM radio broadcasting stations. Tissue heating can occur due to the absorption of the RF energy. This means that the applied RF energy needs to be limited and adjusted depending on scanned part of the body (e. g. head, thorax or extremities), the size and the weight of the patient. The center frequency of the RF signals corresponds to the Larmor frequency of the spins or protons. The bandwidth of the RF signals ranges from $5\,\text{kHz}$ to $100\,\text{kHz}$.

Safety issues

Several safety issues need to be considered during an MRI scan. Any magnetic objects should be avoided in the MRI scanner since such objects experience large forces due to the existence of the static magnetic field. Special attention is required regarding the RF magnetic fields used in the MRI scanner. The RF signals or energy can couple into conducting structures like cables used for ECG signal acquisition or in cardiac catheters. Due to the large RF power, heating of the cables can occur under certain conditions which can cause severe patient injuries [Kugel 03, Mattei 08, Haik 09, Nordbeck 12]. There is also a potential risk of heating up implants or other conducting structures such as tattoos. Electronic devices which have not been tested for MRI usage (such as patient monitors, pacemakers, etc.) might not function properly inside the MRI environment or may even harm the patient.

Cardiac MRI

Cardiovascular magnetic resonance (CMR) covers the morphological and functional imaging and diagnosis of the heart. Morphological diagnosis includes imaging of the heart valves, wall thickness or size of the heart. Regarding interventional MRI procedures, MRI allows the detection of scar tissue, which is important for catheter-based ablations [Lederman 05, Dukkipati 08, Schmidt 09, Koopmann 13]. Functional imaging includes the analysis of heart motion throughout the cardiac cycle, blood flow in the coronary arteries or the estimation of the cardiac output. With CMR images covering a complete heart cycle, it is possible to detect wall motion abnormalities as observed during ischemia [Nagel 99].

Acquiring high-quality CMR images of the beating heart remains a technical challenge. Image artefacts can occur due to complex heart motion, respiratory movements, movements of the blood vessels, flow patterns and patient movement [Strohm 06]. The problem is that the acquisition time for one or more MR images is longer than the length of one RR-interval, i. e. longer than one cardiac cycle. During the cardiac cycle, the heart is moving (contracting, relaxing) in order to eject blood into the arteries and to fill the atria and ventricles with blood. These movements need to be considered during image acquisition, i. e. the acquisition of the MRI data has to be synchronised with the cardiac. Otherwise, the resulting images would suffer from motion blurring and would not be of diagnostic value. This problem is encountered in Section 3.4.

2.3 The need for an ECG during MRI

2.3.1 ECG-based gating for cardiac motion compensation

CMR requires a synchronisation between the acquisition of the MR image data (or more precisely the k-space data used to build the MR images) and the cardiac activity. This synchronisation is called gating or triggering[8]. The general principle of gating in CMR is depicted in Fig. 2.16. For most CMR sequences, the acquisition of k-space data required for an MR image is split over several cardiac cycles [Nacif 12]. It has to be considered that heart motion is not the same between the different beats. Heart rate and consequently heart motion naturally varies on a beat-to-beat basis [Innes 93, Thompson 06]. Gating is used to acquire the k-space data at the same time-point or phase in every cardiac cycle, e. g. during the ventricular diastole [Fernandez 10]. Instead of acquiring k-space data in one phase of the cardiac cycle, the data can be acquired from several phases. The result is either a static image in a certain cardiac phase or a sequence of MR images covering several phases of the cardiac cycle (cine imaging) [Strohm 06]. Figure 2.17 depicts the a normal MR image (non-gated) and a gated MR image of the thorax including the heart. While the non-gated image (Fig. 2.17a) is affected by motion artefacts (heart motion and respiratory motion), the anatomy is clearly visible in the image where the acquisition was gated using the ECG signal (Fig. 2.17b). This example shows the importance of a reliable gating in CMR.

The most established way to synchronise the acquisition of the k-space data with cardiac activity is based on the ECG signal [Strohm 06, Scott 09]. At the same time, gating is the most important application for an ECG during MRI. As described in Section 2.1.2 , the ECG signal provides an information about the cardiac cycle length and the cardiac phase. Usually, the R-peak or QRS complex, which is the most dominating feature of the ECG, is used to control the acquisition of new k-space data. The cardiac cycle can be roughly divided in a systolic and diastolic phase. The R-peak marks the beginning of the ventricular systole whereas the diastolic phase starts at the time where the aortic valve closes (compare Fig. 2.7, page 11). In CMR, one usually tries to acquire MR data in those phases of the cardiac cycle, where the heart is in an nearly immobile position. There are two periods of isovolumetric contraction and relaxation at the beginning and at the end of the systolic phase which can be used.

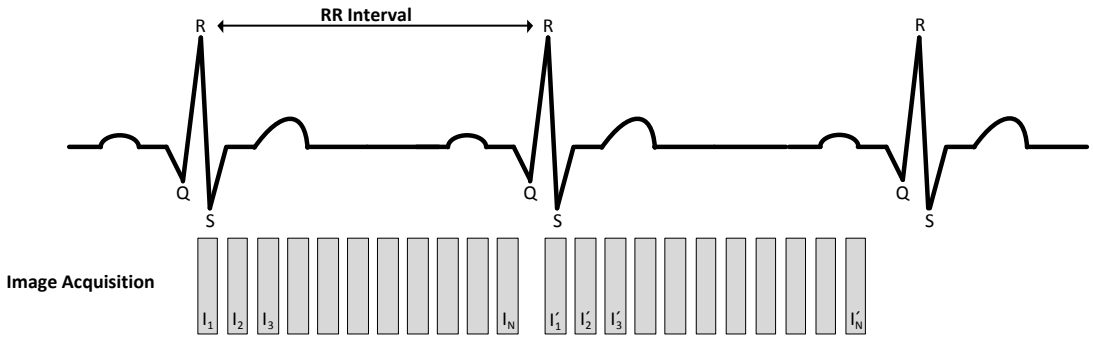

Figure 2.16.: The stepwise k-space acquisition of an cardiac MR image is gated (or triggered) by the ECG's R-peak. To generate an image at one point of the cardiac cycle (e. g. at the location of I_3), k-space data is acquired over several cardiac cycles (I_3,I'_3, ...) in the same phase of the cardiac cycle. Once the k-space is filled with the data, the MR image for one point in the cardiac cycle can be computed.

[8] Both terms are used interchangeably within the thesis.

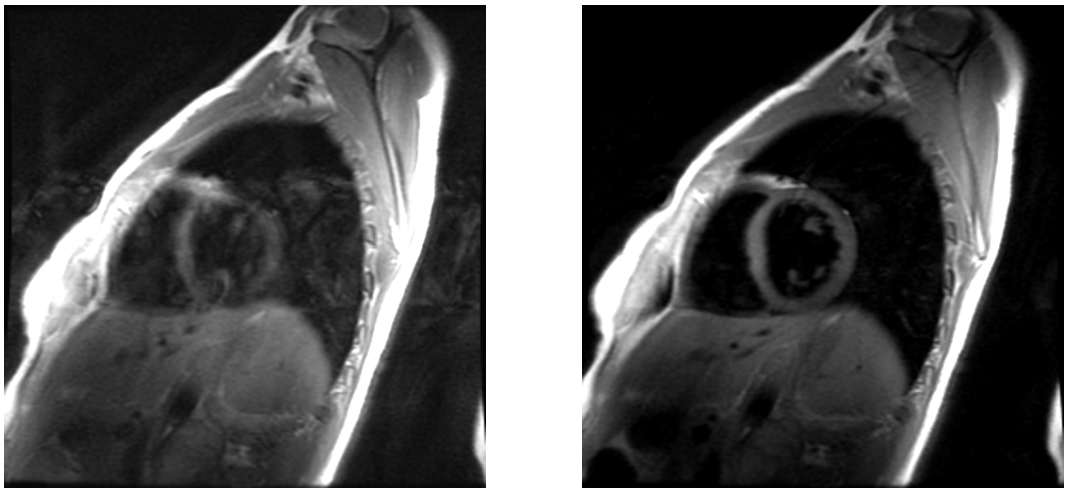

(a) Non-gated MR image of the thorax. **(b)** Gated MR image of the thorax.

Figure 2.17.: MR images of the thorax covering the heart acquired without (a) and with (b) gating using the ECG signal. Severe artefacts due to heart and respiratory motion are visible in the non-gated image (a). Using ECG-based gating, motion artefacts can be suppressed, which enables a better analysis of anatomical structures, e. g. of the ventricle wall thickness (b). (Image courtesy: Julien Oster, University of Oxford, UK.)

The end-systolic phase has a length of 60 ms to 80 ms [Shechter 05]. In diastole, least motion occurs during the mid-diastolic phase. The length of the mid-diastolic phase depends on the heart rate: it has an approximate length of 240 ms at a heart rate of 60 bpm and shortens to approximately 75 ms at a heart rate of 80 bpm [Strohm 06, p.10]. Assuming that the repetition time of two consecutive MR data measurements (phase encoding steps) is TR $= 4$ ms, 50-60 measurements can be made at 60 bpm but only 18 at 60 bpm within the mid-diastolic phase. Especially in patients with higher heart rates, the end-systolic phase can be longer than the mid-diastolic phase [Jahnke 06]. Imaging during the end-systolic phase can be advantageous since it was shown that the thin right ventricle wall is better depicted than in the standard mid-diastolic acquisitions [Fernandez 10].

Cardiac gating can be achieved by two different strategies [Scott 09, Nacif 12]. In *prospective* gating, k-space data acquisition is directly synchronized with the cardiac cycle during the acquisition process. Therefore, a predefined number of k-space acquisitions is performed in each cardiac cycle using predefined delays with respect to the ECG's R-peak. In *retrospective* gating, MR images and the ECG signal are acquired simultaneously. The cardiac phase of the acquired MR images is determined retrospectively based on the ECG signals.

Several CMR sequences such as the black blood imaging sequences require a prospective gating regime. Black blood sequences play out inversion recovery pulses before or during the R-peak in order to have an inversion time of the blood while acquiring the MR signal [Slavin 06, Oster 08, Frauenrath 10a]. To suppress the signal of 'fresh' blood flowing into the currently imaged plane, a precise triggering based on an reliable R-peak detection is required [Strohm 06]. RRI prediction was proposed to enable black blood imaging even during the end-systolic phase (instead of the usually used end-diastolic phase) [Oster 08, Fernandez 10].

Due to the natural heart rate variability, the last 10 % of an RRI are usually not sampled during a prospectively gated sequence. Otherwise, if one would try to acquire the k-space data for the complete cardiac cycle in a prospectively gated sequence, the gradient magnetic fields could prevent

the detection of the next QRS complex. The gradient magnetic fields affect the ECG signals in two different ways: they can induce currents inside the tissue and directly couple into the wire of the ECG device [Felblinger 99, Abächerli 05, Wu 11]. Both effects lead to a distortion of the ECG signal. Hence, additional methods are required to filter the gradient artefacts in order to enable a reliable QRS detection [Odille 07, Park 09, Oster 09b, Oster 09a, Sansone 10].

False R-peak detections or cardiac arrhythmias can affect the quality of CMR images in different ways. One problem is shown in Fig. 2.17. False R-peak detections and the resulting false assumptions of RRI length can also lead to artefacts in black blood images. R-peak detection with a high jitter can cause blurred MR images or a wrong estimation of blood flow in phase-contrast MRI sequences [Thompson 04].

2.3.2 Patient monitoring during MRI

Vital signs monitoring can be achieved by different methods including measurements of the blood pressure (invasive or non-invasive), pulse oximetry, gas analysis, ECG, auscultation of the heart sounds or body temperature. The American Society of Anesthesiologists (ASA) states that the patient's ECG has to be displayed during anaesthesia [ASA 11]. This requirement is even more important in an interventional MRI (iMRI) operating theatre. Due to the construction of most MR scanners, the patient may usually not be observed by the anaesthetists. Hence, the anaesthetists are prevented from visually assessing the patient and have to rely on the monitored physiological signals. Figure 2.18 depicts typical scenes in iMRI operating theatres using different MR scanner construction types (closed bore and open bore). Also for intensive care unit (ICU) patients, a reliable monitoring would be required while inside the MRI scanner [Kempen 06].

(a) MRI-guided EP procedure using the IMRICOR system at the Heart Centre Leipzig, Germany. (Image modified according to [Sommer 12].)

(b) Combined MRI and X-ray suite (XMR) at the Evelina London Children's Hospital / St. Thomas' Hospital, London, UK. (Image courtesy: Johannes Krug.)

Figure 2.18.: Examples for two different interventional MRI scenarios. In both examples, MRI is used to guide surgical tools – e. g. catheters or biopsy needles – in minimalinvasive procedures. The combined XMR suite (b) is used for (paediatric) cardiac interventions. While X-ray angiography is used to manoeuvre the catheter in the blood vessels or the heart, MRI is used for detailed anatomical or functional imaging.

During MRI, the ECG is required for patient monitoring under different circumstances, e. g. in cases such as

- MRI guided interventions using anesthesia [ASA 11],
- MRI guided catheterization of the myocardium and electro physiological (EP) diagnostics and ablations [Josephson 02, Razavi 04],
- stress or exercise MRI (either induced by drugs or physical exercise) causing ischemias [Simonson 63, Hill 02],
- intensive care unit (ICU) patients [Balaji 02] and others.

During anaesthesia and surgeries, cardiac arrhythmias occur relatively often. A larger study involving 112721 anaesthetic procedures documented over a 9-year period revealed that cardiac arrhythmias constitute the most common intra-operative complication faced by the anaesthetist [Cohen 86]. There is a wide variety of peri-operative arrhythmias [Dash 02]. A wandering pacemaker which can be diagnosed by a variable P-wave morphology with changing PR interval often occurs with potent volatile anaesthetics. Premature atrial beats are quite common under general anaesthesia precipitated by a myocardial ischemia or intraatrial catheters. Atrioventricular blocks like the first degree heart block can occur when potent volatile anaesthetics are used - especially in patients on beta blockers. During these AV blocks, PR intervals exceed a length of 200 ms. Second degree (type I and II) and third degree heart blocks can also be observed under anaesthesia. Cardiac ischemia during anaesthesia is another very common complication [Smith 85, Mangano 90, Ludbrook 05].

Cardiac catheterization can lead to arrhythmias, e. g. tachyarrhythmia or to conduction blocks [Bogaert 04, p. 524]. These arrhythmias can be recognized by studying the patient's ECG signal. In EP diagnostics, the usage of an intracardial and a surface ECG is required for a complete and reliable diagnosis (see Section 2.1.4). The combination of both ECG signals is commonly used in X-ray EP-catheter labs. Since MRI-guided cardiac interventions become more and more important, there is an increasing demand for a diagnostic ECG during MRI [Razavi 04, Lederman 05, Dukkipati 08, Schmidt 09, Koopmann 13, Piorkowski 13]. Despite the high technical challenges of performing an EP procedure inside an MRI scanner (instead of performing it in an X-ray catheter lab), MRI offers many advantages. For example, one can distinguish normal tissue from scar tissue in MRI, which is not possible in X-ray images. This is important for controlling areas, which were treated by an ablation catheter or for the localisation of infarction substrate [Dukkipati 08, Gutberlet 12, Ranjan 12, Sommer 13].

Heart rate variability (HRV) is another cardiovascular parameter, which can be of interest during an MRI scan. HRV measures are derived from the RRI time series (see Section 2.1.5). Hence, as long as the ECG's QRS complexes can be detected reliably during MRI, HRV analysis is possible. HRV analysis was recently combined with fMRI measurements in order to combine the information about the autonomous nervous system (HRV) with the activity in the brain (fMRI) [Napadow 08, Kim 11]. Due to a higher signal-to-noise ratio, 7 T MR scanners are preferred for fMRI studies [Beisteiner 11]. Hence, this requires QRS detection methods that work reliably at high magnetic field strengths. Although HRV analysis combined with fMRI scans is currently more a research application and not used in clinical routine, it could become important in the future.

3

Problem formulation, impact of the MHD effect on the ECG and state-of-the-art

3.1 Overview

During MRI, an ECG is often required for gating cardiac image sequences or for patient monitoring (see Section 2.3). However, the quality of an ECG signal can be severely degraded during an MRI procedure. One can identify three principal reasons for this degradation: *1)* the RF pulses, *2)* the switched gradient magnetic fields and *3)* the magnetohydrodynamic (MHD) effect which is caused by the interaction of the blood flow with the static magnetic field.

The influence of the RF pulses can be reduced by a careful design of the ECG hardware. Special attention has to be paid to the ECG cables and electrodes in order to avoid resonant effects which could cause a heating of the wire or the electrodes (see Section 2.2) [Kugel 03, Mattei 08, Weiss 11]. Since the frequencies of the ECG signal and of the RF pulses usually differ by at least 6 orders of magnitude, the RF signal components can be attenuated using analogue low pass filters [Shetty 88, Tsitlik 93]. However, a demodulation of the RF impulses can occur at the first stage of the amplifier which can cause a distortion of ECG signal. This problem can be reduced or circumvented by careful hardware design.

The switched gradient magnetic fields can induce currents in the conductive tissue of the patient or in the ECG cables [Felblinger 99, Schaefer 00]. In most cases, gradient artefacts can be distinguished from the ECG signals due to their high slopes and amplitudes. Figure 3.1 depicts an exemplary clean reference ECG acquired outside the MR scanner and an ECG of the same patient acquired inside a 3 T MR scanner during an EPI imaging sequence. In order to enable a reliable QRS detection during MR scanning, dedicated filtering methods are required to eliminate the gradient artefacts. Several filtering

algorithms exist which enable a suppression of the gradient artefacts in most cases. For example, suppression of the gradient artefacts can be achieved using extended Kalman filters (EKF) [Oster 10], independent component analysis (ICA) [Oster 09b] and adaptive filters or finite impulse response filters [Abächerli 05, Park 06, Odille 07, Park 09, Sansone 10, Wu 11]. Within this thesis, gradient artefacts are not considered since MR imaging is switched off during ECG signal acquisition.

The signals caused by the MHD effect distort the ECG signals and obscure most of their diagnostic information. Since the static magnetic field $\mathbf{B}_0$ cannot be switched off during the normal operation of the MR scanner[1], the MHD effect is permanently present in the ECG signal. The MHD effect is responsible for ECG-based gating problems at higher magnetic field strengths ($\geq$7 T) and for the limited diagnostic value of the ECG at all field strengths. Hence, this chapter gives a more detailed exploration of the MHD effect and its consequences.

The theory of the MHD effect, its relation to the cardiac cycle and different MHD simulation models are described in Section 3.2. In Section 3.3, the MHD effect observed in real ECG measurements is investigated considering different parameters such as the strength and orientation of the magnetic field or the variation of the MHD effect between different subjects. Existing solutions for gating and patient monitoring applications are reviewed and discussed in Sections 3.4 and 3.5. A summary of the challenges, existing solutions and remaining problems is given in Section 3.6. Finally, the objectives of this thesis, which arise from the remaining limitations and from the ongoing developments and trends in MRI and CMR are presented in Section 3.7.

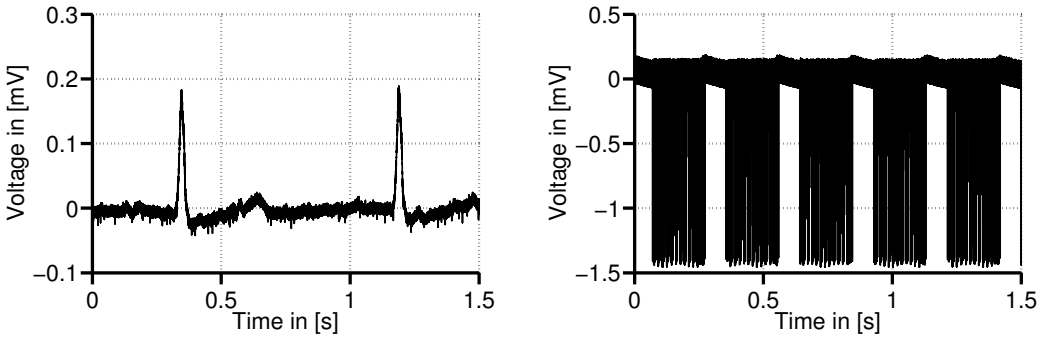

(a) ECG acquired outside the MR scanner.

(b) ECG acquired inside the MR scanner during an EPI sequence.

Figure 3.1.: Comparison of ECG signals acquired outside (a) and inside a 3 T MR scanner (b) during an EPI imaging sequence. The gradient artefacts cover the information of the underlying ECG.

[1] Assuming an MR scanner with a superconducting magnet.

3.2 The magnetohydrodynamic (MHD) effect

3.2.1 Physical basics

The magnetohydrodynamic (MHD) effect results from the interaction between the pulsatile blood flow, which is caused by the rhythmic action of the heart and the static magnetic field of the MR scanner, $\mathbf{B}_0$. Blood plasma, which makes up about $60\,\%$ of the total blood volume, contains approximately $10\,\%$ solutes including electrolytes such as Na^+, Cl^- or HCO_3^- ions and non-electrolytes (glucose, urea) [Schmidt 07, p.525]. The ions (electrolytes) are moving inside the vessels where they experience a force due to the presence of the MR scanner's static magnetic field. This force is known as Lorentz force, $\vec{F}$, where the force per charge is given as

$$\frac{\vec{F}}{q} = (\vec{v} \times \vec{B}). \tag{3.1}$$

It depends on the magnitude and orientation of the blood flow velocity $\vec{v}$ of the charged particles q with respect to the $\vec{B}_0$ field. This force causes the ions to move perpendicularly to the direction of the blood flow and perpendicularly to the MR scanner's static magnetic field. The ions accumulate near the vessel's wall leading to a potential difference across the vessel that may be expressed as

$$V \propto \int_0^l \vec{v} \times \vec{B}_0 \, d\vec{l} \tag{3.2}$$

where l is the diameter of the vessel. The voltage estimated using Eq. 3.2 is called Hall voltage. This basic principle is used in electromagnetic flowmeters as depicted in Fig. 3.2. Figure 3.3 schematically shows how the static magnetic field $\mathbf{B}_0$ affects the moving ions inside the cross section of a blood vessel.

It has to be mentioned that the above equations are a simplification of the real scenario. The Lorentz equation and the Hall voltage are estimated for a conductor with a rectangular cross section. The aorta and other blood vessels have an approximately oval cross-section. Additional parameters such as the density, conductivity and viscosity of blood, the aortic blood pressure or magneto fluid parameters such as the (magnetic) Reynolds number or the Hartmann number have to be considered to estimate the voltages induced across the vessels [Kinouchi 96, Gupta 08]. Maxwell's equations are used to describe the interactions between the moving ions and the electromagnetic fields. The flow can be described using the Navier-Stokes equations. By coupling the flow and electro-dynamical equations, the MHD effect inside a blood vessel can be estimated more precisely [Gupta 08, Martin 11a]. To estimate the resulting body surface potentials, additional transfer functions are used [Martin 11a]. For a more complete description of the underlying physics of the MHD effect, of the flow mechanisms and the coupling with the Maxwell equations, the reader is referred to [Keltner 90, Kinouchi 96, Misra 07, Das 10].

The consideration of the blood flow profiles is an important and critical aspect for a realistic estimation of the MHD voltages. Viscosity and wall sheer stress should also be considered for describing the flow close to the vessel walls in analytical calculations. Turbulent flow profiles have to be expected

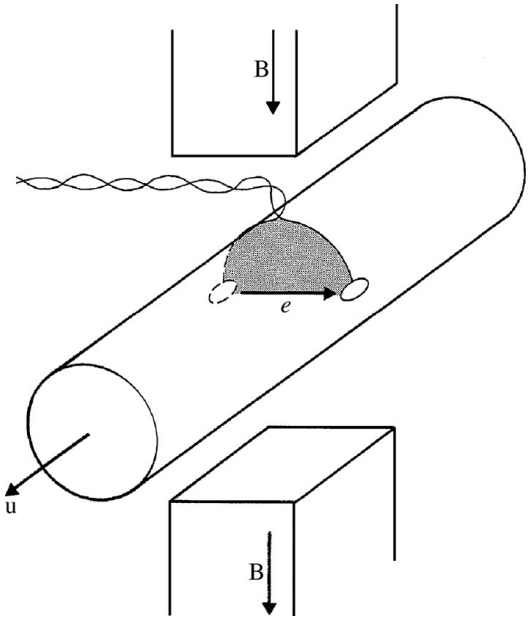

Figure 3.2.: Electromagnetic flowmeters utilize the same physical effect which causes the MHD signal inside the MRI scanner. (Image source: [Webster 92])

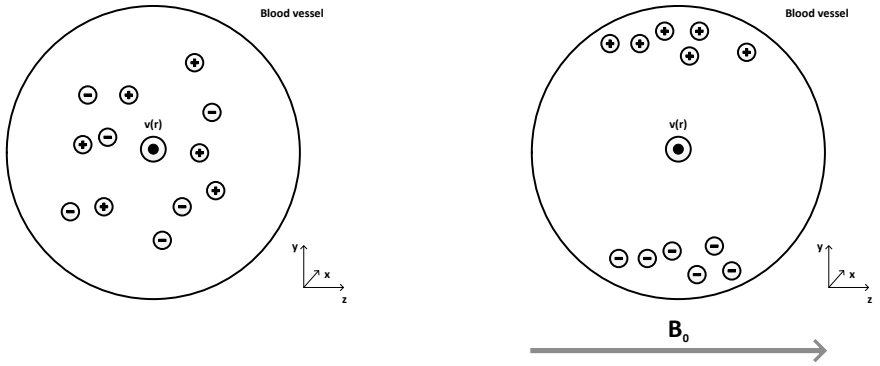

(a) Outside the MR scanner without $\mathbf{B}_0$ present

(b) Inside the MR scanner with $\mathbf{B}_0$ present

Figure 3.3.: A simplified schematic of the MHD effect inside a blood vessel. Positive and negative ions are moving with the velocity $v(r)$ along the blood vessel where r is the vessel's radius. Outside the MR scanner, ions are randomly distributed inside the vessel (a). Inside the MR scanner (under the influence of the static magnetic field), the ions experience the Lorentz force (b). Due to this force, the ions move to the walls of the vessel. Assuming a linear flow profile, the Lorentz force is highest in the centre of the vessel and decreases proportionally with the distance to the vessel walls.

especially in close proximity to the myocardium, where the blood is ejected and high velocities occur. Hence, the assumptions of a laminar and unidirectional flow profile made in most theoretical estimations of the MHD effect are not realistic. Anatomical conditions such as the heart valves, stenoses or aneurysms can affect the flow profiles of the rapidly ejected blood. MRI can be used to reveal the complexity of blood flow inside the vascular system. Phase-contrast encoded MRI data can be utilised to visualise streamlines or estimated blood flow velocities [Markl 03, Markl 07]. Figure 3.4 depicts a series of streamlines at different times of the ventricular systole. A twist of the blood flow can be observed. In order to enable a reliable and realistic estimation of the MHD effect during MRI, these aspects should be considered by simulation studies. Section 3.2.3 explains a model for the simulation

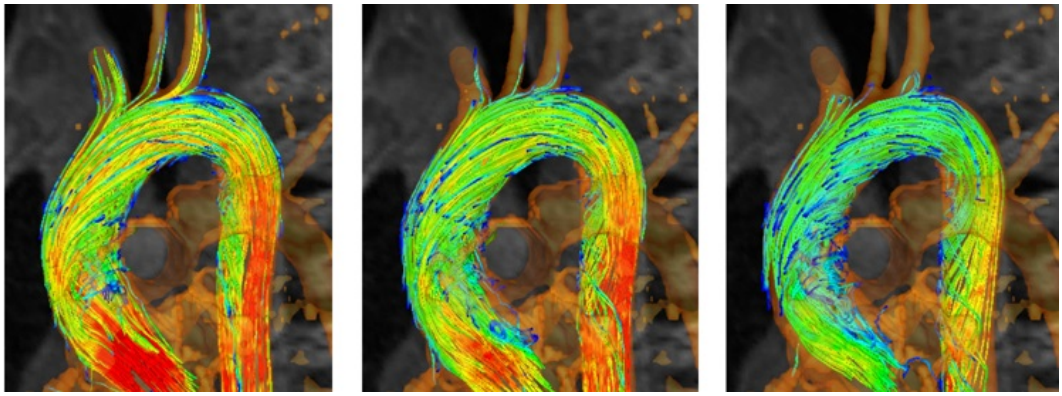

Figure 3.4.: Estimated stream lines of the blood flow in the aortic arch measured using an MRI phase contrast sequence. Blood flow is shown for 140 ms (left), 180 ms (middle) and 220 ms (right) after the beginning of the cardiac systolic phase. (Image modified according to [Markl 11])

of the MHD effect using such an MRI-based blood flow measurement coupled with an electric dipole description to estimate the body surface potentials.

3.2.2 The cardiac cycle, cardiovascular dynamics and the MHD effect

Following the theoretical considerations made in section 3.2.1, the vessel diameter and the blood flow velocity are the most important physiological parameters the MHD effect depends on. The highest blood flow velocities occur in the arteries close heart, e. g. in the aorta or the pulmonary artery [Schmidt 07, pp.626]. The diameter of both arteries is the largest within the human body. Hence, it is usually assumed that these arteries are responsible for the MHD effect observed in ECG signals acquired during MRI [Kinouchi 96, Martin 11a]. Figure 3.5 shows the blood flow velocities measured with MRI in different arteries. The highest blood flow velocities perpendicularly to the MR scanner's static magnetic field occur within the aortic arch. This explains why the MHD effect is mainly induced by the aortic blood flow. The blood flow reaches its maximum during the ejection phase, i. e. during the ventricular systole, where the blood flows from the ventricles into the aorta and the pulmonary artery (Fig. 2.7, p. 11). Hence, the MHD effect is expected to mainly affect the segment between the QRS complex and the end of the T-wave.

The cardiovascular system system is influenced by several external factors, e. g. by physical stress, drugs or diseases and it is controlled by the central and autonomous nervous system (see Section 2.1). The external factors together with the actions of the physiological regulation system (e. g. the autonomous nervous system) can affect the properties and dynamics of the blood flow. Exemples of cardiovascular parameters related to the blood flow properties are depicted in Fig. 3.6. It can be expected that a variation of the blood flow, e. g. increased velocity, results in a variation of the MHD effect's morphology. Hence, a precise description of the MHD effect observed in ECG signals during MRI is a complex problem due the high number of the physiological, anatomical and physical parameters. Moreover, these physiological parameters vary over time. None of these parameters, e. g. the blood flow velocities in the different vessels or the vessel diameter can be monitored continuously during MRI[2].

[2]Although ultrasound (US) order Doppler-US would enable a continuous measurement of these parameters in a certain vessel, it is usually not available during MRI.

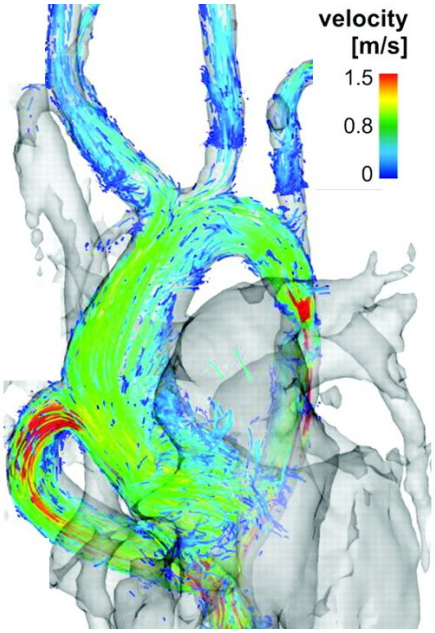

Figure 3.5.: Blood flow velocities in the aortic arch, the supra-aortic vessels and a bypass conduit (in the lower left part). Maximum blood flow velocities occur in the aortic arch (not considering the bypass conduit). (Image modified according to [Gupta 12].)

Several physiological parameters, which are related to the MHD effect can be measured. These parameters include:

- blood pressure, e. g. measured by an arm cuff or by an intravascular catheter,
- pulse estimation, e. g, using finger plethysmography or
- blood flow measurement in different locations, e. g. by using doppler ultrasound or velocity encoded MRI (not continuously).

During arrhythmic cardiac events, each of these parameters is expected to change resulting in a variation of the MHD effect. An example showing the effect of an irregular depolarisation of the ventricles is depicted in Fig. 3.7. The pattern of the arterial blood pressure (ABP) differs between a normal contraction and a premature ventricular contraction (PVC). Changes in the ABP during a PVC are caused by the missing atrial contraction and the missing ventricular diastolic phase, which normally leads to a filling of the ventricles prior to the ejection phase.

3.2.3 Simulation studies

Simulations overview

As it was generally described in Section 3.2.1, the MHD signal is mainly caused by the blood flow perpendicularly to the MR scanner's static magnetic field $\mathbf{B}_0$. The previous section named several cardiovascular and physical parameters which make it harder to estimate the MHD effect on the surface of the human body inside the MR scanner. Several simulation studies were performed in order to reveal the influence of different physiological and anatomical parameters, and to improve denoising algorithms using the information obtained from simulations. This section summarizes some important

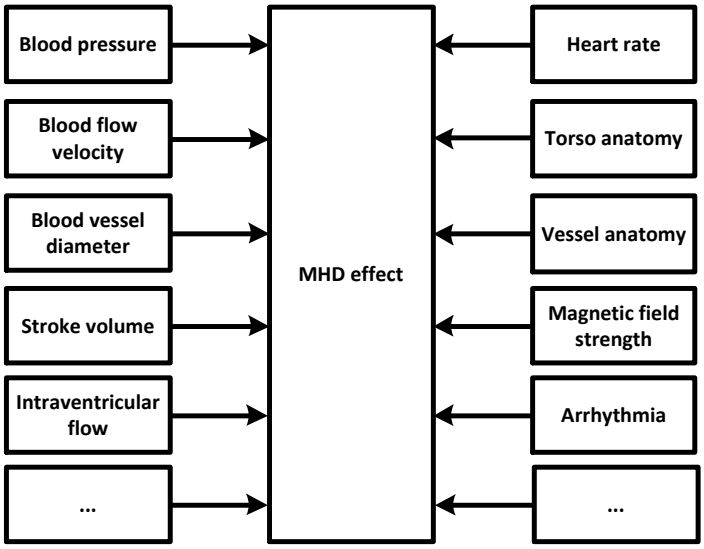

Figure 3.6.: Different parameters which have an influence on the blood flow dynamics and on the resulting MHD effect.

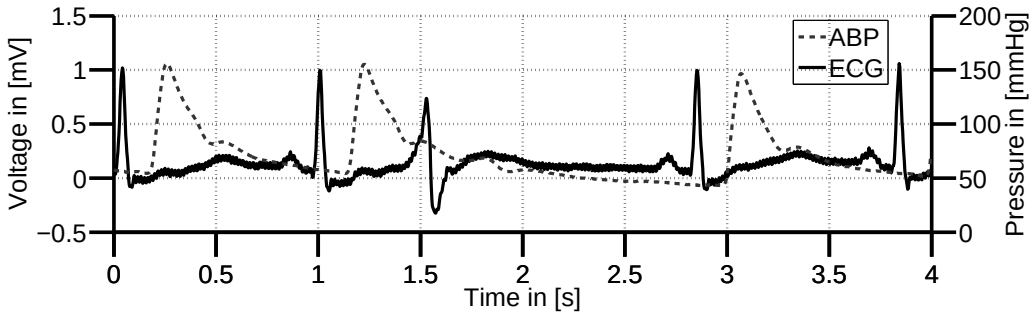

Figure 3.7.: ECG and ABP during normal sinus rhythm and a premature ventricular contraction (PVC) occurring at around $1.5\,\mathrm{s}$. The ABP pattern following the PVC differs from the ABP patterns occurring during the normal beats, i. e. a clear ABP peak is not visible after the PVC (record: *PhysioNet mghdb/mgh133* [Goldberger 00]). Hence, a variation of the MHD effect during PVCs or arrhythmias can be expected due to the changed ABP patterns.

simulation studies and their results.

Early theoretical calculations of the MHD effect were made by Gold *et al.* [Gold 62]. Later, the MHD effect in human blood vessels was studied using a rigid vessel model with non-conducting vessel walls [Keltner 90]. Kinouchi *et al.* considered a vessel model with conducting walls [Kinouchi 96]. Nijm *et al.* simulated the MHD effect using a simplified cylindrical vessel model with a diameter of $2\,\mathrm{cm}$ and a length of $3\,\mathrm{cm}$ [Nijm 07b]. A parabolic blood flow profile was assumed inside the tube whereas the evolution over time was modelled using an exponentially decaying sine-function. Maxwell and Navier-Stokes equations were used to estimate the induced voltages. The partial differential equations were solved using the finite element method implemented in *Comsol Multiphysics*. A similar model was later used by Bhatt *et al.* [Bhatt 09c].

Gupta *et al.* used dynamic magnetofluidic simulations based on a discretisation of the aortic arch and by realistic blood flow profiles obtained from MRI measurements [Gupta 08]. Similarities between the ECG measurement in a $1.5\,\mathrm{T}$ scanner and the simulated signals were shown in terms of morphology and signal amplitudes. The simulations were evaluated quantitatively by measuring the amplitude

difference of the T-wave between the measured ECG and the simulated signal. A maximum error of $0.37\,\mathrm{mV}$ was observed in ECG lead aVR. Although the error of the simulated amplitudes were low, e. g. $0.048\,\mathrm{mV}$ in lead II, the simulation model could not reproduce the overall morphology of the MHD effect.

Abi-Abdallah *et al.* also solved the Maxwell and the Navier-Stokes equations for MHD simulation [Abi-Abdallah 09b]. An unidirectional, axi-symmetric flow without vortices was assumed in a circular, rigid vessel. A three-element Windkessel lumped model was used to simulate the pressure gradient inside the vessel. The three-element lumped model was used to simulate the resistance of the aorta and the large arteries, the compliance of the aorta and the total peripheral resistance of the smaller arteries, the arterioles and the capillaries. The electric dipole moment was calculated for the simulated flow profile in the presence of a static magnetic field [Abi-Abdallah 09a]. Once the electric dipole moments were known, the body surface potentials could be estimated.

Martin *et al.* developed a three components finite element model for the simulation of the MHD effect [Martin 11a, Martin 11b, Martin 12]. It includes the simulation of the MHD effect in the aorta, bidomain equations of the heart[3] and electrical diffusion within the body. Using transfer functions, body-surface potentials were estimated from the ECG and MHD models. Figure 3.8 shows simulation results based on this model. As expected, the MHD effect increases with the magnetic field strength. Compared to real measurements shown in Fig. 3.9 and in later in Figs. 3.12-3.16, the simulations cannot accurately approximate the more complex patterns of the experimentally measured MHD effect.

The simulations of Kyriakou *et al.* investigated patient specific simulations of the MHD effect [Kyriakou 12]. This study aimed at quantifying the cardiac output based on the ECG measurements. Anatomical and flow information were obtained using $3\,\mathrm{T}$ MRI measurements. The anatomical information was used for the generation of a computer model based on the *Virtual Family* [Christ 10]. 4D-flow information of the aorta and of the superior and inferior vena cava (SVC and IVC) as well as other smaller vessels (e. g. the left carotid and left subclavian arteries) were included in the model. Based and these anatomical and functional pieces of information, the MHD effect was simulated. Electromagnetic (EM) simulations were performed using a dedicated low-frequency solver [Kainz 10]. For the estimation of the body surface potentials, more than 200 tissue types were used to describe the torso. Figure 3.9 compares the simulated and measured MHD effect. Although the fairly complex model including several larger blood vessel (aorta, SVC and IVC), the simulated MHD signal did not cover all those peaks observed in a real measurement. The authors give several shortcoming explaining why the model could not predict the real MHD signal: the limited number vessels considered in the model and the inaccuracy of the vessel geometry, the negligence of intra-cardiac blood flow, the inaccuracy of the vessel model geometry and the HRV dynamics.

[3] The bidomain model describes the potential difference across the membrane in two separate domains: the intracellular and the extracellular space [Sundnes 06]. Both domains are separated by the cell membrane which acts as an electrical insulator.

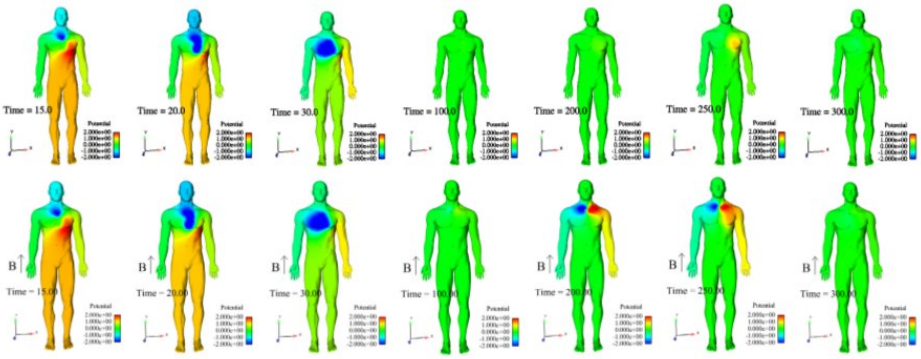

(a) Body-surface potential maps for 0 T (top row), 1 T (middle row) and 3 T (bottom row).

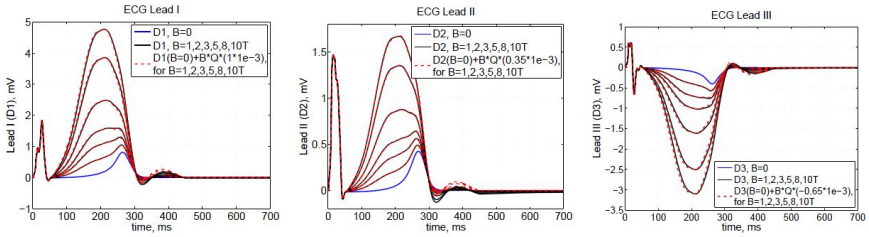

(b) Resulting simulated ECG traces I, II and III with MHD effect at different magnetic field strengths.

Figure 3.8.: Results of the three component model simulating different ECG traces with additional MHD effect. (Images modified according to [Martin 11a, Martin 12].)

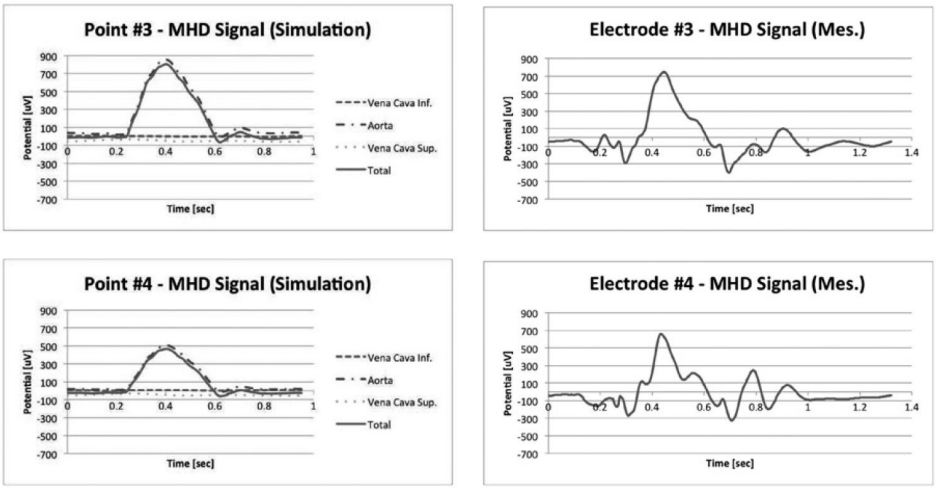

Figure 3.9.: MHD effect based on simulations of the aorta and vena cava (left) and measured MHD effect (right). (Image modified according to [Kyriakou 12].)

MHD modelling based on 4D blood flow measurements from MRI

Oster *et al.* recently combined a realistic anatomical model with the information of an aortic blood flow profile obtained from MRI measurements [Oster 12, Oster 15]. This model shall be explained in further details, since it is used in the course of this thesis. The anatomical model including the torso and the heart combined with a forward model were taken from the *ECGSim* package[4] [van

[4] http://www.ecgsim.org/

Oosterom 04]. *ECGSim* allows to simulate the electrical activity of the ventricles and the resulting body surface potentials based on a human torso model. A model of the aortic arch was adopted from the simulations of Fujioka *et al.* [Fujioka 00]. The resulting model geometry is depicted in Fig. 3.10. 4D blood flow profiles were estimated using a phase contrast MRI sequence [Markl 03]. The blood flow profiles were estimated in four cross sections of the aortic arch, where one slice was placed in the ascending aorta, one in the descending aorta and two within the aortic arch. These flow profiles at different locations were used to describe the blood flow within the model of the aortic arch.

The voltages caused by the blood flow within the static magnetic field were estimated using charge densities inside the aortic arch and corresponding electrical dipole moments. The charge density can be derived using the following (Maxwell) equations

$$\nabla \cdot \vec{E} = \frac{\rho}{\epsilon} = \operatorname{div} \vec{E} \quad \text{(Gauss's law)} \tag{3.3}$$

$$\nabla \times \vec{B} = \mu \vec{j} = \operatorname{rot} \vec{B} \quad \text{(Ampère's law)} \tag{3.4}$$

$$\vec{j} = \sigma(\vec{E} + \vec{v} \times \vec{B}) \quad \text{(Ohm's law).} \tag{3.5}$$

By rearranging eq. 3.3 after σ, eq. 3.4 after $\vec{j}$ and eq. 3.5 after $\vec{E}$ and substitution of the rearranged eqs. 3.4 and 3.5 into 3.3 one obtains

$$\rho = \epsilon \nabla \left(\frac{\nabla \times \vec{B}}{\sigma \mu} - \vec{v} \times \vec{B} \right) = -\epsilon \nabla \left(\vec{v} \times \vec{B} \right) \tag{3.6}$$

since $\nabla \cdot \nabla \times \vec{B} = \operatorname{div} \operatorname{rot} \vec{B} = 0$. ϵ is the permittivity of the blood flow (in Farad/m) and $\vec{v}$ is the blood flow velocity vector. Based on the definition of the charge density ρ, the electric dipole moment of the

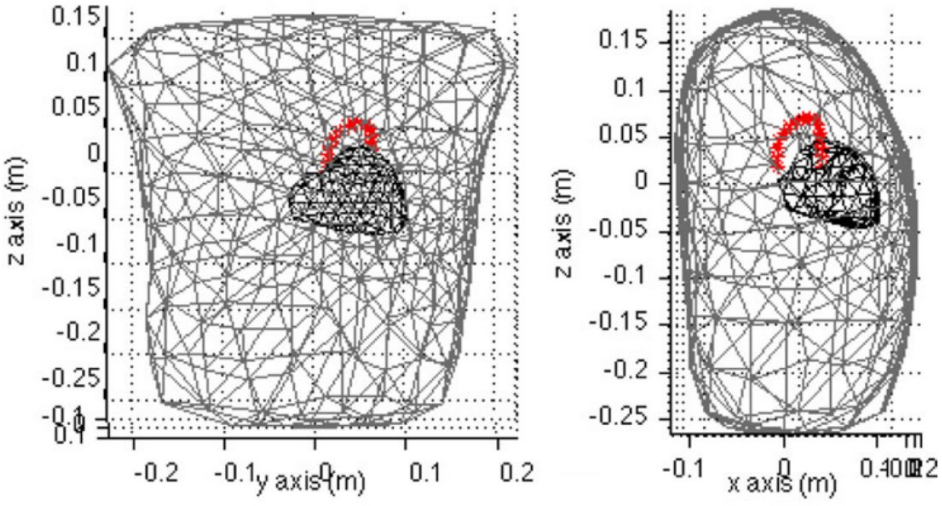

Figure 3.10.: Torso model taken from the ECGSim package in the coronal (left) and sagittal (right) view. The torso model was extended with a model of the aortic arch. (Image modified according to [Oster 15].)

charges can be estimated by integrating the charge density over the volume of one aortic arch section

$$\vec{p} = \int_V \vec{r'}\rho(\vec{r'})d^3\vec{r}. \tag{3.7}$$

The resulting potential $\phi(\vec{r})$ at a certain point of the surface of the body (specified by the vector $\vec{r}$) can be calculated from the electric dipole moment $\vec{p}$

$$\phi(\vec{r}) = \frac{1}{4\pi\epsilon_0}\frac{\vec{r}\vec{p}}{r^3}. \tag{3.8}$$

The charge density was estimated for every section of the aortic arch for the different time steps of one cardiac cycle. Using the geometry of the realistic torso model, the potential on the surface of the torso was estimated from the sum of the dipole moments originating from the different aortic arch sections.

The estimated MHD potentials are in good agreement with the real MHD effect in most of the ECG leads. However, the model could not completely predict the whole complexity of a real MHD signal. This can be partly explained by the underlying blood flow signals which were used to simulated the MHD signal. Since the measurement of the blood flow profile for one cardiac cycle in one anatomical cross section takes several minutes, the resulting flow profile is an average estimate of the blood flow. Hence, the blood flow dynamics and beat-to-beat variations of the blood flow patterns are averaged or low-pass filtered. Larger deviations were observed in leads V5 and V6 and it was assumed that these deviations were caused by the linear propagation through a homogeneous torso model. It was also shown by Kyriakou *et al.* that smaller changes of the electrode positions have a large influence on the error of the simulated signals [Kyriakou 12].

To make the simulations of the MHD signal based on the averaged blood flow profile more realistic, the authors included additional variations of the MHD effect by considering the RRI length and the related cardiac stroke volume. Since the stroke volume decreases with a decreasing RRI lengths, the estimated MHD effect should also decrease due to the reduced amount of blood eject by the ventricles. The cardiac output (CO) which describes the volume of blood eject by the ventricles per minute is directly related to the heart rate [Mark 04]

$$\text{CO} = \frac{11.5}{0.08 + \frac{0.05}{\text{HR}(\text{s}^{-1})}}\text{mL/s} = \frac{0.69}{0.08 + \frac{3}{\text{HR}(\text{min}^{-1})}}\text{L/min}. \tag{3.9}$$

The stroke volume (SV) – which describes the ejected blood volume per heart beat or contraction – is defined by dividing the CO by the HR

$$\text{SV} = \frac{0.69}{0.08 \cdot \text{HR}(\text{min}^{-1}) + 3}1/\text{beat}. \tag{3.10}$$

Based on this definition, a correction factor α_{SV} was used to modulate the amplitude of the MHD

signal [Oster 15]

$$\alpha_{SV} = \frac{SV(HR)}{SV(60)} = \frac{780}{8 \cdot HR + 300} \tag{3.11}$$

where SV(60) is the stroke volume for an average heart rate of 60 bpm. The MHD effect was modified for each new interval RRI based on the instantaneous heart rate which was estimated from the RRI length.

3.3 The MHD effect observed in ECG signals acquired during MRI

3.3.1 Influence of the orientation and magnitude of the magnetic field

As described in Section 3.2, the two most important parameters of a magnetic field for the observed MHD effect are the orientation of the static magnetic field $\mathbf{B}_0$ with respect to the direction of (blood) flow and the magnitude of the static magnetic field. The absolute orientation and magnitude values are predetermined by the MR scanner. Nowadays, two main geometries of MR scanners are used in clinical environments, and they are depicted in Figs. 3.11a and 3.11b. The corresponding orientation of the magnetic field vector with respect to the patient's anatomy is depicted in Figs. 3.11c and 3.11d. In most of the studies described in Section 3.2 it was assumed that the MHD signal mainly originates from the aortic arch. This can be explained by the high blood flow velocities and its perpendicular orientation with respect to $\mathbf{B}_0$ (for the closed bore MR scanner with a horizontally aligned magnetic field vector). Figure 3.12a depicts several traces of ECG signals acquired from one subject at different magnetic field strengths ranging from $0\,$T to $7\,$T (closed bore MR scanners with horizontal magnetic field alignment, compare Figs. 3.11a and 3.11c). As expected from the MHD theory and simulations (see Section 3.2), the magnitude of the MHD effect increases with the magnitude of the static magnetic field $\mathbf{B}_0$. For the open bore MR scanner with a vertical magnetic field vector, a more severe MHD effect can be expected since most parts of the aorta – the *aorta ascendens*, *arcus aortae* and *aorta descendens* – as well as many other blood vessels which have a perpendicular vector component with respect to the magnetic field vector. Figure 3.12b depicts ECG signals acquired in a $1\,$T MR scanner with a vertical magnetic field (compare Figs. 3.11b and 3.11d) and in a $3\,$T MR scanner with a horizontal magnetic field (compare Figs. 3.11a and 3.11c). As it was assumed, the MHD effect in a vertical magnetic field is higher due to its perpendicular orientation to most of the major blood vessels inside the human body. Considering these construction aspects, the detection of the R-peaks can be even more complicated inside a $1\,$T scanner (vertical magnetic field) than in a $3\,$T scanner (horizontal magnetic field) due to the different orientation of the static magnetic field. However, it has to be mentioned that most open-bore MRI scanners with vertical magnetic field alignment have a magnetic field strengths of $1\,$T, which limits the negative impacts of the MHD effect in such scanner types.

As already described above, most of the blood vessels located in the thorax contribute to the MHD effect. Intra-cardiac blood flow, especially during the filling and ejection phase, should also have an impact on the resulting MHD signals. Hence, the ST-segment, the T-wave and the P-wave are affected by the MHD effect. Additionally, the proximity of the ECG electrodes with respect to the blood flow influences the observed MHD signals. For example, in electroencephalographic (EEG) measurements where the electrodes are placed on the skull, the observed MHD signals are mainly caused by the

intracerebral blood flow and not by the aortic flow.

More examples revealing the influence of the orientation and magnitude of the static magnetic field are depicted in Figs. 3.13–3.16. These examples show the 12-lead ECG measurements made at 3 T and 7 T in the head first (Hf) and feet first (Ff) position, i. e. the orientation of the static magnetic field was flipped by 180° due to the different positions of the subject. It can also be seen from these examples that the voltages caused by the MHD effect at 7 T exceed the ECG signals in most of the leads in both subject positions.

From a signal processing perspective, the time-frequency energy distributions (TFED) of the ECG signals acquired outside and inside the MR scanner can be of a certain interest. In order to show the influence of the MHD effect, the TFED of different ECGs were estimated using the smoothed pseudo Wigner Ville distribution (SPWVD) [Boashash 88, Boashash 03, Kiencke 08]. Figure 3.17 depicts the different ECG signals and their corresponding SPWVD. This example, which is based on an ECG signal acquired at 7 T, shows that the frequency components of the MHD effect and of the ECG signal overlap. Hence, the MHD effect cannot be simply suppressed with basic digital filtering techniques. The overlapping frequency range could also affect certain QRS detection methods, which rely on the spectral properties of the R-peak or QRS complex [Koehler 02].

(a) 3 T closed bore MR scanner

(b) 1 T open bore MR scanner (during an interventional procesure)

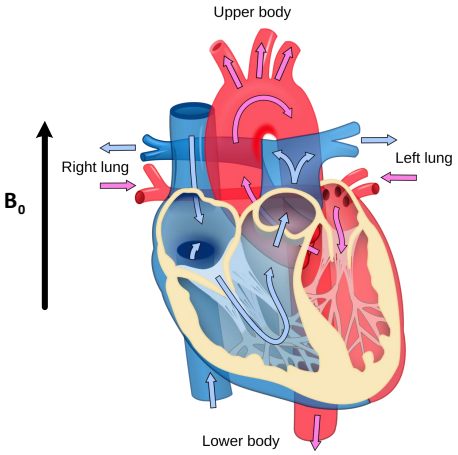

(c) Horizontal $\mathbf{B}_0$ field (from feet to head) of the closed bore scanner (a)

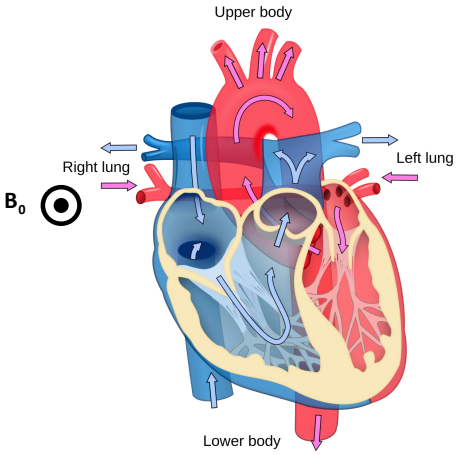

(d) Vertical $\mathbf{B}_0$ field (pointing from posterior to anterior) of the open bore scanner (b)

Figure 3.11.: Closed (a) and open bore (b) MR scanner construction types and the corresponding alignment of the magnetic fields for (c,d). (Image sources: (a): Siemens, (b): Axel Boese, OvGU Magdeburg, (c,d): distributed under the CC-BY 2.0 license, Wikimedia, modified)

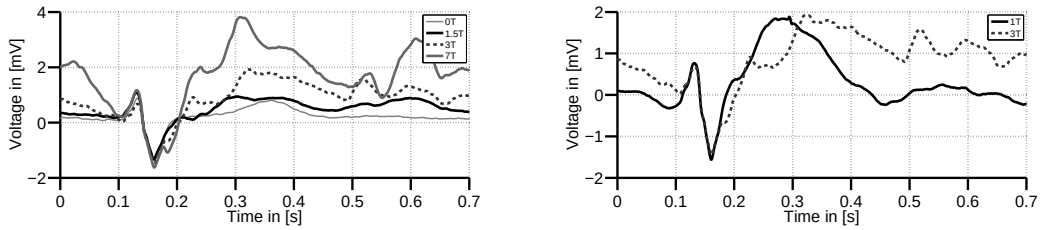

(a) ECG signals acquired at 0 T, 1.5 T, 3 T and 7 T

(b) ECG signals acquired at 1 T (vertical field) and 3 T (horizontal field).

Figure 3.12.: Comparison of ECG signals (lead V2) acquired at different magnetic field strengths and field orientations. An increasing magnetic field strength (from 1.5 T to 7 T) increases the MHD effect observed in the acquired ECG signals (a). The magnitude of the MHD effect observed in a vertically oriented 1 T magnetic field is of similar magnitude when compared to the MHD effect measured in a 3 T MR scanner with a horizontally aligned magnetic field (b). The QRS complexes are located at $t \approx 0.15\,\mathrm{s}$.

3.3.2 The MHD effect in different subjects and ECG leads

There are considerable variations of the MHD effect observed in different subjects. Examples of ECG signals of two different subjects are depicted in Fig. 3.18. All signals were acquired at 7 T. Although similarities can be observed in the same lead of the two subjects, the detailed morphology of the ECG traces are different, e. g. the location, shape and magnitude of the peaks are different in the different records. It can also be observed that the MHD effect is less severe in lead V4 when compared to lead II. Regarding ECG lead II, a robust manual identification of the R-peak is not possible in the shown examples. In ECG lead V4, the MHD effect is less pronounced so that the R-peak (aligned at 150 ms in Fig. 3.18) can be identified by its typical morphology. However, when considering a single ECG lead only, a reliable manual identification of the R-peak does not seem to be possible.

3.3.3 Impact of the MHD effect on the VCG

The vectorcardiogram (VCG, see Section 2.1.3) is a method, which is commonly used in MRI for gating purposes. Since the VCG is derived from the ECG using the inverse Dower matrix given in Eqs. 2.5 and 2.6, p. 13, it can be expected that the MHD effect also affects the VCG signals. Examples for a VCG in different views are given in Fig. 3.19 and the corresponding x, y and z signals of these spatial representations are depicted in Fig. 3.20. Figures 3.19a to 3.19c depict the VCGs outside the MR scanner. A vector pointing at the spatial position of the R-peak of the ECG acquired outside the MR scanner is defined as reference vector **r**. Figures 3.19d–3.19f depict the spatial representation of the VCG from the 3 T ECG measurements. In these VCGs, the QRS loop is clearly separated from the distortions, which were caused by the MHD effect. The distortions are mainly concentrated in the centre of the VCG space. The angle and amplitude of the R-peak vector inside the MR scanner deviates by 3.6° and 0.4 mV from the reference R-peak vector **r**.

Figures 3.19g–3.19i show the spatial VCG from the recordings which were made inside the 7 T MR scanner. It was shown that two essential effects influence the VCG during MRI and degrade its usability for gating purposes at 7 T [Krug 13b]. The *first effect* concerns the spatial expansion of the MHD effect. Compared to the 3 T measurements depicted in Figs. 3.19d–3.19f, the MHD effect covers a much larger area/volume in the 7 T VCGs. This can be explained by the increased amplitudes and complexity of the MHD effect as shown in Fig.3.20. The *second effect* is the altered orientation of the

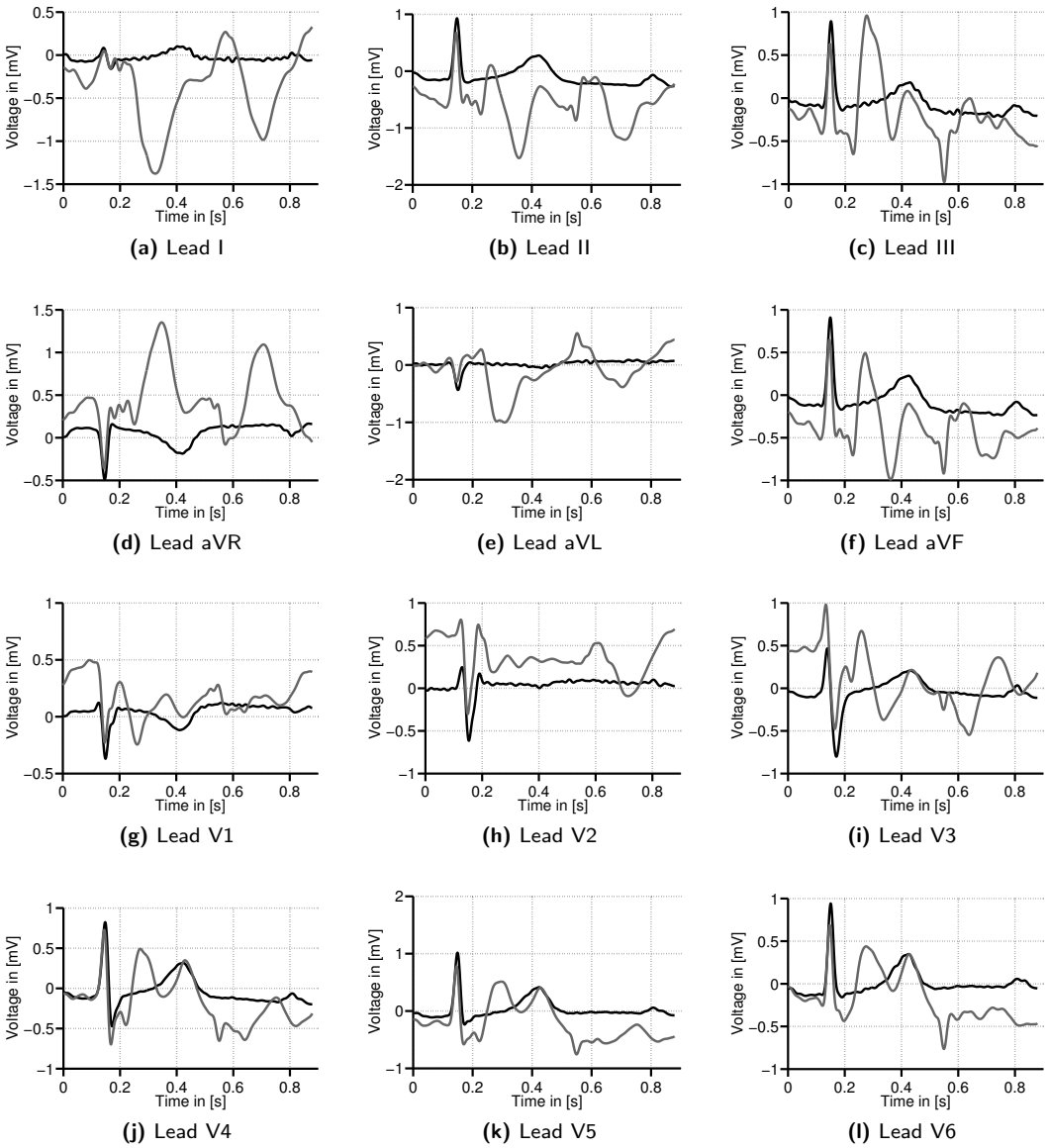

Figure 3.13.: ECGs recorded outside the MR scanner (black) and inside the $3\,\mathrm{T}$ MR scanner in the feet first (Ff) position (grey). The shape or slope of R-peak is preserved in some of the leads, especially in the precordial leads. However, additional signal components with high slopes are caused by the MHD effect. The QRS complexes are aligned at $t \approx 0.15\,\mathrm{s}$.

R-peak vector with respect to the reference vector **r**. Angle and amplitude varied by $68.7°$ and $1.7\,\mathrm{mV}$, respectively. As explained in Sections 3.3.1 and 3.3.2, the MHD effect mainly affects the segment between two QRS-complexes, i. e. the ST-segment, the T-wave and the P-wave. The changing R-peak amplitude can be explained by the analogue high-pass filter of the ECG recorder. Where the ECG signal has a zero mean, the MHD effect exhibits an non-zero DC component which is added to the ECG signal. This additional DC component is removed by the high-pass filter of the ECG recorder. As a result, the baseline of the filtered signal experiences a shift. This effect is depicted in Figure 3.21. The baseline shift varies between the different ECG leads depending on the magnitudes of the MHD effect. Hence, the ECG's amplitudes are altered between the ECG recorded outside which is usually taken as the reference signal **r** and the ECG recorded inside the MR scanner. The altered alignment of

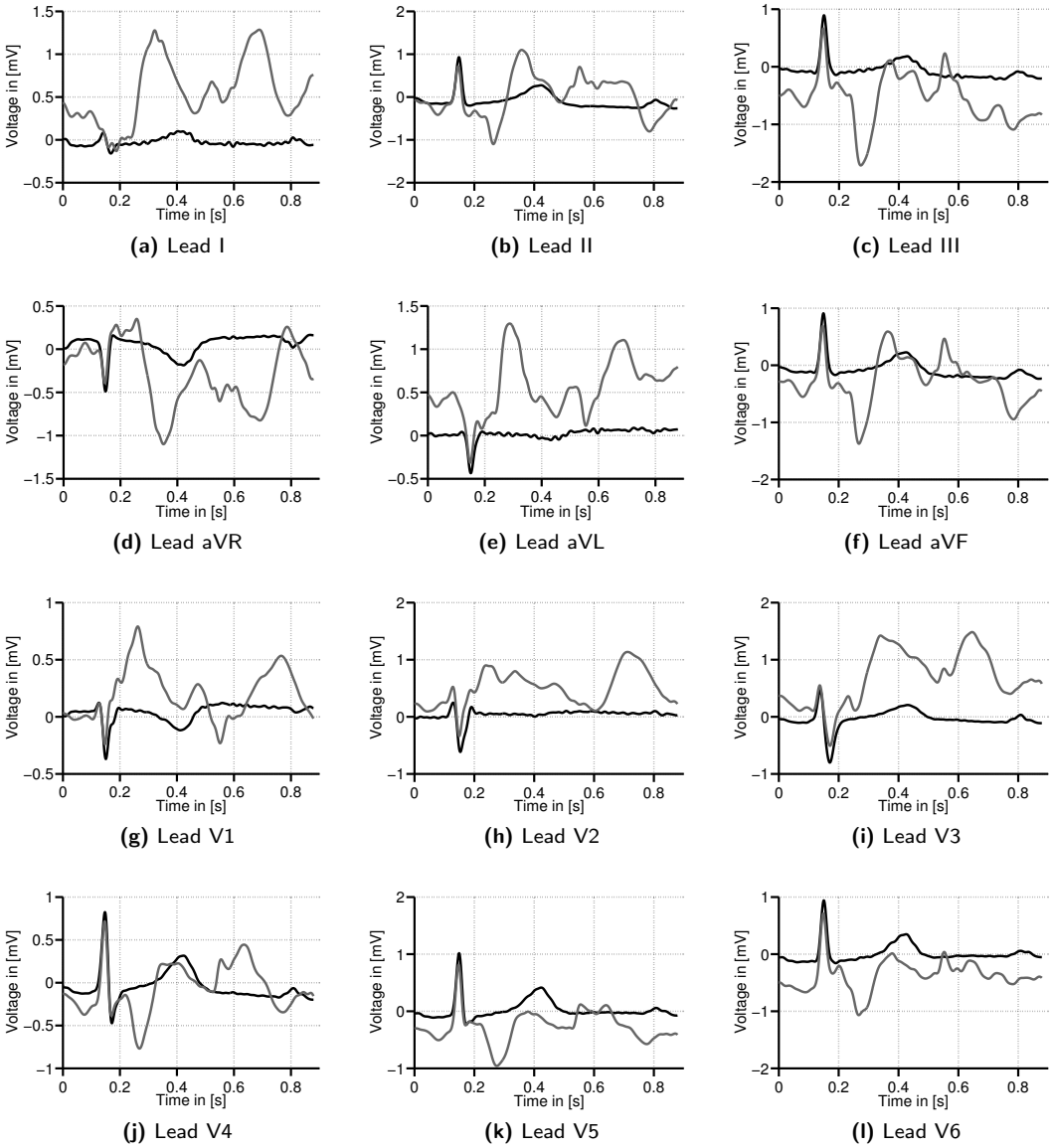

Figure 3.14.: ECGs recorded outside the MR scanner (black) and inside the $3\,\mathrm{T}$ MR scanner in the feet first (Hf) position (grey). The shape or slope of R-peak is preserved in some of the leads, especially in the precordial leads. However, additional signal components with high slopes are caused by the MHD effect. The QRS complexes are aligned at $t \approx 0.15\,\mathrm{s}$.

the R-peak vectors is considered again in Section 5.2 in order to discuss the problems of VCG-based gating methods at $7\,\mathrm{T}$.

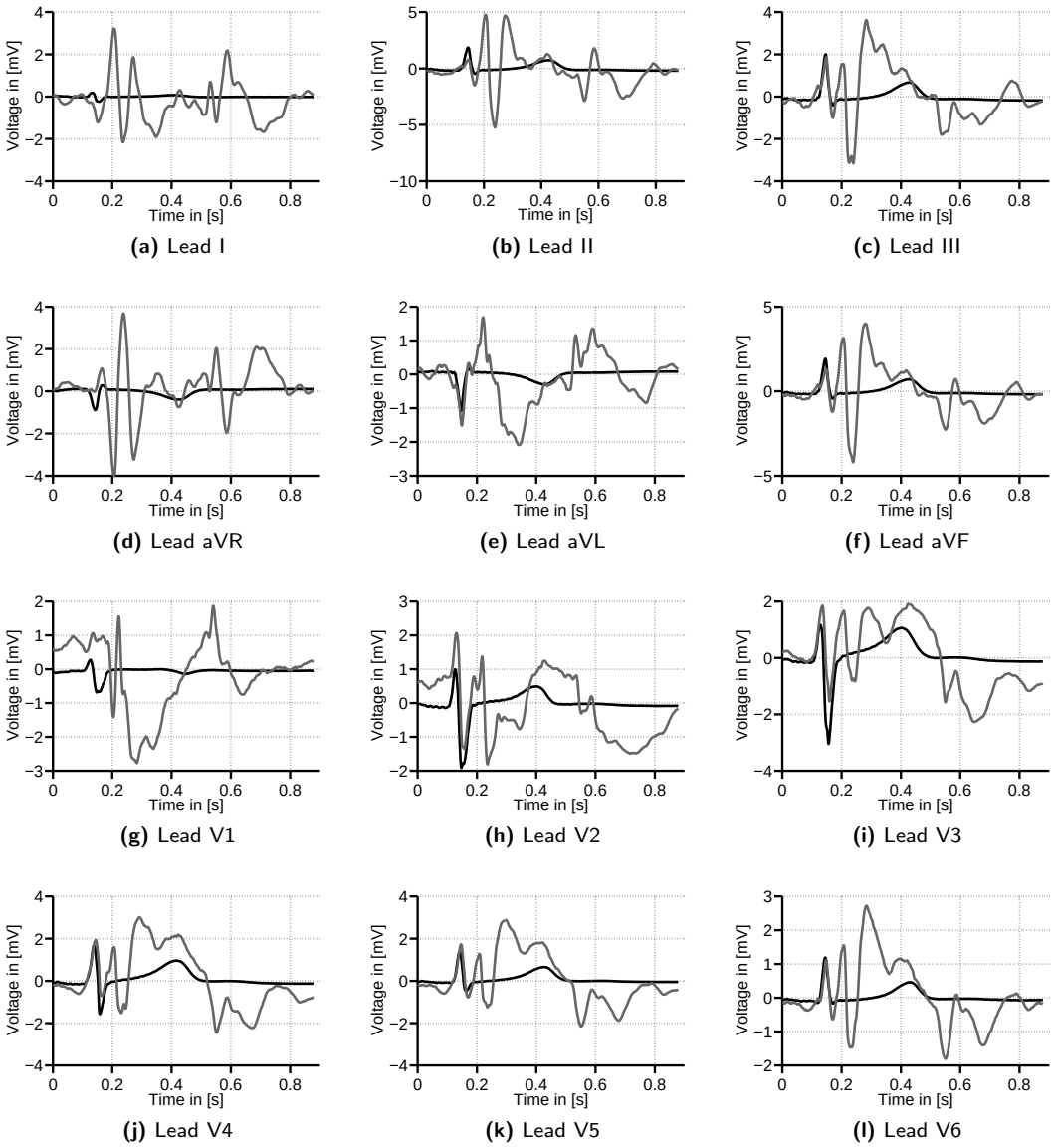

Figure 3.15.: ECGs recorded outside the MR scanner (black) and inside the 7 T MR scanner in the feet first (Ff) position (grey). The shape or slope of R-peak is preserved in some of the leads, especially in the precordial leads. However, additional signal components with high slopes are caused by the MHD effect. The QRS complexes are aligned at $t \approx 0.15\,\mathrm{s}$.

3.3.4 Consequences for ECG-based gating and diagnostics

The ECG measurements shown in the previous sections highlighted the problems caused by the MHD effect. QRS detection becomes more challenging with increasing magnetic field strength due to the higher MHD effect. A reliable R-peak detection is essential for gating CMR sequences and for monitoring the patient's heart rate and rhythm. In CMR, misclassified R-peaks can lead to an incorrect filling of the k-space causing artefacts in the reconstructed images [Ferreira 13].

At typical clinical magnetic field strengths ($\leq 3\,\mathrm{T}$), R-peak detection is reliable and the influence of the MHD effect can be neglected in most of the cases for gating purposes. The main problems at

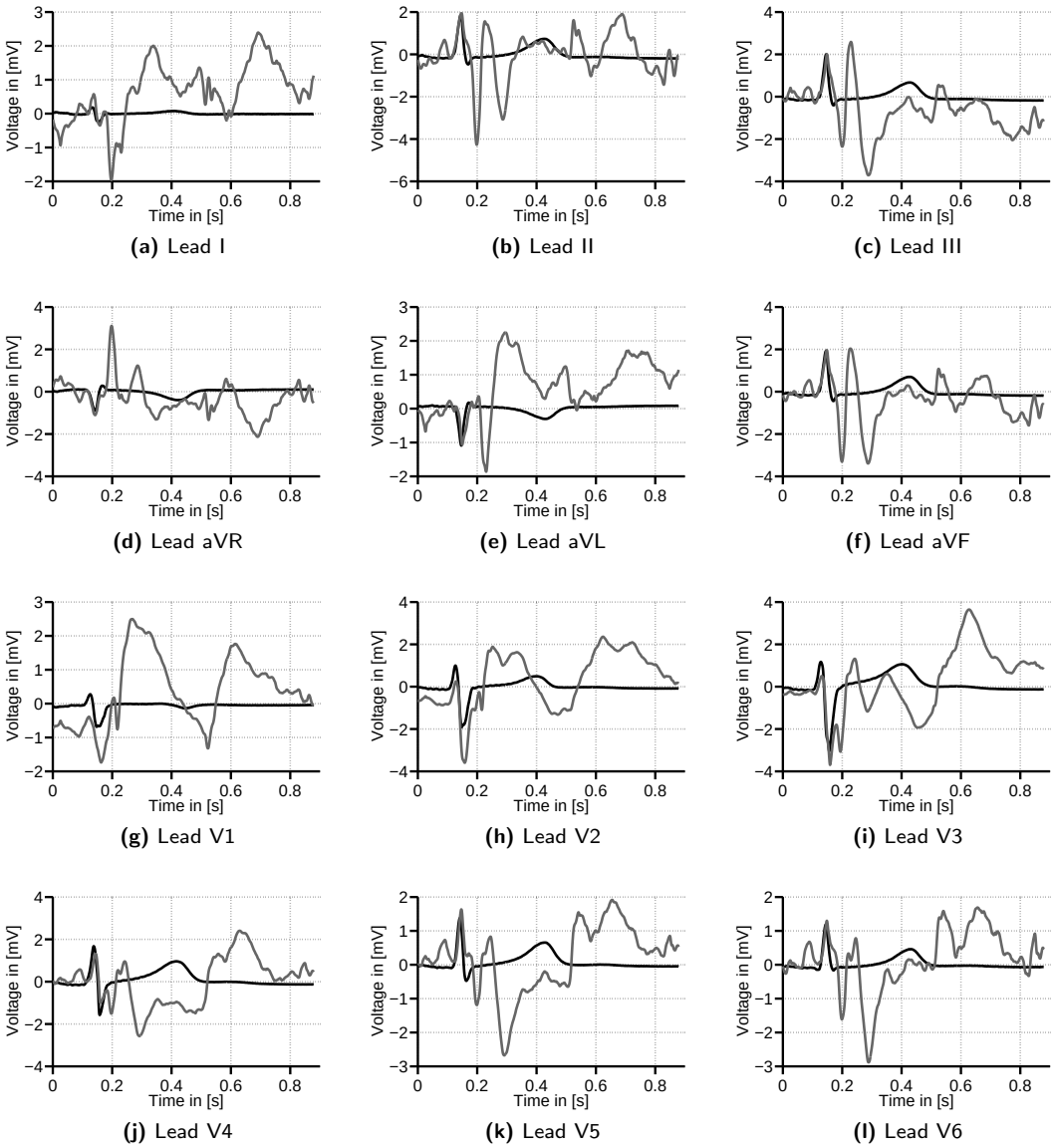

Figure 3.16.: ECGs recorded outside the MR scanner (black) and inside the 7 T MR scanner in the head first (Hf) position (grey). The shape or slope of R-peak is preserved in some of the leads, especially in the precordial leads. However, additional signal components with high slopes are caused by the MHD effect. The QRS complexes are aligned at $t \approx 0.15\,\mathrm{s}$.

these field strengths arise from the gradient magnetic fields [Felblinger 99, Abächerli 05, Oster 09a]. The diagnostic information of the ECG contained in the P-wave, the ST-segment and the T-wave is hidden due to the superimposed MHD signals. This diagnostic information is often required for patient monitoring during anaesthesia or for the functional analysis of the myocardium in the EP lab (see Sections 2.1.4 and 2.3.2). Especially the EP procedures are limited since the the P-wave and the T-wave cannot be observed during MRI [Vergara 11]. Hence, the MHD effect is one reason why certain interventional procedures, which required a proper cardiovascular monitoring, cannot simply be transferred into an MRI environment.

The following two sections gives an overview over different methods, which enhance the quality of the ECG signal, to enable a reliable gating for CMR and an improved patient monitoring during MRI.

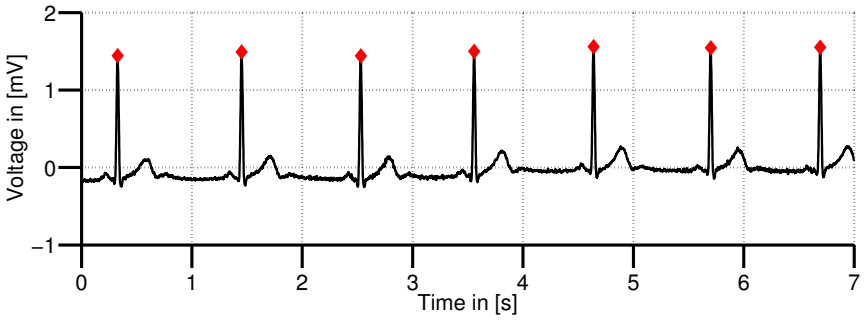

(a) ECG (lead V6) acquired outside the MR scanner.

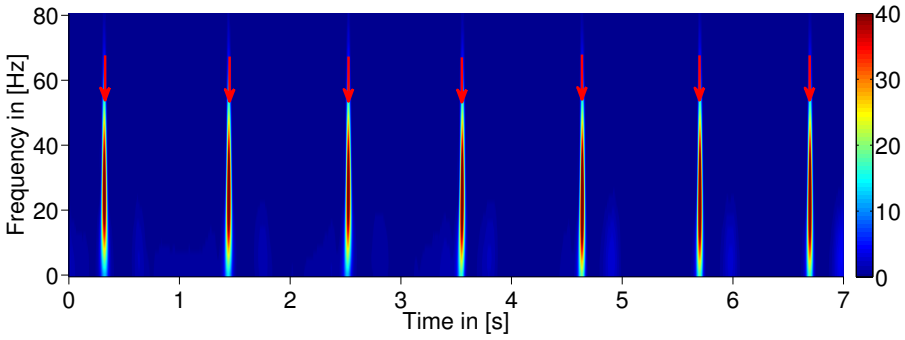

(b) TFED of (a)

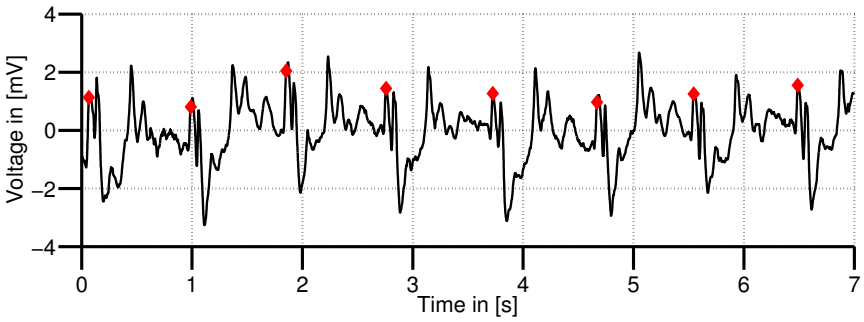

(c) ECG (lead V6) acquired inside a 7 T MR scanner.

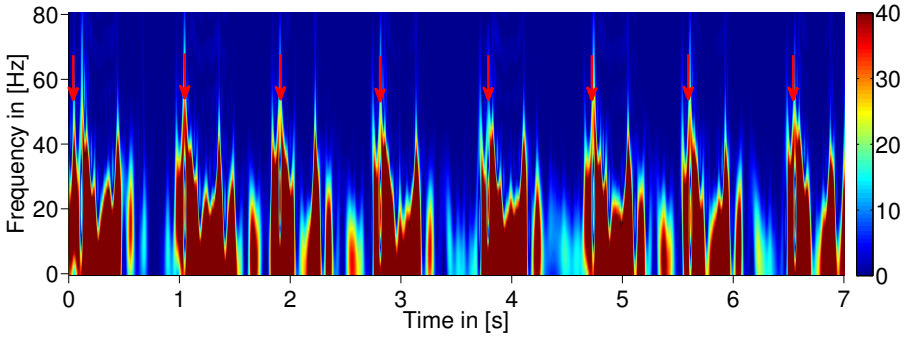

(d) TFED of (c)

Figure 3.17.: ECG signals acquired outside (a) and inside (c) a 7 T MR scanner and their corresponding time frequency energy distributions (TFED) (b,d). For the ECG acquired outside the MR scanner, most of the energy in the time-frequency plane is concentrated around the position of the R-peak whereas a frequency range of approximately 5 Hz to 50 Hz is covered. The TFED of the 7 T ECG contains higher energies in a wider range of frequencies and is spread along the time axis. The TFED were estimated using the smoothed pseudo Wigner Ville distribution (SPWVD). The positions of the QRS complexes are marked by red dots or arrows.

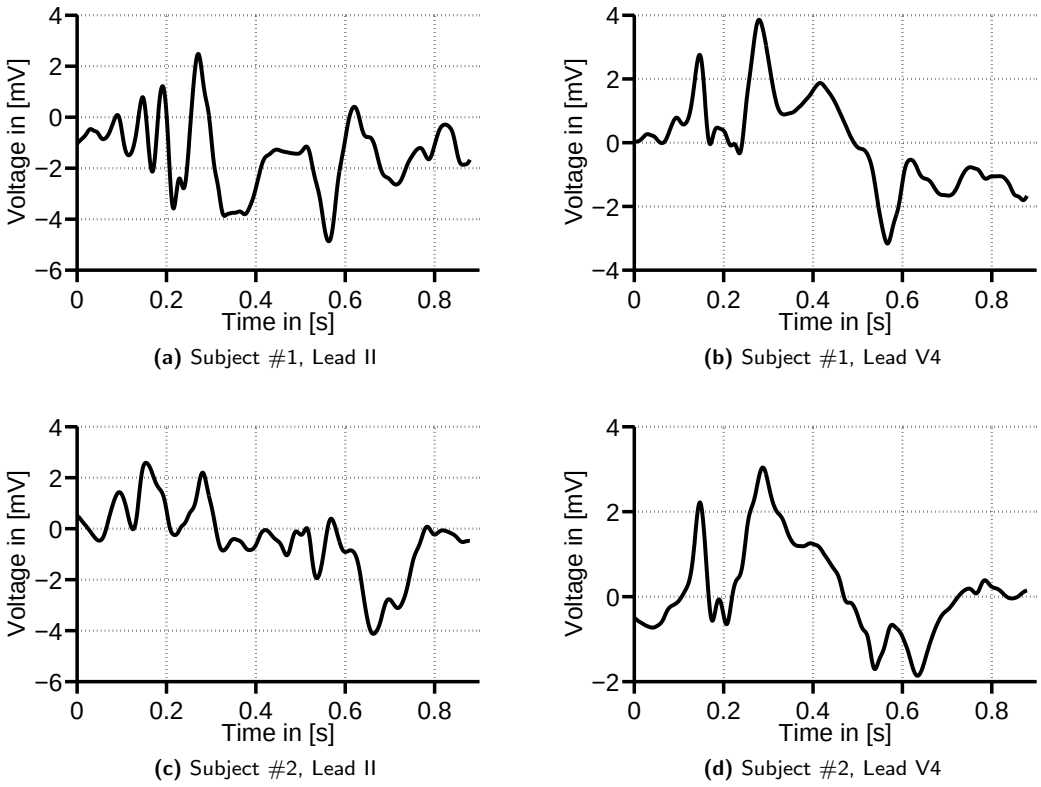

(a) Subject #1, Lead II

(b) Subject #1, Lead V4

(c) Subject #2, Lead II

(d) Subject #2, Lead V4

Figure 3.18.: Comparison of ECG signals acquired from two different subjects at a magnetic field strength of $7\,\mathrm{T}$. Depending on the subject and ECG lead, the MHD effect can exceed the magnitude of the R-peak. The general shape and temporal evolution of the MHD effect is different between the different subjects. (The R-peak is aligned at $t \approx 0.15\,\mathrm{s}$.)

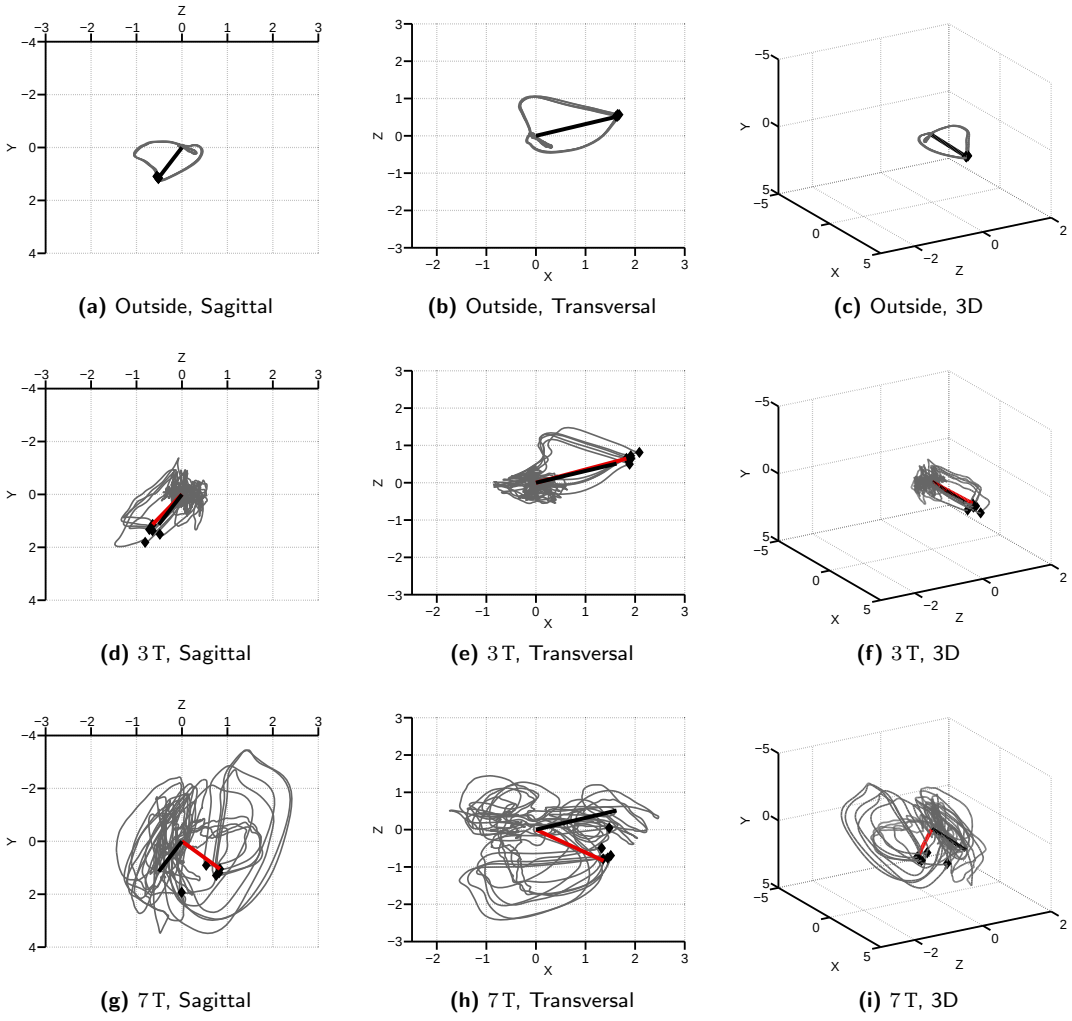

(a) Outside, Sagittal **(b)** Outside, Transversal **(c)** Outside, 3D

(d) 3 T, Sagittal **(e)** 3 T, Transversal **(f)** 3 T, 3D

(g) 7 T, Sagittal **(h)** 7 T, Transversal **(i)** 7 T, 3D

Figure 3.19.: VCGs in different views recorded outside and inside the 3 T and 7 T MR scanners. Black dots mark the positions of the R-peaks. Black lines in (d)-(f) and (g)-(i) represent the reference vector **r** taken from the ECGs (a)-(c) recorded outside the MR scanner. Red lines represent the R-peak vector from the ECG recorded inside the MR scanner. (All axes values are given in mV.)

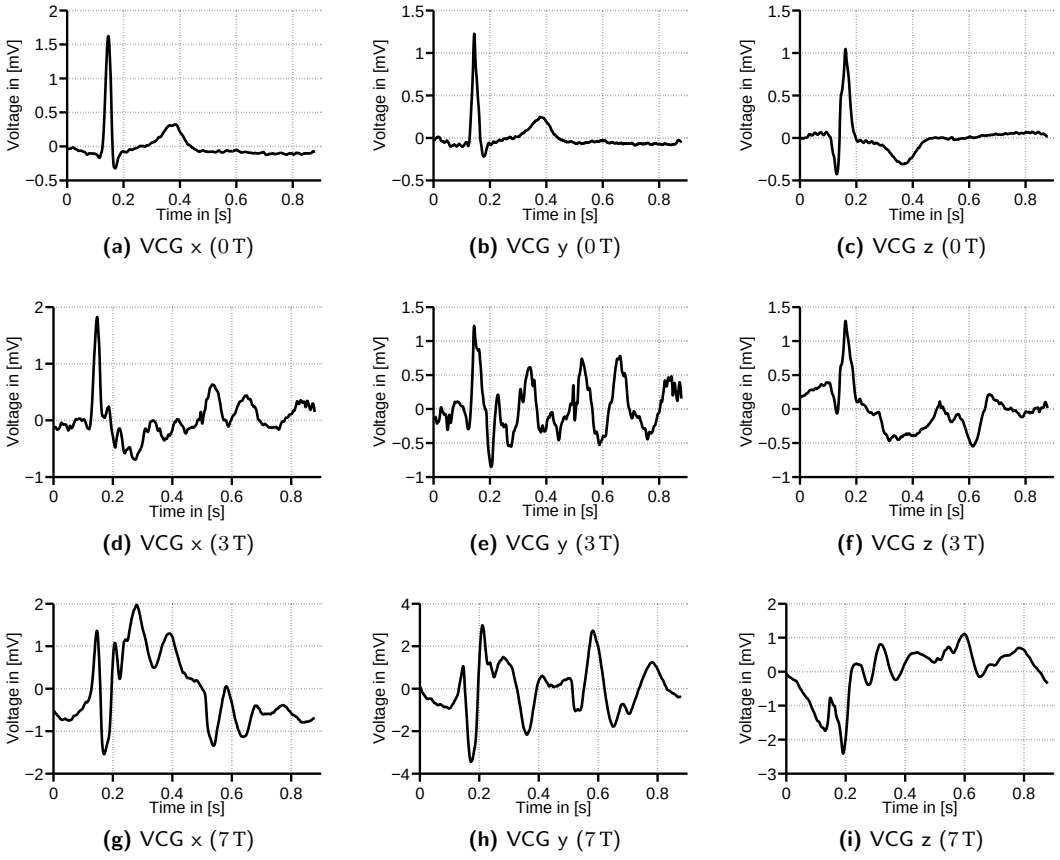

(a) VCG x (0 T) **(b)** VCG y (0 T) **(c)** VCG z (0 T)

(d) VCG x (3 T) **(e)** VCG y (3 T) **(f)** VCG z (3 T)

(g) VCG x (7 T) **(h)** VCG y (7 T) **(i)** VCG z (7 T)

Figure 3.20.: VCGs acquired (a)-(c) outside, (d)-(f) in a 3 T and (g)-(i) in a 7 T MR scanner. The R-peak is aligned at $t \approx 150\,\mathrm{ms}$.

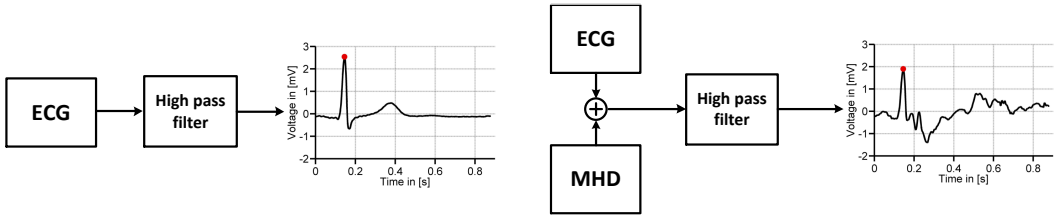

(a) ECG without MHD effect. **(b)** ECG with MHD effect.

Figure 3.21.: Baseline shift caused by the internal high pass filter of the ECG recorder. The MHD effect introduces an additional DC component which is suppressed by the HP filter. Hence, the amplitude of the R-peak is altered. This results in an alteration of the R-peak vector's amplitude and angle in the VCG domain.

3.4 Gating methods for motion compensation in CMR

3.4.1 Existing ECG-based gating methods

VCG-based gating

A widely used method for gating in CMR is based on the VCG [Fischer 99,Chia 00,Fischer 01,Nacif 12]. The VCG-based approach assumes that the ECG (especially the QRS complex), the gradients and the MHD effect are spatially separable within the VCG space. The initial proposal for the VCG-based gating method [Fischer 99] was using the Frank lead system to obtain a three dimensional VCG signal [Frank 56]. Later, an orthogonal lead scheme similar to the one depicted in Fig. 3.22(a) was used to obtain a 2D VCG. This 2D VCG is a simplified version of the VCG described in Section 2.1.3. The proposed method named 'target distance approach' is mainly based on the measurement of the distance between a reference vector $\mathbf{r}$ and the vector of the actual VCG measured inside the MR, $\mathbf{v}(t)$. The vector $\mathbf{r}$ is described by a reference R-peak from an ECG recorded outside the MR scanner with $\mathbf{r} = (r_x, r_y, r_z)$. The vector $\mathbf{v}(t)$ describes the spatial coordinates of the VCG inside the MR scanner at time t with $\mathbf{v}(t) = (v_x(t), v_y(t), v_z(t))$. R-peak detection is realised by measuring the angle and distance between the two vectors. A more detailed description of this method is given in Appendix A.

VCG-based gating methods are well established in typical clinical MR scanners with magnetic field strengths lower than $3\,\mathrm{T}$. However, in ultra-high field (UHF) MRI scanners with magnetic field strengths of $7\,\mathrm{T}$ or $9.4\,\mathrm{T}$ used in clinical research applications, these methods can be prone to errors due to the increased influence of the MHD effect [Frauenrath 09,Frauenrath 10b,Brandts 10,Lamb 12,Gregory 14a]. The analyses made in Section 3.3.3 intended to explain those observations made in clinical scenarios[5].

3D-QRS method

Tse *et al.* recently proposed a method for QRS detection up to $3\,\mathrm{T}$ using the '3D-QRS' method [Tse 11a,Tse 12,Tse 13,Gregory 14a]. The precordial leads of the 12-lead ECG were used to generate a 3D template of the QRS-complex. Such a template is depicted in Fig. 3.23. ECGs were acquired using a commercially available 12-lead ECG device, which was modified in order to make it $1.5\,\mathrm{T}$ MR conditional [Tse 10a, Tse 14]. The method was also tested with $7\,\mathrm{T}$ records[6]. R-peak detection was performed by cross correlating the ECG trace acquired inside the MR scanner with the predefined 3D QRS template. It showed promising results for the lower magnetic field regime ($\leq 3\,\mathrm{T}$). However, the method was tested with a few subjects only and the results clearly showed the limitations of this method for ECGs acquired at $7\,\mathrm{T}$. For the $7\,\mathrm{T}$ records, an average sensitivity $Se = 96.2\,\%$ and positive predictive value $+P = 96.1\,\%$ were achieved.

[5] The results of this study were published by Krug *et al.* [Krug 13b]
[6] The $7\,\mathrm{T}$ records used in the study of Gregory *et al.* [Gregory 14a] were provided by Johannes Krug.

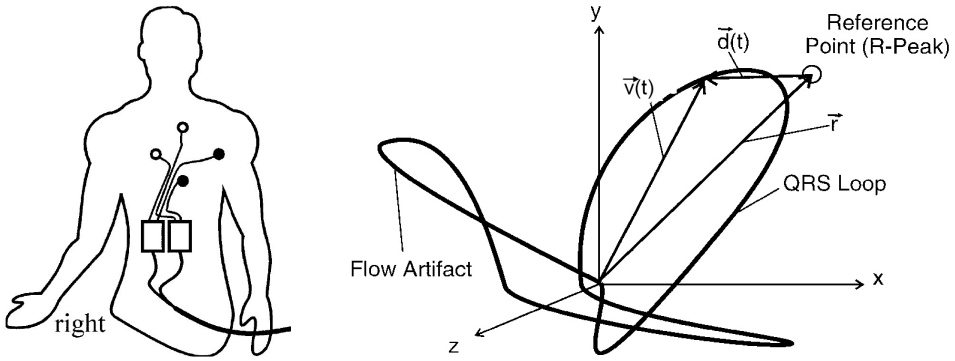

(a) ECG electrode configuration for recording two perpendicular leads [Chia 00].

(b) Principle of the VCG-based gating algorithm visualised using a 3D-VCG [Fischer 99].

Figure 3.22.: ECG electrode positions for acquiring two perpendicular leads (a) and the VCG-based gating principle (b). The gating principle is shown using a 3D-representation of the VCG. The reference vector $\vec{r} = \mathbf{r}$ was defined from an ECG acquired outside the MR scanner. The reference vector points at the position of an R-peak. Basically, the distance $\vec{d}(t)$ between the (static) reference vector $\vec{r}$ and the (moving) VCG vector $\vec{v}(t) = \mathbf{v}(t)$ obtained from the ECG acquired inside the MR scanner is measured. A minimum distance vector $\vec{d}(t)$ is assumed to correspond to the position of an R-peak.

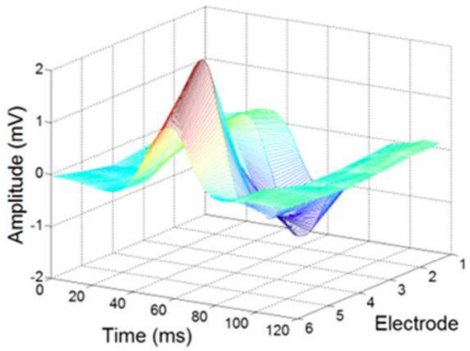

Figure 3.23.: 3D-template of the QRS complex used for R-peak detection. The template was derived from the six precordial leads V1-V6 (corresponds to electodes 1-6 in the figure). R-peak detection was performed by crosscorrelating the template with the signal of the precordial leads. (Image source: [Gregory 14b])

Wavelets

Oster *et al.* utilized the Wavelet transform and a local regularity characterization to detect the QRS complex in ECG signals contaminated by the MHD effect and additional gradient artefacts [Oster 09a]. After applying the wavelet transform using a 'Mexican Hat' wavelet, the scalogram was analysed for singularities. The R-peaks are considered as the most important singularities of the ECG signal. Gradient artefacts constitute singularities as well but with different regularity as estimated in the scalogram. The singularities were identified from the scalogram by measuring the local regularity, which can be measured using the Lipschitz exponent. Based on the detected singularities, R-peaks and gradient artefacts could be detected and classified.

A specific VCG-based R-peak detector for congenital heart diseases (CHD)

The MHD effect is not the only effect that can lead to false or missed R-peak detections. Morphological variations of the QRS complex can also lead to such misclassifications. Such variations can occur in patients suffering from congenital heart disease (CHD). CHDs such as Ebstein's anomaly of the tricuspid valve or the Tetralogy of Fallot cause variations of the ECG signal [Kastor 75, Gatzoulis 97]. Patients suffering from the Ebstein anomaly partially show altered QRS patterns [Kastor 75]. Due to these altered QRS patterns, gating based on the ECG can cause incorrect results, e. g. during MRI-based flow quantifications, or it can make cardiac gating impossible [Fratz 08]. To cope with gating problems in CHD patients, a matched filter, a template matching algorithm and a modified version of the VCG-based method were used for R-peak detection [Knesewitsch 13]. No further details were given about the implementation and combination of these techniques. The method was also partly described in [Frank 11, Frank 13]. No further details were provided about how the templates and the matched filter were designed. Although this method achieved a high R-peak detection quality for ECG signals recorded in a $1.5\,\mathrm{T}$ MR scanner in terms of specificity ($99.76\,\%$) and sensitivity ($100\,\%$), results for the mean delay and jitter of the detected R-peaks were not reported quantitatively. Besides, the proposed method was not tested in MR scanners with higher magnetic field strengths.

Higher order central moments

Higher order central moments constitute another method for QRS detection during MRI. Methods based on the central moments utilise the steep upslope and downslope of the QRS complex. Our previous works showed that such a method enables a reliable QRS detection [Schmidt 14]. The method was evaluated using $3\,\mathrm{T}$ ECGs and PhysioNet's *INCART*[7] arrhythmia database [Goldberger 00]. For QRS detection purposes, the 4$^{\text{th}}$ order central moment[8] was utilised which is defined as

$$\mu_4 = \mathbb{E}\left[(X - \mathbb{E}(X))^n\right] = \frac{1}{n}\sum_{i=1}^{n}\left(x(i) - \bar{x}\right)^4 \tag{3.12}$$

where $\mathrm{E}(X)$ is the expected value of X, $i \in \mathbb{N}$ and n the number of samples. After bandpass filtering the ECG signals (5$^{\text{th}}$ order Butterworth filter, passband ranging from $2\,\mathrm{Hz}$ to $30\,\mathrm{Hz}$), the 4$^{\text{th}}$ order central moments were computed in windows of $20\,\mathrm{ms}$ length [Schmidt 14]. The central moment exhibited high values during during the upslopes and downslopes of the QRS complex. An adaptive threshold was utilised for the QRS detection based on the central moments peaks. Figure 3.24 depicts the 4th order central moments obtained from ECGs acquired outside and inside a $3\,\mathrm{T}$ MR scanner.

[7] http://www.physionet.org/pn3/incartdb/

[8] In contrast, the moment of order n is defined as $m_n = \mathbb{E}\left[(X)^n\right]$ and standardise moment of order n as μ_n/σ^n where μ_n is the n-th central moment and σ the standard deviation.

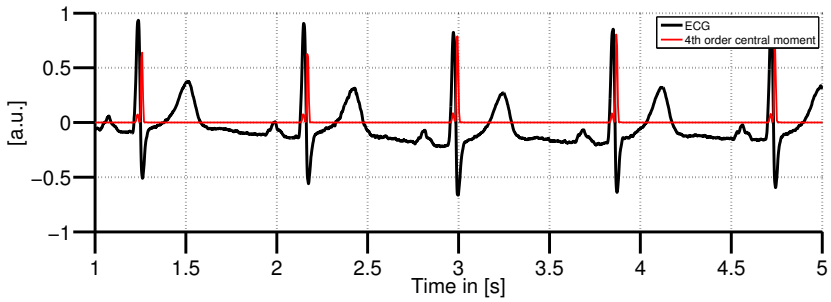

(a) ECG outside MRI and 4th order central moment.

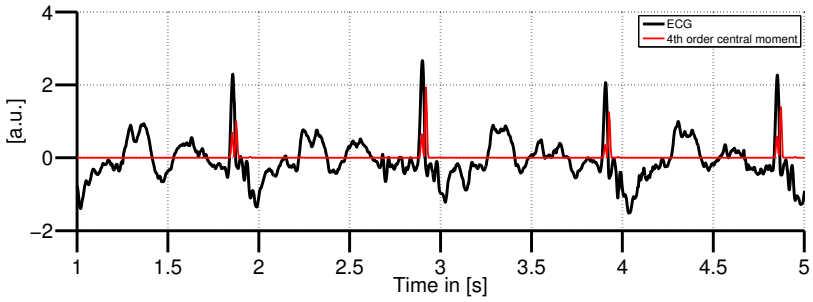

(b) ECG inside MRI (3 T) and 4th order central moment.

Figure 3.24.: QRS detection based on the computation of the 4th order central moments for ECG signals (lead V4) acquired outside (a) and inside (b) a 3 T MRI scanner. The central moment was computed in sliding windows of 20 ms length. During the upslopes and downslopes of the QRS complex, the central moment exhibits high values which were used for a threshold-based QRS detection.

3.4.2 Alternative gating methods

Navigator-based techniques

Navigator-based techniques can be used to measure the motion of the patient's heart muscle or of the diaphragm during normal respiration. The advantage of navigator-based techniques is that they do not require additional hardware. The general principle of this technique is explained and depicted in Fig. 3.25. A pencil beam (navigator) is excited and the resulting profile along this beam is measured. The navigator is placed along a direction of high signal contrast, e. g. along the border of a heart chamber (cardiac motion) or along the border of the lung and the liver (respiratory motion). The position of the border along the navigator is tracked, and as this border moving with respiration (or heart motion) it gives an alternative respiration (or heart motion) signal.

Phonocardiogram (PCG)

The phonocardiogram (PCG) is a representation of the heart sounds, which are caused by the isovolumetric contraction of the ventricles (heart sound S1) and by the closure of the aortic and pulmonary valves (heart sound S2) [Abbas 09]. The PCG was fist used by Henneberg *et al.* for patient monitoring during MRI [Henneberg 92]. It was then further developed by Frauenrath *et al.* for triggering CMR image sequences [Frauenrath 08, Frauenrath 09, Frauenrath 10b, Frauenrath 10c]. The PCG is measured using a purpose-built, MRI-compatible stethoscope whereas the first heart sound (S1) is used to trigger the MR scanner. This method was later used in a commercial device names EasyACT (MRI.TOOLS

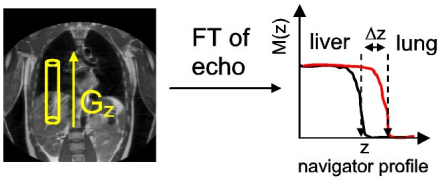

(a) Navigator principle based on motion estimation of the diaphragm. (Image source: [Nehrke 00])

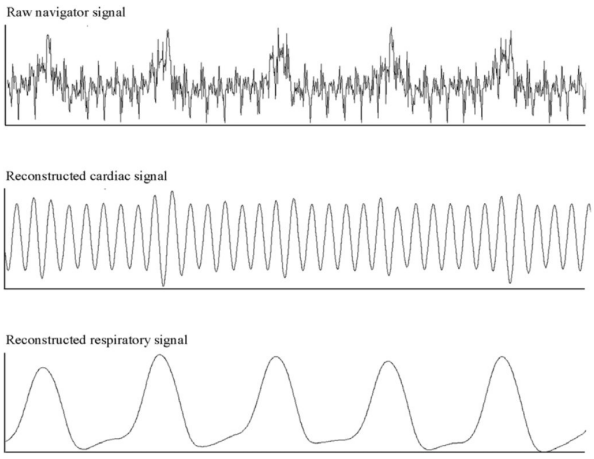

(b) Raw navigator signal (top) and the reconstructed cardiac (middle) and respiratory (bottom) signals. (Image modified according to [den Adel 13])

Figure 3.25.: Navigator-based estimation of the respiratory and cardiac motion. (a): Explanation of the functional principle using the motion of the diaphragm. A pencil beam is aligned through the diaphragm along the z-direction covering the border of the liver and the lung. The magnetisation along the z-axis is estimated by the Fourier transform of the pencil beam's gradient echo signal. The resulting signal distribution along the z-axis is the so-called navigator profile. The contrast in this profile is caused by the different signal intensities of liver and lung tissue. The total time required for applying the navigator pulse, for the acquisition of the gradient echo and the evaluation of the signals is approximately $20\,\mathrm{ms}$. (b): Estimated cardiac and respiratory navigator signals.

GmbH, Berlin, Germany).

Together with the ECG- or VCG-based gating methods, the PCG technique is one of the most reliable methods. This technique has been evaluated with a larger patient cohort in [Nassenstein 12b]. It was shown that this method is robust against acoustic distortions induced by pathological or artificial valves. Compared to the ECG, it is convenient to apply the PCG since a shaving of male patients is not required. The PCG-based gating method is compatible with the MRI environment since no metallic parts or wires have to be inserted into the MR scanner or attached to the patient. Since it is not affected by the MHD effect it can be used even at very high magnetic field strengths.

However, the PCG only worked for retrospectively gated cine imaging. This results from the delay between the R-peak and of the first heart sound S_1. There is a physiological delay between the QRS-complex and the first heart sound of $30\,\mathrm{ms}$ [Rangayyan 87]. The heart sound signal is then further delayed by the time it takes to travel along a wave guide until it reaches the electronic circuits placed outside the MR scanner, filter delays and the latency of the system generating a proper trigger signal [Frauenrath 08]. Hence, in a prospectively triggered cine sequence, the early systole would not be covered. The missed beginning of the systole could lead to a bias when assessing left ventricular (LV) function [Nassenstein 12b]. For retrospective image acquisition, the ECG- and PCG-based method gave comparable results for the assessment of the left ventricle. Another study revealed that PCG-based gating has some limitations in velocity-encoded phase contrast imaging [Nassenstein 12a].

Photoplethysmogram (PPG)

The PPG is a technique to assess the heart rate and can be obtained by a pulse oximeter. Usually, a sensor is applied at the finger tip or the earlobe. This sensor is composed of a light-emitting diode (LED) and a photodiode. The LED is used to illuminate the skin. The photodiode measures the light intensity transmitted through or reflected by the skin (depending on sensor construction). Due to the blood volume variation caused by the pulse pressure wave travelling through the vessels to the distal parts of the body (e. g. the finger tips), the intensity of the transmitted or reflected light varies. This information is used to estimate the heart rate. The PPG is robust against the distortions of the MHD effect and gradients (assuming a proper hardware design). Hence, it is a robust method to obtain the heart rate during MRI.

However, there is a high delay of around $300\,\text{ms}$ between the ECG's R-peak and the peak of the PPG signal [Allen 02]. Relevant parts of the cardiac systole would be missed when the PPG is used for gating in the MR scanner. The PPG-based measurement principle has another disadvantage which is related to the pulse transit time (PTT). The PTT is the time it takes the pulse pressure wave to travel from the heart to the periphery of the body. However, the PTT is not a constant time. It is affected by a variety of different factors including the compliance of the arteries, the blood pressure or the heart rate [Lane 83, Drinnan 01]. Hence, an *a priori* relation between the occurrence of the R-peak and the measured pulse pressure wave cannot be given. Gating methods that are based on measuring the pulse pressure wave would suffer from changes in the PTT. Hence, an exact offset between the occurrence time of the R-peak and the pulse pressure wave cannot be given. It was shown previously that PPG signals suffer from a high jitter [Frauenrath 10b].

These different physiological factors limit the utilisation of the PPG signal for gating purposes. In clinical practice, the PPG is only used if a proper ECG signal is not available which makes its previously mentioned limitations acceptable.

Ultrasound

Ultrasound (US) constitutes another method to measure cardiac motion and to achieve motion compensation. Günther *et al.* and Feinberg *et al.* utilised US to gather information about the motion and position of the diaphragm [Günther 04, Feinberg 10]. Based on the knowledge of cardiac motion, the MRI scan planes were updated in real-time.

The US-based approach by Kording *et al.* utilised the Doppler effect to generate a trigger signal [Kording 14]. For that, the Doppler signal from transmitral flow (the blood flow from the left atrium to the left ventricle) was acquired. The E-wave in the Doppler signal which is present during the early diastole was used as a trigger signal. Retrospectively gated CMR images were acquired using Doppler US, ECG and pulse oximetry as trigger signals. The image quality of US and ECG gated CMR were of comparable quality. The mean jitter difference between the Doppler US ($\sigma = 42\,\text{ms}$) and the ECG ($\sigma = 48\,\text{ms}$) was not significant. It was shown that the US-pulse wave signals can be used as an alternative to the ECG.

Gating methods based on US require additional hardware which can be used inside the MR scanner. This hardware is usually not commercially available and hence, custom modified products are used mostly for research purposes. It is not clear if the method based on Doppler-US functions properly with heart failure patients where the different wave are possibly not clearly determinable [Kording 14].

Patients with a reduced compliance may also negatively affect the quality of the Doppler US signal.

Measurement of oesophagus motion by means of an optical "stethoscope"

Brau *et al.* proposed a fibre-optic measurement system for the detection of oesophageal wall motions caused by the contractions of the heart [Brau 02]. Two attached optical fibres (one for transmitting and one for receiving the light) were inserted into the oesophagus. During the movements of the oesophageal wall, the amount of reflected light changed. This signal was utilised to derive information about cardiac motion. The system was evaluated in rats and mice and it was shown that it provided a robust trigger signal (no quantitative results were given). However, the system was not tested with human subjects. The obvious disadvantage of this method when applied to human subjects is the required insertion of an oesophageal catheter or endoscope.

Methods for a remote PPG using cameras

Non-contact measurements of cardiac activity could constitute another interesting possibility to achieve gating in CMR. Research groups from the *MIT, Cambridge, USA* [Poh 10, Poh 11], from the *University of Oxford, Oxford, UK* [Tarassenko 14, Villarroel 14] and from the *Dresden University of Technology, Dresden, Germany* [Lempe 13a, Lempe 13b, Zaunseder 14] published methods for the camera-based acquisition of a remote PPG (rPPG). Although the rPPG method has not been used for gating in CMR, it shall be briefly introduced since the physiological principle is similar to the contact-based PPG measurements. The rPPG method uses a camera to measure changes of skin color which result from blood volume changes in sub-surface blood vessels [Blazek 00]. An example for a rPPG measurement showing color encoded blood volume changes is depicted in Fig. 3.26. In order to measure the color variations at a dedicated position (e. g. at the forehead), a facial segmentation method was proposed [Díaz Morales 12]. With further improvements and an increasing robustness of the rPPG method it might be suitable for gating applications within the controlled MRI environment (constant lightning, less patient movement). However, the same constraints apply to this method as for the contact-based PPG method. Since the PTT is not constant and underlies the same physiological principles, this is expected to have a negative effect on the quality of CMR images.

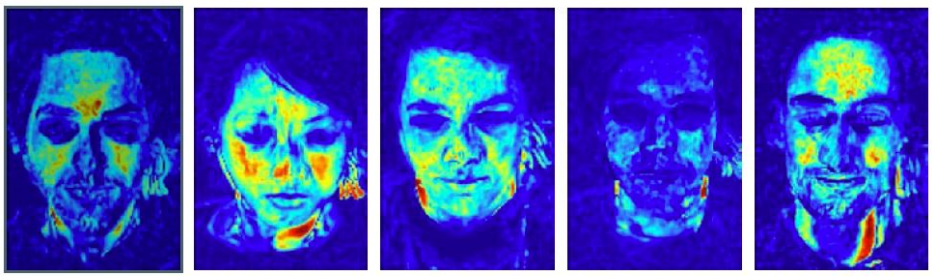

Figure 3.26.: Example for a remote PPG measurement showing pulse amplitude maps (blue: low signal value, red: high signal value). [Lempe 13b]

Camera-based ballistocardiogram acquisition

Ballistocardiograms (BCG) would be a further alternative for cardiac gating during MRI. BCGs measure the repetitive mechanical body movements which are caused by the ejection of blood into the major blood vessels [Weissler 73]. Camera systems with high spatial resolutions utilising interference patterns are one way to to measure microscopic head movements caused by ballistocardographic forces [Armstrong 02]. Such techniques are used to compensate head movements during high-resolution MRI scans of the brain [Stucht 12]. The relation between an optically acquired BCG signal and the ECG was investigated [Krug 14]. Head movements were measured using an MR-compatible camera system (MT 384ib, Metria Innovation, USA). Figure 3.27 depicts ECG signals with concurrently acquired displacement BCG signals and the derived velocity BCG. The delay of the displacement BCG exceeded $200\,\text{ms}$ for all subjects measured in the study. The maximum displacement of the head due to the cardiac activity were in the range of $20\,\mu\text{m}$ to $50\,\mu\text{m}$ [Krug 14]. Hence, sub millimetre movements of the head would cause artefacts in the BCG signal making peak detection more complicated or even impossible. This fact means that a high patient compliance is required to enable a reliable heart beat detection. Additionally, it is not yet fully investigated how certain cardiac arrhythmias affect the BCG signal and how this would influence gating in CMR.

3.4.3 Discussion and remaining problems

Nowadays, the ECG signal is the most common signal used for gating in CMR. The R-peaks or QRS complexes are the most dominant features of the ECG, which mark the beginning of the ventricular systole. Utilising the morphology of the ECG signal, several types of cardiac arrhythmias can be detected and distinguished. An ECG signal is acquired in most of the MR scanners where CMR imaging is performed or where the heart rate of the patient is required for monitoring purposes. This is either done by hardware provided by the manufacturer of the MR scanner or by external, MR safe hardware. Most of the devices and algorithms used for ECG acquisition and QRS detection are tested and approved for MR scanners with magnetic field strengths of up to $3\,\text{T}$.

With an increasing magnetic field strength, the detection of the R-peaks becomes more and more challenging due to the more severe MHD effect. CMR at $7\,\text{T}$ and above is usually referred to as ultra

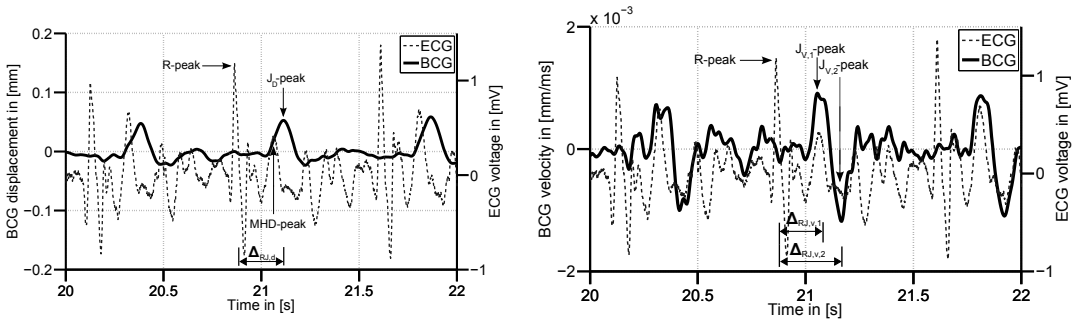

(a) ECG lead II and displacement BCG.

(b) ECG lead II and velocity BCG.

Figure 3.27.: Exemplary measurements of ECG lead II synchronised with the displacement (a) and the velocity (b) BCG signals. The ECG is contaminated by MHD signals which are caused by the flow of blood perpendicular to the static magnetic field.

high field CMR (UHF-CMR). Recent studies showed that ECG-based gating in UHF-CMR is prone to errors due to the increased MHD effect [Brandts 10, Frauenrath 10b, Lamb 12, Suttie 12, Krug 13b]. The impact of MHD-related gating problems at UHF-CMR was recently addressed during the 2013's conference of the *'Society for Cardiovascular Magnetic Resonance' (SCMR)*[9] within the special session: *'Solving the Cardiac Gating/Triggering Conundrum at Higher Fields'* [Carpenter 13]. This shows the high interest within the CMR research community to improve the quality of QRS detection for gating purposes, especially for research applications performed at magnetic field strengths of 7 T and above. The presented solutions were based on the ECG signal [Krug 13a, Tse 13], the phonocardiogram and self-gating techniques.

Other non ECG-based gating approaches, which are not affected by the MHD effect were proposed to overcome the problems of the ECG. However, these methods have other drawbacks which can influence the quality of the acquired MR data. The ECG is well studied and allows the detection of arrhythmias, which is required to obtain high-quality CMR images. Since the ECG's R-peak occurs before the ventricular systole and hence before the contraction of the myocardium, only the ECG enables the usage of certain CMR sequences. The PCG, PPG, rPPG and BCG signals have high delays with respect to the ECG's R-peak, which limits their applicability for certain CMR sequences. Another practical aspect is that physicians often desire an ECG signal to monitor a patients heart rate and to see a trace of the ECG (although the ECG is distorted by the MHD effect). Hence, the ECG signal is already used in most cases.

3.5 ECG-based patient monitoring during MRI scans

3.5.1 Previous works on ECG-based diagnostics

Adaptive filters

Tse *et al.* utilized a 12-lead Cardiolab-IT recording system (GE Healthcare, UK) for the acquisition of ECG signals during MRI [Tse 10a, Tse 11b, Tse 14]. The recording system was modified to be used during MRI [Dukkipati 08]. ECG signal were acquired at 1.5 T in head first and feet first positions. An adaptive least-mean-square (LMS) filter was trained using the ECG records acquired inside and outside the MR scanner. A schematic of the complete filtering procedure is depicted in Fig. 3.28. Before filtering, it was necessary to classify the beats either as normal or as premature ventricular contractions (PVC). Separate adaptive filters were then applied to the normal and PVC beats in order to attenuate the MHD signal components. No details were provided about how the different beats were classified and how the MHD effect could influence the automatic classification procedure. It was reported that the ST-segment was preserved after the MHD effect was filtered. However, no quantitative evaluation was provided. The MHD effect was utilized as a signal for estimating the cardiac output (CO). This was achieved by integrating the extracted MHD signal from the S-wave until the end of the cardiac systole. Differences were observed in the CO signals during normal and PVC beats. Results for the CO were only compared qualitatively and were not underpinned by any reference measurements. Although it is generally assumed that the aortic arch contributes most to the MHD effect, other blood vessels also contribute to this signal. Hence, the differences observed between a normal sinus rhythm and a PVC give no clear indication of how much and in which blood

[9] Meeting abstracts are available at: http://www.jcmr-online.com/supplements/15/S1

vessel the flow changed.

Independent component analysis

Bhatt *et al.* superimposed simulated MHD signals to real 12-lead ECG signals [Bhatt 09a]. MHD signals were simulated using the model described in [Bhatt 09c]. The ECG and arterial blood pressure (ABP) signals were taken from the *PhysioNet MGH/MF Waveform Database*[10] [Goldberger 00]. The simulated MHD signal was added to the 12-lead ECG using a linear mixing matrix. No further details were published about the definition of the weighting factors. The ECG signals and the linearly added MHD signal were separated using independent component analysis (ICA) [Hyvärinen 99a, Hyvärinen 99b]. The ABP signal was used as a reference signal to identify the IC which represented the simulated MHD effect. This IC was eliminated and the remaining ICs were used to construct an MHD-filtered ECG signal. The results are promising showing a good separation of the MHD effect and the underlying ECG signals. Important parts of the T-wave, i. e. its end and amplitude, could be restored. Errors occurred in the ST-segment and in the amplitude of the QRS complex. A limitation of this study is the way the MHD signal was simulated and how it was added to the ECG. The MHD signal was simulated for a single lead and a linear mixing matrix was used to superimpose this signal to the 12-lead ECG. Beat-to-beat variations of the MHD signal, e. g. caused by the different RRI length, were not considered. It can be assumed that the linear mixing model was mainly responsible for the good results obtained by the study. This assumption requires further investigation in order to reveal if ICA is capable of separating more realistic mixtures of ECG and MHD signals.

Time frequency analysis

In another study of Bhatt *et al.*, the simulated MHD effect was mixed into a single artificial ECG trace [Bhatt 09b]. The ECG signals were synthesized using an Gaussian model based ECG generator [McSharry 03b, McSharry 03a]. As with the ICA-based experiments, the aim was to separate ECG and MHD components to obtain an ECG signal for diagnostic purposes. The method utilised a single ECG lead contaminated by the MHD effect. A spectrogram or time frequency distribution of this single lead was obtained using a short-time Fourier transform [Kiencke 08]. Singular value decomposition (SVD) was applied to the STFT matrix (a 2-dimensional matrix) in order to decorrelate the different signal components. The power spectral density was obtained for each component. Those compo-

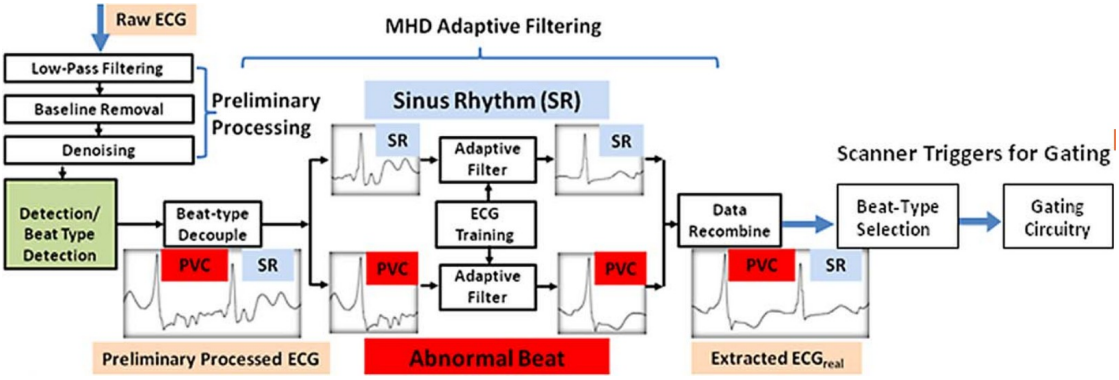

Figure 3.28.: Removal of the MHD effect using adaptive filters [Tse 14]. Preprocessing includes the classification of normal and PVC beats. Separate filters were then applied to the different beat types. (Image modified according to [Tse 14].)

[10] http://www.physionet.org/pn3/mghdb/

nents with high energy between 1 Hz and 4 Hz were assumed to correspond to the MHD effect and were eliminated, i. e. the singular values were set to zero. Filtered ECG signals were reconstructed by performing an inverse STFT. The results show an attenuation of the MHD but due to the remaining errors within the ECG's ST-segment, the method is not suitable for providing an ECG trace for diagnostic purposes.

Extended Kalman filters

Oster *et al.* proposed a model-based approach utilizing an extended Kalman filter (EKF) [Oster 13]. This method is also described in [Clifford 13]. The ECG signal was modelled using a synthetic ECG generator based on the sum of seven Gaussians [McSharry 03b, McSharry 03a]. For modelling the MHD effect, blood flow was measured using a 4D phase contrast MRI sequence (see Section 3.2.3). Muscle artefact and baseline wander noise were added to the simulated ECG signals. Using a 3D model of the aortic arch and the human torso, the body surface potentials caused by the MHD effect were estimated [Oster 12]. The ECG was modelled using an artificial vector model [Clifford 10], which was based on the synthetic ECG models described above. Two different types of pathological ventricular repolarisations were modelled by varying the parameters of the Gaussian functions representing the ECG: the inversion of the T-wave and a prolonged QT-interval. Using the EKF, the simulated pathological changes were detected in the filtered signals. The simulations did not include a variation of the MHD effect during the simulated pathological episodes.

Commercial devices and hardware developments

Several companies provide MR-compatible patient monitors. Depending on the device, different physiological and technical parameters can be measured such as the ECG, pulse and oxygen saturation, (non-)invasive blood pressure, capnography, anaesthesia gases or body temperature. The sensor data is transmitted wireless in most devices using different standards (e. g. Bluetooth® or Zigbee®). To mention the most popular devices: MIPM TeslaM3, Invivo Precess, Schiller MAGLIFE Serenity or GE Healthcare Datex-Ohmeda I4 MRI Monitor. Exemplary devices are depicted in Fig. 3.29. MR-compatible anaesthesia machines provide the support of anaesthesia gases and mechanical ventilation devices (e. g. the from GE Datex Ohmeda Aestiva 5 MRI or the Philips MRI 508 anaesthesia system). Although these devices provide an ECG monitor which can be also used for gating the MR scanner (depending on the manufacturer/model), none of the devices can provide an ECG signal which enables an analysis of the ST-segment or the T-wave for diagnostic purposes. Considering the transmission of the ECG signals, electrical wire are not preferred due to the different magnetic fields. Hence, fibre optical connections were used in the early days to transmit the ECG safely and without additional distortions outside the MR scanner cabin [Felblinger 94, Felblinger 95]. Nowadays, most commercial devices use wireless transmission techniques.

(a) MIPM Tesla M3 (image source: MIPM GmbH, Germany)

(b) Schiller Maglife Serenity (image source: Schiller AG, Switzerland)

(c) GE Healtcare I4 MRI Monitor (image source: GE Healthcare, USA)

Figure 3.29.: Exemplary MR-safe patient monitors from different manufacturers.

3.5.2 Discussion and remaining problems

The existing approaches can be roughly divided into two main groups: *1)* those approaches which developed methods and algorithms using real ECG signals acquired inside an MR scanner and *2)* those approaches that model the ECG or MHD signal or both. The advantage of the former is that the real signals cover the whole complexity of the MHD signal. However, the ground-truth of the ECG and MHD signals is unknown and it has to be assumed that the ECG does not change while the subject is moved into the MR scanner (which is an acceptable assumption for healthy subjects). So far, no detailed studies were published about how different denoising techniques affect the filtered, real ECG signals and if such a filtered signal can be used for diagnostic purposes.

The advantage of the simulated approaches is that both signals are known *a priori*. Hence, the obtained filter results, e. g. the removal of the MHD effect and the remaining ECG signal, can be evaluated quantitatively. Most simulations consider the aortic arch as the main contributor of the MHD effect. Depending on which model is used, the simulated MHD waveforms come close to their realistic counterparts but cannot synthesize the whole complexity of the real MHD signals. This can be explained by the fact that in real measurements, several other blood vessels contribute to the MHD effect as well. Additionally, the MHD effect highly depends on the subject's anatomy. However, models of the MHD effect can be used to better understand the influence on the ECG and to develop filtering methods, which can then be applied to real ECG measurements. Different signal processing methods were used to obtain a diagnostic ECG during MRI.

Adaptive filters were applied to ECG signals with normal and premature ventricular beats. Although it was stated that the adaptive filters preserved the amplitude of the ST-segment, no quantitative studies were made using these methods. Additionally, the proposed method used different filters for normal and PVC beats which required an initial identification of the beat type which again depends on a specific subject. ICA was used to separate simulated mixtures of MHD and ECG signals. The disadvantage of the described procedures is the linear mixing model which was used add the MHD effect to the ECG signals. This assumption is not valid since the real ECG signals measured by the different electrodes cannot be assumed to be linear combination of each other. Both, the ECG and the MHD signal have their origin in different, spatially separated locations. More extensive studies

were made using an EKF. An EKF was used to filter simulated mixtures of ECG and MHD signals with additionally simulated pathologies of the ventricular repolarisation. The results were promising and yielded denoised ECG signals, which allowed a correct detection of the simulated T-wave inversions and the QT prolongations. In the future, the underlying models could be extended by also modulating the MHD effect during pathological episodes. Using the results obtained from the simulated signals, the EKF should be applied to real ECG signals acquired at different magnetic field strengths.

Currently, there is no study available which applied the filtering algorithms to simulated and real ECG records in order to provide an extensive quantitative and qualitative evaluation. However, such an evaluation would be required to discover those methods which could be used for a real clinical application in the future. Since the simulated records can be used to evaluate different algorithms quantitatively, a combined study using simulated and real records would be preferred.

ECG lead configurations

As shown in Section 3.5.1, 12-lead ECGs were already used during MRI for improved patient monitoring purposes. The importance of the 12-lead ECG for cardiac diagnostic was also shown in Section 2.1.4. Typical MR-conditional patient monitors as shown in Section 3.5.1 usually use dedicated electrode configurations. Figure 3.30 compares the 12-lead configuration, which is often used for diagnostic purposes (see Section 2.1.4) to a standard electrode configuration used for gating purposes. With these dedicated and reduced electrode configurations, manufacturers try to minimise the influence of the different magnetic fields in order the optimise the QRS detection for gating and heart rate estimation. However, these non-standard configurations cannot be used for a detailed ECG analysis due to reduced number of leads and the different electrode positions altering the morphology and amplitude of the ECG signal. Hence, to enable an ECG-based gating and patient monitoring during MRI, a standard ECG electrode scheme should be preferred.

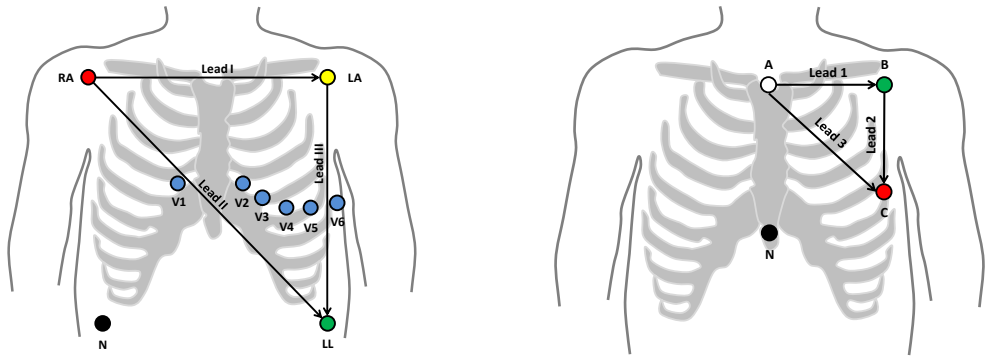

(a) 12-lead ECG configuration **(b)** 2-lead/3-lead system

Figure 3.30.: Different ECG electrode configurations for monitoring (a) and gating (b) purposes. Due to the different locations of the electrodes used during MRI (b), different ECG morphologies and amplitudes are acquired when compared to a standard 12-lead ECG electrode scheme (a) (see Sections 2.1.2 and 2.1.4). Hence, such electrode configurations have a limited value for diagnostic purposes.

3.6 Summary of previous works

Inside the MRI bore, the MHD effect causes distortions of the ECG signal. Experimental measurements showed that these distortions mainly affect the P-wave, the ST-segment and the T-wave. QRS detection within the MR scanner can be hampered due to the signal properties of the the MHD effect. For magnetic field strengths of up to 3 T, the usage of the ECG for gating in CMR is reliable and the MHD effect plays a subordinate role for the detection of the R-peaks. However, previous studies showed that ECG-based gating is less reliable at higher magnetic field strengths of 7 T and above. This can be explained by the increased MHD effect, which is more than twice as high when compared to 3 T measurements (see Section 3.3.1). Hence, those techniques developed for QRS detection at lower magnetic field strengths cannot be directly used at higher magnetic field strengths in all cases. There are no publications dedicated to the acquisition and processing of ECG signals for a reliable QRS detection at magnetic field strengths of 7 T.

The MHD effect also limits the diagnostic value of the ECG signal during MRI at all magnetic field strengths. Most commercial devices utilizing the ECG during MRI focus on its application for gating purposes and heart rate estimation (see Section 3.5.1). *None* of the commercial devices currently available on the market provides a diagnostic ECG trace, which could be used for ST-segment or T-wave analysis. Except for heart rate estimation, only limited information can be obtained from an ECG signal recorded during MRI. Only few research groups addressed the problem of obtaining a diagnostic ECG during MRI, either by using simulated or real ECG signals. The studies described in Section 3.5.1 based on real measurements give no detailed description of the methods or the results, i. e. detailed quantitative or qualitative evaluation of the important sections of the ECG are missing. The proposed methods based on simulated signals provided a helpful reference for the application to real ECG signals. One promising method implemented an EKF utilizing a synthetic model of the ECG signal. ECG signals with simulated MHD effect were used for the analysis. This method could be used for gating and monitoring purposes. However, due to the underlying model, an extension of the Bayesian filter method is required to be used in real-time.

All simulation models were not able to predict the full dynamics and complexity of the MHD signals. This can be explained by the complicated origin of the MHD effect. Practically it is very difficult to simultaneously assess the blood flow dynamics in the larger blood vessels with a high spatial and temporal resolution. The specific patient geometry plays an important role as well, i. e. the geometry of the torso and the location of the vessels and the myocardium. The simulation of all effects and factors might not be feasible in a clinical scenario since this would require a detailed knowledge of the patient's anatomy and of the functional information, i. e. a blood flow quantification. Another aspect is the complex interaction of both effects, i. e. of the ECG and the MHD. A changing ECG signal, e. g. during a pathological event such as an ischemia, could be related to changes in the cardiac output and blood flow. However, the simulation models provide a very helpful tool for the development and evaluation of different filtering algorithms since only simulated signals allow a precise quantitative analysis.

3.7 Objectives of this thesis

Based on the investigations made in this chapter, this thesis aims to improve the quality of ECG signals during MRI exams. More precisely, the following two aims are pursued:

1. Reliable R-peak detection for gating cardiac MRI sequences at 7 T.
2. Improved ECG-based patient monitoring during MRI up to 3 T.

Different simulated and real ECG records are required to improve existing or develop new methods, which can achieve these aims. For diagnostic purposes, a conventional 12-lead ECG is preferred over other lead configurations due to the reasons given in Sections 2.1.2 and 3.5.2. 12-lead ECG hardware shall be used for the acquisition of the ECG signals from several subjects at different magnetic field strengths. To simulate the MHD effect, the model of Oster *et al.* described in Section 3.2.3 is used. The synthetic model which is used for the generation of the ECG is described in Section 4.2.2. Figure 3.31 outlines the different strategies, which are followed to achieve the two main aims.

Gating

The first aim arises from the fact that CMR at 7 T (and above) attracts more and more attention and interest from the CMR research community. Since no dedicated QRS detection algorithms were developed for such high field strengths, problems were reported from different research groups. Real 12-lead ECG records acquired in a 7 T MRI scanner were used for the development and evaluation of the different QRS detection algorithms. At the beginning, the existing VCG-based method were improved based on the analyses made in Section 3.3.3. Following this, an approach based on ICA was pursued to separate ECG and MHD components in order to obtain one independent component, which is dominated by the R-peak or QRS complex. Results obtained by the newly developed method were compared to other QRS detection methods (those described in Section 3.4.1 and standard QRS detection algorithms referenced in Section 5.4). Although the implementation of the developed algorithms on dedicated MRI hardware is not an aspect of this thesis, the developed method should be applicable for an online usage by fulfilling the following requirements:

- Robust QRS detection in ECG records with low SNR.
- Applicable to ECG records with different MHD patterns.
- No user interaction, i. e. fully automated procedure.
- Online processing of the data using low computational resources.
- Small delays and jitter for the QRS detection.

Patient monitoring

Different requirements apply for the ECG-based patient monitoring during MRI. In this case, filtering should not only enhance the QRS complex but also preserve the ST-segment and the T-wave of the ECG signal. These segments are important for several diagnostic applications. Simulated and real ECG signals were used for the development and evaluation of the algorithms. Wiener filters were applied to both signal types since promising results based on adaptive filters were shown previously. ICA was used to identify all independent components, which contain (relevant) information about the ECG signal. Previous works using ICA made assumptions which do not apply in a realistic scenario. Hence, ICA was applied to more realistic simulations and to real ECG signals as well in order to study the

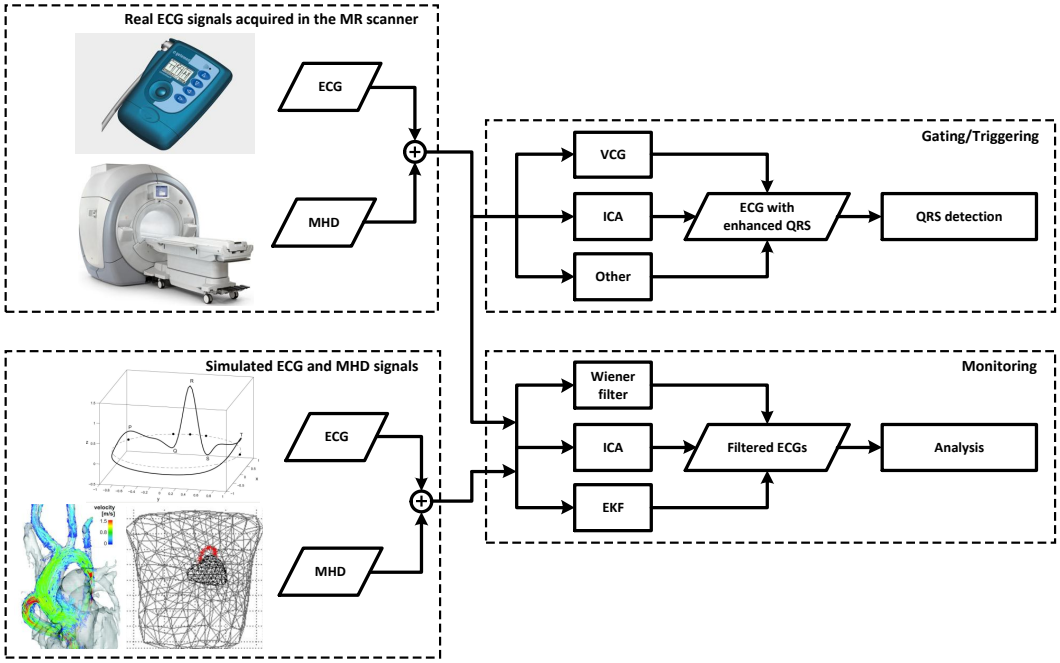

Figure 3.31.: Overview of the thesis objectives. Real and simulated ECG signals are used to develop methods for QRS detection at 7 T and for monitoring purposes at 3 T.

practical applicability of this method. Finally, an existing EKF framework was used since its previous application to ECG signals corrupted by the MHD effect showed promising results [Oster 15]. Based on previous simulation works, the simulation models of the ECG and MHD signals were extended to include more variations of both signals during pathological episodes. The different algorithms were evaluated quantitatively and qualitatively using simulated and real ECG records, respectively.

4

Material and evaluation metrics

4.1 Acquisition of ECG signals during MRI

4.1.1 Experimental setup

As described in Chapter 3, an ECG acquired during MRI is distorted by the gradients and by the MHD effect. Since this work is focused on the suppression of the MHD effect for diagnostic and gating purposes, the effect of the gradients was neglected. Hence, all physiological signals used in this work were acquired in different MR scanners but in the absence of the switched gradient magnetic fields. This means that the acquisition of the signals was performed while the scanner was not in use.

A wide variety of hardware is available for acquiring ECG signals. They can include patient monitors as used during anaesthesia, 12-lead ECG devices used during cardiac stress tests, biosignal amplifiers or portable Holter-ECG devices used for long-term monitoring. Besides, specific devices exist, which can be used in the MR scanner during imaging, either for patient monitoring or for obtaining a limited diagnostic information.

Two major requirements had to be fulfilled by the ECG hardware to be used in this work:

1. 12-lead ECG for diagnostic purposes and
2. access to the raw ECG data.

The first requirement could be fulfilled by biosignal amplifiers, which usually provide a large number of input channels or by a conventional 12-lead ECG device. The advantage of a 12-lead ECG is that it also provides more information about the spatial distribution of the ECG and MHD signals than an ECG device with less channels. The second requirement limited the number of usable devices since

most manufacturers of clinical ECG hardware do not give access to the raw ECG signals. Finally, a conventional 12-lead Holter ECG device (CM3000-12, Getemed, Germany)[1] with the following technical specifications was utilised:

- Number of channels / ECG leads: 12
- Sampling rate: 1024 Hz
- Resolution: 12 Bit
- Input voltage range: ± 6 mV
- Analogue bandwidth: 0.05 Hz to 100 Hz

Additional software enabled a conversion of the proprietary signal format into a readable text format, which could then be used for further processing. This device was slightly modified since it was not safe for the usage in close proximity to the MR scanner. Mechanical forces were caused by the magnetic parts used inside the device. The battery and ferromagnetic screws were identified as the main problems. In order to operate the ECG outside the range of the static magnetic field (outside the 5 Gs line[2]), the lead cables running from the Holter ECG device to the ECG electrodes were extended with flat ribbon cables. For the MR scanner with the highest field strength utilised in this work – the 7 T MR scanner – the 5 Gs line had a distance of ≈ 9 m from the MR scanner's center (this scanner did not have an active shielding of the magnetic field). Figure 4.1 depicts the Holter ECG device with the extended lead cable and the electrode clips. Although such long wired connections are generally prone to coupling effects (especially from the 50 Hz or 60 Hz power grid), no coupling was expected inside the MR scanner room since it is can be considered as a shielded environment.

The Holter ECG as well as the extended lead cables were not MR compatible. This means that there was a potential safety risk causing patient injuries or damages of the electronic components of the ECG recorder (see Section 2.2). As a consequence, the ECG signals were acquired without imaging, i. e. no gradients or RF signals were present during ECG acquisition. Nevertheless, the static magnetic field of the MR scanner was always present meaning that the acquired ECG signals were always affected by the MHD effect.

The ECG signals used within this thesis were acquired in two different MR scanners *without imaging*:

- 3 T Siemens Magnetom Skyra
- 7 T Siemens Magnetom

To investigate the relation between the patient's position and the $\mathbf{B}_0$ field, ECGs were measured in different positions:

1. feet first (Ff) and in
2. head first (Hf) position.

As described in Sections 3.2.1 and 3.3.1, a change between those two positions reverses the orientation of the static magnetic field vector $\mathbf{B}_0$, which should approximately invert the MHD effect. The subject's sternum was positioned in the centre of the MR scanner's bore during the measurements in order to have a homogeneous static magnetic field close to the myocardium and the adjacent blood vessels. The ECG signal was acquired for 2 min to 3 min outside and 4 min to 5 min inside the MR scanner

[1] The CM3000-12 was kindly provided by Getemed. http://www.getemed.de

[2] The area outside the 5 Gs line is generally considered as safe for the general public. This includes a safe operation of devices such as cardiac pacemakers or other electronic devices (5 Gs$\hat{=}$0.5 mT) [MHRA 07].

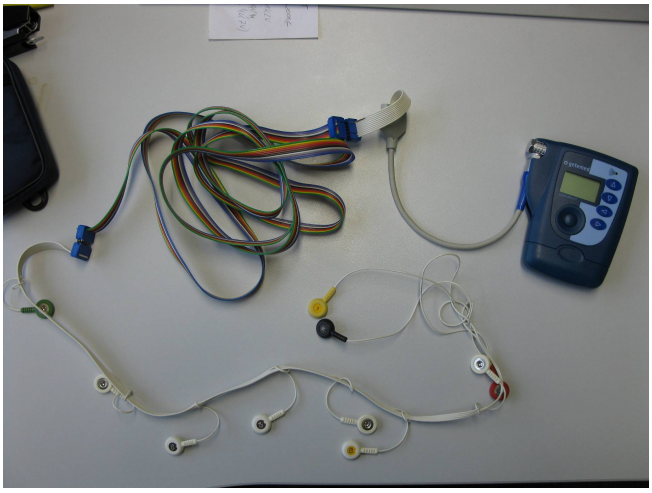

Figure 4.1.: Holter ECG (CM3000-12, Getemed, Germany) with extended cables for the usage inside a 3 T MR scanner room. Electrodes were placed in a Mason-Likar 12-lead ECG configuration (see Section 2.1.2).

in each position (Ff, Hf). The signals acquired outside the MR scanner were used to investigate and compare the different signal properties and were also used as reference signals in some of filtering methods.

4.1.2 Definition of ECG datasets used for the different investigations

Annotation of the QRS complexes

A manual annotation of the QRS complexes was performed in order to assess the quality of the developed algorithms. This manual annotation was set as the gold standard. The signals were independently annotated by two ECG experts: one physician (annotator A) who is regularly working with ECG signals in clinical routine and one medical student (annotator B). Due to the high distortion of the ECG traces caused by the MHD effect, the manual annotation of the QRS complexes was challenging in most cases for the 7 T records. Different ECG leads were provided to the annotators in order to understand the different signal components (ECG and MHD) and to enable a more reliable annotation of the R-peaks. Figure 4.2 shows how different ECG leads were displayed during the manual annotation procedure. Several leads of the clean ECG acquired outside the MR scanner and the ECGs contaminated by the MHD effect were plotted at the same time. With the help of the QRS morphology, which is partly preserved in the contaminated ECGs and the variations of the MHD effect, a manual annotation was possible. Additionaly, a heart rate time-series (tachogram) was displayed to immediately identify misclassified or missed R-peaks (assuming that no arrhythmias were present). However, each record had its specific properties so the annotators had to get used to the different morphologies of the MHD effect. In general, the precordial ECG leads provided the best signal quality, i. e. the QRS complex was more pronounced in these leads. Lead V4 was least affected by the MHD effect in most of the records. Depending on the exact positioning of the ECG electrodes and the subject's anatomy, the best lead for the annotation varied from V2-V4.

For the 7 T ECG records, both annotators initially agreed in 5293 cases. There was a disagreement in 164 cases. By a subsequent simple tachogram analysis it was found that a total of 51 QRS complexes were completely missed by the annotators. These missed QRS complexes were corrected and included

in the annotation vectors. The remaining 113 cases of disagreement were caused by a falsely annotation of MHD peaks. These falsely placed annotations were jointly corrected by both annotators. Finally, a total of 5457 QRS complexes were annotated and used as the gold standard for the evaluation of the different algorithms presented in Chapter 5.

Compared to the annotations of the 7 T ECG, the annotations of the 3 T records was a straightforward task since QRS detection is generally reliable at 3 T (without the gradient magnetic fields). Hence, for these records, one set of annotations was provided by an ECG expert and another set of annotations was obtained using a standard Pan-Tompkins-based QRS detection algorithm [Clifford 02]. Both annotations vectors were checked and corrected according to the above descriptions.

To have each annotation directly on the R-peak, i. e. on the point of maximum or minimum amplitude (depending on the polarity of the R-peak), the annotation's position was automatically corrected. This optimisation was performed in ECG lead V4 in all records since this lead was least affected by the MHD signal in most records (the R-peak has a positive amplitude in this lead). Using a predefined search window of 30 ms positioned around each of the manual annotations, the location with the maximum value within the search window was identified and the previous annotation location was overwritten. This process should ensure a consistent evaluation of R-peak detection delay times as utilised in chapter 5. After this procedure, the a trace of the ECG together with the annotations was manually rechecked to ensure that the annotations were placed at the peak position of QRS complexes and not on an adjacent peak.

ECG records used for QRS detection at 7 T

One of the aims of this thesis was to improve the QRS detection for cardiac gating at 7 T. For this purpose, a total of 18 different ECG records were acquired inside the 7 T MR scanner. These records were divided into a training and a test dataset, where the training dataset consisted of ten records and the training dataset of eight ECG records. The training dataset, which was acquired from five healthy subjects[3] (four male, one female) aged between 24 and 31 years, was used for the development of the QRS detection algorithms. Eight test records (four Ff, four Hf) were acquired inside the MR scanner from four male subjects aged between 26 and 30 years and were used to compose the training dataset[4]. One subject was included in the training and in the test dataset. Table 4.1 summarises the names and properties of the different datasets and records. The separation into the two datasets (training and test) was also used to evaluate the existing QRS detection methods.

Table 4.1.: Definition of a training and as test dataset using the ECG records acquired at 7 T. Ten records were used for the training and eight records used for the test dataset. The two datasets were used to train and validate different methods for QRS detection at 7 T.

	Feet first (Ff)	Head first (Hf)	# R-peaks	Length
Training dataset	D_1 (Ff) - D_5 (Ff)	D_1 (Hf) - D_5 (Hf)	2853	47 min
Test dataset	D_6 (Ff) - D_9 (Ff)	D_6 (Hf) - D_9 (Hf)	2604	40 min

[3] Acquisition of the training records: 25 July 25 2012
[4] Acquisition of the test records: 5 August 2013

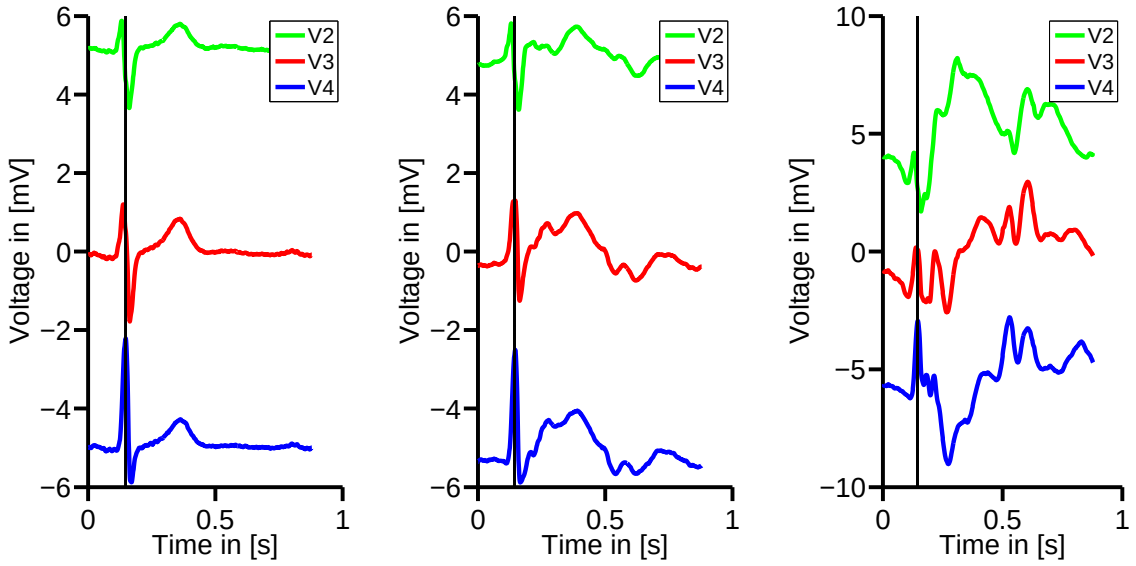

(a) ECG traces at 0 T. **(b)** ECG traces at 3 T. **(c)** ECG traces at 7 T.

Figure 4.2.: Manual annotation of the contaminated ECG traces (3 T and 7 T) based on a visual analysis of multiple leads (V2, V3, V4), the influence of the MHD effect in these traces and the remaining morphology of the QRS complex (a) in the contaminated leads (b),(c). Several ECG leads were utilised because the MHD effect complicated the identification of the QRS complex, especially inside the 7 T MR scanner. (Additional DC components were added to leads V2 and V4 for better visibility of the different leads.)

ECG records used for ECG-based diagnostics at 3 T

The other goal of this thesis was to improve the diagnostic meaningfulness of ECG signals acquired during an MRI scan. Most of the clinical interventions described in Section 2.3.2, which require a diagnostic ECG during MRI, are preformed at lower magnetic field strengths. Hence, additional ECG signals were acquired at 3 T from three male subjects aged between 26 and 29 years. These 3 T ECGs were used for a qualitative evaluation of different filtering approaches utilised in Chapter 6.

4.2 Simulation of ECG and MHD signals

4.2.1 Overview

For diagnostic ECG purposes, a quantitative evaluation was required for the identification of a denoising approach, which would enable a proper suppression of the MHD signal. However, this is not possible using real ECG signals since the ground-truth of the ECG measured inside the MRI scanner is not known. Hence, the real ECG signals described in Section 4.1 could only be used for a qualitative evaluation. To circumvent this problem, ECG and MHD signals were simulated.

A synthetic signal generation model, which is based on Gaussian waves, will be described in Section 4.2.2. This model is used to simulate ECG and MHD signals. Simulations of the MHD signal based on real 7 T ECG measurement can be found in Section 4.2.3. A template of the real MHD signal is computed and modelled by a sum of Gaussians using the model described in Section 4.2.2. The

simulated MHD signals are mixed with real ECG signal acquired outside the MRI scanner. A completely simulated approach is described in Section 4.2.4. The ECG is simulated using the Gaussian model whereas the MHD signal is simulated utilising real, MRI-based blood flow measurement and a realistic torso model (compare Section 3.2.3). The flexibility of the completely synthetic approach is utilised to simulate pathological ECG signals and the corresponding MHD signals. Section 4.2.5 describes the simulation of the pathological ECGs, which included prolonged QT-intervals, inverted T-waves and depressed/elevated ST-segments.

4.2.2 Gaussian wave-based model for the synthetic (ECG) signal generation

McSharry *et al.* introduced a model for the generation of synthetic (ECG) signals based on a sum of several Gaussian functions [McSharry 03b]. The general idea of this model was to represent the different fiducials of an ECG signal such as the P,Q,R,S and T-waves by a Gaussian function in an (x, y, z) coordinate system. Figure 4.3 depicts the formation of a simulated or synthetic ECG signal using seven Gaussian functions. Sameni *et al.* proposed a modification of the original model by using polar coordinates instead of Cartesian coordinates [Sameni 06, Sameni 08]. Using polar coordinates, the state equations of the dynamic ECG model can be written as

$$\begin{aligned} \dot{r} &= r(1-r) \\ \dot{\theta} &= \omega \\ \dot{z} &= -\sum_{i\in\{P,Q,R,S,T\}} \frac{\alpha_i \omega}{b_i^2} \Delta\theta_i \exp\left(-\frac{\Delta\theta_i^2}{2b_i^2}\right) \end{aligned} \tag{4.1}$$

where r is the radial state variable and θ the angular state variable with $\Delta\theta_i = (\theta - \theta_i) \pmod{2\pi}$. The parameters α and b define the magnitude and width of the Gaussian function and θ describes its angular position on the unit circle. The first equation in 4.1 is redundant since the second and third equation are independent of r. Hence, it can be excluded from the model. The simplified, generic model is then described by

$$\begin{aligned} \dot{\theta} &= \omega \\ \dot{z} &= -\sum_{i} \frac{\alpha_i \omega}{b_i^2} \Delta\theta_i \exp\left(-\frac{\Delta\theta_i^2}{2b_i^2}\right). \end{aligned} \tag{4.2}$$

It was shown that a set of seven Gaussians is sufficient for the representation of the $(P^-, P^+, Q, R, S, T^+, T^-)$ fiducials of an ECG signal [Sayadi 10]. The two Gaussians used for the P-wave and for T-wave can account for biphasic or other more complex patterns of these waves which can occur in normal and pathological ECGs (see Section 2.1.4). The Open-Source ECG Toolbox (OSET) was used to generate a synthetic ECG based on the model given in Eq. 4.2 [Sameni 06].

The Gaussian wave-based model can be used to (i) generate synthetic ECG signals based on predefined parameters or (ii) one can fit the model to a given ECG signal and estimate the corresponding parameters. Both approaches were used for different purposes within this thesis and are described in Sections 4.2.3–4.2.5.

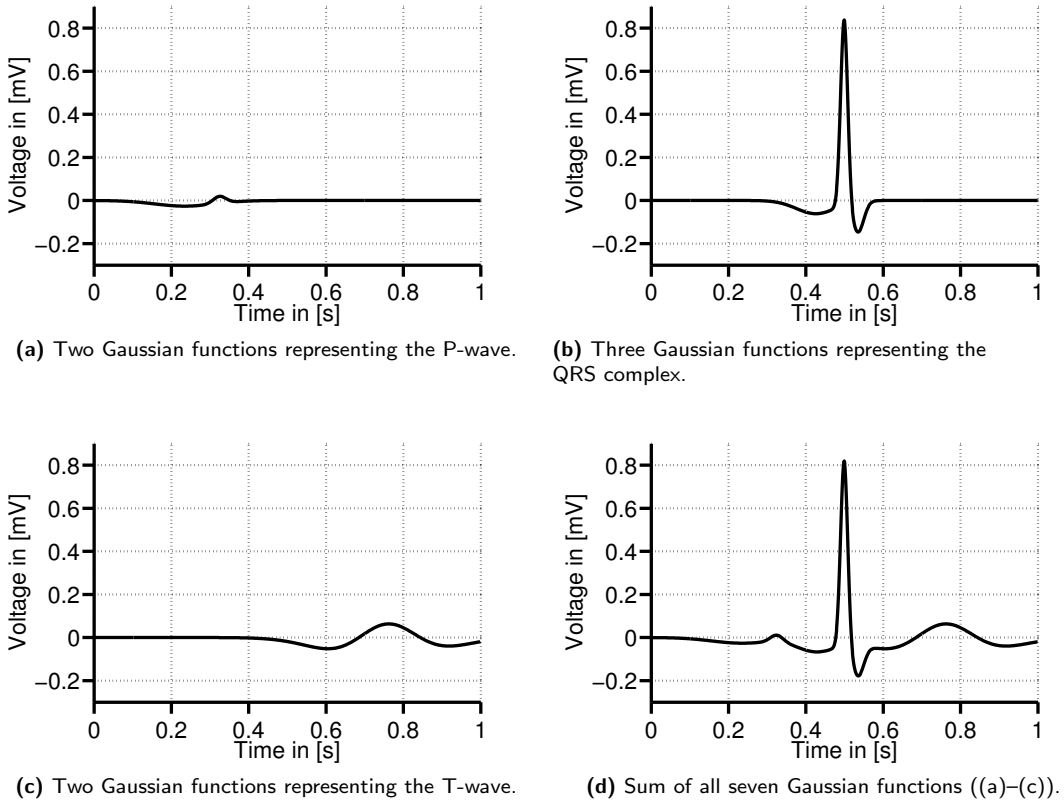

(a) Two Gaussian functions representing the P-wave.

(b) Three Gaussian functions representing the QRS complex.

(c) Two Gaussian functions representing the T-wave.

(d) Sum of all seven Gaussian functions ((a)–(c)).

Figure 4.3.: Simulating ECG signals using the Gaussian wave-based model. The P-wave (a), the QRS complex (b) and the T-wave (c) are simulated using two or three Gaussian functions each. The sum of all Gaussian functions forms the final, simulated ECG (d). Using two or more Gaussians for the P-wave or the T-wave allows to simulate the biphasic morphologies of these waves (see Section 2.1.4).

The selection of the Gaussian parameters for a given template of one ECG cycle was performed using an automated approach described in [Sameni 07, Sameni 08, Behar 14b]. In this approach, the centres of seven Gaussians were placed randomly around the fiducials of the PQRST locations. The optimal parameters of each Gaussian wave were estimated using a non-linear least square approach (*lsqcurvefit()* function of Matlab [MATLAB 10]) which minimised the RMS error between the template of the ECG cycle and the cycle given by the Gaussian functions.

4.2.3 MHD simulations based on real ECG measurements

In this approach, *real ECG signals* acquired outside and inside the MRI scanner were *used to simulate MHD signals*. PQRST templates were generated from the ECGs acquired outside ($T_{\mathrm{ECG,out}}$) and inside ($T_{\mathrm{ECG,in}}$) the 7 T MR scanner according to the description in [Andreotti 14]. A template of the MHD signal was obtained by subtraction of the two ECG templates: $T_{\mathrm{MHD}} = T_{\mathrm{ECG,in}} - T_{\mathrm{ECG,out}}$. The Gaussian parameters of the MHD template (T_{MHD}) were computed as described in Section 4.2.2. Once the Gaussian parameters of the MHD template were estimated for each lead, the MHD signals covering several cardiac cycles were simulated using equation 4.2. The required phase signal was derived from the original RRI time-series of the real ECG signal acquired outside the MR scanner. To obtain more realistic variations of the MHD signal, its amplitude was modified on a beat-to-beat basis depending on

the RRI length as described in Section 3.2.3. Figure 4.4a depicts a real ECG acquired outside the MR scanner. The corresponding MHD signal which was simulated using the (real) template T_{MHD} is shown in Fig. 4.4b whereas Fig. 4.4c shows the superposition both signals. In conclusion, these simulated signals are composed of a real ECG signal (acquired outside the MR scanner) and of a simulated MHD signal based on templates obtained from ECG measurements in a 7 T MR scanner.

Ten different 12-lead ECG records acquired inside the MR scanner from five subjects (each subject measured in Hf and Ff position) and the corresponding ECGs acquired outside the scanner (see the descriptions of the 7 T training dataset in Section 4.1.2) were used to generate the simulated records. Finally, the simulated records were used for the computation of the initialisation parameters required for the extended Kalman filter, which is described in Section 6.4.

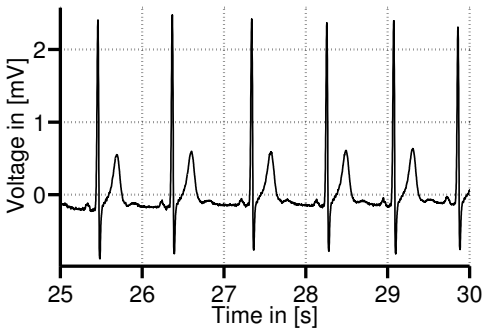

(a) Real ECG acquired outside the MR scanner.

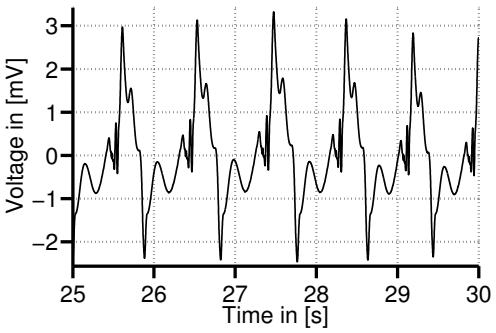

(b) Simulated MHD signal based on real measurement.

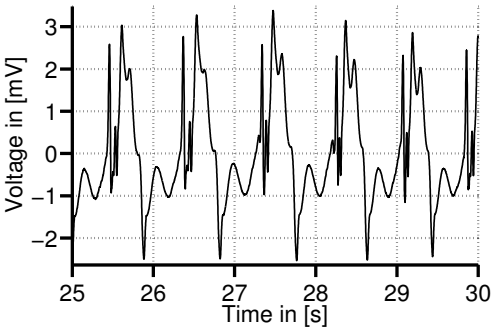

(c) Superposition of the real ECG and the simulated MHD signals.

Figure 4.4.: Simulation of an ECG signal superimposed by the MHD effect based on real measurements. ECG signals were acquired outside (a) and inside the MRI scanner. Templates were computed from each of these signals. By subtracting both templates, a template of the MHD effect was obtained. Using the MHD template, an MHD time-series was computed (b). This MHD time-series was superimposed to the real ECG signal (c).

4.2.4 ECG and MHD simulations using the Gaussian model and blood flow measurements

Instead of using templates from real ECG records as described in Section 4.2.3, a completely synthetic 12-lead ECG signal was generated using the Gaussian model. Firstly, the *FECGSYN* toolbox[5] was used to model a realistic VCG cycle using a set of pre-defined parameters for the Gaussian functions which described the waveform of the three VCG leads [Behar 14a]. As for the template-based method, an RRI time-series was required to generate the phase signal for the Gaussian model. Since a completely synthetic solution was preferred, an additional model for the heart rate variability (HRV) was used to generate this RRI time-series. This was achieved using the HRV model introduced by McSharry *et al.* [McSharry 03b, Clifford 06][6,7]. The power spectrum of the RRI time-series was modelled by two Gaussian functions. One Gaussian describes the parasympathetic (0.3 Hz) and one the sympathetic (0.1 Hz) activity of the autonomous nervous system (see Section 2.1.5). The average heart rate was set to 60 bpm with a standard deviation of 5 bpm. This resulting time-series had a bimodal power spectrum, which described the contributions of autonomous nervous system (sympathetic and parasympathetic) and also covered the influence of the respiratory sinus arrhythmia and the Mayer waves.

The simulated signals obtained from the synthetic model did not contain additional noise. Several noise types can occur in ECG signals. According to [Friesen 90], baseline wander, muscle artefacts and electrode movements are the most common ECG noises types with high amplitudes, which cannot be removed by simple bandpass filtering. It was shown that many QRS detectors are prone to errors when ECG signals are contaminated by muscle artefact (MA) noise [Friesen 90]. Hence, MA noise was added to the clean, synthetic ECG signals. The *MIT-BIH Noise Stress Test Database (NSTDB)*[8] provides samples of real muscle artefact noise [Goldberger 00]. These samples were used in combination with the *FECGSYN* toolbox to simulate MA noise over the complete length of the simulated VCG signal [Behar 14a]. The noise power was adjusted to obtain two different VCG signals: one with a SNR$=3$ dB and one with a SNR$=9$ dB. These noise levels did not include the additional contribution of the MHD effect. The simulated VCG signals contaminated by MA noise were converted into 12-lead ECG signals using the Dower transform (see Eq. 2.9, p. 14). Examples for the simulated ECG signals with different noise levels are depicted in Fig. 4.5. It can be seen that additional MA noise hampered the analysis of the ECG waveform, e. g. the manual identification of the end of the T-wave.

The MHD effect was simulated utilising the model introduced by Oster *et al.* [Oster 15] (see Section 3.2.3). Based on this model, 12-lead MHD signals were simulated for the RRI time-series described in Section 4.2.4. The MHD model was used to generate the signal for one cardiac cycle. Depending on the RRI length (or heart rate) and certain simulated pathologies (i. e. the inversion of the T-waves or depression of the ST-segments), the MHD signal was modified accordingly to achieve more realistic variations. A detailed description of the adjustments of the MHD signal for the different pathologies is given in the following section.

[5] http://www.physionet.org/physiotools/ipmcode/
[6] http://www.physionet.org/physiotools/ipmcode/
[7] http://www.physionet.org/physiotools/ecgsyn/
[8] http://www.physionet.org/physiobank/database/nstdb/

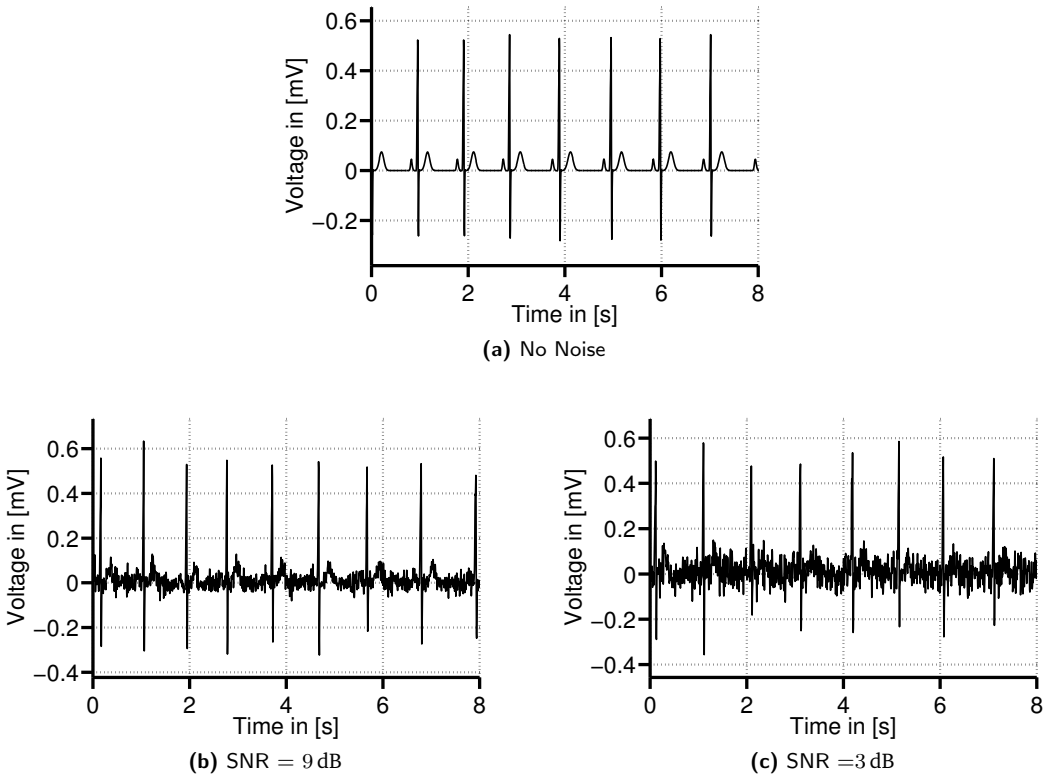

(a) No Noise

(b) SNR $= 9\,\mathrm{dB}$

(c) SNR $= 3\,\mathrm{dB}$

Figure 4.5.: Synthetic ECG signals (lead II) based on the Gaussian model with different MA noise levels.

4.2.5 Simulation of pathological episodes - variation of ECG and MHD signals

Motivation

One aim of this thesis was the ECG-based detection of pathological episodes during MRI. However, all real ECG records described in Section 4.1.2 were acquired from healthy subjects and no pathological patterns were observed in these ECG traces. Additionally, a quantitative analysis was not possible using real ECGs since the ground-truth (an undistorted trace of the ECG) was not known. An exact quantitative analysis can only be achieved using simulated ECG and MHD signals. Hence, the different pathological episodes were simulated using the models described above. Examples and background information concerning different pathologies were given in Section 2.1.4. Generally, the QT-interval can be prolonged due to a delayed T-wave. The ECG's ST-segment, which is important for the diagnosis of an ischemia, can be elevated, depressed or flattened . The T-wave's morphology can also change: it can be inverted, biphasic, flattened or have an increased amplitude. In order to cope with these variations, the following pathologies were simulated:

1. prolongation of the QT-interval,
2. inversion of the T-wave and
3. elevation/depression of the ST-segment.

The cardiac pathologies were simulated by simple modifications of the synthetic ECG signal generator (Eq. 4.2, p. 70). A different record was generated for each pathological type using different Gaussian models (see Section 4.2.4). Hence, a simulated ECG either contained the inverted T-waves,

a prolonged QT-intervals or elevated/depressed ST-segments.

Simulated prolongation of the QT-interval

A prolongation of the QT-interval was achieved by increasing the θ_i variables representing the T-wave in Eq. 4.2, p. 70 by $0.3\,\text{rad} \approx 17.2\,°$. At an average heart rate of $60\,\text{bpm}$ (as it was used for the simulations), this corresponds to a prolongation of $\approx 50\,\text{ms}$. If the QT-interval is prolonged by more than $30\,\text{ms}$, the patient should to be carefully analysed (see Section 2.1.4). The initial normal (non-pathological) QT-interval had a length of $\approx 350\,\text{ms}$. In order to obtain a smooth transition between the normal and pathological segments of the ECG (in this case between the normal and the prolonged QT-intervals), the θ_i was slowly increased using a hyperbolic tangent function over a $10\,\text{s}$ window. Examples for one cycle of the simulated ECG with normal and prolonged QT-interval are depicted in Fig. 4.6a. The transition from the normal to the pathological phase is shown in Fig. 4.6b.

Simulated T-wave inversion

The inversion of the T-wave was achieved by manipulating (inverting) the parameter α_i of the Gaussian functions representing the T-wave. In order to obtain a smooth transition between the normal and pathological segments of the ECG (in this case between a normal and an inverted T-wave), the α_i parameters were modified over a length of $10\,\text{s}$ using a hyperbolic tangent function ranging from -1 to 1, i e. the initial T-wave amplitude of the normal (non-pathological) segment was completely inverted. Figure 4.7a shows one cycle of the simulated ECGs with normal and inverted T-wave. The transition of the amplitude between the normal and pathological segment is depicted Fig. 4.7b.

Simulated elevation/depression of the ST-segment

An additional Gaussian wave was included in the simulation model. This Gaussian was placed between the Gaussians representing the R-peak and the T-wave. By manipulating the amplitude α_i of this additional Gaussian, an elevation or depression of the ST-segment was possible. For the ST depression, the additional Gaussian was adjusted such that the resulting ECG signal had an ST depression of $\approx 0.1\,\text{mV}$ (e. g. in lead I). The amplitude of the ST-segment was increased by $\approx 0.2\,\text{mV}$ (e. g. in lead aVF) for ECGs with simulated the ST elevation. Examples of an ECG with normal and depressed ST-segment are depicted in Fig. 4.8a and the transition between these two morphologies is shown in Fig. 4.8b. The corresponding example with ST elevation is depicted in Fig. 4.9.

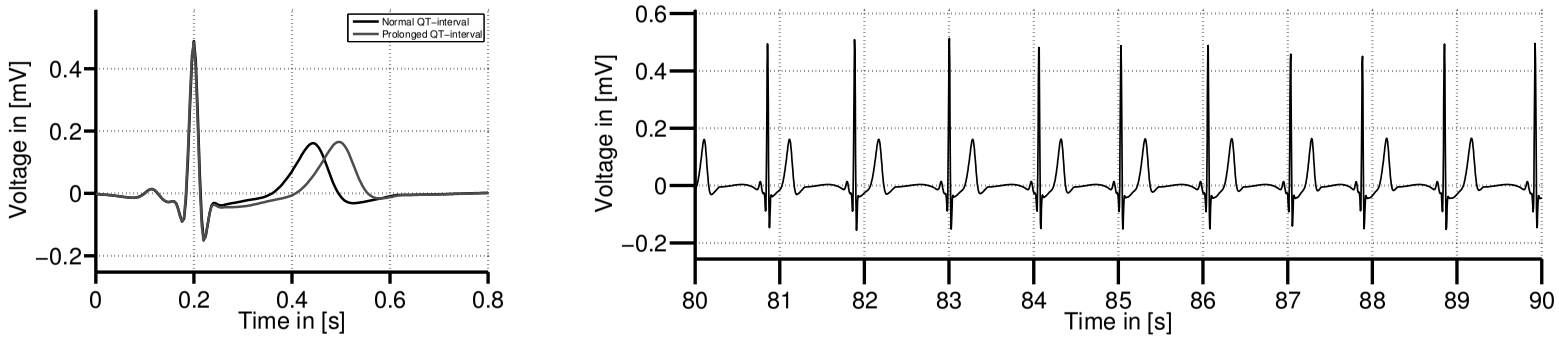

(a) Normal and pathological ECG cylce

(b) Transition from normal to pathological

Figure 4.6.: One cycle of an ECG (lead III) with normal and prolonged QT-interval length (a) and the transition from the normal to the pathological segment (b). The Gaussian which represented the T-wave was shifted by $\approx 50\,\mathrm{ms}$ over length of $10\,\mathrm{s}$ using a hyperbolic tangent function.

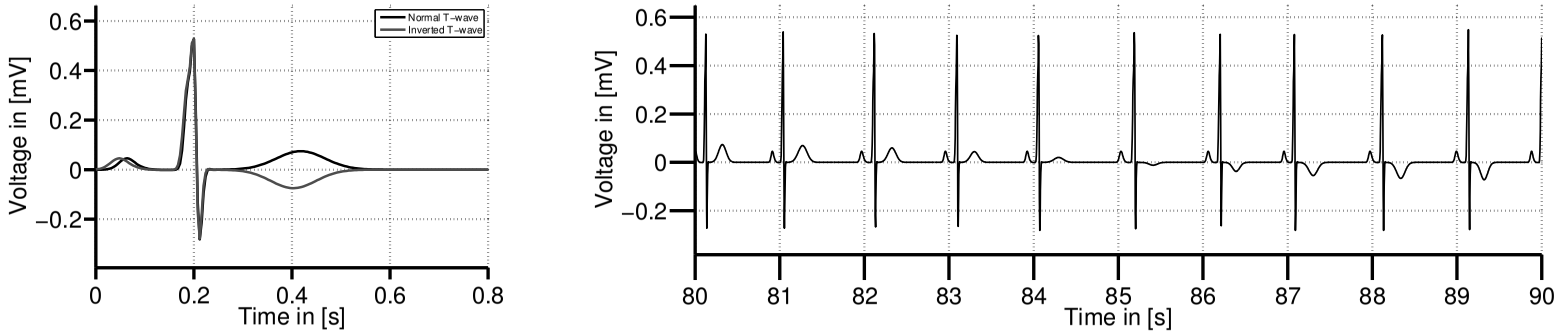

(a) Normal and pathological ECG cylce

(b) Transition from normal to pathological

Figure 4.7.: One cycle of an ECG (lead II) with normal and simulated T-wave inversion (a) and the transition from the normal to the pathological segment (b). The amplitude of the T-wave was slowly inverted over a length of $10\,\mathrm{s}$ using a hyperbolic tangent function.

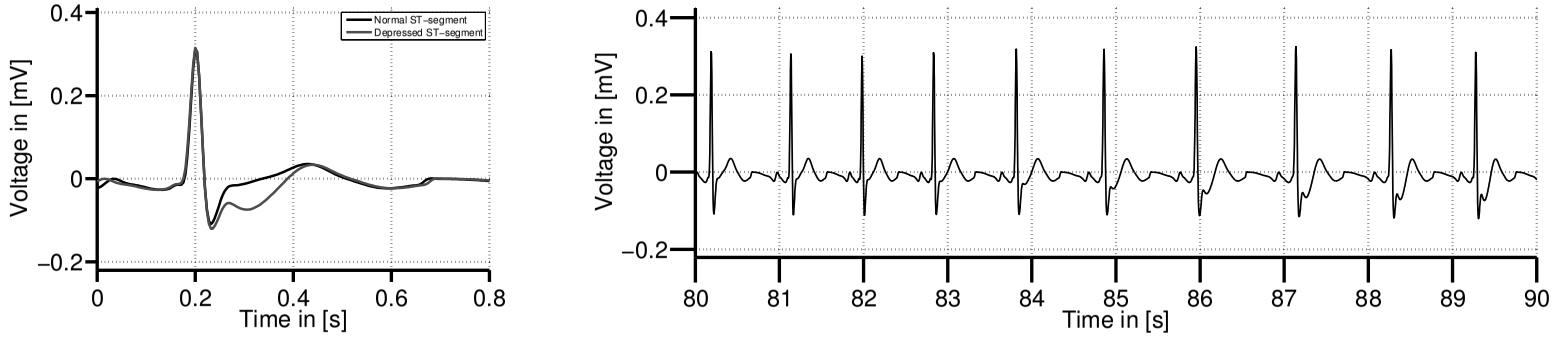

(a) Normal and pathological ECG cylce

(b) Transition from normal to pathological

Figure 4.8.: One cycle of an ECG (lead I) with normal and simulated depression of the ST-segment (a) and the transition from the normal to the pathological segment (b). The amplitude of the additional Gaussian which was used to modify the magnitude of the ST-segment was slowly increased over length of $10\,\mathrm{s}$ using a hyperbolic tangent function.

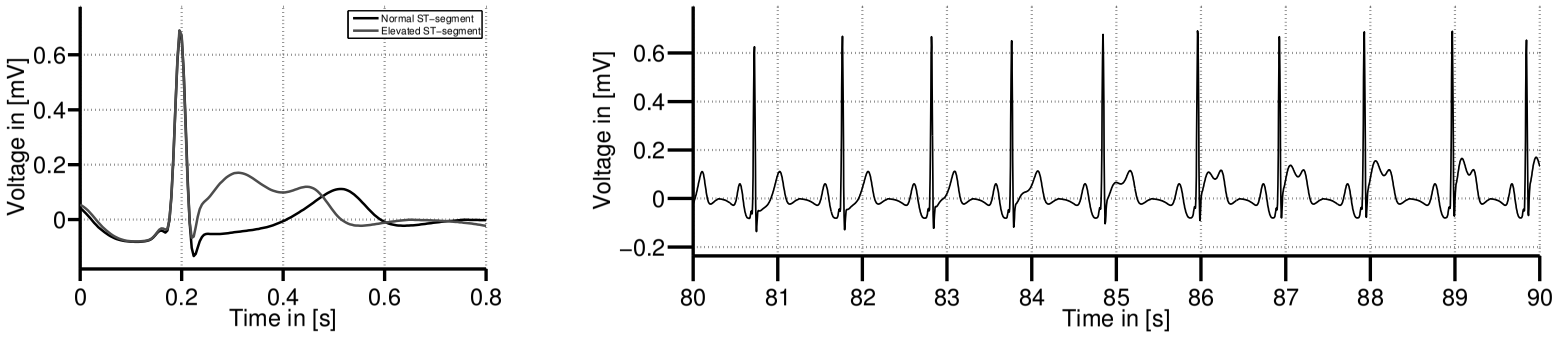

(a) Normal and pathological ECG cylce

(b) Transition from normal to pathological

Figure 4.9.: One cycle of an ECG (lead aVF) with normal and simulated elevation of the ST-segment (a) and the transition from the normal to the pathological segment (b). The amplitude of the additional Gaussian which was used to modify the magnitude of the ST-segment was slowly increased over length of $10\,\mathrm{s}$ using a hyperbolic tangent function.

Hemodynamic variations during the T-wave inversion and ST depression/elevation

Pathological episodes observed in the ECG signal are accompanied by hemodynamic variations. Stroke volume (SV) was reported to decrease during stress induced ischemia or myocardial infarct [Dymarkowski 03, p.52]. During stress echocardiography induced by dobutamine it was shown that there is a generally decreased SV during cardiac stress (increased HR), but there exists an even more decreased SV during stress induced ischemia [Poldermans 99]. Simultaneous acquisition of the ECG and hemodynamic parameters revealed the delay between the onset of certain changes. For an ischemia it was shown that a change in the left ventricular volume occurred several seconds before a change of the ST-segment [Davies 88, Table 3].

Both parameters – the decreased SV and the delay between the changes in SV and changes in the ECG's ST-segment or T-wave – were considered to enable a more realistic simulation of the pathologies. Hence, $20\,\mathrm{s}$ before the beginning of a T-wave inversion or ST depression/elevation, the magnitude of the simulated MHD effect was decreased from $100\,\%$ to $70\,\%$. Similar to the modification of the ECG described above, a smooth transition was realised by modifying the amplitude of the MHD using a hyperbolic tangent over a length of $10\,\mathrm{s}$. Figure 4.10 depicts a simulated MHD signal before the onset of an ST depression.

Figures 4.11a and 4.11b show simulated ECG traces of a non-pathological segment and of a segment with ST depression. The same ECGs but with additional MA noise resulting in an SNR$=3\,\mathrm{dB}$ are depicted in Figs. 4.11c and 4.11d. The simulated MHD signals corresponding to the two segments are depicted in Figs. 4.11e and 4.11f. In addition to its the pathological changes, the MHD signal was also modified (by manipulating the stroke volume) depending on the RRI lengths according to the descriptions in Section 3.2.3, pp. 35. The final mixture of ECG and MHD signals and MA noise is depicted in Figs. 4.11g and 4.11h.

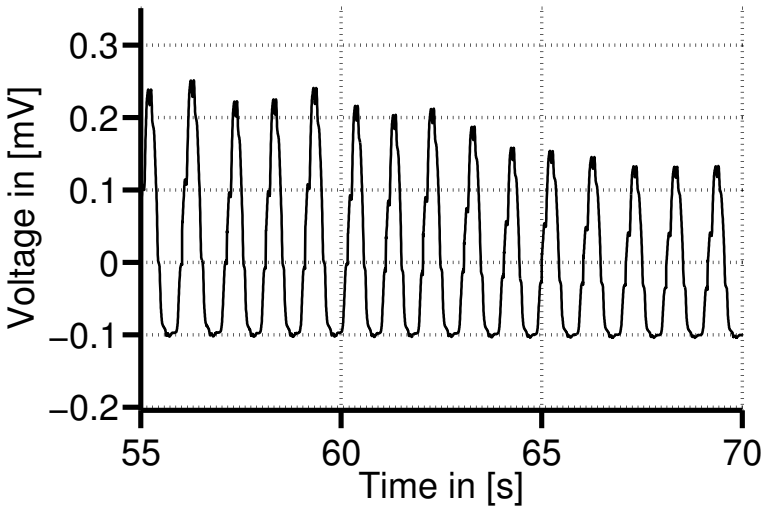

Figure 4.10.: Simulated MHD signal before the onset of an ST depression. The amplitude of the MHD signal decreases from $\approx 0.23\,\mathrm{mV}$ to $\approx 0.12\,\mathrm{mV}$ in the time between $60\,\mathrm{s}$ and $70\,\mathrm{s}$.

Summary of simulated records used for the quantitative evaluation

For the quantitative evaluation of different denoising techniques described in Chapter 6, four simulated records were used:

1. Pathological ECG with prolonged QT-interval + simulated MHD effect + MA noise.
2. Pathological ECG with inverted T-wave + simulated MHD effect + MA noise.
3. Pathological ECG with depressed/elevated ST-segment + simulated MHD effect + MA noise.
4. Normal (healthy) ECG + simulated MHD effect + MA noise.

The ECGs were simulated using four different Gaussian models in order to obtain ECG signals with different morphologies. Each simulated record had a length of $140\,\mathrm{s}$. No modifications were made in the first $60\,\mathrm{s}$ of a record. For the records with a simulated inversion of the T-wave or depression of the ST-segment, the amplitude of the MHD signal was modified after $60\,\mathrm{s}$ according to the descriptions made above. $80\,\mathrm{s}$ after the beginning of a record, the simulated pathologies of the ECG (i. e. QT prolongation, T-wave inversion or depression/elevation of the ST-segment) were included. As described above, there was a transitional phase with a duration of $10\,\mathrm{s}$ where the ECG changed from normal to pathological. Hence, $90\,\mathrm{s}$ after the beginning of the record, the final pathological phase was reached. This phase was simulated until the end of the record. For the healthy ECG, no pathological variation of the parameters was performed.

4.3 Performance metrics and evaluation

4.3.1 Performance metrics for the QRS detection at 7 T

QRS detection performance

In order to evaluate the results of the different R-peak detection methods, a gold standard measurement was required. Here, the manual annotation of the R-peaks described in Section 4.1.2 served as the gold standard. The total number of false positives (FP) in each record was determined by searching for a manually annotated R-peak within a given window placed around an automatically detected peak. According to the *ANSI/AAMI/ISO standard EC57* [ANSI 98], this search window had a width of $300\,\mathrm{ms}$ and was centred around the annotated or detected peaks. If no manually annotated R-peak lied within this search window, the detected peak was defined as FP. The total number of false negatives (FN) was determined by searching within the window width around a manually annotated R-peak. If there was no peak identified by the QRS detection algorithm within this window, this peak was defined as FN. The remaining detected peaks, i. e. those peaks which lied within the search windows placed around the manually annotated peaks were defined as true positives (TP). A practical example for the definition of these values is depicted in Fig. 4.12.

The measured quantities can be used to define the sensitivity Se

$$Se = \frac{TP}{TP + FN} \tag{4.3}$$

and the positive predictive value $+P$

$$+P = \frac{TP}{TP + FP}. \tag{4.4}$$

These two metrics were utilised to assess the performance of different QRS detection algorithms.

Trigger delay and jitter of the QRS detection

The temporal precision of the QRS detection algorithms was evaluated based on the propagation delay and the jitter. The mean trigger propagation delay μ_{pd} was defined as the absolute difference between the position of the manually annotated R-peak and the R-peak detected by the QRS detection algorithm and was averaged over each record

$$\mu_{\text{pd}} = \frac{\sum_{i=1}^{N} |t_{R_{Ref}(i)} - t_{R_{Det}(i)}|}{N} \tag{4.5}$$

where N is the total number of annotated R-peaks and $t_{R_{Ref}(i)}$ and $t_{R_{Det}(i)}$ are the points in time of the reference annotation and the detected R-peak position. For gating applications, μ_{pd} should be less than $20\,\text{ms}$ because the systole's mechanical contraction begins $30\,\text{ms}$ to $70\,\text{ms}$ after the R-peak [Lentner 90, Chia 00].

The standard deviation of the trigger propagation delays was denoted as jitter σ_{pd}. It was estimated using

$$\sigma_{\text{pd}} = \frac{\sqrt{\sum_{i=1}^{N} (pd(i) - \mu_{\text{pd}})^2}}{N} \tag{4.6}$$

where $pd(i)$ is the propagation delay of the i-th annotation pair. A large jitter could cause a blurring of the cardiac MR image, lead to ghost artefacts in the phase encoding direction or to a false estimation of the blood flow rate in phase contrast MRI. Currently existing literature does not provide limit values for the maximum jitter, which can be accepted for the acquisition of CMR images. However, for the estimation of physiological parameters such as the blood flow rate within a vessel, the jitter should be less than $15\,\text{ms}$ [Thompson 04, Nijm 07a].

Computation of an optimal threshold for QRS detection based on Se and $+P$ measurements

Some of the methods described in Chapter 5 required a threshold for the R-peak or QRS detection. Where required, a brute force search was utilised to find the optimal threshold. The average value of Se and $+P$ served as an optimisation criterion. For each record i of the training dataset ($i \in \mathbb{N} | 1 \leq i \leq 10$), the mean value

$$\mu(i,j)_{Se,+P} = \frac{Se(i,j)}{2} + \frac{+P(i,j)}{2} \tag{4.7}$$

was computed for a given threshold j. By maximising the expression

$$\mu(j)_{Se,+P} = \frac{1}{10}\sum_{i=1}^{10}\mu(i,j) \rightarrow \max, \tag{4.8}$$

the optimal threshold j was identified.

4.3.2 Performance metrics for the diagnostic quality of simulated ECG records

The simulated ECG records enable a quantitative analysis of the denoising results since the ground-truth (a clean reference ECG signal without the MHD effect) is known. There are several metrics which can be utilised to measure to quality of a (filtered) signal. The signal-to-noise (SNR) ratio is a very popular measurement, which is often used in the signal processing community with applications in communications or image processing. However, this metric has no clinical meaning, i. e. it is not used diagnose an ECG signal. The SNR can be used for optimisation purposes, e. g. for finding an optimal number of filter coefficients. For diagnostic purposes, other metrics exist, which are often used in clinical practice. These metrics include the measurement of the T-wave polarity, QT-interval length or the amplitude of the ST-segment. In the following, the computation of these parameters is briefly summarised. These parameters were computed for the simulated signals described in Sections 4.2.4 and 4.2.5 and were used for the evaluation and comparison of the different filter methods.

SNR

The SNR was computed as

$$\mathrm{SNR} = \frac{\sum_{i=1}^{N}\left(\mathrm{ECG}_{\mathrm{sim,out}}(i)\right)^2}{\sum_{i=1}^{N}\left(\mathrm{ECG}_{\mathrm{sim,out}}(i) - \mathrm{ECG}_{\mathrm{sim,filt}}(i)\right)^2} \tag{4.9}$$

where $\mathrm{ECG}_{\mathrm{sim,out}}$ is the simulated reference ECG, $\mathrm{ECG}_{\mathrm{sim,filt}}$ is the filtered ECG and N is the number of data points. A high SNR means that the residual between the filtered and the reference signal is small. Concerning the clinical application of the filtered signals, a high SNR does not necessarily mean that the filtered signal is of high clinical relevance. Within this thesis, the SNR was used as a metric for optimising the parameters (e. g. the number of filter coefficients or the number of independent components) of the different filter approaches.

Separate analysis of the different ECG sections (normal, transitional, pathological)

The ECGs with simulated pathologies were separated into different sections (see the descriptions of the records in Section 4.2.5). The analysis of the different parameters was performed separately for each segment, i. e. for the *normal* (healthy) section at the beginning, the *translational* section in the middle and the *pathological section* at the end of the records. The following section lengths were used for the evaluation:

- Normal segment: 30^{th} s to 60^{th} s
- Transitional segment: 60^{th} s to 110^{th} s

- Pathological segment: 110$^{\text{th}}$ s to 140$^{\text{th}}$ s

For the healthy ECG without a simulated pathology, the analysis was performed over the complete record, i. e. from the 30$^{\text{th}}$ s to the 140$^{\text{th}}$ s.

QT prolongation and T-wave morphology

The length of the QT-interval was estimated utilising the *ECGPUWAVE*[9] algorithm written by Pablo Laguna *et al.*, which was included in the WFDB Toolbox for Matlab and Octave by Ikaro Silva [Laguna 97, Goldberger 00, Silva 14]. For each simulated record, the QT-interval lengths were measured in the filtered ECG and the corresponding reference ECG. The mean absolute error, its standard deviation and the p_5 and p_{95} percentiles were computed separately for the normal, the transitional and the pathological sections of each record. QT measurements were only performed if the same QT-intervals were found in the reference and the filtered ECG signal (QT-interval pairs). For each section (see above) of one lead of the ECG, at least half of the available QT-intervals should be detected by *ECGPUWAVE*. If this was not the case, no results were given for this section and there were no average results computed for this lead (i. e. the average results of all segments of one lead were only computed if a result was computed for each of the three segments).

The morphological type of the T-waves was also classified by the *ECGPUWAVE* algorithm (see above). The *ECGPUWAVE* algorithm distinguishes between six different types of T-waves: 1) normal, 2) inverted, 3) positive monophasic, 4) negative monophasic, 5) biphasic negative/positive and 6) biphasic positive/negative. T-wave analysis was performed for the reference ECGs (simulated ECG signal without MHD effect and MA noise) and for the filtered ECG signal. As for the evaluation of the QT measurements, only those pairs of T-waves which were detected in the reference and the filtered ECG were used for the analysis. This step was necessary to avoid a negative impact of the detection quality of *ECGPUWAVE* on the results. The example depicted in Fig. 4.13 showed that *ECGPUWAVE* misses some of T-waves although they are clearly visible in the filtered output signal. Similar problems with *ECGPUWAVE* were reported in a recent study made by Natarajan *et al.* [Natarajan 14]. Another problem which occurred with *ECGPUWAVE* was a varying detection of normal/inverted and biphasic waves (either positive/negative or negative/positive). This can be seen from Fig. 4.13b where a mostly negative T-wave is classified as negative or as biphasic positive/negative. Since the main purpose of this thesis was to detect larger variations during the inversion of the T-wave, only two classes of T-waves were considered for the evaluation:

- The *normal (positive) T-wave class* was composed of: normal (positive), positive monophasic and positive/negative biphasic T-waves.

- The *inverted (negative) T-wave class* was composed of: inverted (negative), negative monophasic and negative/positive biphasic T-waves .

Se and $+P$ values were computed for each segment (normal, transitional, pathological) of an ECG record considering the different T-wave types. These values were computed based on the T-wave morphologies found in the reference signal. If there was only one type of T-wave morphology per segment (e. g. only normal T-waves), a $+P$ of $100\,\%$ was expected since it was not possible to detect any false positives (FP) in this case (because only pairs of T-waves detected in both signal were used for the analysis). As for the evaluation of the QT-intervals, the T-wave detection performance was only

[9] http://www.physionet.org/physiotools/ecgpuwave/

computed for those sections of a lead where at least half of the available QT-intervals were detected.

ST elevation/depression

For the measurement of the ST-segment amplitude, the ECG's J-point (see Fig. 2.6, p. 10) needed to be located [Clifford 06]. Therefore, one ECG lead showing a good representation of the S-peak and of the J-point was manually selected. This was necessary since the J-point was not clearly identifiable in some of the leads. The S-peaks were automatically detected based on the locations of the R-peaks; the J-points were then defined at a fixed distance with respect to the S-peaks. The computed J-point locations were used for all other ECG leads. ST-segment amplitudes are usually estimated at the J+80 ms location (i. e. the location 80 ms after the J-point) [Clifford 06]. To reduce the influence of noise on the measurement of the ST amplitude, a window (length=20 ms) was placed around the J+80 ms location and the median of the sample values within this window was taken as the amplitude of the ST-segment. In contrast to the evaluation of the QT-intervals and the T-waves which required an additional detection of the Q-peak and T-wave using *ECGPUWAVE*, the ST-segments were located with respect to the R-peak annotations. This means that the ST-segments were evaluated for each annotated R-peak. The evaluation of the QT-intervals and of the T-waves, however, was only possible if *ECGPUWAVE* was able to detect the required fiducials.

4.3.3 Performance metrics for the diagnostic quality of real ECG records

Compared to the simulated signals, the quality assessment of the real ECG signals was more difficult since the ground-truth (the ECG without MHD effect) is unknown. In order to evaluate the filter results for the real ECG records, it was assumed that the underlying average morphology of the ECG signals remained stable within one record, i. e. there are no pathological variations of the ECG signal outside and inside the MRI scanner. This is a valid assumption since the ECG signals were acquired from healthy subjects and no pathological variations were observed in the ECG traces acquired outside the MRI scanner. Moreover, the lengths of the recordings was sufficiently short to assume that the ECG was relatively stationary. Hence, a qualitative analysis was possible by comparing traces of the ECG signal acquired outside the MR scanner and of the filtered ECG signals. Due to the natural variations of the different parts of an ECG signal, e. g. due to respiration, different heart rates or signal artefacts (e. g. from electrode movements or muscle contractions), a quantitative analysis was nevertheless not performed for the real ECG records.

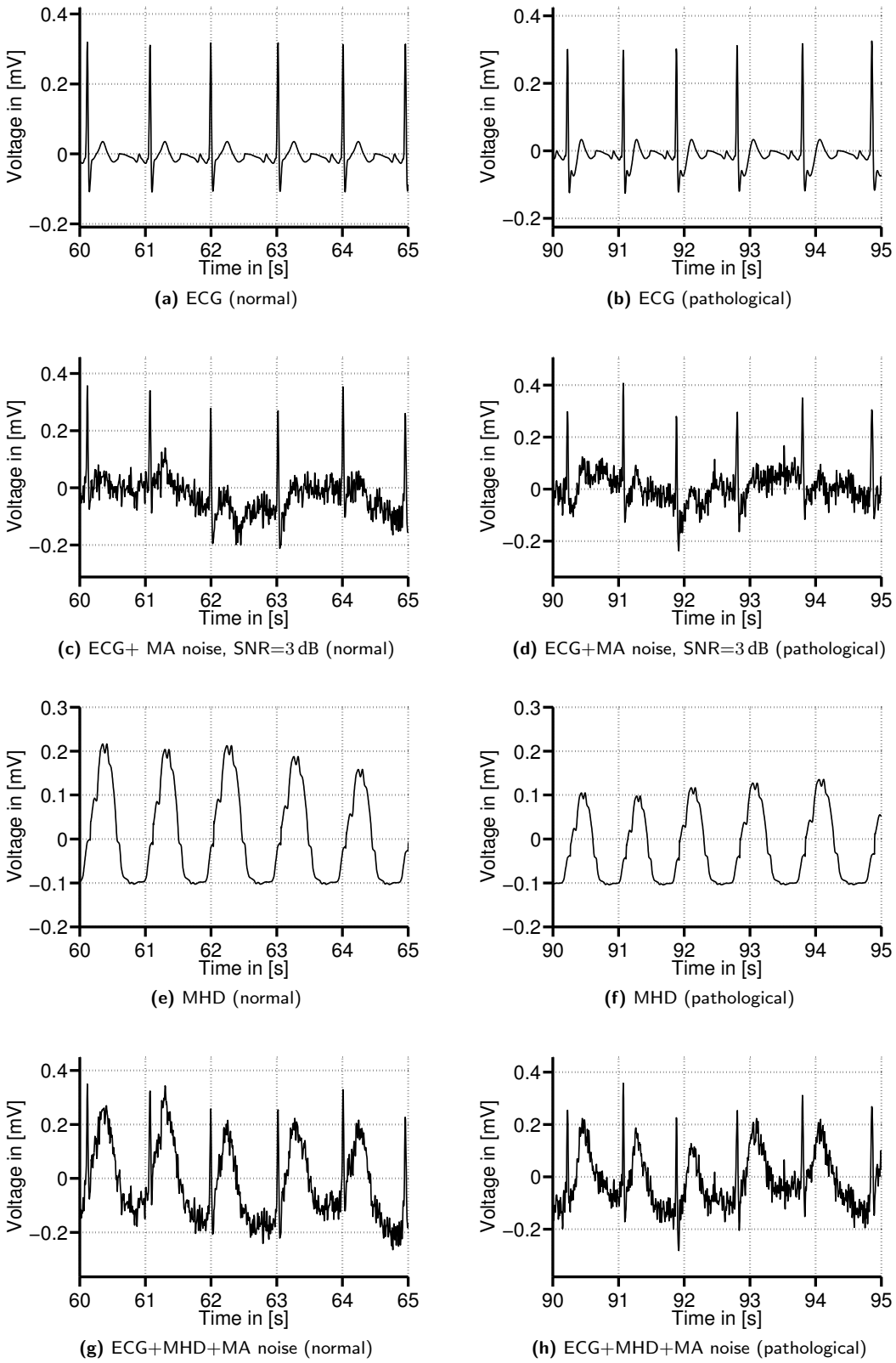

(a) ECG (normal)

(b) ECG (pathological)

(c) ECG+ MA noise, SNR=3 dB (normal)

(d) ECG+MA noise, SNR=3 dB (pathological)

(e) MHD (normal)

(f) MHD (pathological)

(g) ECG+MHD+MA noise (normal)

(h) ECG+MHD+MA noise (pathological)

Figure 4.11.: Variations of the ECG and MHD signals (lead I) during a simulated depression of the ST-segment. Simulated ECG signals (a,b), MHD signals (c,d), sum of ECG and MHD signal (e,f) and with additional MA noise (g,h) in the normal and pathological segments, respectively.

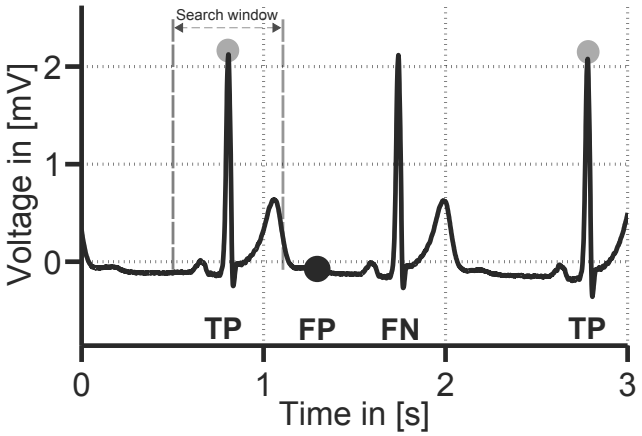

Figure 4.12.: Example for the classification of detected peaks. The grey dots mark TP since they are inside the serach windows around the QRS complex. The black dot is outside of the search window, hence it is a FP. The second QRS complex which was not detected is a FN.

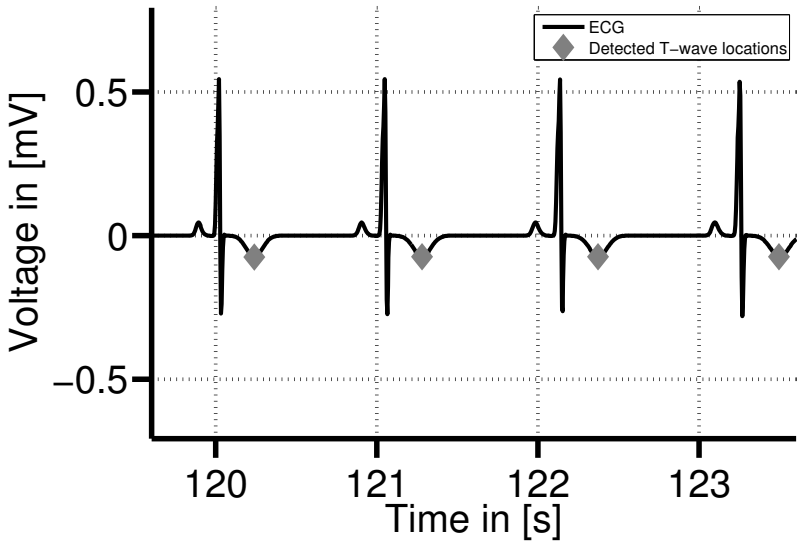

(a) T-waves detected in the clean reference ECG.

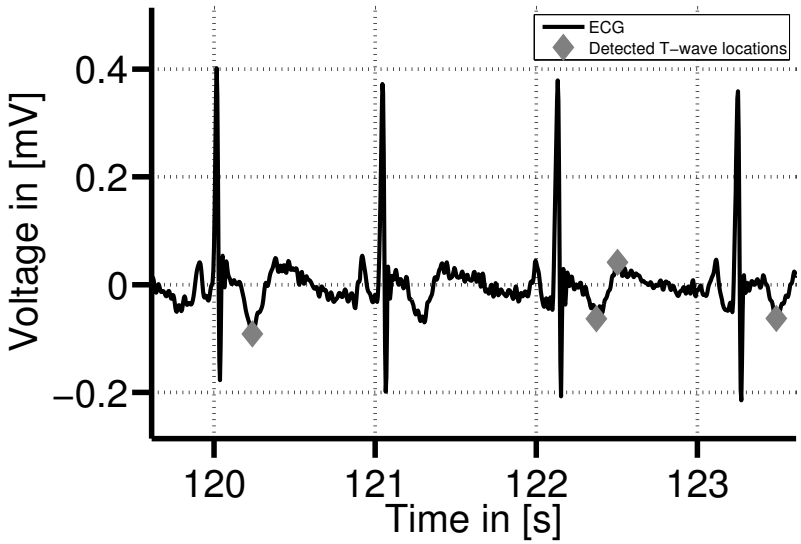

(b) T-waves detected in the ECG contaminated by noise.

Figure 4.13.: T-wave detection problem occurring for certain morphologies in the and ECG (lead II) with simulated T-wave inversion (SNR=9 dB) when using ECGPUWAVE. In the reference signal (a), all negative T-waves were detected. In the noise filtered signal (b), one T-wave was missed by the ECGPUWAVE algorithm.

5

QRS detection for ECG-based cardiac gating at 7 T MRI

5.1 Chapter overview

Gating in CMR is one of ECG's main applications during MRI. Several dedicated methods were developed in the past to enable an R-peak detection in an MRI environment (see Section 3.4). Despite the existing variety of algorithms, 7 T CMR applications still lack signal processing techniques, which enable a reliable QRS detection. The amplitude of the MHD effect, which increases with the magnetic field strength of the MR scanner, can exceed the amplitude of the ECG signal and especially of the R-peak. Signal properties (e. g. the frequency range) of the ECG and MHD signal can also overlap, which can hamper the QRS detection (see Section 3.3). The VCG-based method which is widely used for R-peak detection during MRI was reported to be prone to errors at 7 T (see Section 3.4).

In order to overcome some of the limitations, an improvement of the existing VCG-based QRS detection is described in Section 5.2.1. In this approach, the reference vector used in the normal VCG-based method is modified in order to compensate the distortions caused by the MHD effect (see Section 3.4.1). The modified reference vector is defined from the ECG/VCG signal acquired inside the MR scanner. A further modification of this vector-based approach is then presented in Section 5.2.2. This method named *6D-sECG* extends the three dimensions of the original VCG to six dimensions by using the six precordial ECG leads V1-V6 instead of the three VCG leads. This additional modification shall utilise the superior quality of the precordial ECG leads, which was shown shown in Section 3.3.

All the vector-based QRS detection methods require an initial R-peak detection to define the reference vector(s). To circumvent this additional pre-processing step, a new method for the detection of QRS complexes at high magnetic field strengths is proposed and described in Section 5.3. This

method is based on an independent component analysis (ICA) algorithm. The ICA-based method is used to separate ECG and MHD components in order to suppress the MHD effect and to improve the QRS detection. A set of basis functions or independent components (ICs) $\widehat{\mathbf{s}}_k$ are estimated by the ICA algorithm. Each of these components is dominated by different signal components, e. g. by the ECG signal, the MHD effect or noise. One of the challenges occurring during the application of ICA is the selection of an IC ($\widehat{s}_{\text{ECG}}$) which corresponds to the ECG signal, i. e. an IC which is dominated by the QRS complex or R-peak. For the feasible and reliable practical clinical application of this method, an automated identification of $\widehat{s}_{\text{ECG}}$ out of $\widehat{\mathbf{s}}_k$ is required. Two different methods are investigated for the automated identification.

To highlight the advances of the modified and newly developed QRS detection techniques presented in Sections 5.2.2 and 5.3, both techniques are compared to other methods described in Section 5.4. These methods include QRS detection using the raw 12-lead ECG signal, the raw VCG signal, the ICA of the VCG signal and the '3D-QRS' method (see Section 3.3).

5.2 Vector-based QRS detection

5.2.1 Improved VCG-based gating using a modified reference vector

As described in Section 4.1, all ECG signals used in this work were recorded using a 12-lead ECG device. VCG signals used for gating purposes were synthesised from the ECG signals using the inverse Dower transform (Eq. 2.9, p. 14).

The algorithm for VCG-based cardiac gating proposed in [Fischer 99] was implemented according to the descriptions in Appendix A. At first, the reference vector $\mathbf{r} = (r_x, r_y, r_z)$ was calculated from the ECG recorded outside the MR scanner. This was shown in Figs. 3.19a–3.19c, p. 47. The vector $\mathbf{r}$ points at the turning point of the large VCG loop which represents the QRS complex in a spatially manner. As explained in Appendix A, the distance and angle between the vector $\mathbf{r}$ and the vector $\mathbf{v}(t)$ from the ECG recorded inside the MR scanner were compared using minimum distance algorithm.

The VCG-based gating procedure proposed in [Fischer 99] obtains the reference vector $\mathbf{r}$ from the ECG signal recorded outside the MR scanner. As reported in current literature (see Section 3.4.1), this method is not fully suitable for gating applications in MR scanners with field strengths of $\geq 7\,\text{T}$. Two explanations for the error proneness of the VCG-based method were given in Section 3.3.4. To cope with this problem, a modified approach of the VCG-based gating method is introduced in this section.

The proposed method slightly modifies the original VCG-based method by utilising a different reference vector defined as $\mathbf{r}_{\text{in}}$. Instead of obtaining the reference vector outside the MR scanner it was obtained from an ECG signal recorded inside the 7 T MR scanner. This procedure can be subdivided in the following steps:

1. Recording a short trace of the ECG (few seconds) inside the MR scanner.
2. Manual annotation of one or more QRS complexes in the recorded ECG signal.
3. Calculation of the VCG using the inverse Dower transform (see Section 2.1.3).
4. Estimation of the reference vector $\mathbf{r}_{\text{in}}$ from the VCG using the manual annotations.
5. Application of the QRS detection algorithm (see Section 3.4.1 and Appendix A).

The manual annotation (step 2) makes the whole procedure unemployable in a practical clinical scenario. In the first instance, however, the aim is to investigate if it is possible to improve the VCG-based gating method at 7 T. If this is the case, one could consider a combination of the VCG-based method with an additional, initial QRS detection method.

5.2.2 Higher dimensional vector space method ('6D-sECG')

Motivation

In addition to the method described in Section 5.3, a new approach using the spatial information of the ECG signal in a 6-dimensional (6D) vector space will be presented here. It was demonstrated in Section 5.2 that the 3-dimensional (3D) VCG is severely affected by the MHD effect at 7 T, which can hamper the detection of the QRS complexes. The MHD effect mainly causes complex spatial patterns and an alteration of the R-peak vector in the VCG domain. In Section 3.3.2, the higher quality of the precordial leads was demonstrated. Compared to the (augmented) limb leads, the MHD effect is less pronounced in the precordial leads.

A regular VCG, which usually consists of leads x, y and z, can be obtained by a linear combinations of the 12 leads of an ECG using the inverse Dower transform as described in Section 2.1.3. As depicted in Fig. 5.1, the QRS complex is less pronounced in some of the VCG leads (e. g. in leads y and z) when compared to the precordial ECG leads. Instead of using the VCG leads obtained from the 12-lead ECG, the method introduced in this section uses the original information of the precordial leads without combing them. A 6D vector space was derived based on the six precordial leads V1-V6. The aim was to develop another robust method for QRS detection at 7 T.

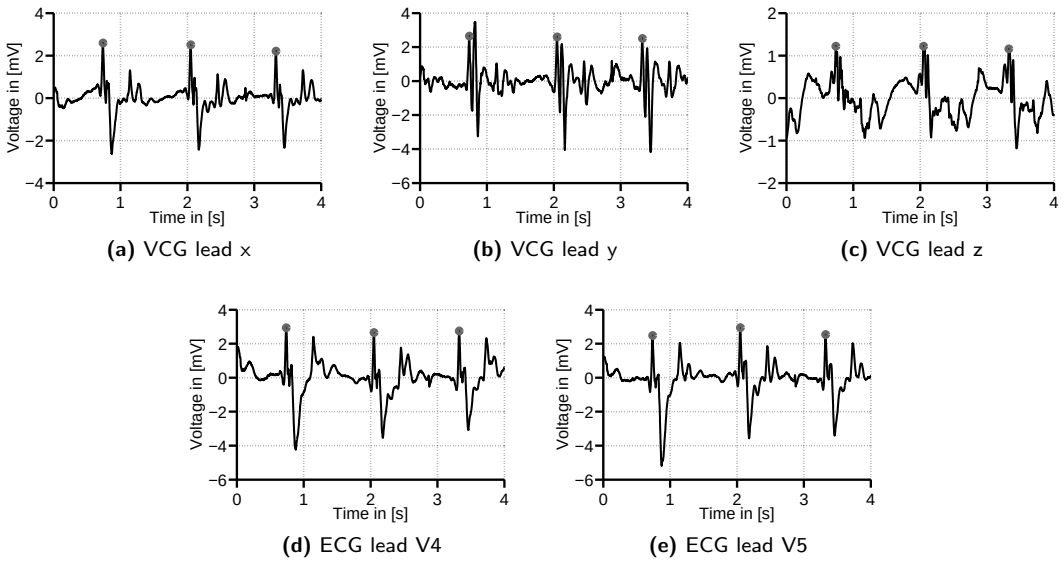

(a) VCG lead x **(b)** VCG lead y **(c)** VCG lead z

(d) ECG lead V4 **(e)** ECG lead V5

Figure 5.1.: (a)-(c) VCG leads x,y,z and (d)-(e) ECG leads V4 and V5. Except for VCG lead x, the different VCG leads show several peaks of high frequency and amplitude next to the R-peak. In contrast, the original ECG leads V4 and V5 show a better separation of the R-peak and the MHD signal. Grey dots mark the positions of the R-peaks.

Description of the method

A VCG $\mathbf{v}_{6D}(t)$ of six dimensions was defined as a vector consisting of the six precordial ECG leads V1-V6

$$\mathbf{v}_{6D}(t) = \begin{pmatrix} \mathrm{ECG}_{V1} \\ \mathrm{ECG}_{V2} \\ \mathrm{ECG}_{V3} \\ \mathrm{ECG}_{V4} \\ \mathrm{ECG}_{V5} \\ \mathrm{ECG}_{V6} \end{pmatrix}. \tag{5.1}$$

Normal VCGs obtained from the 12-lead ECG using the inverse Dower transform are shown in Figs 5.2a and 5.2b. The position of the R-peaks is obscured by the MHD effect. Figures 5.2c and 5.2d show the spatial representation of the precordial leads V3 and V4. Using the precordial leads instead of the VCG leads, the spatial locations of the R-peaks are better separated from the contaminations caused by the MHD effect.

However, for certain combinations of the precordial leads in some of the training records, the R-peaks were not located on one of the extreme outer positions of the VCG domain. Examples are depicted in Figs. 5.3a and 5.3b. Although the R-peaks were located in an off-centre position, the remaining overlapping distortions due to the MHD effect could lead to false R-peak detections. Taking the first derivative is one method to enhance the more rapidly changing components of a signal [Pan 85, Clifford 02]. This step could diminish the influence of the MHD effect on the QRS loop. Hence, a more precise detection of the R-peaks was expected. Examples for such 6D-VCGs obtained from the differential ECG signals are shown in Figs. 5.3c and 5.3d. For the implementation of the proposed method, the first derivative of the precordial ECG leads was used for the spatial 6D representation of the ECG.

As for the normal VCG-based gating method discussed in Section 5.2, a reference vector was required for detecting the R-peaks. Defining the reference vector $\mathbf{r}$ from the VCG recorded outside the MRI is not preferred since the MHD effect can affect the orientation and magnitude of the R-peak vector in its spatial representation (see Section 3.3.3). Hence, the reference vector was defined from the ECG signal recorded inside the MR scanner.

The main steps of the proposed method are: *1)* record the ECG inside the (7 T) MR scanner, *2)* take the first derivative and locate the R-peaks (manually), *3)* define a 6D reference vector $\mathbf{r}_{6D}(t)$ using these R-peaks, *4)* QRS detection using the algorithm described in Sections 3.4.1 and Appendix A.

These steps are summarised in Fig. 5.4. As described in Appendix A, the following redefined equations

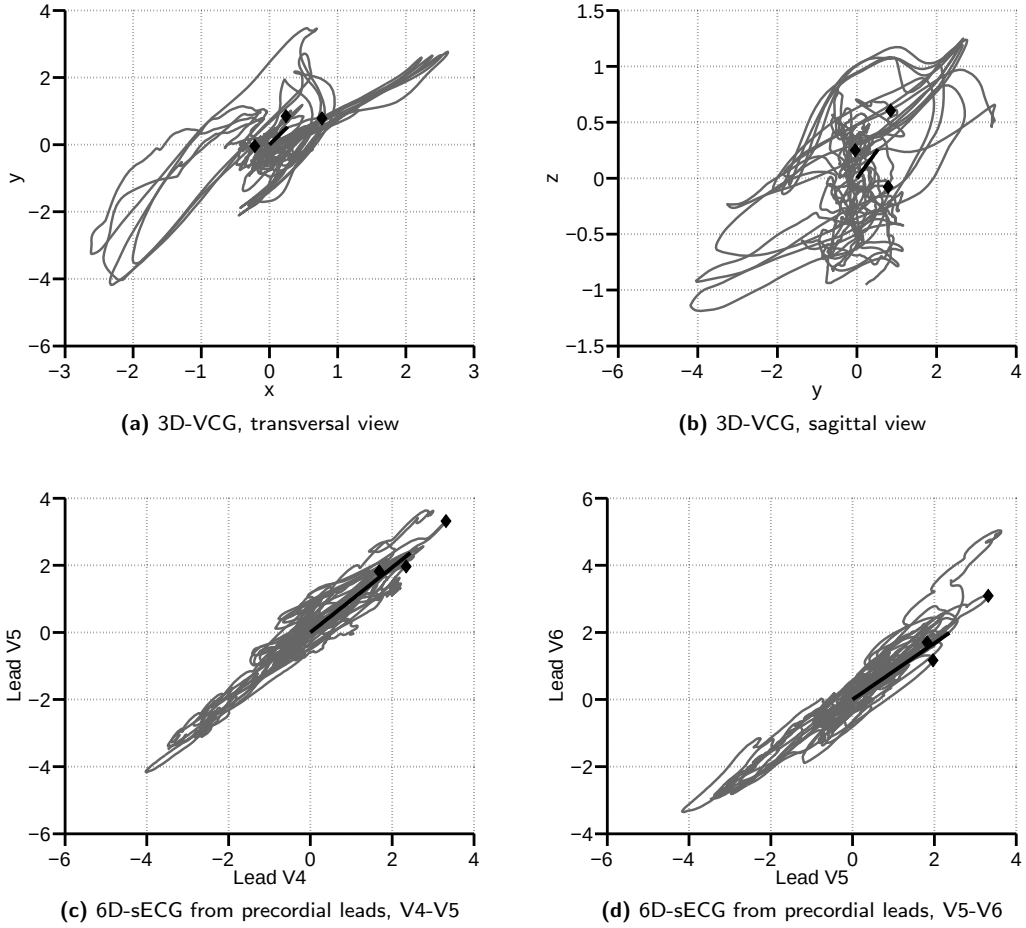

(a) 3D-VCG, transversal view

(b) 3D-VCG, sagittal view

(c) 6D-sECG from precordial leads, V4-V5

(d) 6D-sECG from precordial leads, V5-V6

Figure 5.2.: Spatial differences between the (a)-(b): *normal* 3D-VCG obtained using the inverse Dower transform of the 12-lead ECG and (c)-(d) the 6D-VCG obtained from the precordial leads of the same ECG. Selected 2D representations of the six axes are shown. For the 6D-VCG, the R-peaks are located at the outer corners of the spatial representation. Hence, the R-peaks and the MHD signals are better separated than in the normal 3D-VCG.

were used for QRS detection

$$
\begin{aligned}
A_1(t) &= \frac{\mathbf{r}_{6D}(t)}{|\mathbf{r}_{6D}(t)|}\mathbf{v}_{6D}(t) \\
A_2(t) &= \frac{A_1(t)}{d(t)^2} \quad \text{with} \quad d(t) = \max(|\mathbf{v}_{6D}(t) - \mathbf{r}_{6D}(t)|, 0.01) \\
A_3(t) &= \frac{A_2(t)}{\arccos\left(\frac{\mathbf{r}_{6D}(t)\cdot\mathbf{v}_{6D}(t)}{|\mathbf{r}_{6D}(t)||\mathbf{v}_{6D}(t)|}\right)}.
\end{aligned}
\tag{5.2}
$$

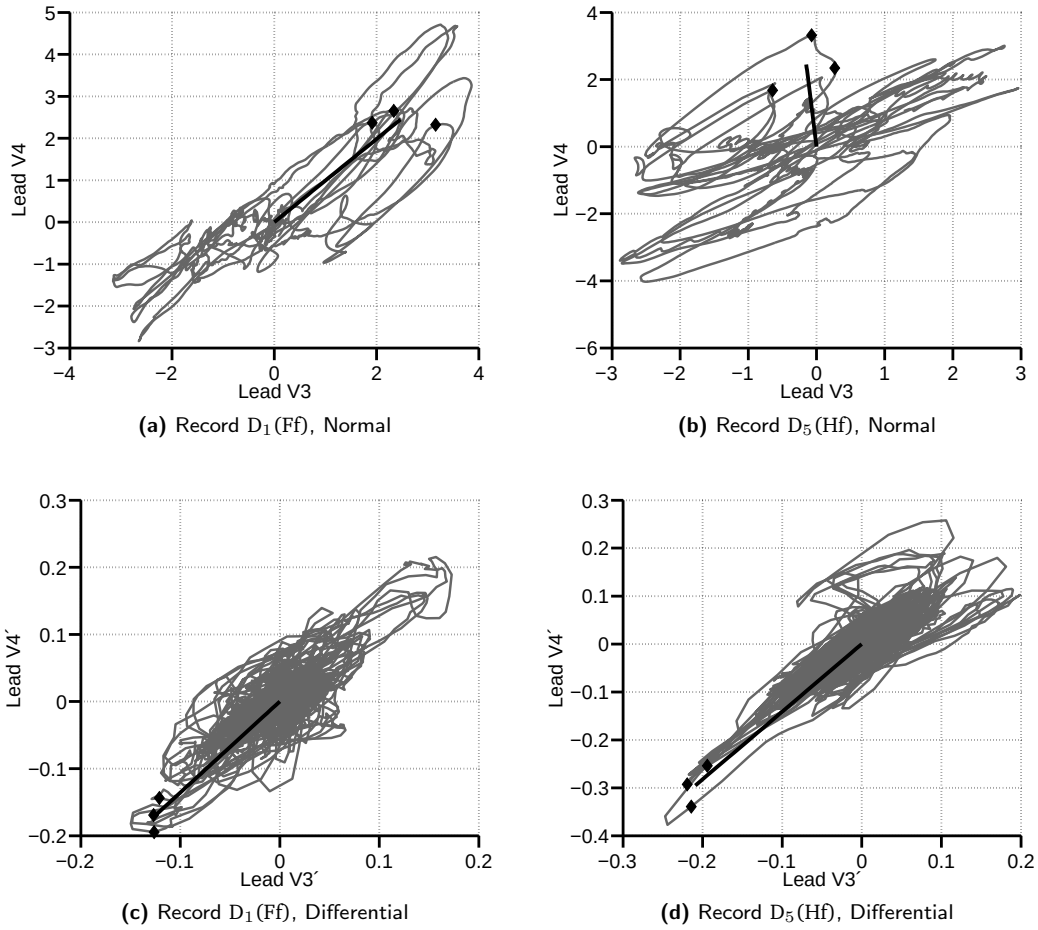

(a) Record $D_1(Ff)$, Normal

(b) Record $D_5(Hf)$, Normal

(c) Record $D_1(Ff)$, Differential

(d) Record $D_5(Hf)$, Differential

Figure 5.3.: Comparison of the 6D-sECG representations from two different records. (a),(c): representation based on the normal ECG signal. (b),(d): representation based on the 1st derivative of the ECG signal.

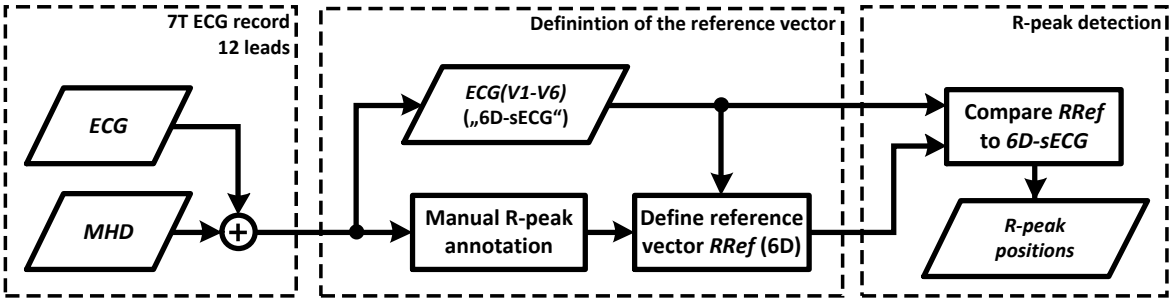

Figure 5.4.: Principle of the proposed 6D-sECG gating method. A reference vector was defined using the manual annotations and the precordial leads V1-V6. This reference vector was compared to the current 6D-sECG. Based on the distance and angle between both vectors, the positions of the R-peaks were identified using local, relative thresholds.

5.3 ICA-based QRS detection

5.3.1 Independent component analysis (ICA)

Overview

Independent Component Analysis (ICA) is a method used for the the separation of signal mixtures assuming statistical independence of the source signals. These methods try to recover unknown source signals from mixtures where the mixing coefficients are unknown. Hence, these methods are called 'blind'. In the past 20 years, ICA has received wide attention in several fields such as image or speech processing, communications or biosignal processing, e. g. for EEG, MEG and ECG processing [He 06, Castells 05].

In this work, ICA is applied to ECG signals, which were recorded inside MR scanners. The aim is to separate the ECG and MHD signal components in order to obtain an estimate of the original ECG source for different purposes. ICA was previously applied to ECG signals mixed with simulated MHD signals whereas it was shown that ICA is able to separate the MHD effect from the ECG signal (see Section 3.5.1). In this chapter, ICA is applied to real ECG signals acquired in a 7 T MR scanner. As in the previous Section 5.2, the focus is put on a robust detection of the QRS complex. One of the source signals or independent components estimated by ICA shall be used to achieve this aim. In the following, the theory of ICA and one algorithm used within this work are briefly introduced.

Underlying source mixing model

It is assumed that the observed signals $\mathbf{x}_k$ (in the context of this work the measured ECG signals) are a mixture of stochastic processes where k describes the k-th sampled measurement value. The observation vector $\mathbf{x}_k = \left(x_{k,1}, x_{k,2}, ..., x_{k,N}\right)^T, k = 0, ..., K$ which contains the different observations (i. e. the different ECG leads $1...N$) at time instant k has to be decomposed into the underlying source signals or independent components (ICs). The observations are generated from a mixture of different sources summarised in the corresponding source signal vector $\mathbf{s}_k = \left(s_{k,1}, s_{k,2}, ..., s_{k,M}\right)^T, k = 0, ..., K$. The mixing can be generally described by any linear or non-linear function f

$$\mathbf{x}_k = f(\mathbf{s}_k) + \mathbf{n}_k \tag{5.3}$$

where $\mathbf{n}_k$ represents the additional sensor noise, which is usually assumed to have zero mean [Roberts 01]. Only the linear case will be considered in this work

$$\mathbf{x}_k = \mathbf{A}\mathbf{s}_k + \mathbf{n}_k \tag{5.4}$$

where $\mathbf{A} = [a_{ij}]; i = 1, ..., N; j = 1, ..., M$ is the constant mixing matrix, which relates the different sources $\mathbf{s}_k$ to the observations $\mathbf{x}_k$. Since most classical ICA models are noiseless [Roberts 01], Eq. 5.4

reduces to

$$\mathbf{x}_k = \mathbf{A}\mathbf{s}_k. \tag{5.5}$$

Initially, the source signals $\mathbf{s}_k$ are unknown. ICA tries to recover the sources through a linear transform of the observed signals $\mathbf{x}_k$. This decomposition or demixing is defined as

$$\widehat{\mathbf{s}}_k = \mathbf{W}\mathbf{x}_k \tag{5.6}$$

where $\widehat{\mathbf{s}}_k$ are the estimated sourcethoses signals and $\mathbf{W} = [w_{ji}]; j = 1, ..., M; i = 1, ..., N$ is the demixing matrix. The demixing matrix $\mathbf{W}$ is usually assumed to be orthogonal such that $\mathbf{W}^T\mathbf{W} = \mathbf{I}$ where $\mathbf{I}$ is the $N \times N$ identity matrix. The determined matrix $\mathbf{W}$ should minimise the information of the estimated source signals $\widehat{\mathbf{s}}_k$.

Besides the independence of the different sources $\mathbf{s}_k$, most ICA algorithms[1] require at least as many sensors or measurement signals $\mathbf{x}_k$ as sources $\mathbf{s}_k$, i. e, $N \geq M$.

The drawback of ICA is that the sources cannot be estimated uniquely, that is the sources can only be estimated with following indeterminacies:

- Scaling and sign of the sources/ICs: both, the mixing matrix $\mathbf{A}$ and the source signals $\mathbf{s}_k$ are unknown. Hence, each source can have a scaling factor α, which can be compensated by a corresponding scale factor within the matrix $\mathbf{A}$

$$x_j = \sum_i \left(\frac{1}{\alpha_{ij}} a_{ij} \right) (s_{ij}\alpha_{ij}). \tag{5.7}$$

- Order of the sources/ICs: The order of the estimated sources $\widehat{\mathbf{s}}_k$ is not known. A permutation matrix $\mathbf{P}$ and its inverse can be included in the mixing model so that the order of resulting observations $\mathbf{x}_k$ remains the same

$$\mathbf{x}_k = \mathbf{A}\mathbf{P}^{-1}\mathbf{P}\mathbf{s}_k \tag{5.8}$$

  whereas $\mathbf{A}\mathbf{P}^{-1}$ modifies the mixing matrix $\mathbf{A}$. $\mathbf{P}\mathbf{s}_k$ are the sources $\mathbf{s}_k$ but with a different source order.

The unknown order of the estimated sources or ICs will be considered in Section 5.3.3. An automatic identification of one IC, which is dominated by the ventricular activity, is required for the QRS detection at 7 T CMR.

[1] There are also ICA algorithms developed for underdetermined systems [Taleb 99, Li 06]

ICA preprocessing

Two main preprocessing steps are performed before the different sources are estimated by ICA. In a first step, the measured data is *centred*, i. e. the mean vector $\mathbf{m} = E\{\mathbf{x}_k\}$ is subtracted from $\mathbf{x}_k$. Hence, the estimated sources $\widehat{\mathbf{s}}_k$ have a zero mean as well which can be shown by computing the expectations on both sides of Eq. 5.5. To include the mean in the estimated sources $\mathbf{s}_k$, it can be calculated as $\mathbf{A}^{-1}\mathbf{m}$.

The second step is a linear transform, aiming at representing the data $\mathbf{x}_k$ on a new basis, where the components $\tilde{\mathbf{x}_k}$ are uncorrelated and have unit variance [Hyvärinen 00]. This step is called *whitening* or *sphering*. Hence, the covariance matrix of $\tilde{\mathbf{x}_k}$ has to equal the identity matrix

$$E\{\tilde{\mathbf{x}}_k\tilde{\mathbf{x}}_k^T\} = \mathbf{I}. \tag{5.9}$$

Eigen-value decomposition (EVD) can be used to achieve whitening of the data. The covariance matrix of $\mathbf{x}_k$ can be written as

$$E\{\mathbf{x}_k{\mathbf{x}_k}^T\} = \mathbf{E}\mathbf{D}\mathbf{E}^T \tag{5.10}$$

where $\mathbf{E}$ is the orthogonal matrix of eigenvectors[2] of $E\{\mathbf{x}_k{\mathbf{x}_k}^T\}$ and $\mathbf{D}$ is the diagonal matrix of its eigenvalues, $\mathbf{D} = diag(d_1, ..., d_n)$. The following step performs the whitening of the input data $\mathbf{x}_k$

$$\tilde{\mathbf{x}}_k = \mathbf{E}\mathbf{D}^{-1/2}\mathbf{E}^T\mathbf{x}_k \tag{5.11}$$

with $\mathbf{D}^{-1/2} = diag(d_1^{-1/2}, ..., d_n^{-1/2})$. It can be shown that $E\{\tilde{\mathbf{x}}_k\tilde{\mathbf{x}}_k^T\} = \mathbf{I}$. By the whitening step, the matrix $\mathbf{A}$ was transformed into

$$\tilde{\mathbf{x}}_k = \mathbf{E}\mathbf{D}^{-1/2}\mathbf{E}^T\mathbf{A}\mathbf{s}_k = \tilde{\mathbf{A}}\mathbf{s}_k. \tag{5.12}$$

With the steps described above, the obtained demixing matrix $\tilde{\mathbf{A}}$ now is orthogonal, which can be shown by

$$E\{\tilde{\mathbf{x}}_k\tilde{\mathbf{x}}_k^T\} = \tilde{\mathbf{A}}E\{\mathbf{s}_k{\mathbf{s}_k}^T\}\tilde{\mathbf{A}}^T = \tilde{\mathbf{A}}\tilde{\mathbf{A}}^T = \mathbf{I} \tag{5.13}$$

where $E\{\mathbf{s}_k{\mathbf{s}_k}^T\} = \mathbf{I}$ by initial assumption. The advantage of an orthogonal demixing matrix $\tilde{\mathbf{A}}$ is the reduced number of parameters which need to be estimated. Instead of n^2, only $n(n-1)/2$ parameters need to be estimated [Hyvärinen 01]. Additionally, the dimension of the signals can be reduced during the whitening procedure by removing the components which have low eigenvalues. This is the case in overdetermined systems where there are more measurement signals $\mathbf{x}_k$ than underlying sources $\mathbf{s}_k$.

[2] $E\{\mathbf{x}_k{\mathbf{x}_k}^T\}$ can be estimated from the measured samples $\mathbf{x}_1, ..., \mathbf{x}_n$

Source estimation by means of non-Gaussianity maximisation using the FastICA algorithm

Several mathematical approaches and corresponding algorithms exist for the estimation of the unknown sources $\widehat{\mathbf{s}}_k$. Comprehensive overviews of the different methods can be found in [Hyvärinen 01, Roberts 01, Stone 04, Comon 10]. In this work, the FastICA algorithm was used to estimate the different source signals [Hyvärinen 99a, Hyvärinen 01, Roberts 01].

In general, *non-Gaussianity* is an important metric in the estimation of ICA. Non-Gaussianity can be used to measure the independence of different sources. The *central limit theorem* states that the distribution of the sum of independent random variables tends towards a Gaussian distribution [Hyvärinen 01, Vaseghi 09], [Stone 04, pp.56]. The demixing vector $\mathbf{w}$ can be optimised such that non-Gaussianity of the sources estimated by $\mathbf{w}\mathbf{x}_k$ is maximised.

Negentropy is one measure of non-Gaussianity. It is based on the information theoretic quantity of differential entropy, which in the following is simply called entropy. Entropy can be interpreted as the amount of information of an observed variable. The entropy increases with the randomness of the variable, i. e. the more unstructured or unpredictable a variable, the higher its entropy. A generalised definition of the (differential) entropy H of a random vector $\mathbf{x}$ with density $p(\mathbf{x})$ is defined as

$$H(\mathbf{x}) = -\int p(\mathbf{x}) \log p(\mathbf{x}) \mathrm{d}\mathbf{x}. \tag{5.14}$$

For a random variable with a given variance, the maximum entropy is achieved for a Gaussian distribution. Instead of directly estimating the entropy, one often uses the *negentropy* which is a normalised version of the entropy. The negentropy J is defined as

$$J(\mathbf{x}) = H(\mathbf{x}_{\text{Gauss}}) - H(\mathbf{x}) \tag{5.15}$$

where $\mathbf{x}_{\text{Gauss}}$ is a random variable with Gaussian distribution and where $\mathbf{x}_{\text{Gauss}}$ and $\mathbf{x}$ have the same covariance matrices. Negentropy is either positive or can be zero if and only if $\mathbf{x}$ has a Gaussian distribution. Concerning statistical properties, negentropy is in some sense the optimal estimator of non-Gaussianity [Hyvärinen 01]. However, the computation of negentropy as given in Eq. 5.15 is problematic since it would required an estimate of the pdf. Therefore, approximations of the negentropy exist which are described in [Hyvärinen 01, pp.182]. The FastICA algorithm provides a fixed-point iteration scheme for estimating a maximum of the non-Gaussianity based on an approximation of negentropy [Hyvärinen 99a].

5.3.2 Separation of ECG and MHD signals components

For the given application, the measurement vector $\mathbf{x}_k$ in Eq. 5.6 contained the ECG signals distorted by the MHD effect. The estimated basis functions $\widehat{\mathbf{s}}_k$ were analysed in order to find a component in $\widehat{\mathbf{s}}_k$, which was dominated by the ECG signal. This component is referred to as $\widehat{s}_{\text{ECG}}$. The extraction of $\widehat{s}_{\text{ECG}}$ from the contaminated ECG signals and the subsequent QRS detection were applied in a two-stage process. This procedure is summarised in Fig. 5.5.

In the *first stage*, ICA was applied to a 30 s reference segment $\mathbf{x}_{\text{Ref,k}}$ of the 12-lead ECG signal, which was

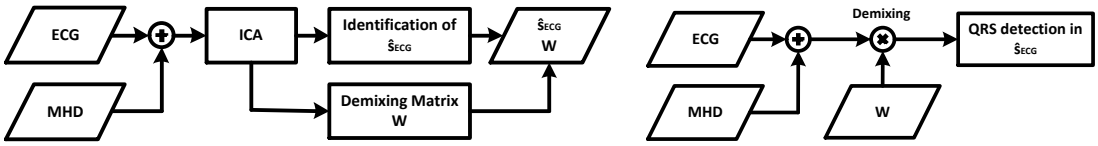

(a) First stage: this preprocessing step included the estimation of the demixing matrix **W** and the identification of the IC $\widehat{s}_{\text{ECG}}$ which was then used for the QRS detection.

(b) Second stage: online estimation of $\widehat{s}_{\text{ECG}}$ followed by the QRS detection.

Figure 5.5.: General functional principle of the ICA-based QRS detection. Using a 30 s long ECG signal, the demixing matrix **W** and the source signal $\widehat{s}_{\text{ECG}}$, which is dominated by the QRS complex, are estimated (a). The demixing matrix **W** obtained in the first stage is now applied the the latest ECG sample. This procedure is followed by applying an QRS detector to $\widehat{s}_{\text{ECG}}$ (b).

recorded inside the MR scanner. The resulting demixing matrix **W** was used to transform the reference ECG $\mathbf{x}_{\text{Ref,k}}$ into a vector $\widehat{\mathbf{s}}_k$ containing the estimated source components of $\mathbf{x}_{\text{Ref,k}}$. This is described by Eq. 5.6. The estimated signals contained in $\widehat{\mathbf{s}}_k$ were dominated by different (physiological) signal sources, e. g. by the ECG signal itself, by the MHD effect, by respiratory motion or by measurement noise. In the practical application of ICA to the given problem, the crucial task was the estimation of one IC $\widehat{s}_{\text{ECG}}$, which was dominated by the R-peak or QRS complex. This pivotal step is described in Section 5.3.3.

After $\widehat{s}_{\text{ECG}}$ was identified, the demixing matrix **W** was reduced to a demixing vector **w** since only $\widehat{s}_{\text{ECG}}$ was required for the QRS detection. The remaining ICs were not required. Hence, it was sufficient to only estimate $\widehat{s}_{\text{ECG}}$. This could be achieved by setting all unused rows in the demixing matrix **W** to zero

$$\mathbf{W} = \begin{pmatrix} w_{11} & w_{12} & \cdots & w_{1l} \\ w_{21} & w_{22} & \cdots & w_{2l} \\ \vdots & \vdots & \ddots & \vdots \\ w_{n1} & w_{22} & \cdots & w_{nl} \end{pmatrix} \quad \rightarrow \quad \mathbf{W} = \begin{pmatrix} 0 & 0 & \cdots & 0 \\ w_{21} & w_{22} & \cdots & w_{2l} \\ \vdots & \vdots & \ddots & \vdots \\ 0 & 0 & \cdots & 0 \end{pmatrix} \tag{5.16}$$

where l is the number of ECG leads and n the number of estimated ICs. This sets all the components in $\widehat{\mathbf{s}}_k$, which are not used for QRS detection to zero:

$$\widehat{\mathbf{s}}_k = \mathbf{W}\mathbf{x}_k. \tag{5.17}$$

Additional computational cost could be saved by only estimating one IC instead of setting the unused ICs to zero. This was achieved by deleting all unused rows in **W** so that only one instead of n components were estimated. In fact, the demixing matrix **W** was reduced to a demixing vector **w**. The IC $\widehat{s}_{\text{ECG}}$ which was utilised for QRS detection was then estimated by vector multiplication

$$\widehat{s}_{\text{ECG,k}} = \mathbf{w}\mathbf{x}_k = \begin{pmatrix} w_1 & w_2 & \cdots & w_l \end{pmatrix} \begin{pmatrix} x_1 \\ x_2 \\ \cdots \\ x_l \end{pmatrix}_k \tag{5.18}$$

where k is time instant of the current sampling value. Once the demixing vector $\mathbf{w}$ was estimated, the calculation of $\widehat{s}_{\mathrm{ECG,k}}$ at time step k required l multiplications and $l-1$ summations. Hence, the value for the current time instant k can be calculated immediately after the arrival of the new measurement $\mathbf{x}_k$ including the sampling values off all 12 ECG leads.

The estimated demixing vector $\mathbf{w}$ remained unchanged, i. e. it was only estimated once for each volunteer. Hence, the *first* processing stage can be summarised as follows:

1. Record the 12-lead ECG for 30 s inside the MR scanner $\rightarrow \mathbf{x}_{\mathrm{Ref,k}}$.
2. Application of ICA to $\mathbf{x}_{\mathrm{Ref,k}}$ leads to a demixing matrix $\mathbf{W}$ and a set of estimated ICs $\widehat{\mathbf{s}}_k$.
3. Identify one IC $\widehat{s}_{\mathrm{ECG}}$ out of $\widehat{\mathbf{s}}_k$ which is dominated by the R-peak or QRS complex.
4. Reduce the demixing matrix $\mathbf{W}$ to a vector $\mathbf{w}$, which is then used to estimate $\widehat{s}_{\mathrm{ECG}}$ from the 12-lead ECG signals.

In the *second stage*, the demixing vector $\mathbf{w}$, which was estimated in the first stage was applied to the most recent ECG samples $\mathbf{x}_k$ recorded at time instant k. This resulted in an estimation of the IC $\widehat{s}_{\mathrm{ECG,k}}$ at the same time instant. Following Eq. 5.18, the estimation of $\widehat{s}_{\mathrm{ECG,k}}$ was defined as a linear combination of the ECG-leads stored in $\mathbf{x}_k$.

The demixing process was followed by the application of a QRS / R-peak detection algorithm[3] [Clifford 02] to $\widehat{s}_{\mathrm{ECG}}$. Since this QRS detector is based on the slope of the ECG signal, the slope of the IC used for QRS detection was compared quantitatively with respect to the slope (first derivative) of the clean ECG signal which was recorded outside the MR scanner.

5.3.3 Identification of the cardiac signal component for QRS detection

Problem overview

One crucial step with the application of ICA to the given problem is the identification of a basis function or IC $\widehat{s}_{\mathrm{ECG}}$, which is suitable for gating in CMR. This IC should represent the ventricular activity, i. e. it should contain the R-peak or QRS complex. It is not possible to determine the order of the estimated independent components $\widehat{\mathbf{s}}_k$ *a priori* (see Section 5.3.1). One obvious solution is the visual inspection and manual selection of one IC, which represents the cardiac activity. However, when considering a future practical implementation of the proposed method, $\widehat{s}_{\mathrm{ECG}}$ should be identified by an automatic approach without any user interaction. In addition to this practical demand, a manual selection of $\widehat{s}_{\mathrm{ECG}}$ can be prone to errors due to the similar periodic properties of the MHD effect. If the morphological features of the MHD effect and the ECG signal are not considered, one may erroneously choose an IC dominated by the MHD effect. To avoid such errors and the additional effort required for a manual selection of $\widehat{s}_{\mathrm{ECG}}$, two different approaches based on

1. a measurement of the IC's kurtosis and on
2. a template matching

were investigated for the automated identification of $\widehat{s}_{\mathrm{ECG}}$.

[3] http://alum.mit.edu/www/gari/code/ecgtools/

Definition of $\widehat{s}_{\text{ECG}}$

For the envisaged gating application, the IC identified as $\widehat{s}_{\text{ECG}}$ should provide the optimal QRS detection results in terms of Se and $+P$. This optimal IC is referred to as $\widehat{s}_{\text{opt}}$. The criterion for the definition of $\widehat{s}_{\text{opt}}$ was the QRS detection quality. Hence, the QRS detection algorithm was applied to all the estimated ICs $\widehat{\mathbf{s}}_k$. The IC, which returned the best QRS detection results, was defined as $\widehat{s}_{\text{opt}}$ (whereas the manual annotations were taken as the reference). The identification algorithm (either the kurtosis- or template-based) should identify this IC as $\widehat{s}_{\text{ECG}}$ in all ECG records.

Identification of $\widehat{s}_{\text{ECG}}$ based on kurtosis measurement

ECG signals exhibit a non-Gaussian distribution. Several metrics such as entropy (see Section 5.3.1) or the kurtosis exist to measure the non-Gaussianity of a signal. For a normal distribution, the kurtosis is $3\sigma^2$. When superimposing two signals with non-Gaussian distributions, the resulting signal tends to be more Gaussian which can be explained by the central limit theorem (see Section 5.3.1). Hence, it was assumed that the ECG acquired inside the MR scanner, which is a mixture of the ECG and MHD signal, has a lower kurtosis than the ECG signals itself. Additionally, it was assumed that the MHD signal has a much lower kurtosis due to its less peaky signals properties when compared to the ECG signal. The ECG acquired outside MR scanner has a peaky waveform and hence, it can be expected to have a high kurtosis. Figure 5.6 depicts exemplary histograms with corresponding kurtosis values of ECG signals acquired outside and inside the MR scanner. In these examples, the

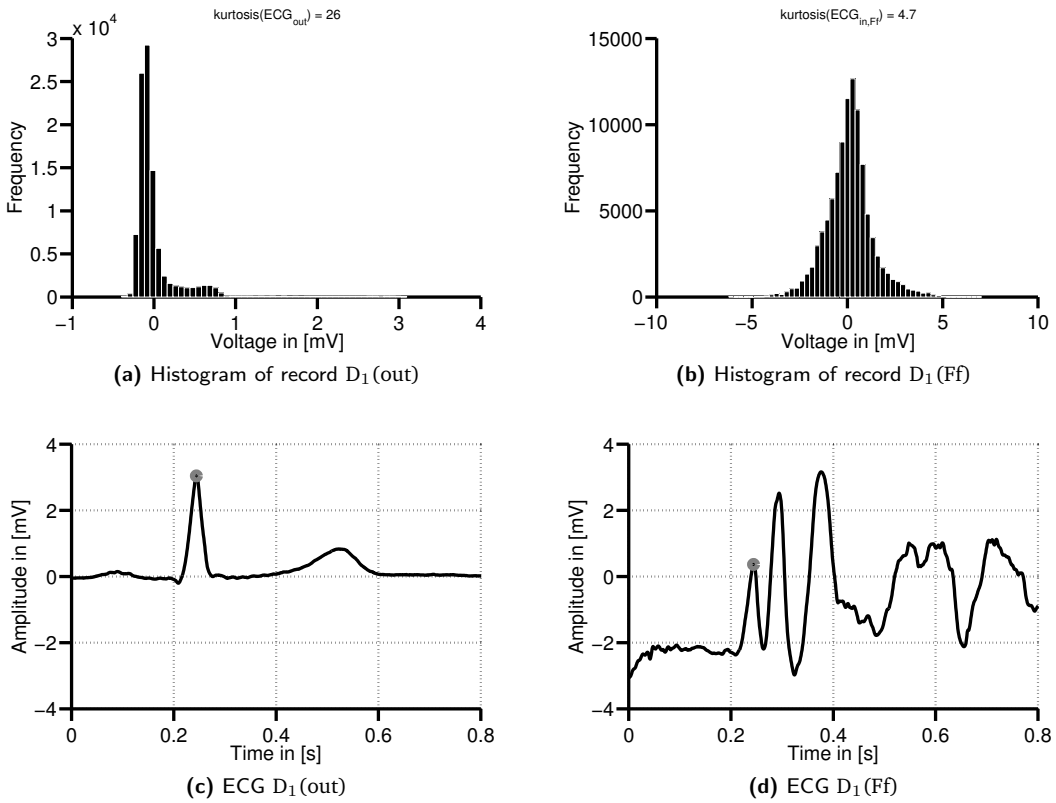

(a) Histogram of record D_1(out)

(b) Histogram of record D_1(Ff)

(c) ECG D_1(out)

(d) ECG D_1(Ff)

Figure 5.6.: Histograms of ECGs (lead II) acquired outside (a) and inside (b) the MR scanner and the corresponding ECG traces (c),(d). The histograms were estimated from segments of $100\,s$ length. Grey dots mark to locations of the R-peaks.

superimposed MHD effect decreased the kurtosis of the signal. Table 5.1 summarises the calculated kurtosis values. The mean and standard deviation values were estimated over all 12 leads of a record. The MHD signals were estimated by a template subtraction procedure. A fixed PQRST-template of the ECG acquired outside was subtracted beat-to-beat from the ECG acquired inside the MR scanner resulting in a series of MHD signal estimates. The kurtosis was averaged over all extracted MHD signal segments. The kurtosis of the ECGs acquired inside the MR scanner and of the estimated MHD signals is of comparable order in all ECG records. Considering the kurtosis of the ECGs acquired outside the MR scanner, it is subject to larger intersubject variations.

In order to identify the independent component of interest, i. e. $\widehat{s}_{\text{ECG}}$, the kurtosis was calculated for all estimated components $\widehat{\mathbf{s}}_k$. It was assumed that the IC with the highest kurtosis is dominated by the ECG signal or QRS complexes, respectively. This IC was then labelled as $\widehat{s}_{\text{ECG}}$.

Kurtosis can also be used as a metric for outlier detection [DeCarlo 97]. Hence, outliers in the ECG records or artefacts in the ICs $\widehat{\mathbf{s}}_k$ can affect the identification of $\widehat{s}_{\text{ECG}}$. A single outlier in one or more ICs could falsify the identification of $\widehat{s}_{\text{ECG}}$ which would decrease the QRS detection quality. To cope with such problems, the estimated ICs $\widehat{\mathbf{s}}_k$ were divided into smaller segments of 5 s length assuming that outliers only existed temporarily. For each IC, the kurtosis was estimated in all segments. The median of the kurtosis of all segments of one IC was considered. Finally, the IC with the highest assigned kurtosis value was identified as $\widehat{s}_{\text{ECG}}$. It has to be kept in mind that kurtosis depends on the heart rate, i. e. with an increasing heart rate, kurtosis decreases (since there are less 'outliers' which broadens the histogram). However, since $\widehat{s}_{\text{ECG}}$ was identified based on the maximum value and the MHD signal was expected to decrease kurtosis, the impact of the heart rate was not considered here.

Identification of $\widehat{s}_{\text{ECG}}$ based on template matching

Two ECG records were required for the template matching approach: *1)* one (clean) ECG, which was acquired outside the MR scanner and was free from MHD-contaminations and *2)* one (contaminated) ECG which was recorded inside the MR scanner. The *first* ECG $\mathbf{x}_{out}$ was recorded on the table of the MR scanner but before the subject was moved into the scanner. It should have a length of at least 20 s to cover enough QRS complexes for the template. This ECG can be acquired while the subject is prepared for the MR scan. Hence, this step should not prolong the overall procedure during the practical application. The *second* ECG trace $\mathbf{x}_k$ was recorded directly after the subject was moved into the MR scanner. ICA was then applied to the measured signal $\mathbf{x}_k$ resulting in the demixing matrix $\mathbf{W}$. Several ICs were obtained by applying the demixing matrix to the ECG measurement: $\widehat{\mathbf{s}}_k = \mathbf{W}\mathbf{x}_k$.

Table 5.1.: Kurtosis (mean and standard deviation of the 12 ECG leads) of the training records $\text{D}_1 - \text{D}_5$ for the ECGs acquired outside and inside the MR scanner (in Ff and Hf position).

Record	Outside	Inside, Ff	Inside, Hf	MHD, Ff	MHD, Hf
D_1	23.1 ± 9.4	4.2 ± 0.9	4.4 ± 1.6	4.2 ± 1.0	4.8 ± 1.6
D_2	18.4 ± 4.3	3.4 ± 0.6	3.9 ± 0.8	3.7 ± 0.8	3.5 ± 0.9
D_3	19.5 ± 6.4	4.1 ± 0.8	4.4 ± 1.0	3.6 ± 0.8	4.5 ± 1.1
D_4	13.5 ± 4.8	4.2 ± 0.9	5.4 ± 1.4	3.7 ± 1.0	3.9 ± 1.6
D_5	9.2 ± 6.0	3.2 ± 0.6	3.5 ± 0.4	3.4 ± 0.7	3.6 ± 0.5

For the identification of $\widehat{s}_{\text{ECG}}$, a proper template $\mathbf{u}_{\text{k,qrs}}$ of the QRS complex was required. Depending on the number of estimated sources in $\widehat{\mathbf{s}}_k$, an appropriate number of QRS templates was required. By defining several QRS templates which are specific for each estimated IC $\widehat{\mathbf{s}}_k$, one of the main problems of ICA could be overcome. These problems are the unknown source order and the arbitrary scaling of the sources $\widehat{\mathbf{s}}_k$. The demixing process also alters the shape of the QRS-complexes in $\widehat{\mathbf{s}}_k$ when compared to the QRS complexes of the original ECG traces in $\mathbf{x}_k$ or $\mathbf{x}_{out}$ due to linear mixing of different channels.

The templates of the QRS complexes were defined by applying the demixing matrix $\mathbf{W}$ (estimated from the contaminated ECG signal $\mathbf{x}_k$) to the clean ECG signal $\mathbf{x}_{\text{k,out}}$ recorded outside the MR scanner

$$\widehat{\mathbf{s}}_{\text{k,out}} = \mathbf{W}\mathbf{x}_{\text{k,out}}. \tag{5.19}$$

For each of the linear combinations $\widehat{\mathbf{s}}_{\text{k,out}}$, a template $\mathbf{u}_{\text{k,qrs}}$ of the QRS complex was generated using the following procedure. First, a QRS detection algorithm [Clifford 02] was applied to one lead of the clean ECG signal $\mathbf{x}_{\text{k,out}}$ in order localise the QRS complexes. The QRS template for each linear lead combination in $\widehat{\mathbf{s}}_{\text{k,out}}$ was then estimated from segments of 80 ms length centred around the detected QRS positions and averaged over ten consecutive QRS complexes. An exemplary template taken from $\widehat{\mathbf{s}}_{\text{k,out}}$ corresponding to the IC which was finally identified as $\widehat{s}_{\text{ECG,k}}$ (later used for QRS detection) is depicted in Fig. 5.7a.

For the identification of $\widehat{s}_{\text{ECG,k}}$, the cross-correlation functions $(\widehat{\mathbf{s}}_k \star \mathbf{u}_{\text{k,qrs}})$ between each QRS template in $\mathbf{u}_{\text{k,qrs}}$ and the corresponding IC in $\widehat{\mathbf{s}}_k$ were calculated. An exemplary IC is depicted in Fig. 5.7b. To avoid the influence of outliers, the same segmentation procedure was applied as described above in the kurtosis-based method. Based on the median value of the cross-correlation functions in the different segments of an IC, one IC in $\widehat{\mathbf{s}}_k$ was identified as $\widehat{s}_{\text{ECG}}$. Figure 5.8 summarises the whole template matching procedure.

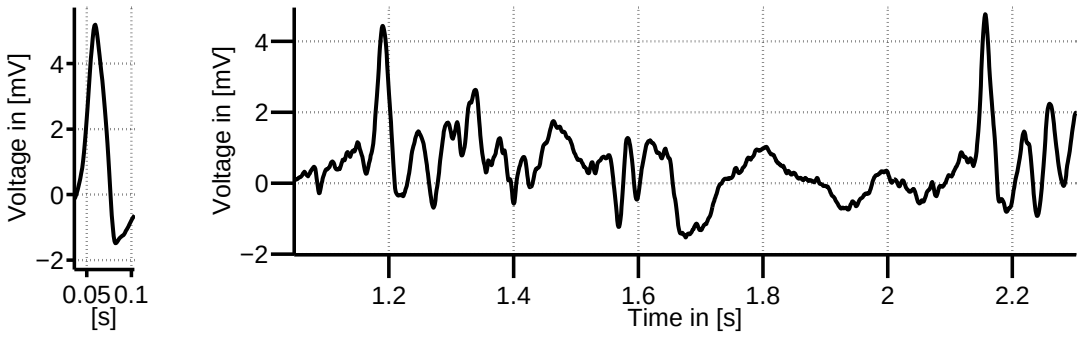

(a) Template **(b)** Estimated component $\widehat{s}_{\text{ECG}}$

Figure 5.7.: Template from the clean ECG acquired outside the MR scanner (a) obtained using $\widehat{\mathbf{s}}_{\text{k,out}} = \mathbf{W}\mathbf{x}_{\text{k,out}}$. The template was used to locates the QRS complexes in $\widehat{s}_{\text{ECG}}$ (b).

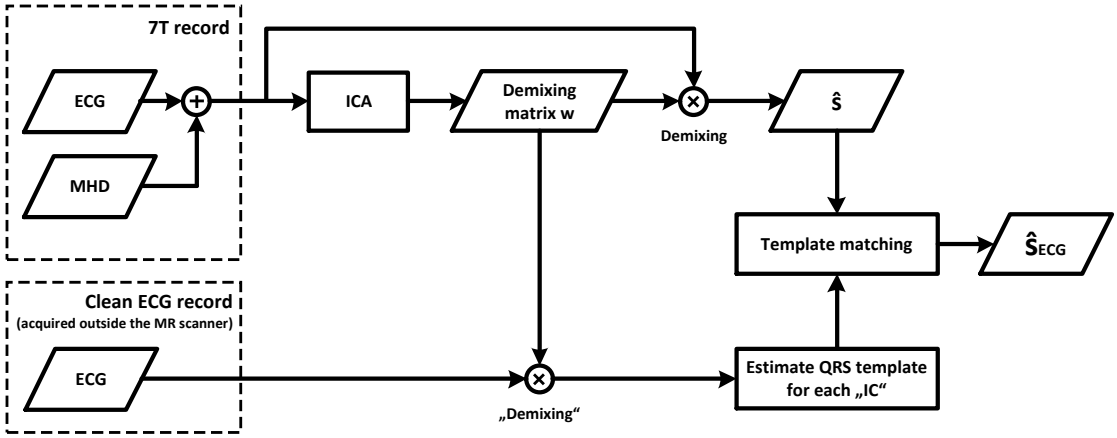

Figure 5.8.: Template matching algorithm for the identification of $\widehat{s}_{\mathrm{ECG}}$. The demixing matrix obtained from the MHD-contaminated ECG record was applied to the clean ECG acquired outside the MR-scanner. A template of the QRS complex $\mathbf{u}_{\mathrm{k,qrs}}$ was generated from each IC obtained from applying $\mathbf{W}$ to the clean ECG. These templates were compared to the corresponding ICs $\widehat{\mathbf{s}}_k$ obtained by the application of $\mathbf{W}$ to the contaminated ECG leads.

Additional criteria for the identification of $\widehat{s}_{\mathrm{ECG}}$

After one IC was identified as $\widehat{s}_{\mathrm{ECG}}$, additional parameters were evaluated to ensure that the identified IC was suited for QRS detection. Therefore, the length of the RR intervals (RRI) of the QRS complexes detected in $\widehat{s}_{\mathrm{ECG}}$ was analysed. The length range of these intervals is determined by the cardiac physiology. It was set to

$$200\,\mathrm{ms} \leq \mathrm{RRI} \leq 1500\,\mathrm{ms}.$$

The lower bound was chosen to consider cardiac arrhythmias such as premature ventricular contractions (PVC) which can cause a minimal RRI length of $\approx 200\,\mathrm{ms}$ [Pan 85, Werner 05, Hick 06]. The maximum RRI length was set to 1500 ms which corresponds to a heart rate of 40 bpm. Certain patient groups, e. g. athletes, can have lower resting heart rate though. The upper bound could be adjusted automatically by using the RRI time-series of the undistorted ECG signal, which was acquired outside the MR scanner.

5.3.4 Configuration and additional quality criteria

Number of ECG leads and of the principal components (PC)

The configurations presented in this section were used to investigate the influence of different ECG leads on the results obtained by ICA. Therefore, ICA was applied to selected leads only, e. g. to combinations of the limb leads or of the limb leads and some precordial leads.

In the first step, ICA was applied to the limb leads I and II and the precordial leads V1-V6. The other four leads (III, aVR, aVL and aVF) were not included because they form linear combinations of limb leads I and II (see Section 2.1.2). Hence, the remaining 4 leads contained no additional information. The usage of 8 leads for the estimation of $\widehat{\mathbf{s}}_k$ is referred to as lead configuration LC1.

In the second step, ICA was applied to the same signals, but with a reduced number of ECG leads. These signals consisted of combinations of the limb leads I and II and of different numbers of precordial leads. Furthermore, the influence of decreasing the dimensionality of the original signals was investigated. The dimensionality of the original signals was reduced by means of PCA [Clifford 05]. Only a limited number of PCs was kept before ICA was applied to the ECG records. The different ECG lead and PC combinations are referred to as configurations LC2a–LC2h. Results for the LC2 configurations are given for the best combinations of different leads and PCs. In order to highlight the influence of a single precordial lead on the QRS detection, combinations of lead I and II and of one additional precordial lead were computed (LC2e–LC2g). Finally, ICA was applied to lead I and II without any additional precordial lead (LC2h) because in most MRI scanners there are only 2 leads available.

Long term stability and robustness of the proposed ICA-based QRS detection method

In order to enable its practical applicability, the proposed method should be able to run in real-time, i. e. $\widehat{s}_{\mathrm{ECG}}$ can be estimated without a negligible delay. It was expected that the estimation of the demixing matrix $\mathbf{W}$ and the identification of the IC $\widehat{s}_{\mathrm{ECG}}$ consumes most of the processing time. As it was depicted in Fig. 5.5a, p. 97, these two problems were solved in the preprocessing phase. This procedure assumed a subject specific demixing matrix $\mathbf{W}$, which was time invariant with respect to the MHD effect. To validate this assumption, the long term stability of the demixing matrix was investigated.

The training records D_5 and the test records D_9, which were acquired from the same volunteer but were separated by one year, were used for this experiment. An additional ECG record of the same volunteer, which was acquired at a 3 T MR scanner, was used to show the robustness of the demixing matrix. In addition to the temporal separation, the position of the ECG electrodes applied according to Fig. 3.30a, p. 61 did not perfectly match.

Two demixing matrices $\mathbf{W}_{\mathrm{D}_5(\mathrm{Ff})}$ and $\mathbf{W}_{\mathrm{D}_5(\mathrm{Hf})}$ were estimated from the 7 T records $\mathrm{D}_5(\mathrm{Ff})$ and $\mathrm{D}_5(\mathrm{Hf})$. Another two demixing matrices $\mathbf{W}_{3\,\mathrm{T}(\mathrm{Ff})}$ and $\mathbf{W}_{3\,\mathrm{T}(\mathrm{Hf})}$ were estimated from the 3 T records $\mathrm{D}_1(\mathrm{Ff}_{3\,\mathrm{T}})$ and $\mathrm{D}_1(\mathrm{Hf}_{3\,\mathrm{T}})$. The four matrices were used to demix the subsets $\mathrm{D}_9(\mathrm{Ff})$ and $\mathrm{D}_9(\mathrm{Hf})$ of record D_9 in the following way:

$$\begin{aligned}
\mathbf{W}_{\mathrm{D}_5(\mathrm{Ff})} \cdot \mathrm{D}_9(\mathrm{Ff}) &\rightarrow \widehat{s}_{\mathrm{ECG,k}}(\mathbf{W}_{\mathrm{D}_5(\mathrm{Ff})}, \mathrm{D}_9(\mathrm{Ff})) \\
\mathbf{W}_{\mathrm{D}_5(\mathrm{Hf})} \cdot \mathrm{D}_9(\mathrm{Hf}) &\rightarrow \widehat{s}_{\mathrm{ECG,k}}(\mathbf{W}_{\mathrm{D}_5(\mathrm{Hf})}, \mathrm{D}_9(\mathrm{Hf})) \\
\mathbf{W}_{3\,\mathrm{T}(\mathrm{Ff})} \cdot \mathrm{D}_9(\mathrm{Ff}) &\rightarrow \widehat{s}_{\mathrm{ECG,k}}(\mathbf{W}_{3\,\mathrm{T}(\mathrm{Ff})}, \mathrm{D}_9(\mathrm{Ff})) \\
\mathbf{W}_{3\,\mathrm{T}(\mathrm{Hf})} \cdot \mathrm{D}_9(\mathrm{Hf}) &\rightarrow \widehat{s}_{\mathrm{ECG,k}}(\mathbf{W}_{3\,\mathrm{T}(\mathrm{Hf})}, \mathrm{D}_9(\mathrm{Hf})).
\end{aligned} \tag{5.20}$$

The application of the four demixing matrices to the subsets of D_9 should reveal their long term stability. The latter two demixing matrices ($\mathbf{W}_{3\,\mathrm{T}(\mathrm{Ff})}$ and $\mathbf{W}_{3\,\mathrm{T}(\mathrm{Hf})}$) should reveal the robustness of the demixing matrices since these two matrices were estimated from the 3 T record. Using the four demixing matrices, four ICs $\widehat{s}_{\mathrm{ECG,k}}$ were identified. Again, these ICs were used for the QRS detection, whose results are given in terms of Se and $+P$ for both datasets.

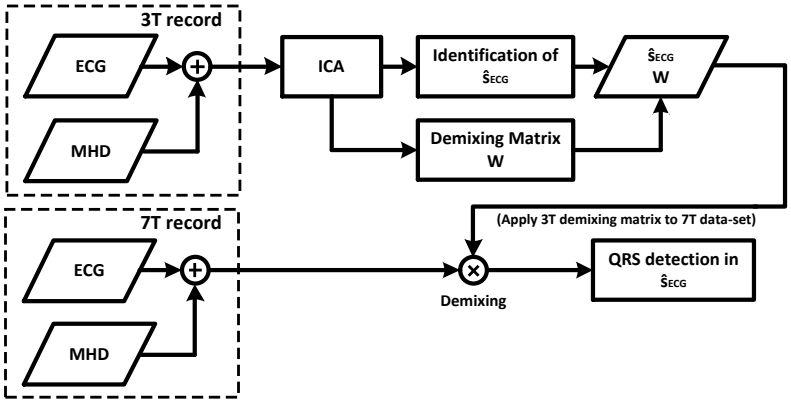

Figure 5.9.: Template matching algorithm for the identification of $\widehat{s}_{\text{ECG}}$. The demixing matrix obtained from the MHD-contaminated ECG record was applied to the clean ECG recorded outside the MR-scanner. A template of the QRS complex $\mathbf{u}_{\text{k,qrs}}$ was generated from each IC obtained from applying $\mathbf{W}$ to the clean ECG. These templates were compared to the corresponding ICs $\widehat{\mathbf{s}}_k$ obtained by the application of $\mathbf{W}$ to the contaminated ECG-leads.

Upslope preservation of the QRS complex in $\widehat{s}_{\text{ECG,k}}$

The algorithm used for QRS detection takes the first derivative of the ECG signal to enhance the QRS complex [Pan 85, Clifford 02]. To ensure a reliable QRS detection inside the MR scanner, the slope of the QRS complex needed to be preserved in the identified IC $\widehat{s}_{\text{ECG,k}}$. This was investigated quantitatively by comparing the upslope differences of the QRS complex in $\widehat{s}_{\text{ECG,k}}$ and in the corresponding IC $\widehat{s}_{\text{k,out,ECG}}$. The estimation of $\widehat{s}_{\text{k,out,ECG}}$ is described in Section 5.3.3. After testing both distributions (upslopes in $\widehat{s}_{\text{ECG,k}}$ and in $\widehat{s}_{\text{k,out,ECG}}$) for normality using a Lilliefors test [Lilliefors 67], a two-sample t-test ($\alpha = 0.05$) was conducted to assess if the mean slopes of $\widehat{s}_{\text{ECG,k}}$ and $\widehat{s}_{\text{k,out,ECG}}$ showed significant differences. The mean and standard variations were estimated for each record $\text{D}_1 - \text{D}_9$. In addition, the slopes of $\widehat{s}_{\text{ECG,k}}$, $\widehat{s}_{\text{k,out,ECG}}$ and of the raw ECG signal acquired inside the MR scanner were compared qualitatively.

5.4 Other QRS detection methods for comparison

Other methods for QRS detection in the contaminated ECG or VCG signals were also investigated. All methods were performed on all the 12 available leads. When required, the VCG $\mathbf{v}(t)$ was obtained using the inverse Dower transform (see Section 2.1.3). An overview of the four additional QRS detection methods M1-M4, which were implemented for comparison with the proposed ICA-based method and the method based on the 6D-vector space are given below. Methods M1-M3 used the QRS detector from [Clifford 02]. The QRS detection performance of methods M1-M5 was evaluated test dataset. This was done to have a better comparability with the results obtained from the vector-based and ICA-based methods. No training was performed for method M1-M5.

M1: QRS detection in the least contaminated ECG lead

The QRS detection algorithm was successively applied to each of the 12 ECG leads of all records. The raw 12-lead ECG signals were used without further preprocessing. For all records, Se and $+P$ values were estimated for each lead. Using these results, the lead giving the best QRS detection results averaged over all records was finally chosen. The results were only reported on the lead providing the best results for all recordings from the the training set. Hence, the final results are given for the same lead.

M2: QRS detection in a single VCG lead

QRS detection was separately performed in all three VCG leads $\mathbf{v}(t) = (v_x(t), v_y(t), v_z(t))$ in all records. The aim was to investigate if the linear combination of the ECG leads using the inverse Dower transform (Eq.řefeq:VCGDowerMatrixInverse, p. 13) improved the QRS detection quality. As in method M1, the VCG lead with the best QRS detection results was chosen, i. e. the same lead (either x,y or z) was used for comparing the QRS detection results in all records.

M3: ICA of the VCG for QRS detection

For a further analysis of the usability of the three lead VCG signal instead of the twelve lead ECG signal, ICA was applied to the three VCG leads $v_x(t), v_y(t), v_z(t)$ of each record. Using the procedure described in Section 5.3.3, $\widehat{s}_{\text{ECG}}$ was estimated from the different ICs and was used for QRS detection. Since the VCG is commonly used for gating in CMR as explained in Section 5.2, the aim was to investigate if the clinically available three leads of the VCG would be sufficient for the estimation R-peak detection.

M4: '3D-QRS' method

Tse *et al.* proposed a method based on 12-lead ECG signals, which exploits the superior quality of the precordial ECG leads (see Section 3.4.1) [Tse 11a, Tse 12, Tse 13]. This method can be regarded as a template matching procedure. A template of the QRS complex was generated from a clean ECG signal recorded outside the MR scanner. This template was built using the six precordial leads V1-V6 covering the complete QRS complex. An exemplary template is given in Fig. 5.10a. A cross-correlation between this template and the contaminated ECG trace was performed. By assuming that the QRS template from the clean ECG and the QRS complex in the contaminated ECG have similar morphologies, a high correlation value was assumed to correspond to the position of the QRS complex.

M5: Higher order central moments

It was shown that higher order central moments can be used for QRS detection by utilising the steep slopes of the QRS complex (see the descriptions in Section 3.4.1 and in [Schmidt 14]). Here, the central moment based method was applied to the 7 T ECG records. The 7 T ECG signals were bandpass filtered (5th order Butterworth filter, passband ranging from 2 Hz to 30 Hz) before the 4th order central moments were estimated in windows of 20 ms length (following the descriptions in [Schmidt 14]).

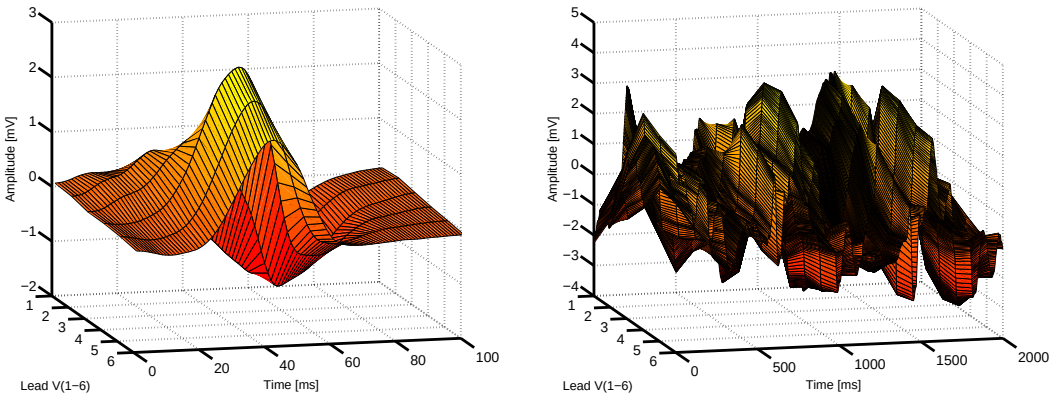

(a) 3D-QRS template

(b) 3D-ECG trace inside the MR scanner

Figure 5.10.: 3D template of the QRS complex (a) as used in gating method M4. A cross-correlation between the template and the contaminated ECG trace (b) was performed to locate the QRS complexes.

5.5 Results

5.5.1 Overview

Table 5.2 summarises the results obtained by the different methods analysed and developed in this chapter. From the vector-based methods, the standard VCG-based QRS detector achieved the lowest QRS detection quality in terms of Se and $+P$. The results of the normal VCG-based method were slightly improved by the modified reference vector proposed in Section 5.2.1. This method was then further improved using the precordial leads V1-V6 within the proposed 6D-sECG method (see Section 5.2.2) instead of the VCG's x, y and z-leads. Due to the superior quality of the precordial leads, the QRS detection quality was drastically improved.

The best overall performance was achieved by the ICA-based QRS detection method proposed in Section 5.3. The IC $\widehat{s}_{\text{ECG}}$ was automatically identified in all records using the template matching procedure. Although the slope of the QRS complex was changed in $\widehat{s}_{\text{ECG}}$ compared to $\widehat{s}_{\text{out,ECG}}$, a successful QRS detection using the identified IC was possible.

Methods M1 to M4 used for comparison did not reach the quality of the 6D-sECG or of the ICA-based method. For the QRS-detection based on a single ECG lead (method M1), the best average results were obtained when the precordial lead V4 was used. Comparable detection results were achieved using methods M2 and M3. Where the results obtained by the 3D-QRS method (M4) were comparable with the results of methods M1 to M3 for the training dataset, the detection performance dropped within the test dataset.

For a deeper understanding of the different methods, the following sections provide more detailed explanations of the results.

Table 5.2.: Overview of the QRS detection performances achieved by the different methods and algorithms (μ_{pd}: mean detection delay; σ_{pd}: jitter).

Methods	Training dataset				Test dataset			
	Se [%]	$+P$ [%]	μ_{pd} [ms]	σ_{pd} [ms]	Se [%]	$+P$ [%]	μ_{pd} [ms]	σ_{pd} [ms]
VCG (normal)	78.3	54.4	7.1	4.4	72.1	57.5	8.9	3.8
VCG (modified reference)	79.3	82.3	5.0	5.9	75.6	77.2	6.1	5.4
6D-sECG	99.3	99.1	2.4	2.0	98.8	98.8	2.7	2.0
ICA LC1	99.5	99.4	3.5	6.5	99.2	99.1	5.8	5.0
M1 (ECG V4)	86.8	88.4	0.2	2.3	87.1	89.4	23.8	19.1
M2 (Single VCG Lead)	89.2	96.7	4.1	4.7	88.9	91.2	3.4	2.3
M3 (ICA of VCG)	88.7	86.3	6.9	9.2	84.3	87.5	5.2	10.7
M4 (3D QRS)	87.6	87.3	48.1	7.0	64.8	73.7	51.2	12.1
M5 (Central moments)	100	68.9	6.2	7.1	100	60.3	7.8	8.8

5.5.2 Vector-based QRS detection

5.5.2.1 State-of-the-art and modified vector-based QRS detection method

Influence of the MHD effect

Both, the 3 T and the 7 T measurements showed variations of the direction and amplitude of the R-peak vector as it was shown in Fig. 3.19, p. 47. The R-peak of the 3 T measurement showed a deviation of 3.6° with respect to the reference R-peak vector. The absolute difference of the norm of the two vectors was 0.4 mV. For the 7 T VCG measurements, an average deviation angle of 68.7° and a difference of the norm of 1.7 mV were observed [Krug 13b]. These variations already described in Sec. 3.3.3 were considered the main reason for the error proneness of VCG-based gating at 7 T. Figure 5.11 compares the peaks occurring in exemplary 3 T and 7 T records as obtained by the standard VCG-based gating method.

QRS detection results

Figure 5.11 depicts exemplary results from the normal VCG-based gating method applied to 3 T and 7 T ECGs [Fischer 99]. The red trace is the signal obtained from the VCG-based algorithm. In the 3 T ECG record depicted in Fig. 5.11a, the peak locations in the red trace coincide with the locations of the QRS complexes. For the 7 T ECG depicted in Fig. 5.11b, the red trace shows several other peaks which do not necessarily coincide with the QRS locations. The examples depicted in Fig. 5.12 show the influence of the modified reference vector at 7 T. Using the modified reference vector, the peaks in the signal obtained by the VCG-based method coincide with the positions of QRS complexes.

Tables 5.3 and 5.4 summarise the QRS detection results for the training and test datasets using the normal reference vector $\mathbf{r}$ and the modified reference vector $\mathbf{r}_{\text{in}}$. Using the modified reference vector $\mathbf{r}_{\text{in}}$, the $+P$ values were increased by 27.9 % for the training dataset and by 19.7 % for the test

dataset. The mean delays μ_{pd} and jitter values σ_{pd} were within an acceptable range for gating applications, which should be less than 20 ms and 15 ms respectively (see Section 4.3.1). For the standard VCG-based method, the average results were $\mu_{pd} = 8.9\,\text{ms}$ and $\sigma_{pd} = 3.8\,\text{ms}$ for the test dataset. Using the modified reference vector, average results of $\mu_{pd} = 6.1\,\text{ms}$ and $\sigma_{pd} = 5.4\,\text{ms}$ were achieved within the test dataset.

5.5.2.2 Higher dimensional vector space

Figure 5.13 depicts exemplary signals obtained by the different VCG- and 6D-sECG-based methods. In terms of its application for cardiac gating, the best QRS detection quality was achieved using the proposed 6D-sECG method with the differential signal. The results of the other methods shown in Fig. 5.13 were not sufficient a high quality QRS detection. Either, the peak amplitudes show high variations as in Figs. 5.13a (normal VCG) and 5.13c (normal 6D-sECG) or additional (false positive) peaks with high amplitudes as in Fig. 5.13b (differential VCG).

The proposed (differential) 6D-sECG method resulted in a high QRS detection quality. A complete summary of the QRS detection results in the training and test datasets is given in tables 5.5 and 5.6, respectively. With $Se = 99.2\,\%$ and $+P = 99.1\,\%$ within the training set and $Se = 98.8\,\%$ and $+P = 98.8\,\%$ within the test set, the superiority of the 6D-sECG compared to the normal VCG-based method was demonstrated. Very low delays μ_{pd} of 2.7 ms and jitters σ_{pd} of 2.0 ms were achieved for the test dataset.

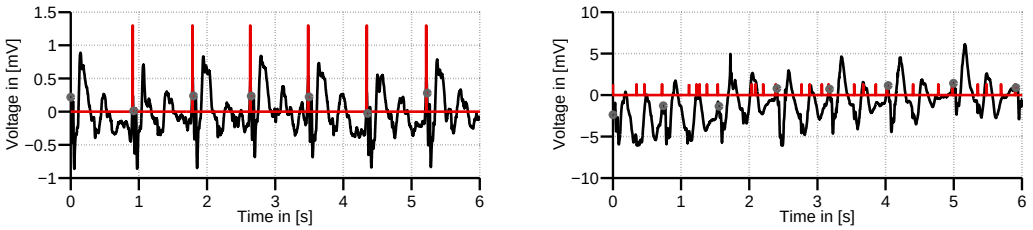

(a) $\mathbf{B}_0 = 3\,\text{T}$. **(b)** $\mathbf{B}_0 = 7\,\text{T}$.

Figure 5.11.: Signals obtained from the VCG-based technique used for QRS detection (red) at 3 T (a) and 7 T (b) together with the ECG signals of lead I (black) and the manual annotations (grey dots). For the 3 T record (a), the peaks obtained by the VCG-based method agree with the manual annotations. In contrast, several additional peak can be observed in the 7 T record (b).

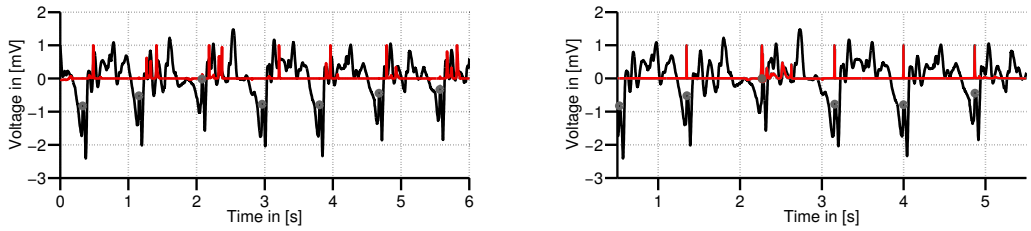

(a) Normal reference vector. **(b)** Modified reference vector.

Figure 5.12.: Signals obtained from the VCG-based technique used for QRS detection (red) at 7 T using the normal (a) and the modified (b) reference vector with VCG lead z (black) and the manual annotations (grey dots). For the normal reference vector, several peak can be observed. These peaks are not located at the positions of the QRS complexes. Using the modified reference vector (b), the peaks are coincide with the locations of the QRS complexes.

Table 5.3.: VCG-based QRS detection results for the training dataset acquired at 7 T. (Normal Ref: reference vector defined outside the MR scanner; Modified Ref: reference vector defined inside the MR scanner). (TP = true positives, FP = false positives, FN = false negatives, Se = sensitivity, +P = positive predictive value, HF = head first, Ff = feet first, μ_{pd} = mean delay, σ_{pd} = jitter)

Training dataset		Normal Ref		Modified Ref	
Dataset	R-peaks	Se [%]	$+P$ [%]	Se [%]	$+P$ [%]
D_1(Ff)	165	72.1	36.6	72.1	52.2
D_1(Hf)	226	100.0	86.9	100.0	98.7
D_2(Ff)	285	67.0	61.4	84.9	95.7
D_2(Hf)	198	78.8	26.4	70.7	95.2
D_3(Ff)	243	95.1	96.7	92.2	70.2
D_3(Hf)	254	86.2	100.0	96.5	96.5
D_4(Ff)	361	97.8	38.2	96.7	71.4
D_4(Hf)	400	83.8	20.9	56.5	65.5
D_5(Ff)	326	89.6	19.4	40.2	86.2
D_5(Hf)	395	12.4	57.6	82.8	91.3
Total	2853				
Mean		78.3	54.4	79.3	82.3

Table 5.4.: VCG-based QRS detection results for the test dataset acquired at 7 T. (Normal Ref: reference vector from outside the MR scanner; Modified Ref: reference vector defined inside the MR scanner). (TP = true positives, FP = false positives, FN = false negatives, Se = sensitivity, +P = positive predictive value, HF = head first, Ff = feet first, μ_{pd} = mean delay, σ_{pd} = jitter)

Test dataset		Normal Ref		Modified Ref	
Dataset	R-peaks	Se [%]	$+P$ [%]	Se [%]	$+P$ [%]
D_6(Ff)	401	77.8	65.1	85.5	77.3
D_6(Hf)	416	71.9	56.0	77.2	77.5
D_7(Ff)	202	78.2	69.6	76.2	79.0
D_7(Hf)	163	42.3	62.2	63.8	60.8
D_8(Ff)	310	84.8	45.7	89.7	81.3
D_8(Hf)	421	77.9	58.0	82.4	70.0
D_9(Ff)	331	92.1	42.7	49.2	85.8
D_9(Hf)	360	51.7	61.0	80.8	86.1
Total	2604				
Mean		72.1	57.5	75.6	77.2

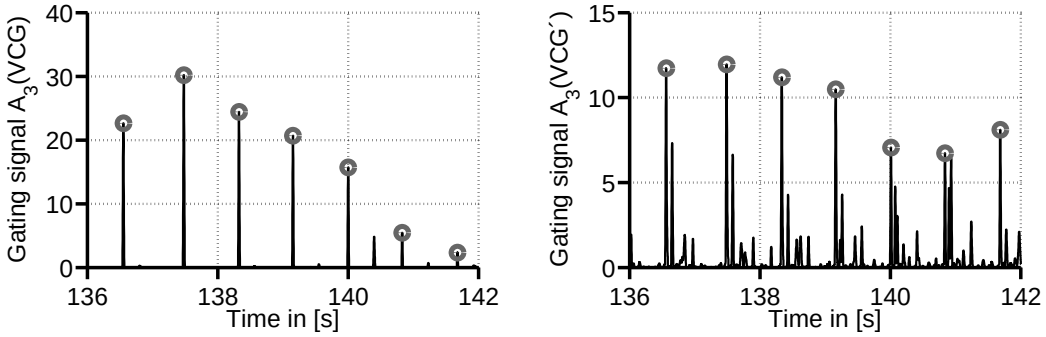

(a) Record D_5(Hf), VCG, Normal

(b) Record D_5(Hf), VCG, Differential

(c) Record D_5(Hf), 6D-sECG, Normal

(d) Record D_5(Hf), 6D-sECG, Differential

Figure 5.13.: Signals used for QRS detection obtained by the state-of-the-art VCG-based method (a,b) and by the newly proposed 6D-sECG method (c,d). For each of the two methods, the results obtained by the normal and by the differential signals are shown. The differential signal of the 6D-sECG method (d) shows the best signal quality in terms of its usage for QRS detection. Manually annotated R-peak locations are marked by grey dots.

Table 5.5.: QRS detection results in the training dataset using the 6D-sECG method. (TP = true positives, FP = false positives, FN = false negatives, Se = sensitivity, +P = positive predictive value, Hf = head first, Ff = feet first, μ_{pd} = mean delay, σ_{pd} = jitter)

Record	# of R-peaks	TP	FP	FN	Se [%]	PPV [%]	μ_{pd} [ms]	σ_{pd} [ms]
D_1(Ff)	165	165	6	0	100.0	96.5	0.3	3.7
D_1(Hf)	226	226	2	0	100.0	99.1	2.9	0.9
D_2(Ff)	285	284	2	1	99.6	99.3	3.4	1.3
D_2(Hf)	198	192	3	6	97.0	98.5	5.9	1.6
D_3(Ff)	243	238	2	5	97.9	99.2	0.5	7.1
D_3(Hf)	254	254	0	0	100.0	100.0	4.6	0.8
D_4(Ff)	361	361	0	0	100.0	100.0	0.2	2.3
D_4(Hf)	400	400	0	0	100.0	100.0	2.2	0.5
D_5(Ff)	326	326	0	0	100.0	100.0	2.5	0.8
D_5(Hf)	395	387	5	8	98.0	98.7	1.3	0.9
Total	2853	2833	20	20				
Mean					99.2	99.1	2.3	1.9

Table 5.6.: QRS detection results in the test dataset using the 6D-sECG method. (TP = true positives, FP = false positives, FN = false negatives, Se = sensitivity, +P = positive predictive value, Hf = head first, Ff = feet first, μ_{pd} = mean delay, σ_{pd} = jitter)

Record	# of R-peaks	TP	FP	FN	Se [%]	PPV [%]	μ_{pd} [ms]	σ_{pd} [ms]
D_6(Ff)	401	397	1	4	99.0	99.7	1.3	1.0
D_6(Hf)	416	413	0	3	99.3	100.0	0.4	1.4
D_7(Ff)	202	197	11	5	97.5	94.7	2.5	1.1
D_7(Hf)	163	157	5	6	96.3	96.9	1.1	1.1
D_8(Ff)	310	310	0	0	100.0	100.0	3.5	0.6
D_8(Hf)	421	419	2	2	99.5	99.5	3.6	0.9
D_9(Ff)	331	329	1	2	99.4	99.7	3.1	1.1
D_9(Hf)	360	357	1	3	99.2	99.7	6.1	8.5
Total	2604	2579	21	25				
Mean					98.8	98.8	2.7	2.0

5.5.3 ICA-based QRS detection

Separation of different signal sources

ICA was applied to the acquired ECG signals in order to separate ECG and MHD signal components. Four exemplary ICs from two different records are shown in Fig. 5.14. All the extracted components still contain mixtures of different signals but those depicted in Figs. 5.14a and 5.14c are dominated by the ECG ($\widehat{s}_{\mathrm{ECG}}$) signal components. Considering these examples it can be seen that it was not possible to extract an original source but only mixtures of different sources.

Identification of $\widehat{s}_{\mathrm{ECG}}$ based on the kurtosis

Table 5.7 summarises the kurtosis values obtained from the ICs of the training and test datasets. For each record, the kurtosis is given for the optimal IC $\widehat{s}_{\mathrm{opt}}$ and for the ICs with the highest and second highest kurtosis values, i. e. for K_{max1} and K_{max2}. As mentioned in Section 5.3.3, the IC with the maximum kurtosis should correspond to the kurtosis of IC $\widehat{s}_{\mathrm{opt}}$ since this IC would be identified as $\widehat{s}_{\mathrm{ECG}}$. As can be seen from Table 5.7, the optimal IC $\widehat{s}_{\mathrm{opt}}$ does not exhibit the maximum kurtosis value in all records. Figure 5.15 depicts an exemplary problem of using the kurtosis for the identification of $\widehat{s}_{\mathrm{ECG}}$. The IC shown in Fig. 5.15a is dominated by the QRS complex whereas the remaining signal is relatively flat. In comparison, Fig. 5.15b depicts an exemplary IC dominated by a 'peaky' MHD component which is located appropriately 200 ms after the QRS complex. The remaining signal is relatively flat as in $\widehat{s}_{\mathrm{ECG}}$ shown in Fig. 5.15a. This means that not only the QRS complex but also the MHD's signal components induced high kurtosis values, which lead to a misidentification of $\widehat{s}_{\mathrm{ECG}}$.

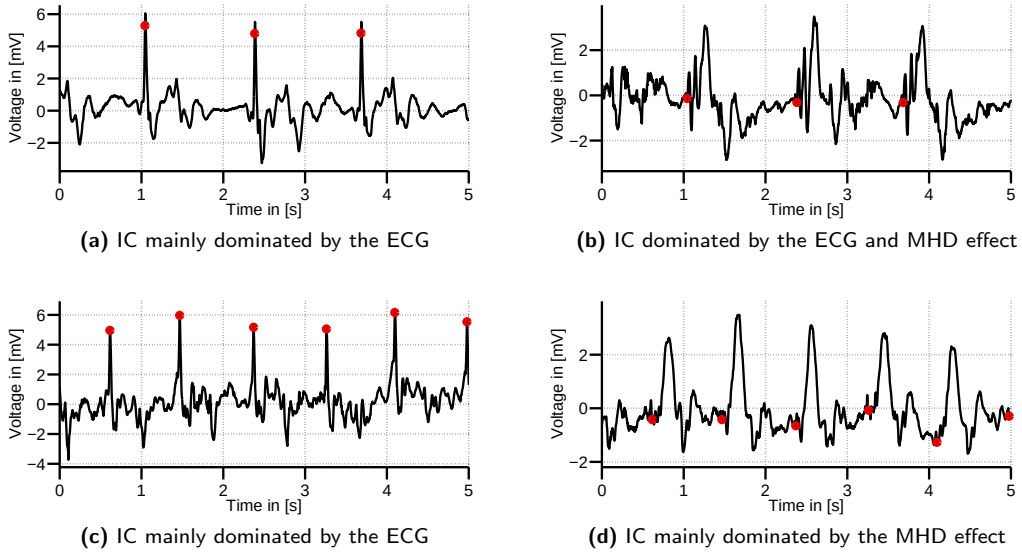

(a) IC mainly dominated by the ECG

(b) IC dominated by the ECG and MHD effect

(c) IC mainly dominated by the ECG

(d) IC mainly dominated by the MHD effect

Figure 5.14.: Different ICs obtained from records D_1(Ff) (a)-(b) and D_2(Ff) (c)-(d). The ICs $\widehat{s}_{\mathrm{ECG,k}}$ shown in (a) and (c) were desired for the QRS detection.

Table 5.7.: Kurtosis of the ICs in the training and test dataset. $K_{\widehat{s}_{\text{opt}}}$ is the kurtosis of the IC which give the optimal QRS detection results and which should be identified as $\widehat{s}_{\text{ECG}}$. K_{max1} and K_{max2} are the highest and second highest kurtosis values of the ICs in each record. Ideally, $K_{\widehat{s}_{\text{opt}}} = K_{max1}$ so that the IC identified as $\widehat{s}_{\text{ECG}}$ gives the best QRS detection results.

	Ff			Hf		
Record	$K_{\widehat{s}_{\text{opt}}}$	K_{max1}	K_{max2}	$K_{\widehat{s}_{\text{opt}}}$	K_{max1}	K_{max2}
D_1	14.1	14.1	6.7	13.5	13.5	11.5
D_2	9.1	9.1	7.4	11.5	16.2	11.5
D_3	5.3	20.2	16.9	21.3	21.3	9.6
D_4	3.8	9.4	9.1	5.6	8.7	8.6
D_5	9.2	9.2	6.4	5.9	14.2	13.5
D_6	7.6	19.8	7.6	4.9	7.9	6.2
D_7	7.8	13.7	8.2	3.2	7.7	7.5
D_8	12.8	12.8	6.6	12.6	12.6	11.5
D_9	10.7	10.7	7.6	8.1	10.6	8.1

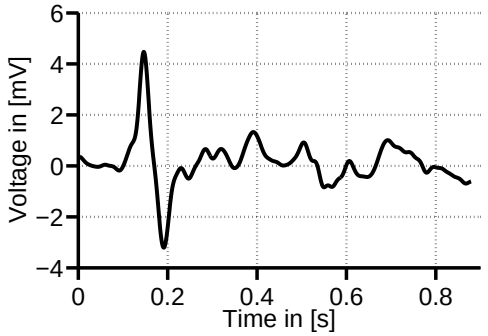

(a) Exemplary IC $\widehat{s}_{\text{ECG}}$ dominated by the QRS complex.

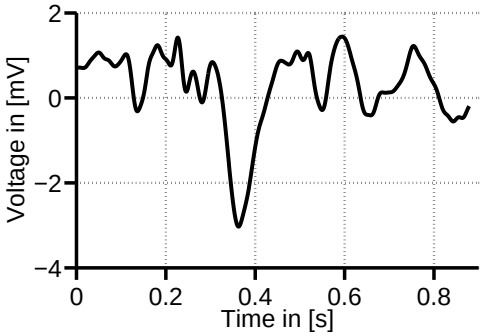

(b) Exemplary IC out of $\widehat{\mathbf{s}}_k$ dominated by the MHD effect.

Figure 5.15.: Two ICs estimated by ICA which are dominated by the QRS complex (a) and by the MHD effect (b). The 'peaky' behaviour of both ICs can cause high kurtosis values which could result in misidentification of $\widehat{s}_{\text{ECG}}$.

Identification of $\widehat{s}_{\text{ECG}}$ based on template matching

The template matching algorithm described in Section 5.3.3 identified the optimal IC $\widehat{s}_{\text{opt}}$ as $\widehat{s}_{\text{ECG}}$ in all training and test records.

Upslope preservation of the QRS complex in $\widehat{s}_{\text{ECG}}$

Figures 5.16(a)–(b) depict the IC $\widehat{s}_{\text{ECG}}$ and its first derivative. In Figure 5.16(c), the IC $\widehat{s}_{\text{out,ECG}}$ obtained from the ECG acquired outside the MR scanner is shown. Its first derivative is depicted in Fig. 5.16(d). For comparison, the raw ECG signal acquired inside the MR scanner and its first derivative are depicted in Figs. 5.16(e)–(f). Hence, when using the first derivative of the raw ECG signal (Fig. 5.16(f)) for QRS detection, several false positives would be detected.

Using the Lillifors test it was shown that the upslopes of the QRS complex measured in $\widehat{s}_{\text{ECG}}$ and $\widehat{s}_{\text{out,ECG}}$ exhibit a normal distribution [Lilliefors 67]. Figure 5.17 compares the mean and standard deviations of the QRS-upslopes in $\widehat{s}_{\text{ECG}}$ to those of the corresponding ICs $\widehat{s}_{\text{out,ECG}}$. The average absolute relative deviation of the slopes in $\widehat{s}_{\text{ECG}}$ compared to $\widehat{s}_{\text{out,ECG}}$ were 14.1 % in the training dataset and 16.7 % in the test dataset. The two-sample t-test revealed a significant change of the slope's mean value. A decreased slope of the QRS complex could potentially complicate their detection.

QRS detection, mean delay and jitter in $\widehat{s}_{\text{ECG,k}}$ using lead configurations LC1 and LC2

Detailed QRS detection results using the training and test datasets with lead configuration LC1 are given in Tables 5.8 and 5.9. For the test dataset, an average sensitivity Se of 99.2 % and an average positive predictivity $+P$ of 99.1 % were achieved. The average values of the mean propagation delay μ_{pd} and jitter σ_{pd} were 5.8 ms and 5.0 ms, respectively. An exemplary section of the contaminated ECG $\mathbf{x}_k$, the identified IC $\widehat{s}_{\text{ECG,k}}$ and correctly classified R-peaks in $\widehat{s}_{\text{ECG}}$ is depicted in Fig. 5.18. This example shows the improved signal quality, which enables a more reliable QRS detection.

Table 5.10 summarises the QRS detection results in $\widehat{s}_{\text{ECG,k}}$ using lead configurations LC2a–LC2g. Se and $+P$ slightly decreased when less precordial leads were used. Compared to lead configuration LC1, the mean propagation delay μ_{pd} and jitter σ_{pd} increased but are still within an acceptable limit for CMR (see Section 4.3.1). The impact of the precordial leads V2–V4 on the QRS detection quality was revealed by the results using configurations LC2e–LC2g. When only considering the 3-lead configurations, the best QRS detection results were obtained using lead V4 in addition to the two limb leads (LC2g). Without using any of the precordial leads as in configuration LC2h, Se and $+P$ decreased to 78.9 % and 65.8 %, respectively.

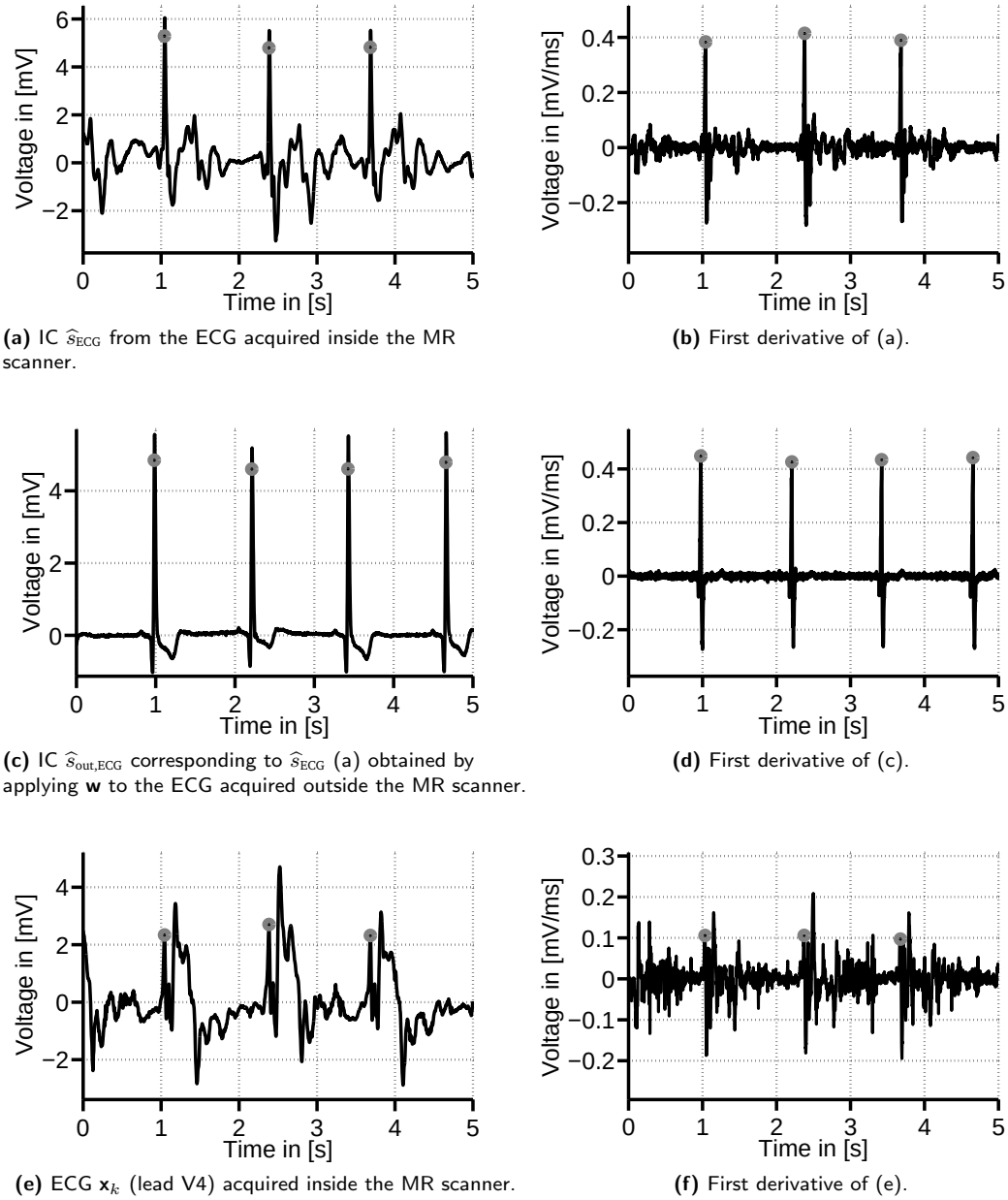

(a) IC $\widehat{s}_{\mathrm{ECG}}$ from the ECG acquired inside the MR scanner.

(b) First derivative of (a).

(c) IC $\widehat{s}_{\mathrm{out,ECG}}$ corresponding to $\widehat{s}_{\mathrm{ECG}}$ (a) obtained by applying $\mathbf{w}$ to the ECG acquired outside the MR scanner.

(d) First derivative of (c).

(e) ECG $\mathbf{x}_k$ (lead V4) acquired inside the MR scanner.

(f) First derivative of (e).

Figure 5.16.: Comparison of the IC $\widehat{s}_{\mathrm{ECG}}$ obtained from the ECG acquired inside the MR scanner (a) and its corresponding IC obtained from the ECG acquired outside the MR scanner (c). The first derivatives of each IC are shown in (b) and (d). The upslope of the QRS complex was preserved inside the MR scanner. Lead V4 of the raw ECG acquired inside the MR scanner and its first derivative are shown in (e) and (f) where several peaks occur in (f). The ECG depicted in (e) (together with the other leads) was used to estimate the IC $\widehat{s}_{\mathrm{ECG}}$ depicted in (a).

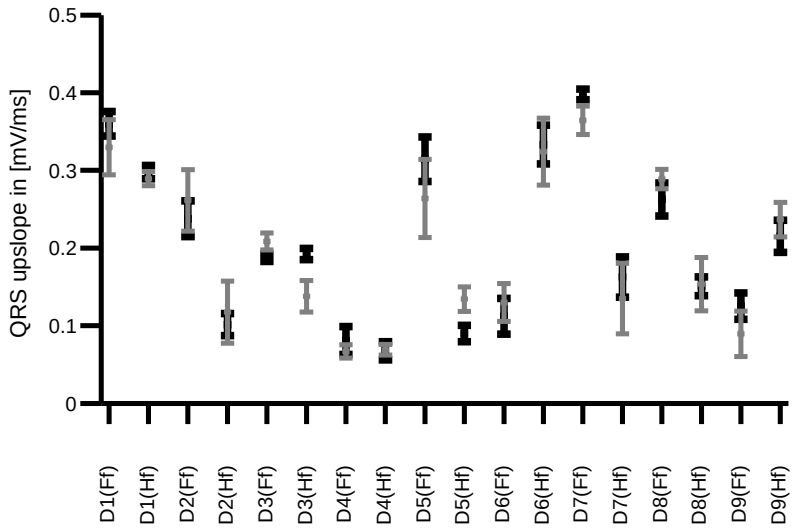

Figure 5.17.: Mean and standard deviations of the QRS-upslopes for the 18 records in $\widehat{s}_{\mathrm{ECG}}$ (black) and of the corresponding IC $\widehat{s}_{\mathrm{out,ECG}}$ obtained from the clean ECG (grey).

Table 5.8.: Detailed QRS detection results for the training records using the ICA-based gating method with lead configuration LC1 (TP = true positives, FP = false positives, FN = false negatives, Se = sensitivity, +P = positive predictive value, Hf = head first, Ff = feet first, μ_{pd}: mean detection delay, σ_{pd}: jitter).

Record	R-peaks	TP	FP	FN	Se [%]	$+P$ [%]	μ_{pd} [ms]	σ_{pd} [ms]
D_1(Ff)	165	165	0	0	100.0	100.0	4.1	4.4
D_1(Hf)	226	226	3	0	100.0	98.7	1.6	0.5
D_2(Ff)	285	284	1	1	99.6	99.6	1.1	3.3
D_2(Hf)	198	193	0	5	97.5	100.0	4.1	2.8
D_3(Ff)	243	239	1	4	98.4	99.6	6.4	10.6
D_3(Hf)	254	254	1	0	100.0	99.6	1.7	4.1
D_4(Ff)	361	361	0	0	100.0	100.0	0.5	18.2
D_4(Hf)	400	399	0	1	99.8	100.0	4.5	0.6
D_5(Ff)	326	326	1	0	100.0	99.7	8	11.3
D_5(Hf)	395	393	15	2	99.5	96.3	4.1	9.9
Total	2853	2840	22	13				
Mean					99.5	99.4	3.5	6.6

Table 5.9.: Detailed QRS detection results for test records using the ICA-based gating method with lead configuration LC1 (TP = true positives, FP = false positives, FN = false negatives, Se = sensitivity, +P = positive predictive value, Hf = head first, Ff = feet first, μ_{pd}: mean detection delay, σ_{pd}: jitter).

Record	R-peaks	TP	FP	FN	Se [%]	$+P$ [%]	μ_{pd} [ms]	σ_{pd} [ms]
D_6(Ff)	401	401	2	0	100.0	99.5	13.4	9.6
D_6(Hf)	416	410	1	6	98.6	99.8	2.2	4.8
D_7(Ff)	202	198	4	4	98.0	98.0	3.6	0.8
D_7(Hf)	163	163	4	0	100.0	97.6	1.9	7
D_8(Ff)	310	310	0	0	100.0	100.0	0.3	0.5
D_8(Hf)	421	416	2	5	98.8	99.5	1.1	0.7
D_9(Ff)	331	330	3	1	99.7	99.1	11.1	9.3
D_9(Hf)	360	353	1	7	98.1	99.7	12.9	7.6
Total	2604	2581	17	23				
Mean					99.2	99.1	5.8	5.0

Table 5.10.: Averaged QRS detection results for the training and test dataset using the ICA-based method with lead configurations LC2a-LC2g. Averaged results of lead configuration LC1 are shown for comparison (Se = sensitivity, +P = positive predictive value, μ_{pd}: mean detection delay, σ_{pd}: jitter).

Configuration				Training dataset				Test dataset			
LC	# leads	# PCs	Leads I, II +	Se [%]	$+P$ [%]	μ_{pd} [ms]	σ_{pd} [ms]	Se [%]	$+P$ [%]	μ_{pd} [ms]	σ_{pd} [ms]
1	8	8	V1-V6	99.5	99.4	3.5	6.6	99.2	99.1	5.8	5.0
2a	7	6	V2-V6	99.2	99.1	5.9	9.6	98.9	99	12.1	8.2
2b	6	6	V1-V4	99.2	99.3	4.5	5.6	99.4	98.3	11.7	13.3
2c	5	4	V2-V4	99.2	99.2	4.5	10.3	98.7	97	14.5	13.6
2d	4	4	V3-V4	98.9	98.5	4.5	6.9	98.3	97.7	16.9	13.4
2e	3	3	V2	94.7	94.5	12.2	10.5	95.2	93.7	12.1	15.9
2f	3	3	V3	97.3	92.8	11.7	8.5	96.5	92.4	14.5	9.7
2g	3	3	V4	98.2	97.3	6.3	11.5	98.5	97.2	13.9	12.2
2h	2	2	–	77.1	66.3	33.3	20.6	78.9	65.8	22.1	11.2

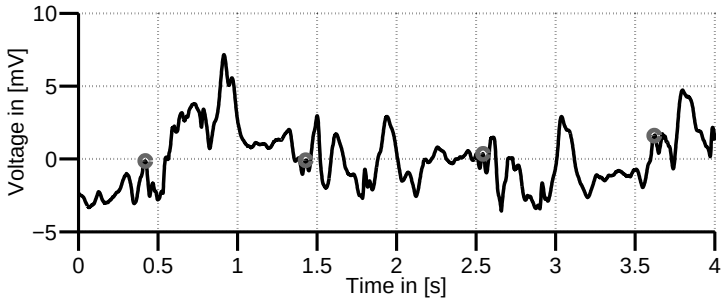

(a) Lead II of the ECG $\mathbf{x}_k$ recorded inside the 7 T MR scanner.

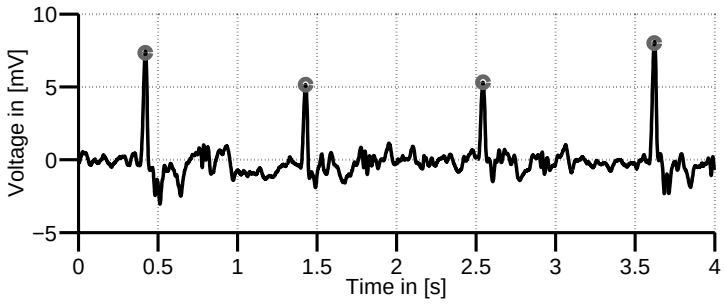

(b) Estimated IC $\widehat{s}_{\mathrm{ECG,k}}$.

Figure 5.18.: (a) ECG $\mathbf{x}_k$ acquired inside the 7 T scanner and (b) the estimated and identified IC $\widehat{s}_{\mathrm{ECG,k}}$. Grey dots mark the manual R-peak annotations (a) and the R-peak position detected by the algorithm (b).

Long term stability of the demixing matrix

The application of the two demixing matrices $\mathbf{W}_{\mathrm{D_5(Ff)}}$ and $\mathbf{W}_{\mathrm{D_5(Hf)}}$ (obtained from two previously recorded 7 T Ff and Hf ECG records of the same subject) lead to the following QRS detection results in the two corresponding ECG records from the same volunteer:

- $\mathbf{W}_{\mathrm{D_5(Ff)}} \rightarrow \mathrm{D_9(Ff)}$: $Se = 99.7\,\%$, $+P = 99.6\,\%$
- $\mathbf{W}_{\mathrm{D_5(Hf)}} \rightarrow \mathrm{D_9(Hf)}$: $Se = 99.1\,\%$, $+P = 99.7\,\%$

The application of the two demixing matrices $\mathbf{W}_{\mathrm{3T}}$ (obtained from two previously recorded 3 T Ff and Hf ECG records) lead to the following QRS detection results in the two corresponding 7 T ECG records from the same volunteer:

- $\mathbf{W}_{\mathrm{3T}}\mathrm{(Ff)} \rightarrow \mathrm{D_9(Ff)}$: $Se = 98.3\,\%$, $+P = 99.1\,\%$
- $\mathbf{W}_{\mathrm{3T}}\mathrm{(Hf)} \rightarrow \mathrm{D_9(Hf)}$: $Se = 97.9\,\%$, $+P = 98.7\,\%$

Figure 5.19 depicts the effect of applying the two different demixing vectors $\mathbf{w}$ and $\mathbf{w}_{\mathrm{3T}}$ to the same 7 T ECG record.

5.5.4 Other QRS detection methods

QRS detection results achieved by methods M1-M4 are summarised in table 5.2. From these alternative approaches, method M2 gave the best average results (in terms of Se and $+P$).

The precordial ECG lead V4 was used in method (M1) in all records because this ECG lead yielded the best QRS detection in terms of the average Se and $+P$. In general, the best QRS detection was achieved using the precordial leads V3-V5 since these leads were less affected by the MHD effect (see Section 3.3.2).

In method M2, the best results were achieved using the single VCG lead x in all records. The obtained results were slightly better than the results obtained by method M1 using the single ECG lead. Method M3 also utilised the VCG leads but applied an ICA in order to separate ECG and MHD signal components. However, this procedure had no positive influence on the achieved results. Instead, it decreased the QRS detection quality when compared to method M2.

An exemplary signal, which was obtained by method M4 is depicted in Fig. 5.20a. The signal depcited in Fig. 5.20b was estimated using the 6D-sECG method proposed in Section 5.2.2. Both methods relied on the information or signal properties of the six precordial leads. However, the 3D-QRS method (M4) caused several peaks of high magnitude (Fig. 5.20a), which did not necessarily correspond to R-peaks. This complicated the detection based on a relative threshold since the amplitude ratio between R-peak related peaks and other peaks was too low.

QRS detection based on the higher order central moments (method M5) showed a very high specificity Se (100 %) but a low $+P$ value in both, the training and test datasets. Although this method was successfully used with 3 T records [Schmidt 14], similar results could not be reproduced when applied to 7 T recordings.

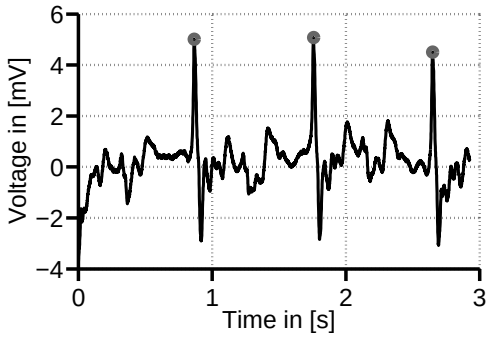

(a) Demixing of the 7 T record $\mathrm{D}_9(\mathrm{Ff})$ using the corresponding demixing matrix $\mathbf{W}_{\mathrm{D}_9(\mathrm{Ff})}$.

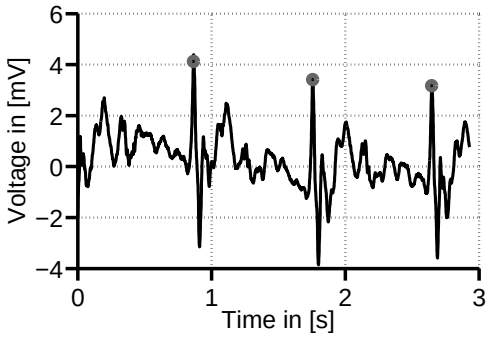

(b) Demixing of a 7 T record $\mathrm{D}_9(\mathrm{Ff})$ using the demixing matrix $\mathbf{W}_{\mathrm{D}_5(\mathrm{Ff})}$.

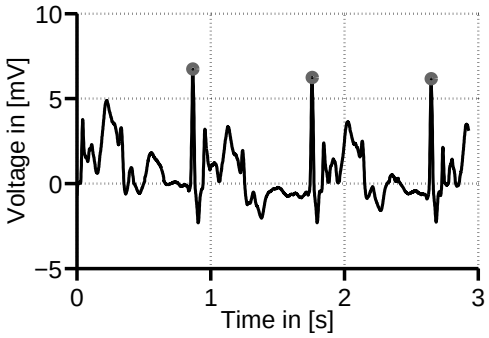

(c) Demixing of a 7 T record $\mathrm{D}_9(\mathrm{Ff})$ using the demixing matrix $\mathbf{w}_{3\mathrm{T}}$.

Figure 5.19.: Estimation of the IC $\widehat{s}_{\mathrm{ECG}}$ from the 7 T ECG record $\mathrm{D}_9(\mathrm{Ff})$ using the demixing matrix $\mathbf{W}_{\mathrm{D}_9(\mathrm{Ff})}$ (a). $\mathbf{W}_{\mathrm{D}_9(\mathrm{Ff})}$ was obtained from record $\mathrm{D}_9(\mathrm{Ff})$. To show the long term stability of the demixing matrices, the previously acquired record $\mathrm{D}_5(\mathrm{Ff})$ was used to estimate the demixing matrix $\mathbf{W}_{\mathrm{D}_5(\mathrm{Ff})}$. $\mathbf{W}_{\mathrm{D}_5(\mathrm{Ff})}$ was then applied $\mathrm{D}_9(\mathrm{Ff})$ (b). The records $\mathrm{D}_5(\mathrm{Ff})$ and $\mathrm{D}_9(\mathrm{Ff})$ were acquired from the same subject with distance. Dataset $\mathrm{D}_5(\mathrm{Ff})$ was acquired one year prior to $\mathrm{D}_9(\mathrm{Ff})$. Another record of the same subject acquired at 3 T (one year prior to $\mathrm{D}_9(\mathrm{Ff})$) was utilised for estimating the demixing matrix $\mathbf{w}_{3\mathrm{T}}$. Again, $\mathbf{w}_{3\mathrm{T}}$ was applied to the 7 T record $\mathrm{D}_9(\mathrm{Ff})$. The results show that the demixing matrix of one subject is stable over a long time (b,c) and that it is possible to use a demixing matrix obtained at a different magnetic field strength (c).

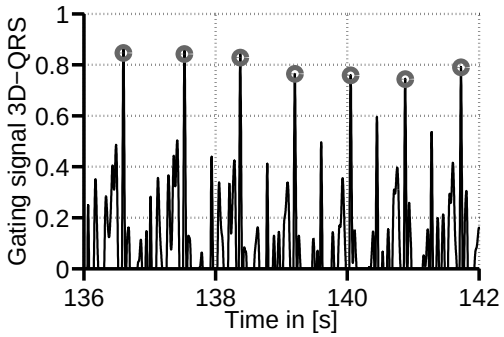

(a) Signal used for QRS detection obtained by the 3D-QRS method (M4).

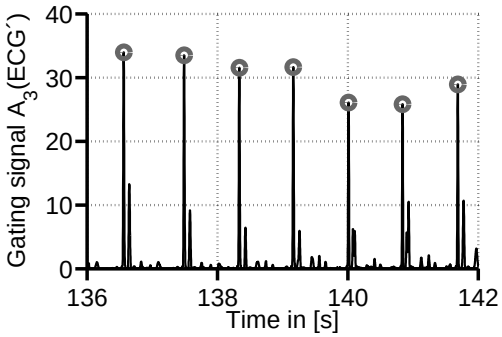

(b) Signal used for QRS detection obtained by the 6D-sECG method.

Figure 5.20.: Comparison of the gating signals obtained by the 3D-QRS method [Tse 11a] (a) and by the 6D-sECG method (b) proposed in this work. Several peaks of high magnitude complicate a proper threshold-based QRS detection. Grey dots mark the manual annotations of the underlying QRS complexes.

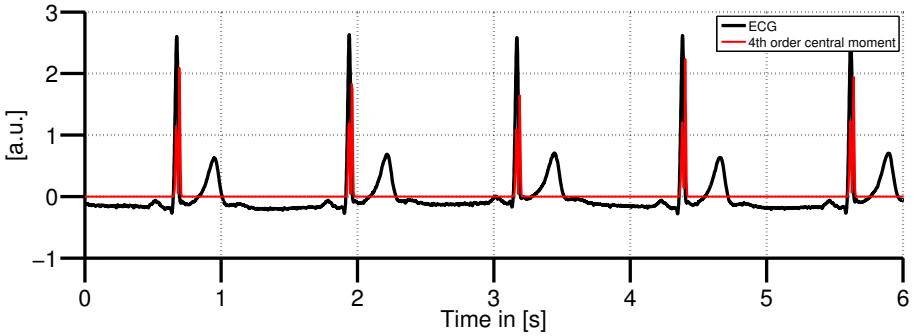

(a) ECG outside MRI and 4th order central moment.

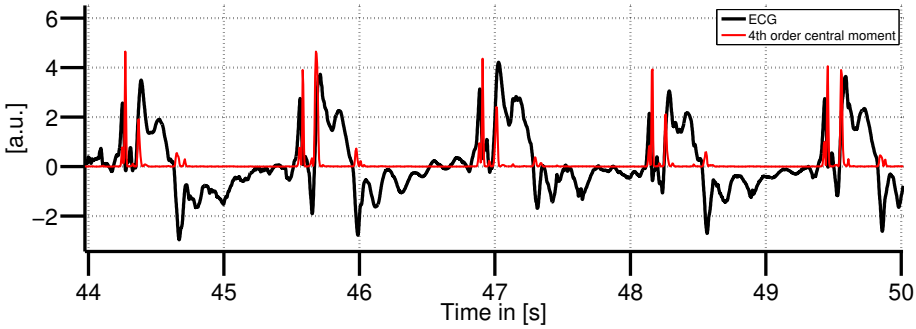

(b) ECG inside MRI (7 T) and 4th order central moment.

Figure 5.21.: Signals used for QRS detection obtained by the 4th order central moments method and corresponding ECG signals (lead V4) outside (a) and inside (b) the 7 T scanner. For the ECG outside the MRI scanner, the central moments show one peak caused by the upslope and one by the downslope of the QRS complex. Other ECG signal components are suppressed. Inside the MRI scanner (b), additional larger peaks were caused by the MHD effect.

5.6 Discussion

5.6.1 Vector-based QRS detection

State-of-the-art VCG-based QRS detection

As it was shown in Fig. 3.19 (p. 47), the VCGs obtained from the 3 T and from the 7 T records were affected by the MHD effect. Besides the more complex patterns of the MHD effect in the 7 T VCGs, the angle and amplitude of the R-peak vector were altered inside the MR scanner when compared to the VCG recorded outside the MR scanner. These alterations are considered as one of the main reasons for the error proneness of the VCG-based gating method in 7 T CMR.

Based on the measurement data and the observations of the altered R-peak vectors, a modified approach of the well established VCG-based gating method was introduced in Section 5.2.1. A new reference vector was defined using the ECG signal acquired inside the MR scanner. Based on this modification, the $+P$ was improved by 27.9 %. However, the definition of the new reference vector requires an initial manual annotation of the R-peaks inside the MR scanner, which is a major drawback of this method and may limit its clinical applicability. One could cope with this limitation by defining a reference vector near the entrance of the MR scanner's bore where the magnetic field strength does

not reach its full magnitude. This could give a better estimation of the reference vector but could also enable a better QRS detection during the initialisation stage. However, this new reference would still be altered by the additional MHD effect in the centre of the scanner. The ICA-based QRS detection proposed in Section 5.3 could overcome this limitation.

Another issue are cardiac arrhythmias[4]. Cardiac arrhythmias can cause morphological alterations of the QRS complex and can change the heart rhythm. This in turn can alter the spatial position of the R-peak in the vector space. An example for such an alteration during an arrhythmia is depicted in Fig. 5.22. While a QRS-detector relying on the ECG trace detects this QRS complex, it is obvious that the VCG-based method would miss this cardiac activity due to the large deviation compared to the reference vector $\mathbf{r}$. Although this ECG was acquired outside the MR scanner, a similar detection behaviour can be expected for an ECG acquired inside the MR scanner. For gating applications it is (usually) preferred to skip image acquisition during non-regular heart beat activity.

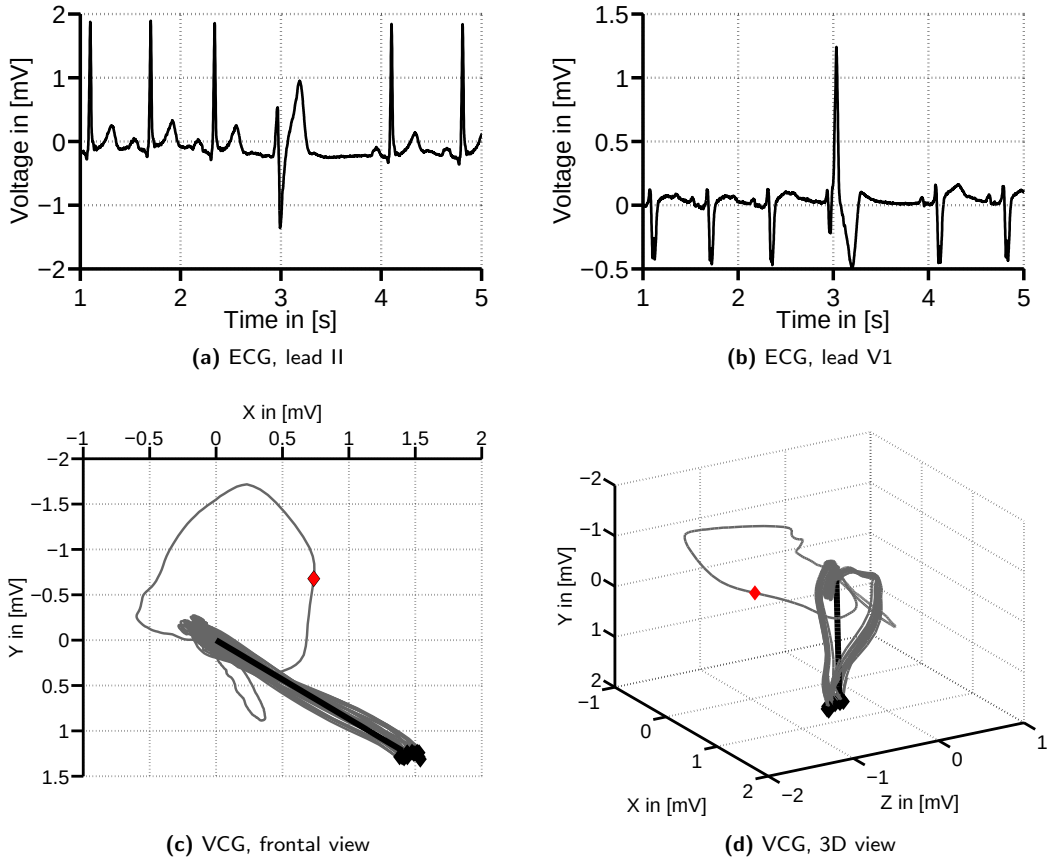

(a) ECG, lead II **(b)** ECG, lead V1

(c) VCG, frontal view **(d)** VCG, 3D view

Figure 5.22.: ECG leads II and V1 (a,b) and the corresponding VCG in frontal and 3D view (c,d) during arrhythmia (ventricular extrasystole). The arrhythmias is occurring at $t \approx 3\,\mathrm{s}$. The single separated loop is caused by the arrhythmia. Black dots mark the normal R-peak position. The red dots mark the position of the R-peak during an arrhythmia. Due to the detection principle of the VCG-based method, the arrhythmic beat would be missed.

[4]Due to the lack of appropriate ECG data recorded at 7 T, this issue was not further investigated in this thesis.

Higher dimensional vector space

Based on the findings made in Section 3.3.3, which showed that the VCG is severely distorted by the MHD effect at 7 T, a new spatial representation of the ECG signal was presented. This spatial representation is based on the six precordial ECG leads V1-V6. It was shown that the signal quality of those leads is superior when compared to those of the VCG leads obtained by the inverse Dower transform. However, as it was shown in Fig. 5.3, not all precordial lead combinations give a proper discrimination between the QRS complex and the MHD effect. Taking the first derivative of the 6D-VCG enhances the separability of the QRS complex and of the MHD effect. Hence, the first derivative of the ECG's precordial leads was used to build the 6D vector space.

General drawbacks

All vector-based QRS detection methods require a reference vector. This reference vector is defined from an QRS complex detected in a pre-processing step. Whereas this is a trivial task for the reference vector defined outside the MR scanner, it limits the application of those methods utilising the reference vector defined inside the MR scanner. Hence, without an additional algorithm for the initial detection of the QRS complex inside the MR scanner, the vector-based methods are not suitable for the usage in a clinical setting. This limitation could be overcome by using the ICA-based QRS detector for the definition of the reference vector.

5.6.2 ICA-based QRS detection

A new method for QRS detection in 7 T MRI based on ICA was proposed in this chapter. ICA was applied to 7 T ECG records in order to separate ECG, MHD and other signal components. 12-lead ECGs were used for these experiments whereas the 4 linear combinations of lead I and II were excluded from the analysis[5]. Hence, a maximum of 8 leads and their 8 PCs were used for the estimation of the ICs $\widehat{\mathbf{s}}_k$. A general problem of ICA is that the order of the estimated source signals $\widehat{\mathbf{s}}_k$ is unknown, i. e. it is not known which source in $\widehat{\mathbf{s}}_k$ corresponds to the ECG, MHD, mixtures of both or other signal sources. Additionally, there were more sources $\mathbf{s}_k$ than measurements or observations $\mathbf{x}_k$. This can be explained by the spatial origin and distribution of the ECG and MHD signals. The different parts of the atria and the ventricles can be seen as different sources contributing to the cardiac (ECG) signal. All blood vessels and even small segments of them, e. g. the ascending and descending aorta or the aortic arch can be considered as separate sources contributing to the MHD signals. The crucial task was to automatically identify one component $\widehat{s}_{\text{ECG}}$ from the set of estimated ICs $\widehat{\mathbf{s}}_k$ where $\widehat{s}_{\text{ECG}}$ was the IC mainly dominated by the QRS complex or the R-peak. It was desired to perform this identification automatically since a manual selection of $\widehat{s}_{\text{ECG}}$ limits the practical value of the proposed method. Two different methods were investigated to achieve this aim.

The automatic identification of $\widehat{s}_{\text{ECG}}$ based on the maximum kurtosis of the ICs was shown to be not reliable and should not be used in a practical application of this method. In several cases, the optimal IC $\widehat{s}_{\text{opt}}$, which gave the best QRS detection results did not have the maximum kurtosis. A non-optimal selection for $\widehat{s}_{\text{ECG}}$ would be made using the kurtosis as an identification criterion. It was shown that the strong MHD effect occurring in some ICs exhibits a 'peaky' behaviour. This problem was depicted in Figure 5.15. Hence, the identification of $\widehat{s}_{\text{ECG}}$ based on the higher order statistics was not considered

[5] These are leads III, aVR, aVL and aVF.

since it was not applicable to all records.

The problems occurring in the kurtosis-based identification method were overcome by the template-based method. This method required a 30 s long trace of the ECG recorded outside the MR scanner. Based on a 'demixing' of this clean ECG as described in Section 5.3.3, QRS templates were generated and compared to the corresponding ICs $\widehat{\mathbf{s}}_k$. In all training and test records, the maximum correlation value corresponded to the optimal IC $\widehat{s}_{\text{opt}}$. Hence, this method was used for the identification of $\widehat{s}_{\text{ECG}}$.

Following the automated identification of $\widehat{s}_{\text{ECG}}$, the initially estimated demixing matrix $\mathbf{W}$ was reduced to a vector $\mathbf{w}$. This demixing vector was applied to the measurement signal $\mathbf{x}_k$ at time instants k. As described by Eq. 5.18, p. 97 this corresponds to a linear combination of all leads in $\mathbf{x}_k$ at time k. Due to this computationally simple and efficient calculation, the sample $\widehat{s}_{\text{ECG,k}}$ at time instant k could be estimated in real-time. It was shown that the demixing vector $\mathbf{w}$ is stable over a long time (1 year) and is even robust against the non-exact placement of the electrodes[6]. Additionally, a demixing matrix obtained from a 3 T measurement could be applied to a 7 T record (from the same subject). This means that it is possible to estimate $\mathbf{W}$ at the entrance of the MR scanner's bore where the magnitude of the static magnetic field and the resulting MHD effect are lower. Although it did not occur with the records used in this thesis, the properties of the MHD effect at 7 T could eventually cause a false identification of $\widehat{s}_{\text{ECG}}$. This is less likely at a lower magnetic field strength (as at the entrance of the bore). The computation of the demixing matrix was required only once per subject and position (head and feet first position). This fact and the low computational cost of the signal demixing using the vector $\mathbf{w}$ make the ICA-based method applicable in clinical scenarios.

The ICA-based method achieved the best QRS detection results – it outperformed the different vector-based methods. In a first step, ICA was applied to the complete ECG records (i. e, to 8 leads and 8 PCs). Following this, the number of the ECG leads and of the PCs was reduced. This was done to investigate on how certain leads affect the R-peak detection quality. It was found that the precordial leads generally have a positive effect on the R-peak detection quality. By only using lead V4 together with limb leads I and II, Se and $+P$ approximately decreased by 2 % in the training and test dataset when compared to the best result (lead configuration LC1). This is an important fact for the future development of proper MRI conditional ECG hardware since it was shown that the combination of the standard limb leads I and II and one additional precordial lead strongly improved the results. Nowadays, ECG devices with a clinical approval for the usage in an MRI environment are limited to two or three leads and do not include precordial leads. By adding at least one additional precordial lead to the existing hardware, the quality of the ECG signals and hence, the quality of triggering CMR sequences at a high magnetic field strengths can be improved.

The following points were achieved using the ICA-based method:

1. Extraction of different signal components $\widehat{\mathbf{s}}_k$.
2. The $\widehat{s}_{\text{ECG}}$ component in $\widehat{\mathbf{s}}_k$ is dominated by the R-peak or QRS complex.
3. Automatic identification of $\widehat{s}_{\text{ECG}}$ based on template matching.
4. Reduction of the demixing matrix $\mathbf{W}$ to a demixing vector $\mathbf{w}$.
5. The robustness and long term stability of $\mathbf{W}$ (or $\mathbf{w}$) were shown.
6. The demixing vector $\mathbf{w}$ only needs to be estimated once per subject and direction (Ff or Hf).
7. Extraction of $\widehat{s}_{\text{ECG}}$ can be performed in real-time using $\mathbf{w}$.
8. Superior quality of the precordial leads was shown.

[6] Non-exact means that the electrodes were not placed in exactly the same positions in the different experiments.

9. Improved R-peak detection with only one additional precordial is possible.

In summary, the proposed fully automated method based on ICA and a custom developed template matching approach enables a reliable detection of the ECG's QRS complexes at 7 T. Due to the robustness of the demixing vector **w**, ICA only has to be applied once per volunteer and the IC dominated by the ECG signal ($\widehat{s}_{\text{ECG}}$) can be estimated in real-time. Hence, the proposed method can also be used as a pre-processing step to estimate the reference vector for the modified VCG-based approach and for the 6D-sECG method.

5.6.3 Other QRS detection methods

Several other methods were used for the QRS detection in the 7 T ECG records. Again, the results revealed the superior quality of the precordial leads. The standard QRS detection algorithm [Pan 85, Clifford 02] gave the best (on average) results using lead V4. Using the VCG or the ICA of the VCG could not improve the results. The 3D-QRS method, which was initially proposed for the QRS detection at 3 T was shown to be prone to errors when applied to the 7 T ECG records.

QRS detection using method M5 was also successfully used with 3 T ECG records. The fact that this method had low $+P$ values at 7 T can be explained by the high slope of the MHD signals. The 4th central moment can exhibit high values at the slopes of the MHD signal. Hence, parts of the MHD signal are falsely identified as QRS complexes.

5.6.4 ECG recording hardware

Typically, the positioning of the ECG electrodes depends on the manufacturer of the ECG device. Those devices are typically designed and developed for MRI purposes. Dedicated hardware including wiring, circuits and electrode enables a safe operation of these devices in the hostile environment of an MR scanner. Usually, these devices use two or three different ECG leads to provided a signal for gating and heart rate monitoring.

In this work, the number of ECG leads was extended by using a commercial 12-lead ECG device, which is usually used in diagnostic cardiology. Such devices are not designed for a usage inside the MR scanner. This is one limitation for the methods presented in this chapter since all of them rely on one or more precordial ECG leads. However, the MRI research community as well as commercial manufacturers are more and more interested to have such devices within the MRI environment [Tse 10a, Tse 14]. The interest in an MR compatible 12-lead ECG is mainly driven from the need for a diagnostic ECG as it used in heart catheter labs. Hence, this current hardware limitation might be overcome in the future when such hardware is commercially available. For the acquisition of the 12-lead ECGs used in this work, the standard electrode placement scheme was used (see Section 3.30a). Since the placement of the ECG electrodes affects the amplitudes and morphologies of the ECG and MHD signals, further studies are required for an optimal placement of the 12-lead ECG during MRI. However, in such an optimisation, the diagnostic ECG which is investigated in the next chapter should be considered since this usually requires a standard scheme for the placement of the electrodes.

5.7 Summary

The aim of this chapter was to develop reliable QRS detection methods for ECG signals, which were acquired in a 7 T MRI scanner. Whereas QRS detection is well established for clinical MR scanners with typical magnetic field strengths of up to 3 T, QRS detection can be hampered in 7 T MRI. For the experiments described in this chapter, several ECG records were recorded from different subjects inside a 7 T MRI scanner. This enabled a realistic analysis of the underlying problems and allowed the development of methods, which are applicable in real CMR scenarios.

This chapter started with an improvement of the state-of-the-art VCG-based gating method (Section 5.2). Based on the analysis of the standard VCG-based method made in Section 3.3.3, the reference vector **r**, which is usually used for R-peak detection in this method was modified. With this modification, the positive predictivity $+P$ was increased by 27.9 % for the training dataset and by 19.7 % for the test dataset when compared to the standard configuration. A further modification of this method utilised the superior signal quality of the precordial ECG leads V1-V6. Instead of using the 3D VCG, a new 6D vector space was composed from the first derivatives of the six precordial leads (6D-sECG). Similar to the VCG-based method, a reference vector was defined for the detection of the R-peaks. Using the 6D-sECG method, a high QRS detection quality was achieved (Se and $+P \geq 98\,\%$). However, the modified reference vector used in both methods requires a manual annotation of the R-peaks which can be challenging due to the MHD contaminations and might be impractical for the clinical application of this method. In order to avoid this impractical and risky pre-processing step, another QRS detection method was proposed.

The method for QRS detection utilising an ICA-based algorithm can be used without any manual user input. ICA is used for the decomposition of a 12-lead ECG signal into a set of source or basis functions. Although ICA was not able to fully separate the ECG, MHD and other signal and noise sources in the 7 T ECG records, it was able to extract one IC or source signal $\widehat{s}_{\text{ECG}}$ in each record, which was dominated by the R-peaks. Two different methods for an automated identification of $\widehat{s}_{\text{ECG}}$ were investigated whereas the technique based on a template matching outperformed the method based on the higher order statistics (kurtosis). Using the template matching technique, $\widehat{s}_{\text{ECG}}$ was correctly identified in all training and test records. This is an important fact since an automated identification of the desired source signal is an essential step with the application of ICA. R-peak detection in $\widehat{s}_{\text{ECG}}$ was performed using a standard algorithm [Pan 85, Clifford 02]. The method outperforms the state-of-the-art VCG-based gating method. Since the estimation of the demixing matrix **W** and the identification of $\widehat{s}_{\text{ECG}}$ only has to be performed once per subject at the beginning of the measurement, $\widehat{s}_{\text{ECG}}$ could be estimated in real-time. Based on practical experiments it was shown that the demixing matrix **W** is robust against electrode placement, stable over a long time and can even be estimated at a different (lower) magnetic field strength.

The two new QRS detection methods proposed in Sections 5.2.2 and 5.3 were compared to several other techniques. These methods evaluated in Section 5.4 included conventional R-peak detection in the ECG or VCG (methods M1 and M2), an experimental application of the ICA technique to the VCG instead of the ECG (method M3), a method using a 3D template of the QRS complex (method M4) and the 4th order central moment (method M5). From these methods, the ECG-based gating method (M1) using a single precordial lead (V4) gave the best results in terms of Se and $+P$. This fact again showed that the MHD effect had a lower impact on the precordial leads. Without further investigation, this finding could be helpful for future experiments regarding the placement of the electrodes or for the

development of MR safe and compatible ECG hardware with (at least) one precordial lead in addition to the standard limb leads.

6

Accessing diagnostic information from the ECG during MRI

6.1 Overview

Several applications for a diagnostic ECG during MRI were discussed in Section 2.3. It was shown in Section 3.3 that the MHD effect limits the diagnostic value of the ECG signal. The aim of this chapter is to improve the diagnostic quality of ECG signals acquired during MRI. Particular focus was put on the ST-segment, T-wave and QT-interval. These segments of the ECG contain important diagnostic information, which can be required during MR-guided interventions such as EP procedures or for patients under anaesthesia (see Section 2.1.4). This chapter investigates and compares different methods to access the diagnostic information of the ECG.

In Section 6.2, the Wiener filter is applied to single ECG leads in order to suppress the MHD effect. PQRST templates are used to compute the Wiener filter coefficients. In Section 6.3, ICA is applied to simulated and real ECG records. ICA was already used in Chapter 5 where it was applied to ECGs acquired at 7 T for gating purposes. The aim was to extract only one IC dominated by the R-peak. This chapter investigates if ICA can be used to obtain additional diagnostic information for a 3 T ECG signal.

Section 6.4 describes how an extended Kalman filter (EKF) is applied to filter the MHD signal from different ECGs. The ECG and MHD signals are modelled using a synthetic signal generator based on a Gaussian model (see Section 4.2.2). The developed methods and algorithms are evaluated quantitatively and qualitatively using the simulated and real ECG records described in Sections 4.1.2 and 4.2 and the metrics described in Section 4.3.

6.2 MHD suppression by means of the Wiener filter

6.2.1 Theory of the Wiener filter

Overview

Andrej Kolmogorv (1941) and Norbert Wiener (1949) initially formulated the least square error (LSE), where the first one was based on time-domain analysis and the latter one on frequency domain analysis[1] [Vaseghi 09]. The theory of the LSE filters forms the foundation for linear adaptive, data dependent filters. Therefore, the filter coefficients are calculated to minimise the average squared distance between a desired, known target signal and the filter's output. The basic formulation of the LSE filter theory, for which the filter coefficients are not updated periodically, assumes stationary processes. For a strict-sense stationary process, all distributions and statistics are required to be time-invariant. In contrast, a process is said to be wide-sense stationary if its mean and autocorrelation functions are time invariant [Vaseghi 09]. By recalculating the coefficients over time for a block of input signal samples, the filter coeffients are updated to the average of the signal characteristics within this block. Wiener filters can be designed as finite impulse response (FIR) or as infinite impulse response (IIR) filters. FIR filters are relatively simple to compute, inherently stable and more practical. However, the main drawback of this type of filters compared to IIR filters is that they may need a large number of coefficients to approximate the desired response.

Derivation of the Wiener filter

The relation between the filter input x and its output $\widehat{y}(m)$ is given by

$$\begin{aligned} \widehat{y}(m) &= \sum_{k=0}^{P-1} w_k x(m-k) \\ &= \mathbf{w}^T \mathbf{x} \end{aligned} \tag{6.1}$$

where $\mathbf{w}^T = [w_0, w_1, ..., w_{P-1}]$ is the vector representing the Wiener filter coefficients, $\mathbf{x}(m)^T = [x(m), x(m-1), ..., x(M-P-1)]$ are the input signal samples and $\widehat{y}(m)$ are the output signal samples with m as the discrete time index. Equation 6.1 expresses the filtering process in two equivalent representations: as a convolutional (upper equation) sum and as an inner product (lower equation). The error of the Wiener filter is defined as the residual between the estimated filter output $\widehat{y}(m)$ and the desired signal $y(m)$

$$\begin{aligned} e(m) &= y(m) - \widehat{y}(m) \\ &= y(m) - \mathbf{w}^T \mathbf{x}. \end{aligned} \tag{6.2}$$

Hence, the error of the filter, $e(m)$, depends on the filter coefficients $\mathbf{w}$ (for a given input and a desired signal). In the sense of minimising the mean squared error, the Wiener filter is the best filter [Vaseghi 09].

[1] For the sake of simplicity, both filters are referred to as Wiener filter.

In a matrix notation for a number of N input samples, Eq. 6.2 can be written as

$$\begin{pmatrix} e(0) \\ e(1) \\ e(2) \\ \vdots \\ e(N-1) \end{pmatrix} = \begin{pmatrix} y(0) \\ y(1) \\ y(2) \\ \vdots \\ y(N-1) \end{pmatrix} - \begin{pmatrix} x(0) & x(-1) & \cdots & x(1-P) \\ x(-1) & x(-2) & \cdots & x(2-P) \\ x(-2) & x(-3) & \cdots & x(3-P) \\ \vdots & \vdots & \ddots & \vdots \\ x(N-1) & x(N-2) & \cdots & x(N-P) \end{pmatrix} \begin{pmatrix} w_0 \\ w_1 \\ \vdots \\ w_{P-1} \end{pmatrix}, \tag{6.3}$$

which can be rewritten as

$$\mathbf{e} = \mathbf{y} - \mathbf{X}\mathbf{w}. \tag{6.4}$$

Equation 6.3 depends on the number of signal samples N, which corresponds to the number of equations in Eq. 6.3. If the number of signal samples is the same as the number of coefficients, so $N = P$, then the matrix is square. Hence, there are as many equations as unknowns, which leads to a theoretically unique filter solution $\mathbf{w}$ (if the matrix $\mathbf{R}_{xx}$ can be inverted, see below) with an zero estimation error $\mathbf{e} = \mathbf{0}$ such that $\widehat{\mathbf{y}} = \mathbf{X}\mathbf{w} = \mathbf{y}$.

If $N < P$, the matrix is *under-determined* since there are more unknowns than equations. This case leads to an *infinite number of solutions* with zero estimation error. In most practical cases, the number of signal samples is larger than the number of filter coefficients. For this case where $N > P$, Eq. 6.3 is *over-determined* and has a unique solution, usually with a non-zero error. This is the case if the linear system $\mathbf{y} = \mathbf{X}\mathbf{w}$ is consistent and if the rank of the matrix $\mathbf{X}$ is equal to the number of unknowns, i. e. $\text{rank}(\mathbf{X}) = P$ (Rouché-Frobenius theorem) [Zapatero 14]. For an overdetermined system, the filter coefficients are computed in such a way that an average error cost function, e. g. the least mean square error (LSE) or the absolute error, is minimised. In the Wiener filter theory, the LSE is the objective criterion between the filter input and its output. The LSE criterion leads to a linear and closed form solution for FIR filters. [Vaseghi 09]

The Wiener filter coefficients are obtained by minimising $\mathbb{E}[e^2(m)]$ with respect to the filter coefficients $\mathbf{w}$. According the Eq. 6.2, the mean square estimation error is given by

$$\begin{aligned} \mathbb{E}[e^2(m)] &= \mathbb{E}\left[\left(y(m) - \mathbf{w}^T\mathbf{x}\right)^2\right] \\ &= \mathbb{E}[y^2(m)] - 2\mathbf{w}^T\mathbb{E}[\mathbf{x}y(m)] + \mathbf{w}^T\mathbb{E}[\mathbf{x}\mathbf{x}^T]\mathbf{w} \\ &= r_{yy}(0) - 2\mathbf{w}^T\mathbf{r}_{xy} + \mathbf{w}^T\mathbf{R}_{xx}\mathbf{w} \end{aligned} \tag{6.5}$$

where $\mathbf{R}_{xx}$ is the autocorrelation matrix of the input samples and $\mathbf{r}_{xy} = \mathbb{E}\left[x(m)y(m)\right]$ is the cross-correlation vector of the input and the desired signal.

From Eq. 6.5 it can be seen that the mean square error for an FIR filter is a quadratic function of the filter coefficient $\mathbf{w}$ and has a single minimum point as shown in Fig. 6.1. The LSE corresponds to the minimum error power - the mean square error surface has a zero gradient at this point. The gradient

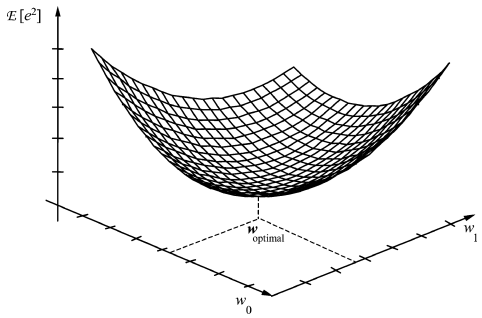

Figure 6.1.: Mean square error surface for a FIR filter with two filter coefficients [Vaseghi 09, p.176].

of Eq. 6.5 with respect to the filter coefficient vector $\mathbf{w}$ is given as

$$\begin{aligned}\frac{\partial}{\partial \mathbf{w}}\mathbb{E}[e^2(m)] &= -2\mathbb{E}[y(m)\mathbf{x}(m)] + 2\mathbf{w}^T\mathbb{E}[\mathbf{x}(m)\mathbf{x}^T(m)] \\ &= -2\mathbf{r}_{xy} + 2\mathbf{w}^T\mathbf{R}_{xx}\end{aligned} \tag{6.6}$$

with

$$\frac{\partial}{\partial \mathbf{w}} = \left[\frac{\partial}{\partial w_0}, \frac{\partial}{\partial w_1}, \frac{\partial}{\partial w_2}, ..., \frac{\partial}{\partial w_{P-1}}\right]^T. \tag{6.7}$$

Setting Eq. 6.6 to zero leads to the minimum mean square error Wiener filter

$$\mathbf{R}_{xx}\mathbf{w} = \mathbf{r}_{xy} \tag{6.8}$$

After rearranging Eq. 6.8, the Wiener filter (WF) coefficients can be computed as

$$\mathbf{w} = \mathbf{R}_{xx}^{-1}\mathbf{r}_{xy}. \tag{6.9}$$

Hence, the WF coefficients can be computed from the autocorrelation matrix of the input signals (the unfiltered signals) and the crosscorrelation vector of the input and the desired signals.

6.2.2 Configuration of the Wiener filter and the ECG signals

Estimation of the WF coefficients using complete ECG records

The simplest way was to apply the WF to a complete ECG record. As described in Section 6.2.1, the WF minimises the LSE between the reference or target signal $y(m)$ and the filter output $\widehat{y}(m) = \mathbf{w}^T\mathbf{x}$. The underlying target signal in $x(m)$ should have similar properties as the target signals $y(m)$ itself, so that the error between $\widehat{y}(m)$ and $y(m)$ can be minimised. However, for real ECG records with physiological beat-to-beat variations, the underlying ECG in $x(m)$ and the target signal are unlikely to perfectly correlate with each other. This aspect shall be pointed out using the following two examples.

In both examples, ECG and MHD signals were simulated as described in Section 4.2.3.

Example 1: In this example, the simulated ECG signals in $x(m)$ and $y(m)$ were the same but with the MHD signal included in $x(m)$

$$\begin{aligned} y(m) &\leftarrow ECG_{out,1a} = ECG_{clean}(1s:10s) \\ x(m) &\leftarrow ECG_{in,1a} = ECG_{clean}(1s:10s) + MHD(1:10s) \\ \widehat{y}(m) &= \sum_{k=0}^{P-1} w_k ECG_{in,1b}(m-k) \quad \text{with} \quad ECG_{in,1b} = ECG_{clean}(21s:30s) + MHD(21:30s) \end{aligned} \tag{6.10}$$

where the WF coefficients w_k were estimated using $x(m)$ and $y(m)$. The underlying ECG (the desired ECG_{clean}) is the same in both signals. Once the coefficents were estimated, the WF was applied to a different segment $ECG_{in,1b}$ of the simulated record. An exemplary result is depicted in Fig. 6.2a. In the filtered ECG signal, the shape of the QRS complex was preserved and the MHD signal was attenuated such that the shape of the underlying T-wave can be recognised.

Example 2: A more realistic scenario is simulated in this second example. Instead of taking the same ECG in $x(m)$ and $y(m)$, time shifted versions of the ECG of one record were used

$$\begin{aligned} y(m) &\leftarrow ECG_{out,2a} = ECG_{clean}(1s:10s) \\ x(m) &\leftarrow ECG_{in,2a} = ECG_{clean}(11s:20s) + MHD(11:20s) \\ \widehat{y}(m) &= \sum_{k=0}^{P-1} w_k ECG_{in,2b}(m-k) \quad \text{with} \quad ECG_{in,2b} = ECG_{clean}(21s:30s) + MHD(21:30s). \end{aligned} \tag{6.11}$$

Due to the simulated RRI variations (see Section 4.2.4), the underlying ECG signals ECG_{clean} in $x(m)$ and $y(m)$ were different. This again affects the cross-correlation of $ECG_{out,2a}$ and $ECG_{in,2a}$ and the resulting WF coefficients. An exemplary trace of the so filtered ECG signal is depicted in Fig. 6.2b. In contrast to the previous example, the QRS complex was attenuated and could not be recovered. The end of the T-wave was not as clearly visible as in the previous example.

These two examples showed that the estimation of the WF coefficients from complete ECG records (10 s in these examples) is not feasible for a practical application. This approach only works for signals where the underlying ECG is the same in $x(m)$ and $y(m)$. Based on this preliminary investigation, this approach for the WF coefficient estimation was discarded and a template-based approach was chosen instead.

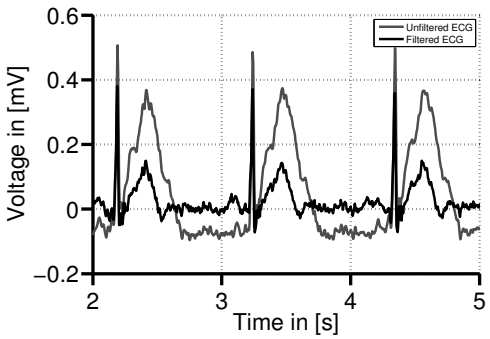

(a) Unfiltered and Wiener filtered ECG.

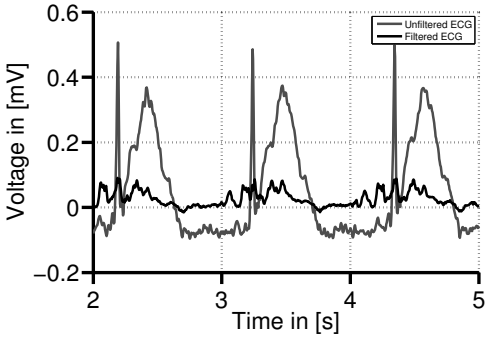

(b) Unfiltered and Wiener filtered ECG.

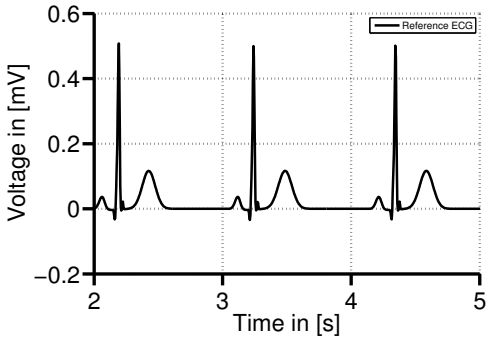

(c) Reference signal used for the computation of the filter coefficients in (a). This reference has the same periodicity as the signal in (a).

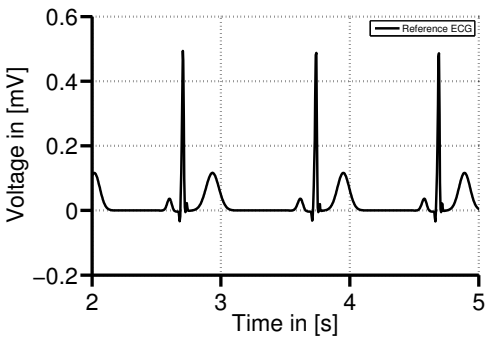

(d) Reference signal used for the computation of the filter coefficients in (b). This reference has a different periodicity as the signal in (a).

Figure 6.2.: Examples for the computations of the Wiener filter coefficients using different input signals. The coefficients for the signals shown in (a) were computed using a reference signal (c) which was the same as the underlying ECG in the unfiltered ECG in (a) (but without the additional noise). With the computed coefficients, the filtered signal in (a) showed a good estimate of the reference signal (c). In contrast, the underlying ECG of the unfiltered ECG depicted in (b) was not the same as the reference signal (d) used for the computation of the filter coefficients, i. e. it was from the same simulated record but from a difference section. Hence, the reference and the unfiltered ECGs did not match each other and the estimated filter coefficients were not optimal in the sense of filtering the ECG in (b) such that it corresponds to the morphology of the reference signal.

Estimation of the WF coefficients using PQRST templates

In order to avoid the problems mentioned above, another approach for the WF coefficient estimation based on PQRST templates was chosen. PQRST templates were estimated for the simulated and real ECG signals acquired outside ($T_{\text{ECG,out}}$) and inside ($T_{\text{ECG,in}}$) the MR scanner according to [Andreotti 14] with

$$\begin{aligned} y(m) &\leftarrow T_{\text{ECG,out}} \\ x(m) &\leftarrow T_{\text{ECG,in}}. \end{aligned} \tag{6.12}$$

Ten cardiac cycles were used to build the templates. Templates were computed from normal episodes only, i. e. *pathological variations were not considered*. Exemplary PQRST template estimated from real ECG records acquired outside and inside a 3 T MRI scanner are shown in Fig. 6.3. The WF coefficients estimated from these PQRST templates were then applied to the remaining parts of the simulated ECGs, which included normal and pathological episodes and to the real ECGs.

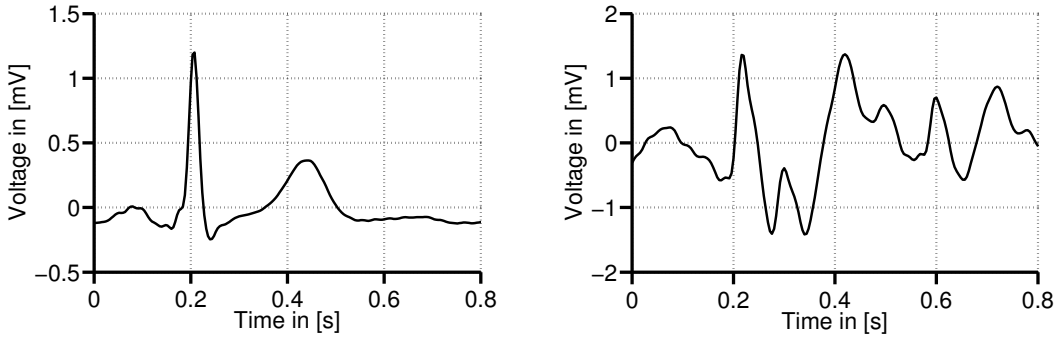

(a) PQRST template of a real ECG acquired outside the MR scanner.

(b) PQRST template of a real ECG acquired inside the MR scanner.

Figure 6.3.: PQRST templates of a real ECG signal (lead II) acquired outside (a) and inside $3\,\mathrm{T}$ MR scanner (b). The templates were used to compute the Wiener filter coefficients for lead II of this ECG.

Previous investigations using concatenated ST-T-wave segments

Previous investigations using the WF were published by Krug *et al.* in [Krug 12]. This study was focused on the estimation of dedicated WF coefficients $\mathbf{w}$ for the section of the cardiac cycle containing the ST-segment and the T-wave. The aim was to optimise $\mathbf{w}$ on this section of the ECG. Concatenated ST-T-wave segments were used for the estimation of $\mathbf{w}$. Once $\mathbf{w}$ was calculated, it was applied to extracted ST-T-wave segments. The filtered segments were then used to analyse the elevation of the ST-segment and the end of the T-wave. Using this procedure, errors in the ST-segment were below $0.1\,\mathrm{mV}$ in several leads. However, larger errors in certain leads could cause a false diagnosis. The T-wave could be observed in the filtered signals but the quantitative evaluation showed that the manual annotation of the end of the T-wave was not precise [Krug 12]. Due to these findings, no further analysis of this configuration or its variations (e. g. concatenated PQRST segments) were made in this work since our previous works could not show an improvement for the filtering of the T-wave.

Order of the Wiener filter

The result of the Wiener filter depends on the order of the filter. A higher order can improve the quality of the filter results, but it increases the computational complexity. The number P of filter coefficients used during the experiments was investigated empirically. The SNR computed between the filtered and the reference signal was used as the quality metric for the estimation of $\mathbf{w}$. The normal (non-pathological) section of the simulated ECG without additional noise or MHD effect served as the reference signal. Muscle artefact noise as well as a MHD signal using the model described in Section 4.2 was added to the clean ECG signal. This noisy ECG was used as an input for the Wiener filter. Pathological episodes were not considered during the estimation of the number of filter coefficients. Figure 6.4 depicts the SNR of a filtered, simulated, non-pathological ECG signal using different numbers of WF filter coefficients. From the results it can be seen that for a sampling frequency of $250\,\mathrm{Hz}$, $P = 50$ is a reasonable choice for the number of WF coefficients. Since the WF coefficients were estimated from the PQRST templates, the total number of coefficients is limited by the length of the template.

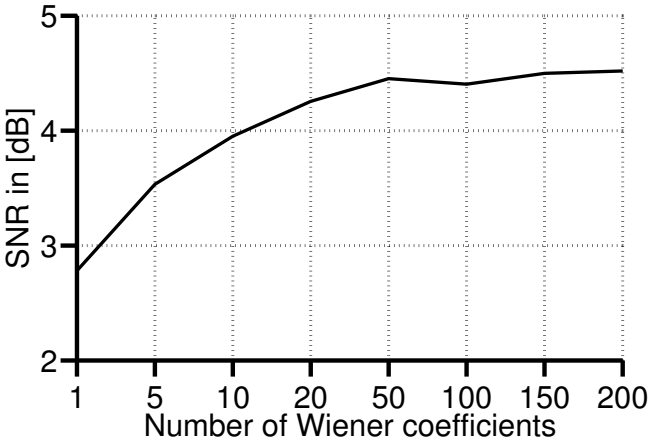

Figure 6.4.: SNR of the obtained filter results using different numbers of Wiener filter coefficients.

6.3 Separating ECG and MHD components using ICA

This section introduces an ICA-based method for the denoising of ECG signals during MRI. ICA is used to estimate a set of independent components (ICs) from the distorted ECG signals (see Chapter 5). Denosing is performed by eliminating certain ICs, e. g. those ICs dominated by the MHD signal or by noise components. An approach for the automatic identification of the ICs is described in the following.

Identification of cardiac, MHD and noise sources: problem formulation

One crucial aspect with the application of ICA was the selection of the ICs, which should be used for the reconstruction of the filtered signal. For the given problem, all ICs contributing to the ECG had to be kept whereas the ICs dominated by the MHD effect or other noise sources should be cancelled out.

The challenging aspect in the selection process of appropriate ICs came from the fact that the ECG signal is originating from different sources. ICA was previously used to separate atrial and ventricular activity with the application in the detection of atrial fibrillation analysis [Castells 05, Phlypo 07, Chang 10]. In [Castells 05], noise, atrial and ventricular activity were separated in a two-stage process. First, ICs with high kurtosis values are assumed to have their origin in ventricular activity. The remaining ICs with a frequency peak between 3 Hz and 10 Hz were assigned to the atrial activity. Atrial activity is mainly represented by the P-wave. However, most energy of the MHD effect at 3 T is in the frequency range below 10 Hz [Krug 11], which makes the usage of the frequency spectra impractical for the selection of appropriate ICs.

It was also shown in Chapter 5 that ICA is not able extract separate source signals but only mixtures of them. As depicted in Fig. 5.14, p. 112, it was possible to compute ICs, which were mainly dominated by the ECG ($\widehat{s}_{\mathrm{ECG}}$) or the MHD ($\widehat{s}_{\mathrm{MHD}}$) signal, but none of the ICs was clearly assignable to a single underlying source or process.

The mixture of different underlying sources $\mathbf{s}_k$ in the extracted components $\widehat{\mathbf{s}}_k$ was expected to affect the quality of the filtered ECG signals. A trade-off between the suppression of the MHD effect and the accuracy of the ECG had to be made. Especially by removing the ICs containing a relevant amount

of energy from both source signals (ECG and MHD: $\widehat{s}_{\text{E+M}}$), information about the ECG would be lost. However, when keeping those ICs, the filtered measurement signals would still be influenced by the MHD effect.

Selection of the required ICs

As mentioned above, the selection of the ICs required for the computation of a filtered version of the ECG is a non-trivial problem. Several methods to identify certain ICs were already investigated in this thesis, e. g. those using kurtosis or template matching (see Section 5.3.3 and [Mattern 12]). As explained above, the usage of frequency spectra was not considered due to overlapping frequency ranges of the ECG and MHD signals.

In Chapter 5, ICA was used to extract one IC dominated by the R-peak or QRS complex. For diagnostic purposes, however, other components of the ECG are important as well (see Section 2.1.4). Hence, all the ICs mainly containing information of the ECG should be identified and used for the estimation of the filtered version of the ECG. Since the properties of the ECG and MHD components are not unique and clearly separable (e. g. the spectral properties), the identification of ICs based on a set of predefined features could possibly lead to a non-ideal result. The manual selection of appropriate ICs would be another way to cope with this problem. However, ICs which are dominated by the atrial activity or the repolarisation of the ventricles might be misinterpreted and would highly depend on the user. Hence, a manual selection of the ICs was not considered.

Filtering using ICA was achieved by finding an optimal combination of the estimated ICs for each reconstructed or filtered ECG lead. One way to optimise the quality of the ICA filtered ECG signal was to *minimise the SNR* between a reference ECG (e. g. the simulated, clean ECG or the real ECG acquired outside the MR scanner) and the ICA filtered ECG. For an optimal selection of the ICs, the SNR was calculated for all possible IC combinations (see below). The normal, non-pathological sections at the beginning of each record (length=30 s) were used to construct a vector of concatenated PQRST sections from the reference and the unfiltered ECG, where each PQRST section had the same constant length. The concatenation was required to compute the SNR for the real ECG records where the reference signal acquired outside the MR scanner did not match the ECG acquired inside the MR scanner. The concatenated signals estimated from the ECGs inside the MRI scanner (simulated and real) were used to compute the ICs $\widehat{\mathbf{s}}_k$.

For l estimated ICs $\widehat{\mathbf{s}}_k$, the total number[2] of investigated combinations C was

$$C = 2^l - 1. \tag{6.13}$$

For a record with 8 ICs, 255 different combinations were used. The SNR of each combination was computed (using the reference ECG signal). This step was performed separately for each lead. Using the combinations giving the lowest SNR in each lead, an optimised mixing matrix $\mathbf{A}_{\text{opt}}$ was defined. Finally, the ICA filtered ECG signal was computed as

$$\mathbf{x}_{\text{filt}}(n) = \mathbf{A}_{\text{opt}} \cdot \widehat{\mathbf{s}}_k(n). \tag{6.14}$$

[2]The combination which set all ICs to zero was not investigated.

An overview of the whole procedure is depicted in Fig. 6.5. Pathological episodes of the simulated ECG records were not included in the computation of $\mathbf{A}_{\text{opt}}$. The reason for not including pathological episodes in the 'training set' was to estimate whether the ICA technique was able to detect pathological variations automatically.

6.4 MHD suppression using an EKF framework

6.4.1 Theory of the (extended) Kalman filter

If we assume that a (non)-linear system can be fully described by a set of hidden variables, then the state $\mathbf{x}_k$ (with $\mathbf{x}_k$ usually being unknown) can be estimated through a set of measurements (observations), $\mathbf{y}_k$ [Haykin 01]. A Bayesian or Kalman filter (KF) tries to estimate hidden variables, $\mathbf{x}_k$, based on a series of noisy observations, $\mathbf{y}_k$. In such a state-space formalism, the evolution of the state $\mathbf{x}_k$ is described by the *evolution equation* given by a non-linear function f. Observations $\mathbf{y}_k$ are related to the hidden state described by the *observation equation* using a non-linear function g.

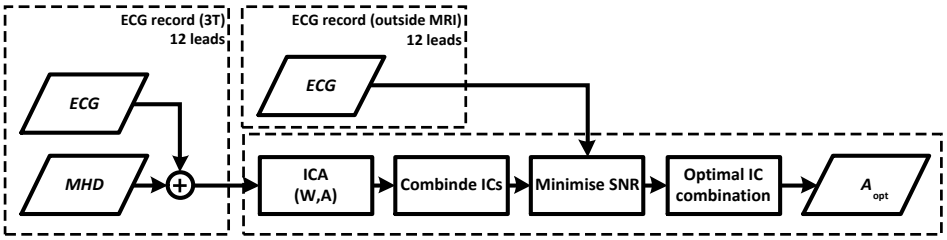

(a) Preprocessing stage: Minimisation of the SNR by an optimised combination of ICs.

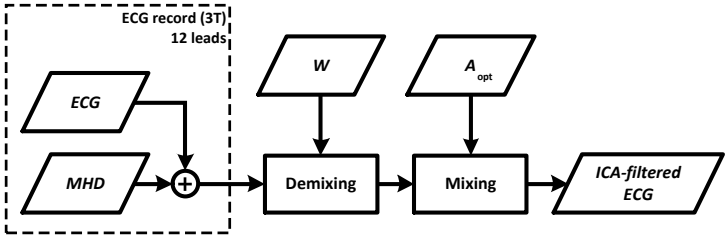

(b) Filtering of the ECG signals by mixing the ICs using an optimised mixing matrix.

Figure 6.5.: Principle of the ICA-based filtering scheme. In the preprocessing step (a), all possible combinations of the ICs obtained by ICA were tested with respect to the obtained SNR. For each lead of the ECG, the combination of ICmainlys which achieved the maximum SNR was chosen. Based on these lead-by-lead optimisation, an optimised mixing matrix was defined. This matrix was used in the filtering step (b) to obtain an ECG where MHD and noise components were suppressed.

The (linear) KF algorithm

The Kalman filter (KF) is used for estimating a state $\mathbf{x}_k \in \mathbb{R}^n$ of a discrete-time process [Welch 04]. A system of linear stochastic difference equations is used to describe this process. The state ($\mathbf{x}_k$) evolution is given by[3]

$$\mathbf{x}_k = \mathbf{A}\mathbf{x}_{k-1} + \mathbf{w}_k, \tag{6.15}$$

where the $n \times n$ matrix $\mathbf{A}$ relates the state $\mathbf{x}_{k-1}$ at the previous time step $k-1$ to the the state $\mathbf{x}_k$ at the current time step k. $\mathbf{w}_k$ represents the process noise.

The measurements or observations $\mathbf{y}_k$ are linked to the state by

$$\mathbf{y}_k = \mathbf{H}\mathbf{x}_k + \mathbf{v}_k, \tag{6.16}$$

where $\mathbf{y}_k \in \mathbb{R}^m$ is the vector containing the measurements at time k. The $m \times n$ measurement matrix $\mathbf{H}$ relates the state $\mathbf{x}_k$ at time k to the observations $\mathbf{y}_k$. Similarly to the state vector in Eq. 6.15, the measurement vector $\mathbf{y}_k$ is contaminated by a noise process $\mathbf{v}_k$.

The random variables $\mathbf{w}_k$ and $\mathbf{v}_k$ representing the process and measurement noises are assumed to be independent of each other, white, with normal probability distribution and a zero mean

$$\begin{aligned} p(w) =& N(0, \mathbf{Q}) \\ p(v) =& N(0, \mathbf{R}) \end{aligned} \tag{6.17}$$

where $\mathbf{Q}$ and $\mathbf{R}$ are the process noise and measurement noise covariance matrices respectively. The states $\mathbf{x}_k$ need to be estimated from the (noisy) measurements $\mathbf{y}_k$. Therefore, two state estimates are defined:

1. $\widehat{x}_k^- \in \mathbb{R}^n$ is the *a priori* estimate of the state at step k based on the observations made until sample $k-1$.

2. $\widehat{x}_k \in \mathbb{R}^n$ is the *a posteriori* estimate of the state $\mathbf{x}_k$ at step k using the k measurement.

These state estimates are used to define the *a priori* error e_k^- and *a posteriori* error e_k

$$\begin{aligned} e_k^- =& \mathbf{x}_k - \widehat{x}_k^- \\ e_k =& \mathbf{x}_k - \widehat{x}_k, \end{aligned} \tag{6.18}$$

with the *a priori* and *a posteriori* error covariance matrices

$$\begin{aligned} \mathbf{P}_k^- =& \mathbb{E}[e_k^- {e_k^-}^T] \\ \mathbf{P}_k =& \mathbb{E}[e_k {e_k}^T]. \end{aligned} \tag{6.19}$$

[3] The additional control matrix $\mathbf{B}$ and control input u_{k-1} are neglected in Eq. 6.15 since they are not used here.

Given the definitons above, the aim is to give a definiton for the *a posteriori* state estimate $\widehat{x}_k$ using the *a priori* state estimate $\widehat{x}_k^-$ and the actual measurement $\mathbf{y}_k$. This is defined as

$$\widehat{x}_k = \widehat{x}_k^- + \mathbf{K}(\mathbf{y}_k - \mathbf{H}\widehat{x}_k^-). \tag{6.20}$$

The difference $\mathbf{y}_k - \mathbf{H}\widehat{x}_k^-$ is called residual or measurement innovation. If the predicted and the actual measurements are in complete agreement, the residual is zero. The $n \times m$ matrix $\mathbf{K}$ is called Kalman gain. It is adjusted to minimise the *a posteriori* error covariance in Eq. 6.19. Finally, $\mathbf{K}$ is defined as

$$\mathbf{K} = \mathbf{P}_k^- \mathbf{H}^T (\mathbf{H}\mathbf{P}_k^- \mathbf{H}^T + \mathbf{R})^{-1}. \tag{6.21}$$

If the measurement $\mathbf{y}_k$ is precise, i. e. $\mathbf{R} \to 0$, then the Kalman gain $\mathbf{K}$ has a stronger effect on the residual

$$\lim_{\mathbf{R}\to 0} \mathbf{K} = \mathbf{H}^{-1}. \tag{6.22}$$

If, on the other hand, the estimated value is close to the systems state value, then the *a priori* estimate error covariance matrix $\mathbf{P}_k^-$ will approach zero and hence the Kalman gain has less influence on the weight of the residual in Eq. 6.21

$$\lim_{\mathbf{P}_k^- \to 0} \mathbf{K} = 0. \tag{6.23}$$

For the first case, the KF trusts the measurement value $\mathbf{y}_k$, for the second case it trusts the predicted value $\widehat{x}_k^-$, or the evolution equation.

The discrete KF algorithm

The equations of the KF can now be divided into two groups: the prediction (time update) and the correction (measurement update) equations. The prediction equations are responsible for the *a priori* estimates using the current state. The correction equations can be regarded as a feedback, which takes the new measurement value $\mathbf{y}_k$ into account for the *a posteriori* estimation. The equations for the KF prediction step are given as

$$\begin{aligned} \widehat{x}_k^- &= A\mathbf{x}_{k-1} \\ \mathbf{P}_k^- &= A\mathbf{P}_k A^T + Q \end{aligned} \tag{6.24}$$

and for the correction step as

$$\begin{aligned} \mathbf{K} &= \mathbf{P}_k^- \mathbf{H}^T (\mathbf{H}\mathbf{P}_k^- \mathbf{H}^T + R)^{-1} \\ \widehat{x}_k &= \widehat{x}_k^- + \mathbf{K}(\mathbf{y}_k - \mathbf{H}\widehat{x}_k^-) \\ \mathbf{P}_k &= (I - \mathbf{K}\mathbf{H})\mathbf{P}_k^-. \end{aligned} \tag{6.25}$$

During the correction, the Kalman gain $\mathbf{K}$ has to be estimated first. This step is followed by the acquisition of a new measurement value $\mathbf{y}_k$, which is used to generate the *a posteriori* estimate $\widehat{x}_k$. Finally, the *a posteriori* error covariance matrix $\mathbf{P}_k$ has to be updated. Using the previous *a posteriori* estimates from Eq. 6.25, the next *a priori* estimates are predicted using Eq. 6.24. The recursive operation of the KF is one of its advantages since it updates the current estimates depending on the past measurements and can be performed online.

The extended Kalman filter (EKF)

The extended Kalman filter (EKF) enables the application of the standard Kalman filter formalism to non-linear systems. For the EKF, the (unknown, unobserved) state vector $\mathbf{x}_k$ and the observation vector $\mathbf{y}_k$ can be written as

$$\begin{cases} \mathbf{x}_{k+1} = f(\mathbf{x}_k, \mathbf{w}_k, k) \\ \mathbf{y}_k = g(\mathbf{x}_k, \mathbf{v}_k, k) \end{cases} \tag{6.26}$$

where $f(\cdot)$ is the non-linear state evolution function and $g(\cdot)$ describes the non-linear relation between the state vector $\mathbf{x}_k$ and the observation vector $\mathbf{y}_k$. $\mathbf{w}_k$ is the process or evolution noise vector, $\mathbf{v}_k$ the measurement or observation noise vector and k the time instant. The corresponding covariance matrices are defined as $\mathbf{Q} = E\left\{\mathbf{w}_k \mathbf{w}_k^T\right\}$ and $\mathbf{R} = E\left\{\mathbf{v}_k \mathbf{v}_k^T\right\}$. In order to use the Kalman filter formalism for finding the MMSE estimate of $\mathbf{x}_k$, a linear approximation of Eq. 6.26 near a desired reference point $(\widehat{\mathbf{x}}_k, \widehat{\mathbf{w}}_k, \widehat{\mathbf{v}}_k)$ is required [Haykin 01, Vaseghi 09]. The approximation of Eq. 6.26 is given as

$$\begin{cases} \mathbf{x}_{k+1} \approx f(\widehat{\mathbf{x}}_k, \widehat{\mathbf{w}}_k, k) + \mathbf{A}_k(\mathbf{x}_k - \widehat{\mathbf{x}}_k) + \mathbf{F}_k(\mathbf{w}_k - \widehat{\mathbf{w}}_k) \\ \mathbf{y}_k \approx g(\widehat{\mathbf{x}}_k, \widehat{\mathbf{v}}_k, k) + \mathbf{C}_k(\mathbf{x}_k - \widehat{\mathbf{x}}_k) + \mathbf{L}_k(\mathbf{v}_k - \widehat{\mathbf{v}}_k) \end{cases} \tag{6.27}$$

where $\mathbf{A}_k$ and $\mathbf{F}_k$ are the Jacobians of the evolution function and $\mathbf{C}_k$ and $\mathbf{L}_k$ are the Jacobians of the observation function

$$\begin{aligned} \mathbf{A}_k &= \left.\frac{\partial f(\mathbf{x}, \widehat{\mathbf{w}}_k, k)}{\partial \mathbf{x}}\right|_{\mathbf{x}=\widehat{\mathbf{x}}_k} & \mathbf{F}_k &= \left.\frac{\partial f(\widehat{\mathbf{x}}_k, \mathbf{w}, k)}{\partial \mathbf{w}}\right|_{\mathbf{w}=\widehat{\mathbf{w}}_k} \\ \mathbf{C}_k &= \left.\frac{\partial g(\mathbf{x}, \widehat{\mathbf{v}}_k, k)}{\partial \mathbf{x}}\right|_{\mathbf{x}=\widehat{\mathbf{x}}_k} & \mathbf{L}_k &= \left.\frac{\partial g(\widehat{\mathbf{x}}_k, \mathbf{v}, k)}{\partial \mathbf{v}}\right|_{\mathbf{v}=\widehat{\mathbf{v}}_k} \end{aligned} \tag{6.28}$$

6.4.2 Description of the models

Basic Bayesian approach

The discrete form of the Gaussian model described in Section 4.2.2 can be rewritten as

$$\begin{aligned} \theta_k &= (\theta_{k-1} + \omega\delta) \bmod(2\pi) \\ z_k &= -\sum_i \delta \frac{\alpha_i \omega}{b_i^2} \Delta\theta_{i,k-1} \exp\left(-\frac{\Delta\theta_i^2}{2b_i^2}\right) + z_{k-1} + \eta \\ &= -\sum_i \delta \frac{\omega}{b_i^2} \Delta\theta_i G(\alpha_i, \Delta\theta_{i,k-1}, b_i) + z_{k-1} + \eta \end{aligned} \tag{6.29}$$

where θ_k is the angle in cylindrical coordinates and z_k the ECG given in mV at time k [Sayadi 10]. $\omega = {}^{2\pi}/_{RRI}$ is the angular velocity, RRI the RR interval, δ the (small) sampling period and η represents physiological noise, e. g. MA noise as used in this thesis. α_i, b_i, ξ_i are the amplitude, width and angular position of the i^{th} Gaussian with $\Delta\theta_{i,k-1} = (\theta_{k-1} - \xi_i) \bmod(2\pi)$ and $G(a,b,c) = a\exp\left(-\frac{b^2}{2c^2}\right)$.

The evolution equations can be written as

$$\begin{cases} \theta_k = (\theta_{k-1} + \omega\delta) \bmod 2\pi \\ p_k = -\sum_{i=1}^{2} \delta \frac{\omega \Delta\theta_{i,k-1}^E}{\left(b_{i,k-1}^E\right)^2} G\left(\alpha_{i,k-1}^E, \Delta\theta_{i,k-1}^E, b_{i,k-1}^E\right) + p_{k-1} + \eta_p \quad \text{(P-wave)} \\ q_k = -\sum_{i=3}^{5} \delta \frac{\omega \Delta\theta_{i,k-1}^E}{\left(b_{i,k-1}^E\right)^2} G\left(\alpha_{i,k-1}^E, \Delta\theta_{i,k-1}^E, b_{i,k-1}^E\right) + q_{k-1} + \eta_q \quad \text{(QRS complex)} \\ t_k = -\sum_{i=6}^{7} \delta \frac{\omega \Delta\theta_{i,k-1}^E}{\left(b_{i,k-1}^E\right)^2} G\left(\alpha_{i,k-1}^E, \Delta\theta_{i,k-1}^E, b_{i,k-1}^E\right) + t_{k-1} + \eta_t \quad \text{(T-wave)} \end{cases} \tag{6.30}$$

and the observation equations as

$$\begin{cases} \phi_k = \theta_k + v_{1,k} \\ s_k = \underbrace{p_k + q_k + t_k}_{\text{ECG}} + \underbrace{v_{2,k}}_{\text{MHD + other noises}} \end{cases}. \tag{6.31}$$

Here, p, q, t represent the P-wave, the QRS complex and the T-wave, respectively [Sayadi 10]. The observation s_k represents the ECG signal acquired inside the MRI scanner whereas ϕ_k is the phase signal, which is linearly assigned from 0 to 2π and was rescaled from $-\pi$ to π. η_p, η_q and η_t model the noise of the evolution equations. The estimated ECG signal is given by the sum of the three components of the evolution equations: $p_k + q_k + t_k$. In the approach described above, the MHD effect was considered by the additional noise component $v_{2,k}$.

Extended Bayesian approach

As it was shown in Sections 3.2 and 3.3, the MHD signal has the same periodicity as the ECG. These periodic cycles of the MHD signal can also be modelled by a sum of Gaussian functions. In [Oster 13], a new observation equation was introduced, which considered the MHD effect as an additional, periodic signal. The newly observed signals were assumed to be a sum of the MHD signal, noise and the *a priori* knowledge of the ECG, where the ECG was described by the Gaussian model. One can consider this new observation as equivalent to observing a synthetic signal, which represents the noisy ECG but from which the prior on the ECG was subtracted (which is equivalent to observing a synthetic MHD signal + noise). [Oster 13]

The updated state-space is then defined by the new evolution equations

$$
\begin{cases}
\theta_k = (\theta_{k-1} + \omega\delta) \mod 2\pi \\
p_k = -\sum_{i=1}^{2} \delta \frac{\omega \Delta\theta^E_{i,k-1}}{\left(b^E_{i,k-1}\right)^2} G\left(\alpha^E_{i,k-1}, \Delta\theta^E_{i,k-1}, b^E_{i,k-1}\right) + p_{k-1} + \eta_p \quad \text{(P-wave)} \\
q_k = -\sum_{i=3}^{5} \delta \frac{\omega \Delta\theta^E_{i,k-1}}{\left(b^E_{i,k-1}\right)^2} G\left(\alpha^E_{i,k-1}, \Delta\theta^E_{i,k-1}, b^E_{i,k-1}\right) + q_{k-1} + \eta_q \quad \text{(QRS complex)} \\
t_k = -\sum_{i=6}^{7} \delta \frac{\omega \Delta\theta^E_{i,k-1}}{\left(b^E_{i,k-1}\right)^2} G\left(\alpha^E_{i,k-1}, \Delta\theta^E_{i,k-1}, b^E_{i,k-1}\right) + t_{k-1} + \eta_t \quad \text{(T-wave)} \\
m_k = -\sum_{i} \delta \frac{\omega \Delta\theta^M_{i,k-1}}{\left(b^M_{i,k-1}\right)^2} G\left(\alpha^M_{i,k-1}, \Delta\theta^M_{i,k-1}, b^M_{i,k-1}\right) + m_{k-1} + \underbrace{\eta_m}_{\text{MHD variation}} \quad \text{(MHD)} \\
\alpha^E_{i,k} = \alpha^E_{i,k-1} + \epsilon_{\alpha,i} \\
b^E_{i,k} = b^E_{i,k-1} + \epsilon_{b,i} \\
\xi^E_{i,k} = \xi^E_{i,k-1} + \epsilon_{\xi,i}
\end{cases}
\tag{6.32}
$$

and by the new observation equations

$$
\begin{cases}
\phi_k = \theta_k + v_{1,k} \\
s_k = \underbrace{p_k + q_k + t_k}_{\text{ECG}} + \underbrace{m_k}_{\text{MHD}} + v_{2,k} \\
s_k = m_k + \sum_i G\left(\alpha^E_{i,k}, \Delta\theta^E_{i,k}, b^E_{i,k}\right) + v_{3,k}.
\end{cases}
\tag{6.33}
$$

The MHD signal is represented by m_k with the Gaussian parameters $\alpha^M_{i,k}, \Delta\theta^M_{i,k}, b^M_{i,k}$. The Gaussian parameters representing the MHD signal were not included in the state vector. However, the non-stationary nature of the MHD signal is taken into account by the noise parameters η_m.

The state vector $\mathbf{x}_k$ and the observation vector $\mathbf{y}_k$ are defined as

$$\begin{aligned}\mathbf{x}_k &= \left(\theta_k, p_k, q_k, t_k, m_k, \alpha^E_{1,k}, ..., \alpha^E_{7,k}, b^E_{1,k}, ..., b^E_{7,k}, \xi^E_{1,k}, ..., \xi^E_{7,k}\right)^{\mathrm{T}} \\ \mathbf{y}_k &= (\phi_k, s_k, s_k)^T\end{aligned} \tag{6.34}$$

and the process (or evolution) noise vector $\mathbf{w}_k$ and the measurement (or observation) noise vector $\mathbf{v}_k$ are given as

$$\begin{aligned}\mathbf{w}_k &= \left(\omega, \eta_p, \eta_q, \eta_t, \eta_m, \alpha^M_{i,k}, b^M_{i,k}, \xi^M_{i,k}\right)^{\mathrm{T}} \\ \mathbf{v}_k &= (v_{1,k}, v_{2,k}, v_{3,k})^T.\end{aligned} \tag{6.35}$$

In order to apply the Kalman filter formalism to Eq. 6.32 and Eq. 6.33, an approximation of these functions according to Eq. 6.27 and Eq. 6.28 was required.

6.4.3 Model parameter estimation and filtering procedure

Estimation of the Gaussian model parameters

Several parameters were required before applying the EKF to different ECG recordings. The first problem was to find the optimal parameters of the Gaussian model described by Eq. 6.29. Using the ECG signals acquired outside and inside the MR scanner ($\mathrm{ECG_{out}}, \mathrm{ECG_{in}}$), average templates T were estimated from the ECG acquired outside the MR scanner ($T_{\mathrm{ECG,out}}$) and from the MHD signal $T_{\mathrm{MHD}} = T_{\mathrm{ECG,in}} - T_{\mathrm{ECG,out}}$. The Gaussian model parameters of these two templates were required for the application of the EKF (see Eqs. 6.32 and 6.33) and were estimated using the non-linear optimisation approach described in Section 4.2.2. It should be noted that the Gaussian parameters were estimated using an offline approach, i. e. they were estimated only once for each record.

Optimisation of the Q and R matrices using random initialisations

The process noise and measurement noise covariance matrices **Q** and **R** play an important role in the application of the EKF. A main problem with the definition of both matrices is that their parameters are neither known nor cannot be measured directly. The parameters of both matrices could be tuned manually by considering the available information about the process and measurement noises. Since such a procedure usually considers specific ECG records to adjust and test the parameters, an overfitting of the parameter could occur. Besides, manually set parameters limit the tested value range of both matrices and hence, one could miss a better or even the optimal solution. To avoid this problem, the parameters for **Q** and **R** were set by using a random search technique [Bergstra 12]. For each parameter in **Q** and **R**, random values were generated within predefined boundaries. For each set of random parameters, the EKF was applied to a training dataset consisting of ten ECG records, which were simulated based on real ECG measurements during MRI (see Section 4.2.3). The SNR measured between a clean reference ECG and the filtered ECG was used as a quality metric for the definition of an optimal set of parameters. The **Q** and **R** parameters resulting in the highest SNR were used for filtering all other simulated and real ECG records.

Filtering procedure

Once the Gaussian model parameters were estimated for the specific ECG record, the EKF was applied. Since the Gaussian model required an information about the location of the QRS complexes, an QRS detection was required as a first step. The phase signal θ (see Eq. 6.29) had to be known before the EKF was applied to a new cardiac cycle. In order to estimate θ, the angular frequency ω was required, which again depends on the length of the RR-interval. Hence, the output of the EKF was delayed with respect to the input signal since filtering could not be started before the next QRS complex was detected. This fact has consequences for the practical application of the EKF-based method because it (currently) limits its usage for real-time applications such as cardiac gating (see chapter 5), but it is a perfectly usable solution for monitoring purposes, since a delay of a few seconds is acceptable for this task. To investigate the general applicability of the EKF to ECG signals acquired during MRI, an offline implementation was used, i. e. the QRS complexes of a complete ECG record were estimated prior to the application of the EKF.

6.5 Results

6.5.1 Simulated ECG signals

6.5.1.1 Qualitative result analysis

The following three paragraphs provide a qualitative overview of the different filtering methods (Wiener filter, ICA, EKF). Using exemplary traces of the filtered ECG signals, the strengths and weaknesses of the different methods should be highlighted. A quantitative results analysis is then given in Section 6.5.1.2.

Wiener filter: Exemplary results obtained by the WF applied to the different records with different noise levels are depicted in Fig. 6.6. These results show that the WF was generally able to suppress the influence of the MHD signal and could cope with different levels of noise. Qualitatively speaking, the filter output followed the desired reference ECG during a non-pathological ECG (compare Figs. 6.6a and 6.6b). Although the positive amplitude and shape of the T-wave was preserved in the shown example, the filtered signal shows a biphasic (positive/negative) waveform. During episodes with simulated T-wave inversion depicted in Figs. 6.6c and 6.6d, the WF did not follow the target ECG $y(m)$, i e. it was not possible to detected the inverted T-waves in the shown examples. Considering the T-wave in the case of the prolonged QT-interval, the output of the Wiener filter still followed the shape of the reference T-wave, which would result in a false estimation of the QT-interval length. The WF was not able to follow the depression of the ST-segment which as depicted in Figs. 6.6g and 6.6h. Qualitatively, the WF is not suitable for monitoring applications as it cannot detect changes in the ECG morphology.

ICA: ICA was used to attenuate the MHD effect by reducing the number of ICs required for the computations of $\mathrm{x}_{\mathrm{filt}}(n)$. The selected results depicted in Figure 6.7 show that the ICA filtered signals could generally be used to obtain the morphology of the underlying ECG signals in the simulated recordings. For the normal ECG signals depicted in Figs. 6.7a and 6.7b, larger errors can be observed in the ST-segment and in the shape of the T-wave, i. e. the filtered T-wave shows a biphasic morphology. The filtered inverted T-waves depicted in Figs. 6.7c and 6.7d are broadened and biphasic. This could cause a false detection of the T-wave's peak position and polarity. The filter results were more precise for the ECG with QT-interval prolongation (Figs. 6.7e and 6.7f), i. e. the filtered signal follows the morphology of the shifted T-wave. The exemplary filtered signals with a depression of the ST-segment (Figs. 6.7g and 6.7h) show that ICA would enable the detection of changes in the ST-segment in the shown leads. However, larger errors in the ST-segment were observed in the signals depicted in Figs. 6.7e and 6.7f. This shows that ICA does not enable a reliable detection of changes in the underlying ECG morphology.

EKF: Figure 6.8 depicts an example of the filtering results using the EKF. It can be seen that the EKF was able to track the variations of the normal ECG (Figs. 6.8a and 6.8b) and of those with inverted T-waves (Figs. 6.8c and 6.8d) and prolonged QT-intervals (Figs. 6.8e and 6.8f) at different noise levels (SNR$=9$ dB and SNR$=3$ dB). While the inverted T-wave was almost ideally represented in the filtered signals, smaller deviations can be recognised in the records with simulated QT prolongation. The P-wave was also correctly tracked in Figs. 6.8a–6.8f. However, larger errors can be observed in the ECGs with simulated ST suppression. In this case, the EKF output signal followed the model of the

clean ECG too closely but not the variations of the pathological segment. This effect was observed in most of the leads for the simulated ST elevation/depression (see the detailed quantitative results in Section 6.5.1.2).

6.5.1.2 Quantitative result analysis

Measurement of the QT-interval lengths

QT measurements were performed for the ECGs with simulated QT prolongation, T-wave inversion and for the healthy ECGs with SNR=9 dB and SNR=3 dB. Tables 6.1 and 6.2 show the detailed QT measurement results in each section (normal, transitional, pathological) of the ECG records with simulated prolongation of the QT-interval. Results for the complete records (measured over the normal, transitional and pathological section) are given in Table 6.3. The best results in all segments and at different MA levels (SNR=9 dB and SNR=3 dB) were achieved by the EKF. The mean errors in the different segments and leads obtained by the EKF were within the range of the manual determination accuracy (20 ms to 40 ms) [Goldenberg 06]. However, greater p_{95} values were observed in certain leads in the pathological segment with the SNR=9 dB. Comparing the results obtained by ICA and the Wiener filter, better results were obtained by ICA for the record with SNR=9 dB and better results by the Wiener filter for the record with SNR=3 dB. Figure 6.9 shows how the different filter methods were able to track the variations of the QT-interval lengths in the records with simulated QT prolongation at SNR=9 dB (a moving average filtered result is depicted in Fig. 6.10). For each method, the lead with the best and the worst results is shown (i. e. the lead with lowest and highest measurement errors). The results obtained by the Wiener filter and by ICA show several outliers which degrade the measurement quality. However, when neglecting these outliers, the visual analysis of the results obtained by ICA (see Figs. 6.9c and 6.9d) enables the detection of prolonged QT-interval – even in the worst example. Still, a precise estimation is not possible using ICA (see Table 6.3). The EKF filtered signals allowed the most precise tracking of the varying QT-interval length and are the only ones enabling monitoring quality.

Detailed quantitative results for the measurement of the QT-interval length in records with simulated inversion of the T-wave (SNR=9 dB and SNR=3 dB) are given in Tables C.1–C.2, p. 188. A summary is given in Table C.3, p. 189. Again, the best results were obtained by the EKF with mean errors below the manual determination accuracy [Goldenberg 06]. Greater p_{95} values were observed in the transitional section of the EKF filtered signals with SNR=3 dB (see Table C.2, p. 188). The results obtained by the Wiener filter and by ICA were not sufficient for monitoring purpose because of the large errors in most sections of the simulated signals.

For the QT measurements in the normal ECGs (without simulated pathologies), the best results were achieved in the EKF filtered signals followed by the WF and by ICA filtered signals (see Table C.4, p. 189).

T-wave polarity and type

Measurements of the T-wave polarity were performed for the ECGs with simulated QT prolongation, T-wave inversion and for the healthy ECGs with SNR=9 dB and SNR=3 dB. Tables 6.4 and 6.5 show the results for the records with simulated T-wave inversion. From the results it can be seen that the *ECGPUWAVE* algorithm was not able to detect enough T-waves in all leads and that for each technique. Hence, these leads were not considered for the computation of the averaged results. The ECG signals filtered by the *EKF enabled the best T-wave detection performance* in terms of the Se and $+P$ measurements. The main problem of the Wiener or ICA-filtered signals was the occurrence of biphasic T-waves. Figures 6.7c and 6.7d, which depict the ICA filtered signals with an inversion of the T-wave, highlight this observation. In these examples it can be seen that the inverted T-waves are visible in the filtered signal but are accompanied by an additional positive T-wave (biphasic negative/positive T-waves). This problem is also highlighted by Fig. 6.11, which shows the classification of the different T-wave types as made by *ECGPUWAVE*. Similar observations were made for the ECG signals filtered by the EKF. The normal, non-pathological ECG depicted in Fig. 6.12a shows positive/negative biphasic T-wave patterns. In the corresponding EKF filtered signal depicted in Fig. 6.12b, the small negative part of the T-wave was not completely represented, which resulted in the detection of a normal T-waves instead of the biphasic ones. Because of the constraints made in Section 4.3.2, all positive/negative biphasic T-waves were classified as a normal T-wave within an additional post-processing step.

Considering the results for the records with inverted T-waves shown in Tables 6.4 and 6.5, it can be observed that the detection performance of the EKF drops in the transitional section, i. e. in that section of the ECG where the polarity of the T-wave was inverted. This observation can be explained by the example depicted in Fig. 6.13. The example shows a delay between the onset of the T-wave inversion in the reference ECG and the EKF filtered ECG. Hence, it took up to 10 s to detect the inverted T-wave in the filtered ECG signal, which caused a misclassification of the T-waves in this segment. Additional T-wave measurement results for the records with other pathologies are summarised in Tables C.5–C.7, pp. 190.

ST measurements

Amplitudes of the ST-segment were measured in the ECG with simulated ST depression, ST elevation, QT prolongation and T-wave inversion and in the ECGs without simulated pathology. Detailed results (normal, transitional and pathological sections of each record) for the ECGs with simulated elevation or depression of the ST-segment are given in Tables 6.6 to 6.11. Additional ST measurements for the records with other pathologies can be found in Tables C.8–C.14, pp. 192. In contrast to the filter results for the other pathologies described above, the EKF could not completely outperform the other methods for the ST measurements. For the records with simulated ST depression at SNR=9 dB (see Table 6.6), the EKF achieved the best results in the normal section. For the transitional and pathological section, better results were achieved by the Wiener filter. Similar results were observed for the ECG with simulated ST elevation (see Tables 6.8 and 6.9). In the case of an ST elevation/depression, the EKF followed the trace of the reference ECG (which did not contain an information about the pathological variations). The examples depicted in Figs. 6.14a and 6.14b show that the EKF (with its currently configured parameters) was not able to track the depression of the ST-segment. In contrast, the Wiener filtered signals of the same input ECG, which are depicted in Figs. 6.14c and 6.14d enable a better detection of the simulated ST depression. For all other records (QT prolongation, T-wave

inversion, normal ECG), the EKF outperformed the other methods in terms of the ST measurements (compare Tables C.8–C.11, pp. 192 and Tables C.12–C.14, pp. 194).

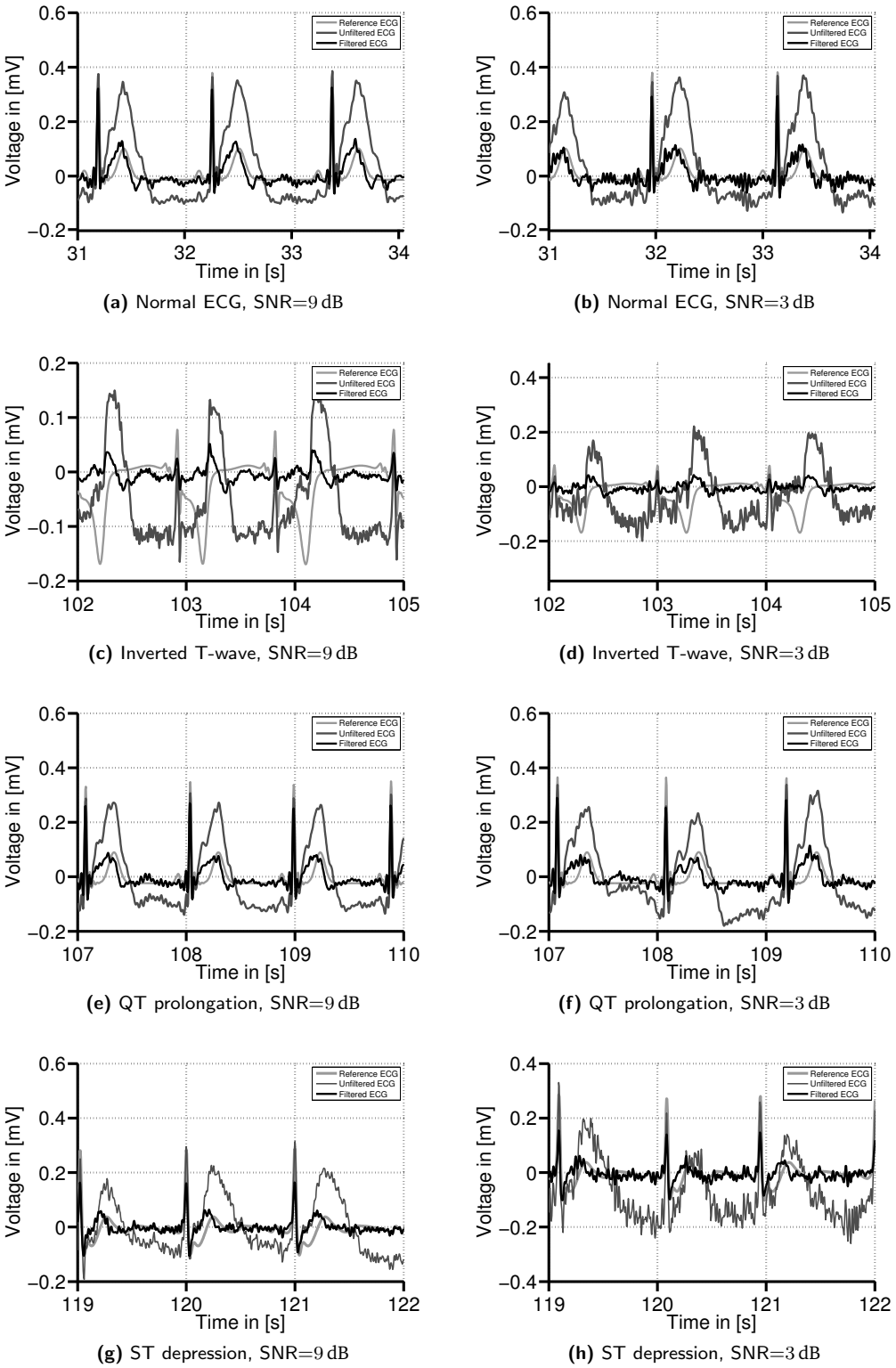

(a) Normal ECG, SNR=9 dB

(b) Normal ECG, SNR=3 dB

(c) Inverted T-wave, SNR=9 dB

(d) Inverted T-wave, SNR=3 dB

(e) QT prolongation, SNR=9 dB

(f) QT prolongation, SNR=3 dB

(g) ST depression, SNR=9 dB

(h) ST depression, SNR=3 dB

Figure 6.6.: Exemplary Wiener filtered signals in simulated ECG records without pathology (a,b), inverted T-waves (c,d), QT prolongation (e,f) and ST depression (g,h) at different SNR levels using $P = 50$ filter coefficients at a sampling rate of $f_s = 250\,\mathrm{Hz}$. In the non-pathological ECG (a,b), the filter output follows the reference ECG. During episodes with inverted T-waves, the filter output did not follow these underlying changes. In episodes with prolonged QT intervals (shifted T-wave), the filter output followed the shape of the desired T-wave but could not precisely follow its location. Errors in the ST-segment are present in all records.

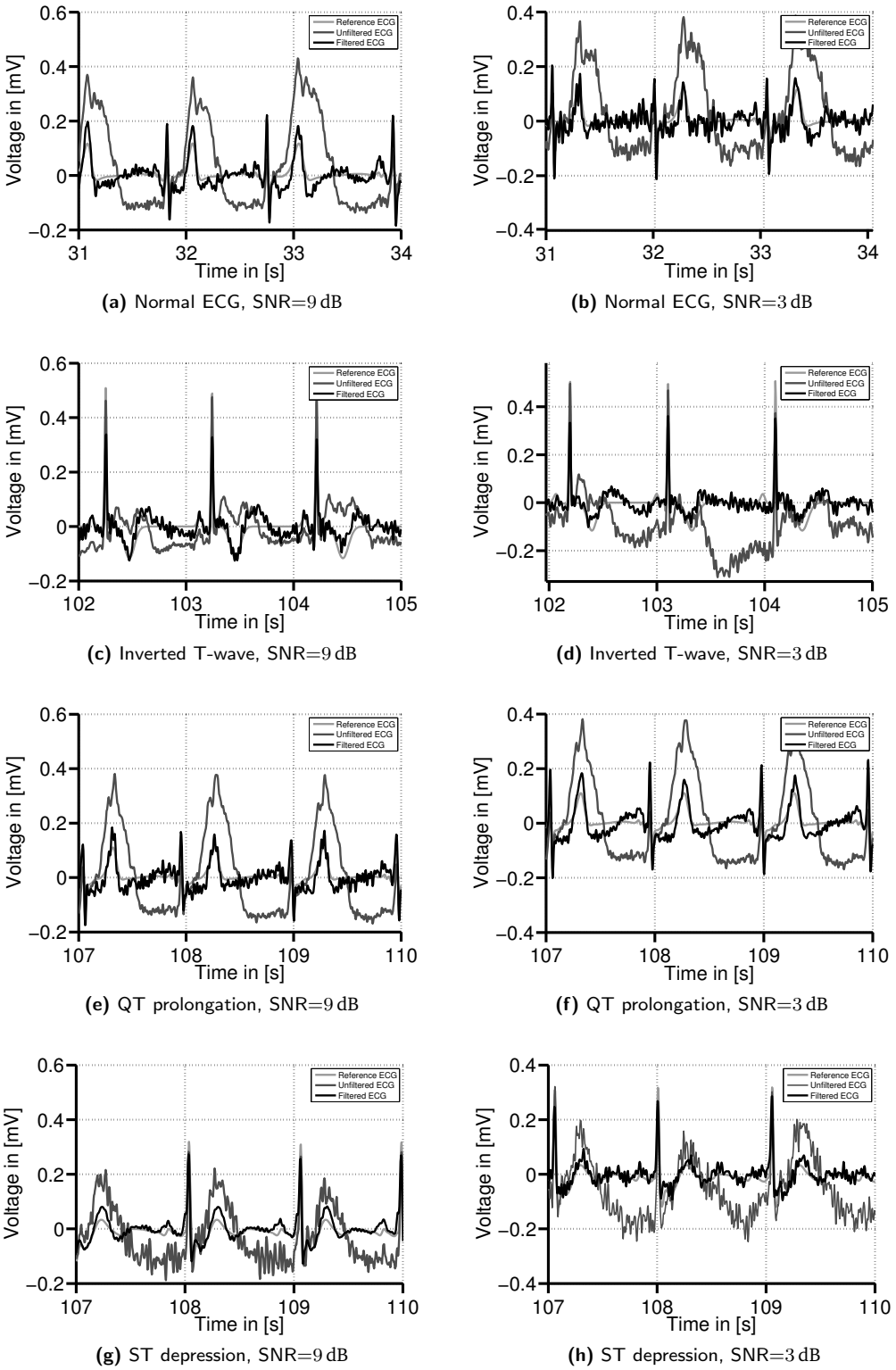

(a) Normal ECG, SNR=9 dB

(b) Normal ECG, SNR=3 dB

(c) Inverted T-wave, SNR=9 dB

(d) Inverted T-wave, SNR=3 dB

(e) QT prolongation, SNR=9 dB

(f) QT prolongation, SNR=3 dB

(g) ST depression, SNR=9 dB

(h) ST depression, SNR=3 dB

Figure 6.7.: Exemplary ICA filtered signals in the simulated ECG records without pathology (a,b), inverted T-waves (c,d), QT prolongation (e,f) and ST depression (g,h) at different SNR levels. In all cases, the ICA filtered signal followed the waveform of the reference ECG but a visible error between the reference ECG and the filter output signal remained. The additional MA noise was not suppressed by this technique, i. e. the IC containing this noise was included in the optimised mixing matrix or it could not be separated from the other signal components.

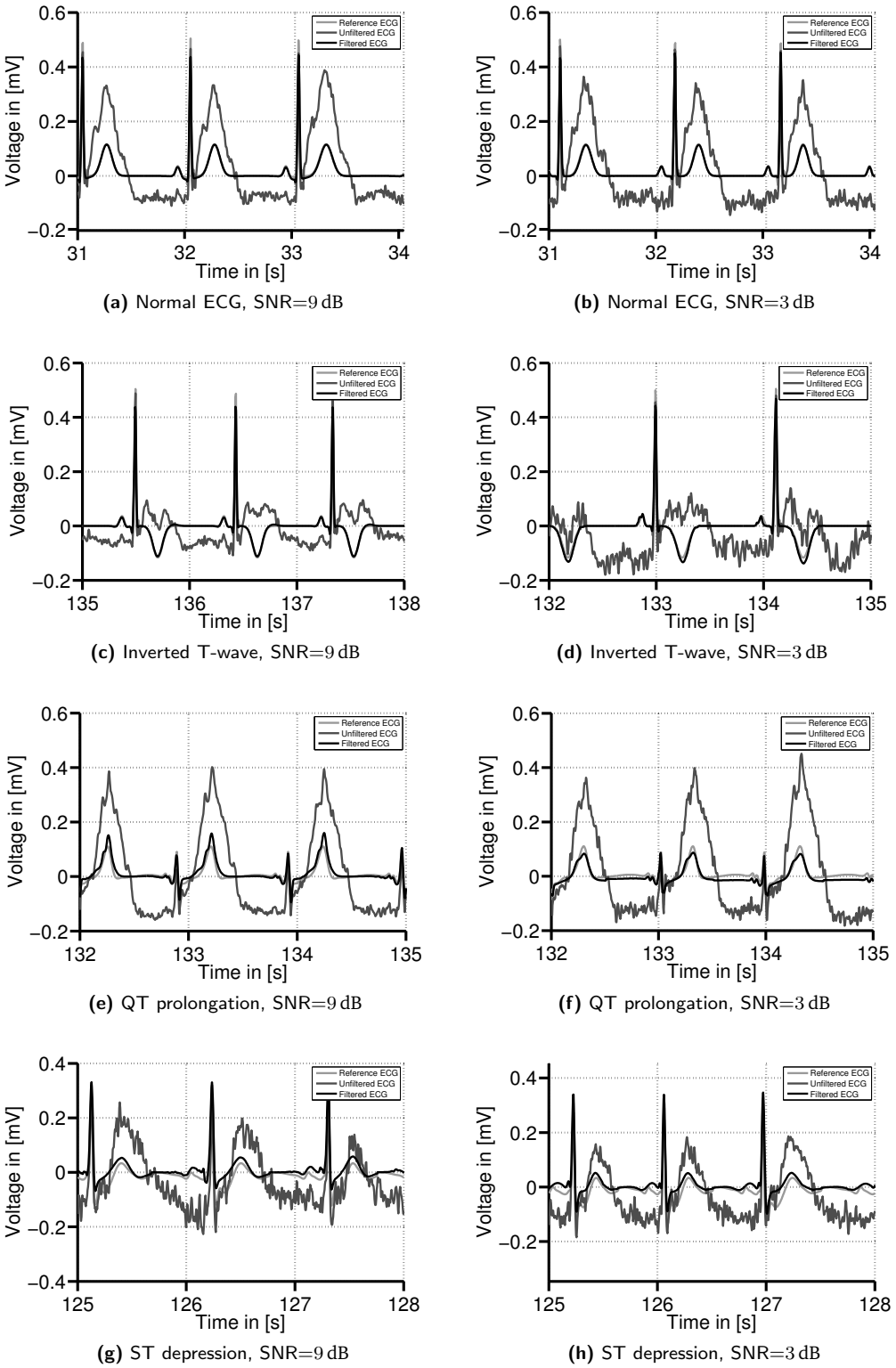

(a) Normal ECG, SNR=9 dB

(b) Normal ECG, SNR=3 dB

(c) Inverted T-wave, SNR=9 dB

(d) Inverted T-wave, SNR=3 dB

(e) QT prolongation, SNR=9 dB

(f) QT prolongation, SNR=3 dB

(g) ST depression, SNR=9 dB

(h) ST depression, SNR=3 dB

Figure 6.8.: Exemplary EKF filtered signals in the simulated ECG records without pathology (a,b), inverted T-waves (c,d), QT prolongation (e,f) and ST depression (g,h) at different SNR levels. In all cases, the filtered signal followed the waveform of the reference ECG whereas the additional MA noise was suppressed by the EKF procedure. Inversions of the T-wave and the QT prolongation were detectable. Larger errors remained in the records with simulated ST depression.

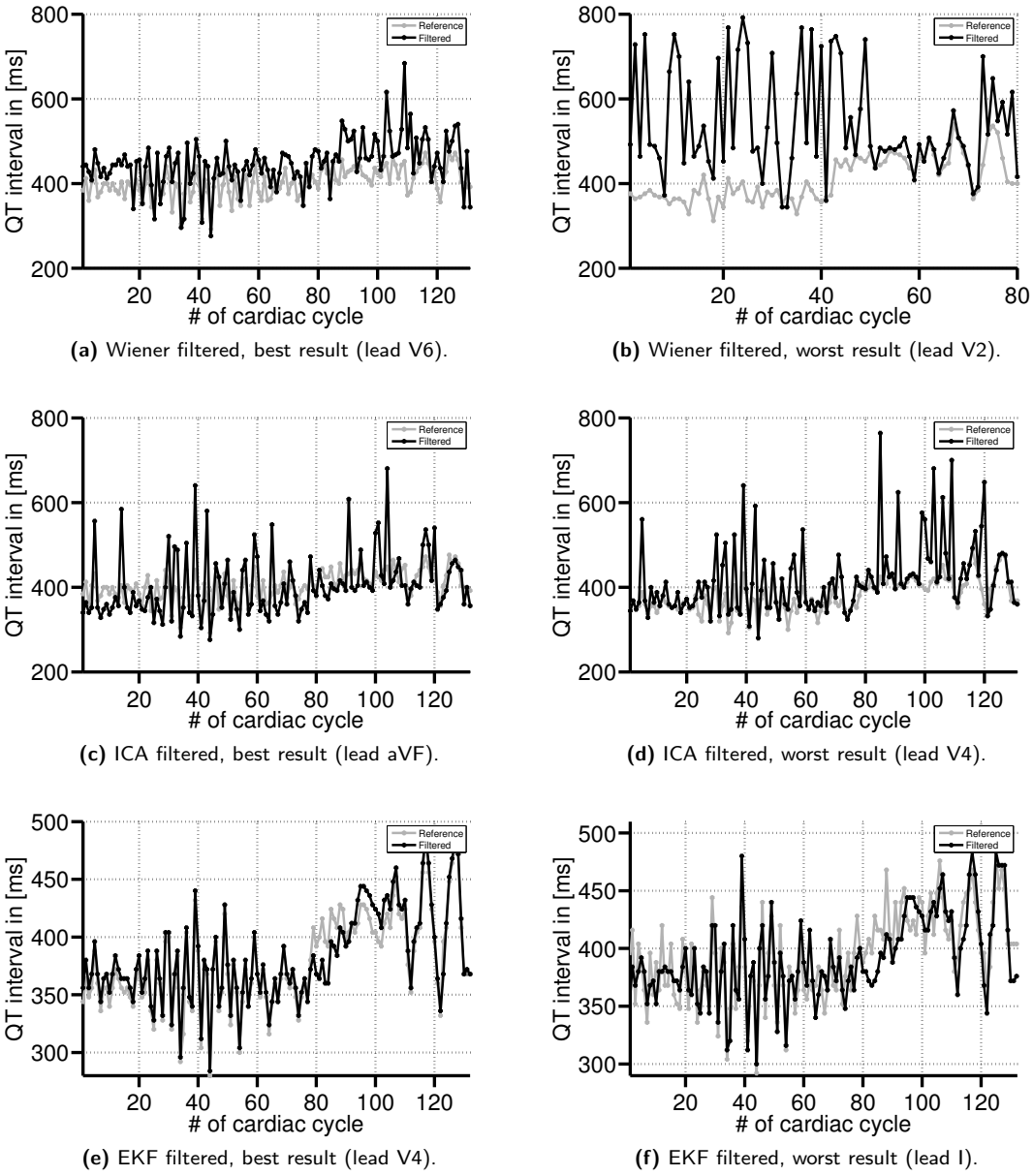

(a) Wiener filtered, best result (lead V6).

(b) Wiener filtered, worst result (lead V2).

(c) ICA filtered, best result (lead aVF).

(d) ICA filtered, worst result (lead V4).

(e) EKF filtered, best result (lead V4).

(f) EKF filtered, worst result (lead I).

Figure 6.9.: Comparison of QT measurements made in the simulated clean reference ECG (grey) and the filtered ECG (black) for the record with simulated QT prolongation (SNR=9 dB). For each filtering method (Wiener, ICA, EKF), the leads with the best and the worse measurement results are shown (compare Table 6.1). The different number of cardiac cycles depends on how many corresponding QT-intervals were detected by *ECGPUWAVE* in the reference and in the filtered ECG. The least distortions are visible in the EKF filtered signals.

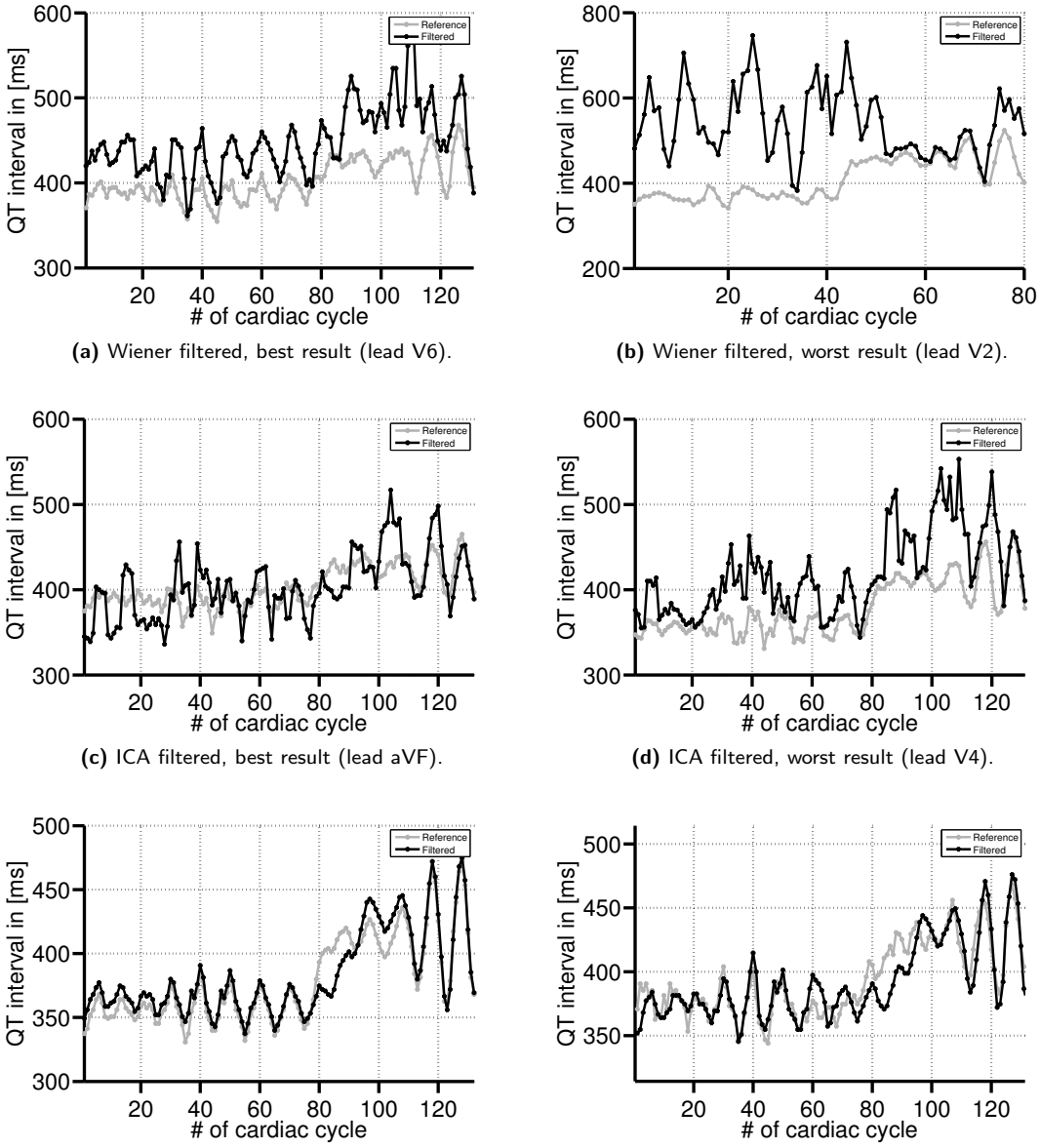

(a) Wiener filtered, best result (lead V6).

(b) Wiener filtered, worst result (lead V2).

(c) ICA filtered, best result (lead aVF).

(d) ICA filtered, worst result (lead V4).

(e) EKF filtered, best result (lead V4).

(f) EKF filtered, worst result (lead I).

Figure 6.10.: Comparison of the filtered (moving average, window length=4) QT measurements of Fig. 6.9 made in the simulated clean reference ECG (grey) and the filtered ECG (black) for the record with simulated QT prolongation (SNR=9 dB). For each filtering method (Wiener, ICA, EKF), the leads with the best and the worse measurement results are shown (compare Table 6.1). The different number of cardiac cycles depends on how many corresponding QT-intervals were detected by *ECGPUWAVE* in the reference and in the filtered ECG. The least distortions are visible in the EKF filtered signals.

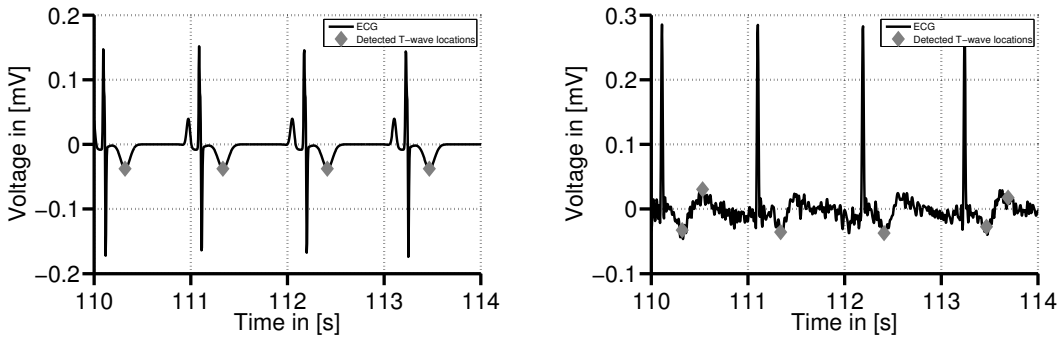

(a) T-waves detected in the reference ECG (negative).

(b) T-waves detected in the ICA filtered ECG (negative/positive biphasic and negative) .

Figure 6.11.: ECG (lead V2) with simulated T-wave inversion. In the reference ECG (a), the *ECGPUWAVE* algorithm classified the the T-waves as inverted (grey dots mark the detected T-wave positions). The ICA filtered ECG (b) shows T-waves with high negative amplitude followed by a smaller wave of positive amplitude. The waves were partly classified as negative T-waves (single annotation as in the 2nd or 3rd T-wave) or as negative/positive biphasic (double annotations as in the 1st or 4th T-wave).

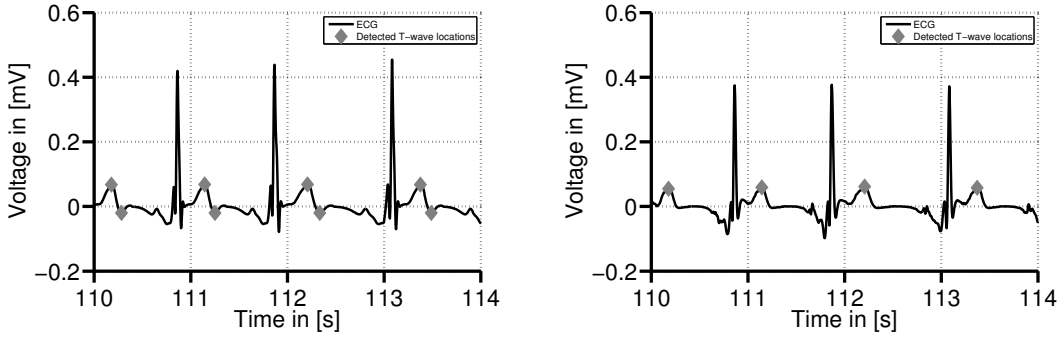

(a) T-waves detected in the reference ECG (positive/negative biphasic).

(b) T-waves detected in the EKF filtered ECG (positive).

Figure 6.12.: ECG (lead III) of the record without simulated pathology (normal ECG). The T-waves in the reference ECG (a) were classified as biphasic by the *ECGPUWAVE* algorithm. In the EKF filtered ECG (b), only a small negative wave was visible and hence, these T-waves were classified normal.

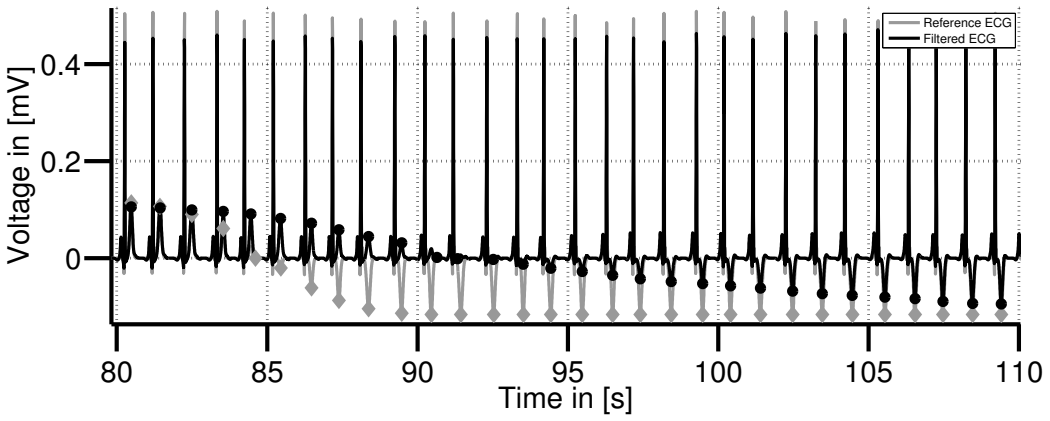

Figure 6.13.: Delayed response of the EKF output to the inverted T-wave in lead V4. The inversion of the T-wave can be detected with a delay of $\approx 10\,\mathrm{s}$ at the filter output. (For illustration purposes, the shown annotations are the reference annotations of the T-waves.)

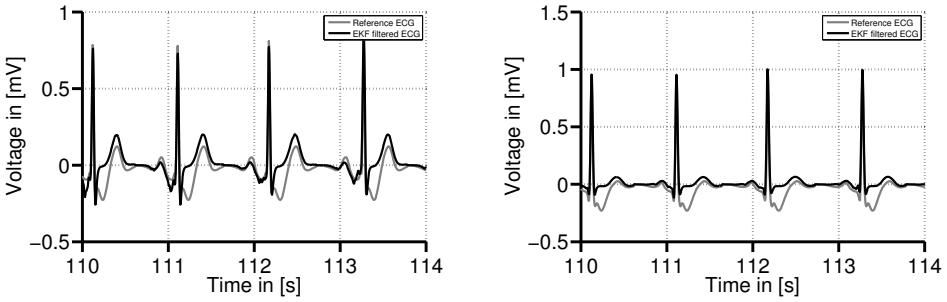

(a) EKF filtered ECG, lead II.

(b) EKF filtered ECG, lead V6.

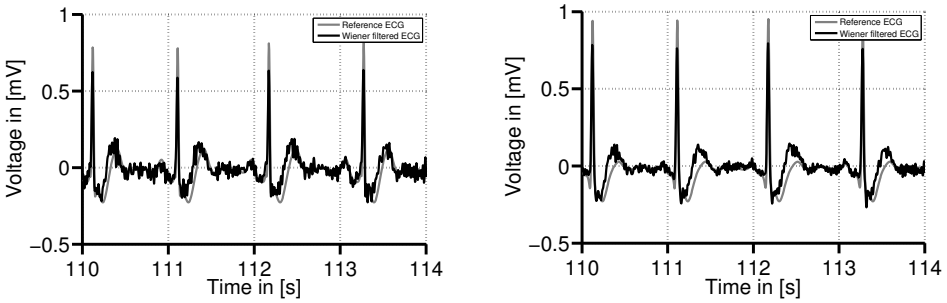

(c) Wiener filtered ECG, lead II.

(d) Wiener filtered ECG, lead V6.

Figure 6.14.: Comparison of EKF (a,b) and Wiener filtered (c,d) signals of two ECG leads (II and V6) with simulated ST depression. It can be seen that the EKF was not able to track the depressed ST-segment. In contrast, the ST depression can be recognised in the Wiener filtered signal.

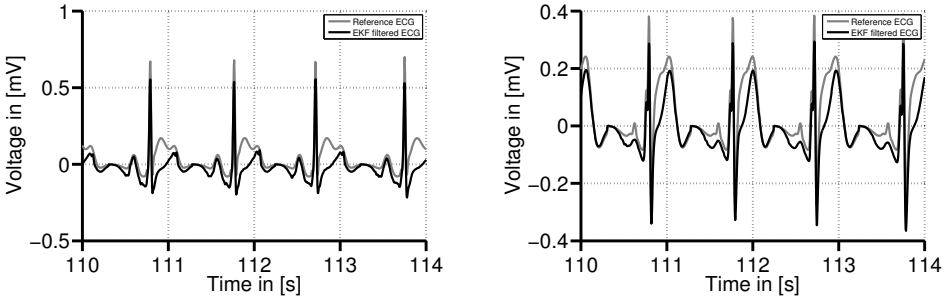

(a) EKF filtered ECG, lead aVF.

(b) EKF filtered ECG, lead V4.

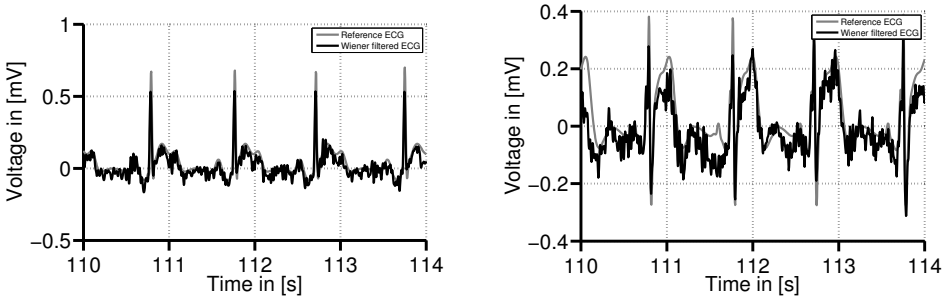

(c) Wiener filtered ECG, lead aVF.

(d) Wiener filtered ECG, lead V4.

Figure 6.15.: Comparison of EKF (a,b) and Wiener filtered (c,d) signals of two ECG leads (aVF and V4) simulated ST elevation. It can be seen that the EKF was not able to track the elevated ST-segment. In contrast, the ST elevated can be recognised in the Wiener filtered signal.

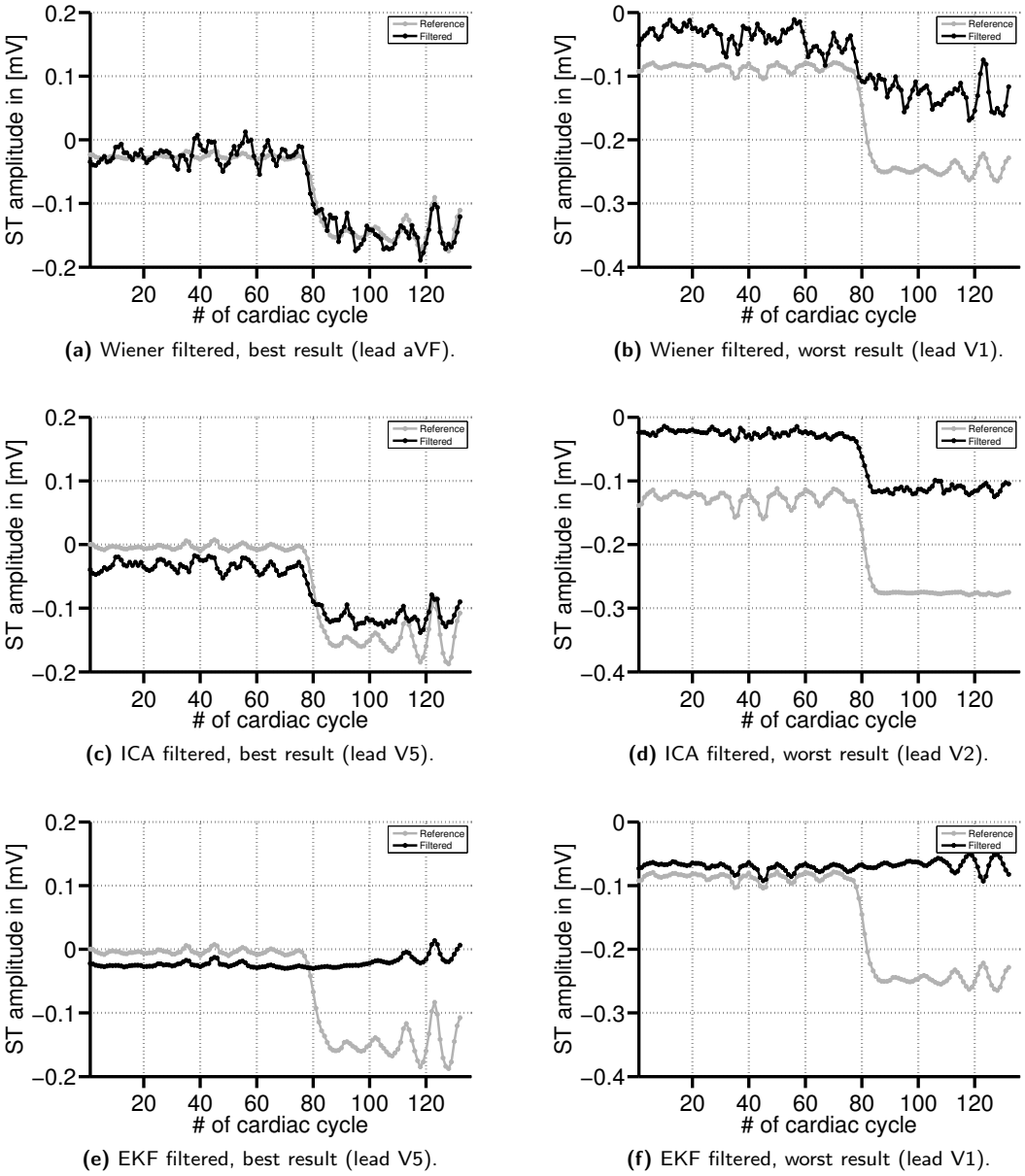

(a) Wiener filtered, best result (lead aVF).

(b) Wiener filtered, worst result (lead V1).

(c) ICA filtered, best result (lead V5).

(d) ICA filtered, worst result (lead V2).

(e) EKF filtered, best result (lead V5).

(f) EKF filtered, worst result (lead V1).

Figure 6.16.: Comparison of ST measurements made in the simulated clean reference ECG (grey) and the filtered ECG (black) for the record with simulated ST depression (SNR=9 dB). For each filtering technique (Wiener, ICA, EKF), the leads with the best and the worse measurement results are shown (compare Table 6.6).

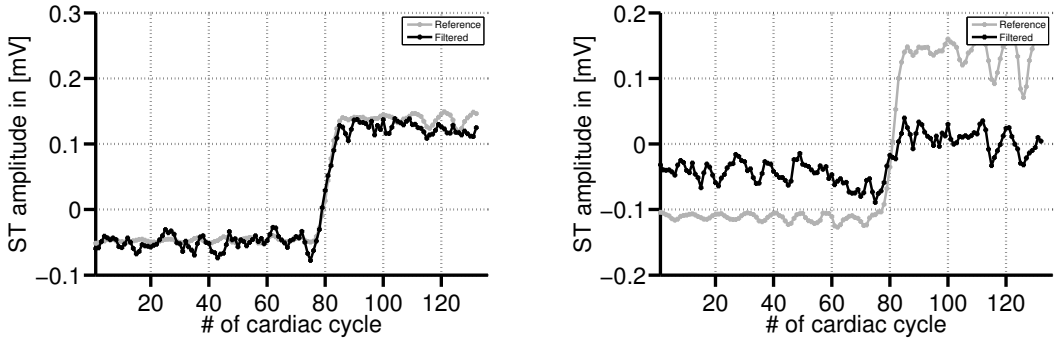

(a) Wiener filtered, best result (lead aVF).

(b) Wiener filtered, worst result (lead V1).

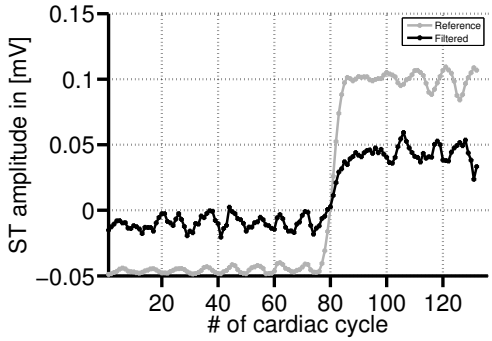

(c) ICA filtered, best result (lead III).

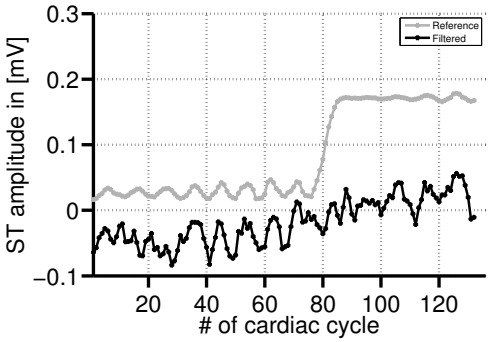

(d) ICA filtered, worst result (lead V4).

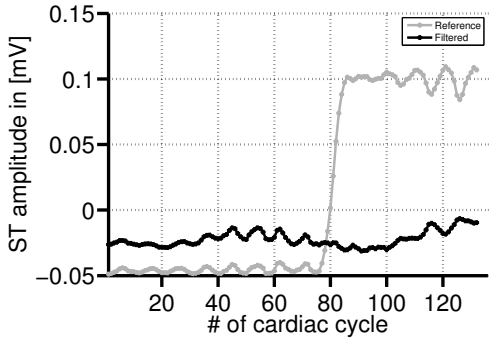

(e) EKF filtered, best result (lead III).

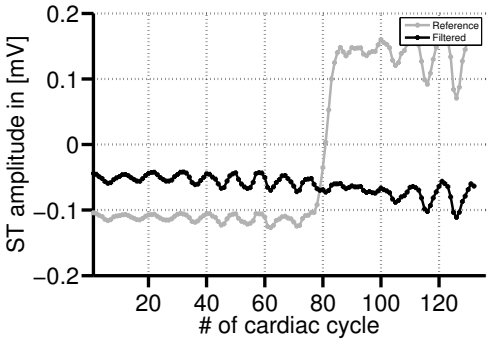

(f) EKF filtered, worst result (lead V1).

Figure 6.17.: Comparison of ST measurements made in the simulated clean reference ECG (grey) and the filtered ECG (black) for the record with simulated ST elevation (SNR=9 dB). For each filtering technique (Wiener, ICA, EKF), the leads with the best and the worse measurement results are shown (compare Table 6.8).

Table 6.1.: QT measurement errors in the ECG with simulated QT prolongation (SNR=9 dB) using the different filtering methods (Wiener filter, ICA, EKF). The measured errors are reported for the normal (non-pathological), the transitional and the pathological (QT prolongation) sections of the ECG. All values are given in [ms]. (μ = mean absolute error, σ = standard deviation of the measurement errors, p_5 = 5th percentile, p_{95} = 95th percentile.)

	Wiener filter									ICA									EKF								
	Normal			Trans			Patho			Normal			Trans			Patho			Normal			Trans			Patho		
Lead	$\mu \pm \sigma$	p_5	p_{95}	$\mu \pm \sigma$	p_5	p_{95}	$\mu \pm \sigma$	p_5	p_{95}	$\mu \pm \sigma$	p_5	p_{95}	$\mu \pm \sigma$	p_5	p_{95}	$\mu \pm \sigma$	p_5	p_{95}	$\mu \pm \sigma$	p_5	p_{95}	$\mu \pm \sigma$	p_5	p_{95}	$\mu \pm \sigma$	p_5	p_{95}
I	66 ± 28	20	108	94 ± 44	32	152	101 ± 40	62	172	53 ± 70	4	220	54 ± 69	0	248	40 ± 57	0	158	17 ± 10	4	32	21 ± 13	0	44	20 ± 9	4	32
II	69 ± 37	12	144	81 ± 31	10	126	- ± -	-	-	39 ± 48	0	120	63 ± 73	4	240	85 ± 88	8	289	24 ± 16	0	44	29 ± 18	4	60	26 ± 15	12	60
III	36 ± 21	6	76	- ± -	-	-	- ± -	-	-	64 ± 75	0	216	57 ± 67	0	213	20 ± 28	0	74	12 ± 6	4	21	- ± -	-	-	- ± -	-	-
aVR	93 ± 22	56	124	106 ± 32	61	154	112 ± 27	59	150	35 ± 58	0	144	46 ± 73	0	212	41 ± 67	0	198	7 ± 6	4	24	13 ± 11	0	28	11 ± 6	4	24
aVL	59 ± 15	39	85	60 ± 27	24	118	68 ± 42	11	128	59 ± 78	8	208	59 ± 72	8	212	20 ± 28	4	65	18 ± 9	8	24	17 ± 9	4	32	13 ± 9	0	30
aVF	- ± -	-	-	- ± -	-	-	- ± -	-	-	- ± -	-	-	- ± -	-	-	- ± -	-	-	10 ± 14	0	26	9 ± 11	0	22	10 ± 11	4	20
V1	53 ± 38	8	124	66 ± 48	4	168	70 ± 46	14	160	- ± -	-	-	- ± -	-	-	- ± -	-	-	43 ± 33	4	88	72 ± 51	8	164	47 ± 33	4	87
V2	198 ± 114	57	388	169 ± 160	8	433	71 ± 81	0	260	59 ± 89	4	268	73 ± 80	0	252	109 ± 96	12	324	7 ± 13	0	12	15 ± 21	0	68	11 ± 15	0	26
V3	61 ± 44	4	140	105 ± 107	4	356	110 ± 80	11	268	62 ± 53	4	188	68 ± 62	8	208	64 ± 60	4	222	49 ± 43	4	104	80 ± 35	8	140	58 ± 38	0	100
V4	51 ± 50	8	168	84 ± 81	0	220	111 ± 95	4	291	48 ± 59	0	208	52 ± 78	0	240	46 ± 78	0	277	7 ± 7	4	12	13 ± 11	0	36	6 ± 6	0	17
V5	52 ± 45	4	120	88 ± 98	0	312	92 ± 89	4	280	49 ± 75	0	216	37 ± 63	0	180	18 ± 32	0	76	15 ± 9	0	24	16 ± 11	0	36	18 ± 14	4	46
V6	45 ± 23	8	72	58 ± 50	4	112	64 ± 54	0	189	53 ± 49	12	200	45 ± 45	4	164	31 ± 25	0	69	17 ± 13	0	44	26 ± 15	8	56	15 ± 9	4	32
μ	71 ± 40	20	141	91 ± 68	15	215	89 ± 62	18	211	52 ± 65	3	199	55 ± 68	2	217	47 ± 56	3	175	19 ± 15	3	38	28 ± 19	3	62	21 ± 15	3	43
p_5	41 ± 18			59 ± 29			66 ± 32			37 ± 48			41 ± 53			19 ± 26			7 ± 6			11 ± 10			8 ± 6		
p_{95}	146 ± 82			141 ± 136			112 ± 93			63 ± 84			71 ± 79			98 ± 92			46 ± 38			76 ± 43			53 ± 36		

Table 6.2.: QT measurement errors in the ECG with simulated QT prolongation (SNR=3 dB) using the different filtering methods (Wiener filter, ICA, EKF). The measured errors are reported for the normal (non-pathological), the transitional and the pathological (QT prolongation) sections of the ECG. All values are given in [ms]. (μ = mean absolute error, σ = standard deviation of the measurement errors, p_5 = 5th percentile, p_{95} = 95th percentile.)

	Wiener filter									ICA									EKF								
	Normal			Trans			Patho			Normal			Trans			Patho			Normal			Trans			Patho		
Lead	$\mu \pm \sigma$	p_5	p_{95}	$\mu \pm \sigma$	p_5	p_{95}	$\mu \pm \sigma$	p_5	p_{95}	$\mu \pm \sigma$	p_5	p_{95}	$\mu \pm \sigma$	p_5	p_{95}	$\mu \pm \sigma$	p_5	p_{95}	$\mu \pm \sigma$	p_5	p_{95}	$\mu \pm \sigma$	p_5	p_{95}	$\mu \pm \sigma$	p_5	p_{95}
I	65 ± 35	16	132	95 ± 69	16	280	106 ± 88	0	294	152 ± 100	12	352	136 ± 101	20	332	129 ± 104	16	290	23 ± 20	0	52	29 ± 21	0	60	26 ± 18	4	57
II	112 ± 84	18	283	153 ± 100	52	336	- ± -	-	-	178 ± 100	36	412	158 ± 106	12	353	124 ± 101	12	282	19 ± 26	0	64	19 ± 16	0	40	27 ± 9	12	38
III	98 ± 87	10	271	79 ± 75	4	223	81 ± 67	4	202	95 ± 85	6	300	95 ± 94	8	300	55 ± 65	7	213	13 ± 14	0	40	24 ± 16	0	49	- ± -	-	-
aVR	104 ± 39	68	221	116 ± 68	47	277	130 ± 82	3	264	169 ± 101	42	354	146 ± 91	36	332	146 ± 110	4	302	11 ± 15	0	44	16 ± 15	0	40	24 ± 13	4	44
aVL	70 ± 32	16	124	80 ± 69	15	231	101 ± 67	21	224	127 ± 95	8	344	155 ± 98	12	350	95 ± 96	3	272	13 ± 14	0	44	24 ± 15	4	52	29 ± 15	11	52
aVF	107 ± 109	2	293	119 ± 136	1	408	98 ± 71	10	193	127 ± 138	5	379	144 ± 117	4	356	151 ± 93	6	305	9 ± 7	0	22	- ± -	-	-	- ± -	-	-
V1	78 ± 63	8	188	70 ± 45	8	168	59 ± 40	0	118	- ± -	-	-	- ± -	-	-	- ± -	-	-	30 ± 26	3	70	42 ± 41	0	92	- ± -	-	-
V2	195 ± 120	36	452	147 ± 136	4	429	108 ± 78	15	296	124 ± 107	4	292	103 ± 93	4	284	173 ± 104	15	319	9 ± 15	0	16	15 ± 19	0	64	10 ± 5	0	20
V3	129 ± 110	12	296	148 ± 116	8	348	131 ± 84	7	250	114 ± 81	28	288	104 ± 89	12	308	120 ± 87	7	254	49 ± 42	0	108	51 ± 39	0	116	56 ± 35	8	100
V4	165 ± 107	24	416	174 ± 96	44	364	192 ± 92	30	337	158 ± 91	16	312	147 ± 101	8	344	136 ± 108	8	321	15 ± 18	0	48	17 ± 15	0	44	18 ± 15	0	60
V5	151 ± 106	12	404	159 ± 91	64	356	194 ± 86	63	345	145 ± 93	28	312	146 ± 101	16	364	129 ± 111	4	329	17 ± 18	0	52	25 ± 17	0	52	34 ± 28	0	71
V6	91 ± 94	16	332	97 ± 84	8	252	111 ± 86	17	246	120 ± 95	16	336	113 ± 93	8	320	106 ± 93	20	272	17 ± 19	0	44	27 ± 23	0	68	20 ± 18	0	48
μ	114 ± 82	20	284	120 ± 90	23	306	119 ± 76	15	252	137 ± 99	18	335	132 ± 99	13	331	124 ± 97	9	287	19 ± 20	0	50	26 ± 22	0	62	27 ± 17	4	54
p_5	68 ± 34			75 ± 58			70 ± 54			105 ± 83			99 ± 90			75 ± 76			9 ± 11			16 ± 15			13 ± 7		
p_{95}	179 ± 115			166 ± 136			193 ± 90			174 ± 123			157 ± 112			162 ± 111			39 ± 33			47 ± 40			47 ± 32		

Table 6.3.: QT measurement errors in the ECG with simulated QT prolongation (SNR=9 dB and SNR=3 dB) using the different filtering methods (Wiener filter, ICA, EKF). The measured errors are reported for the complete ECG (covering the normal (non-pathological), the transitional and the pathological (QT prolongation) sections). All values are given in [ms]. (μ = mean absolute error, σ = standard deviation of the measurement errors, p_5 = 5th percentile, p_{95} = 95th percentile.)

	SNR=9 dB									SNR=3 dB								
	Wiener filter			ICA			EKF			Wiener filter			ICA			EKF		
Lead	$\mu \pm \sigma$	p_5	p_{95}	$\mu \pm \sigma$	p_5	p_{95}	$\mu \pm \sigma$	p_5	p_{95}	$\mu \pm \sigma$	p_5	p_{95}	$\mu \pm \sigma$	p_5	p_{95}	$\mu \pm \sigma$	p_5	p_{95}
I	88 ± 41	31	145	50 ± 66	0	223	20 ± 11	0	36	89 ± 68	16	259	139±101	16	333	26 ± 20	0	56
II	- ± -	-	-	62 ± 72	4	241	27 ± 17	4	60	- ± -	-	-	155±104	12	345	21 ± 18	0	45
III	- ± -	-	-	49 ± 64	0	206	- ± -	-	-	86 ± 77	4	224	83 ± 85	8	267	- ± -	-	-
aVR	103 ± 29	56	149	42 ± 67	0	208	10 ± 9	0	28	116 ± 65	37	259	152 ± 99	19	325	17 ± 15	0	44
aVL	61 ± 29	21	119	49 ± 67	8	201	16 ± 9	4	32	82 ± 60	16	222	131 ± 99	7	331	22 ± 16	3	52
aVF	- ± -	-	-	- ± -	-	-	10 ± 12	0	20	110±115	4	325	142±115	4	320	- ± -	-	-
V1	64 ± 45	8	160	- ± -	-	-	55 ± 43	4	158	69 ± 49	8	161	- ± -	-	-	- ± -	-	-
V2	152±139	4	416	78 ± 88	4	278	12 ± 18	0	68	150±122	15	418	127±103	4	293	12 ± 15	0	56
V3	94 ± 89	4	280	65 ± 59	4	209	66 ± 40	4	114	138±107	8	332	111 ± 86	12	294	52 ± 39	0	108
V4	82 ± 80	0	229	49 ± 73	0	226	9 ± 9	0	28	176 ± 98	39	357	147±100	8	329	17 ± 16	0	48
V5	79 ± 85	4	278	35 ± 61	0	183	17 ± 11	0	36	166 ± 95	46	356	141±101	12	346	25 ± 21	0	68
V6	56 ± 45	4	113	44 ± 43	4	132	21 ± 14	4	52	99 ± 87	12	273	113 ± 93	12	309	23 ± 21	0	56
μ	87 ± 65	15	210	52 ± 66	2	211	24 ± 18	2	57	116 ± 86	19	290	131 ± 99	10	317	24 ± 20	0	59
p_5	58 ± 29			38 ± 50			10 ± 9			76 ± 55			97 ± 86			14 ± 15		
p_{95}	132±119			72 ± 81			61 ± 42			171±119			154±110			42 ± 32		

Table 6.4.: T-wave detection performance in the ECG records with simulated T-wave inversion (SNR=9 dB) filtered using the different methods (Wiener filter, ICA and EKF). The sensitivity Se and the positive predictive value $+P$ (given in [%]) were computed separately for each section (normal, transitional and pathological) and for the complete ECG record. (μ = mean detection performance, p_5 = 5th percentile, p_{95} = 95th percentile.)

	Wiener filter								ICA								EKF							
	Normal		Transition		Pathological		Complete		Normal		Transition		Pathological		Complete		Normal		Transition		Pathological		Complete	
Lead	Se	$+P$	Se	$+P$	Se	$+P$	Se	$+P$	Se	$+P$	Se	$+P$	Se	$+P$	Se	$+P$	Se	$+P$	Se	$+P$	Se	$+P$	Se	$+P$
I	100.0	100.0	62.1	62.1	.0	.0	61.5	85.3	-	-	-	-	-	-	-	-	100.0	100.0	90.9	90.9	91.7	100.0	94.7	97.3
II	100.0	100.0	80.0	77.4	-	-	-	-	91.7	100.0	88.2	88.2	100.0	92.0	93.8	93.8	100.0	100.0	100.0	100.0	100.0	100.0	100.0	100.0
III	46.7	100.0	61.0	61.0	98.0	75.0	67.3	75.9	76.0	100.0	100.0	100.0	100.0	100.0	90.4	100.0	100.0	100.0	100.0	100.0	100.0	100.0	100.0	100.0
aVR	100.0	100.0	-	-	-	-	-	-	-	-	-	-	-	-	-	-	100.0	100.0	97.8	97.8	100.0	100.0	99.3	99.3
aVL	-	-	-	-	-	-	-	-	-	-	-	-	-	-	-	-	-	-	-	-	-	-	-	-
aVF	46.2	100.0	65.0	61.9	81.1	71.4	62.0	74.1	92.0	100.0	97.1	97.1	100.0	97.6	96.0	98.4	100.0	100.0	100.0	100.0	100.0	100.0	100.0	100.0
V1	100.0	100.0	95.2	95.2	92.6	100.0	95.2	98.3	88.2	100.0	96.0	96.0	79.2	100.0	85.6	98.7	100.0	100.0	97.7	97.7	100.0	100.0	99.0	99.0
V2	27.6	100.0	35.0	34.1	26.3	45.5	29.4	50.6	-	-	-	-	-	-	-	-	100.0	100.0	92.5	92.5	93.2	100.0	95.8	97.9
V3	20.7	100.0	58.5	55.8	69.8	73.2	46.5	68.8	91.7	100.0	85.7	85.7	93.9	91.2	90.8	93.4	100.0	100.0	89.8	89.8	90.6	100.0	93.8	96.8
V4	47.6	100.0	-	-	73.3	91.7	-	-	81.0	100.0	78.6	78.6	73.6	92.9	77.4	89.8	100.0	100.0	91.7	91.7	92.3	100.0	95.0	97.4
V5	39.1	100.0	62.5	60.6	71.4	83.3	56.7	78.2	77.8	100.0	90.0	90.0	88.9	95.2	85.6	95.0	100.0	100.0	93.8	93.8	94.2	100.0	96.3	98.1
V6	62.5	100.0	52.6	51.3	63.2	68.6	59.7	71.2	-	-	-	-	-	-	-	-	100.0	100.0	95.7	95.7	96.1	100.0	97.5	98.7
μ	62.8	100	63.5	62.2	64	67.6	59.8	75.3	85.5	100	90.8	90.8	90.8	95.6	88.5	95.6	100	100	95.4	95.4	96.2	100	97.4	98.6
p_5	24.2	100	42	41	10.5	18.2	35.4	57	76.5	100	80.7	80.7	75.3	91.4	79.9	90.9	100	100	90.4	90.4	91.2	100	94.3	97.1
p_{95}	100	100	89.1	88.1	95.8	96.7	85.4	93.8	91.9	100	99.1	99.1	100	100	95.3	99.6	100	100	100	100	100	100	100	100

Table 6.5.: T-wave detection performance in the ECG records with simulated T-wave inversion (SNR=3 dB) filtered using the different methods (Wiener filter, ICA and EKF). The sensitivity Se and the positive predictive value $+P$ (given in [%]) were computed separately for each section (normal, transitional and pathological) and for the complete ECG record. (μ = mean detection performance, p_5 = 5th percentile, p_{95} = 95th percentile.)

	Wiener filter								ICA								EKF							
	Normal		Transition		Pathological		Complete		Normal		Transition		Pathological		Complete		Normal		Transition		Pathological		Complete	
Lead	Se	+P	Se	+P	Se	+P	Se	+P	Se	+P	Se	+P	Se	+P	Se	+P	Se	+P	Se	+P	Se	+P	Se	+P
I	9.5	100.0	10.8	10.8	23.4	40.7	15.1	27.9	65.0	100.0	50.0	48.5	31.4	64.7	49.5	69.7	100.0	100.0	88.6	88.6	89.6	100.0	93.4	96.6
II	67.9	100.0	57.1	53.3	43.2	73.1	57.0	74.3	67.9	100.0	88.9	88.9	88.2	95.7	80.9	94.6	100.0	100.0	81.6	81.6	83.7	100.0	90.1	94.8
III	33.3	100.0	62.2	57.1	51.0	73.5	48.0	70.3	66.7	100.0	91.3	91.3	98.0	94.2	84.7	94.8	-	-	-	-	88.0	100.0	-	-
aVR	57.1	100.0	-	-	85.0	100.0	-	-	94.1	100.0	88.2	88.2	73.9	100.0	82.5	95.2	100.0	100.0	85.0	85.0	100.0	100.0	95.3	95.3
aVL	-	-	-	-	-	-	-	-	-	-	-	-	-	-	-	-	-	-	-	-	-	-	-	-
aVF	45.8	100.0	58.7	56.3	56.8	69.4	53.6	69.8	82.1	100.0	88.6	88.6	100.0	90.7	89.9	93.1	100.0	100.0	-	-	92.3	100.0	-	-
V1	27.3	100.0	44.7	43.6	54.5	100.0	45.2	68.1	76.9	100.0	60.5	59.0	33.3	100.0	53.8	78.1	100.0	100.0	80.8	80.8	-	-	-	-
V2	95.8	100.0	58.6	58.6	-	-	-	-	100.0	100.0	-	-	-	-	-	-	100.0	100.0	93.3	93.3	93.9	100.0	96.1	98.0
V3	84.6	100.0	97.8	97.8	95.6	97.7	92.3	98.5	80.0	100.0	81.5	81.5	84.6	91.7	82.3	90.8	100.0	100.0	90.9	90.9	91.7	100.0	94.7	97.3
V4	60.0	100.0	63.0	60.4	42.0	72.4	55.1	76.1	73.1	100.0	75.0	75.0	66.0	88.6	71.2	87.6	100.0	100.0	86.4	86.4	89.6	97.7	92.7	95.2
V5	100.0	100.0	70.7	69.0	40.9	85.7	71.9	85.8	72.0	100.0	56.1	56.1	57.1	80.0	62.1	77.7	100.0	100.0	90.2	90.2	91.3	100.0	94.5	97.2
V6	-	-	-	-	-	-	-	-	-	-	51.7	51.7	35.5	73.3	-	-	100.0	100.0	87.8	87.8	89.1	100.0	93.1	96.4
μ	58.1	100	58.2	56.3	54.7	79.2	54.8	71.4	77.8	100	73.2	72.9	66.8	87.9	73	86.8	100	100	87.2	87.2	90.9	99.8	93.7	96.4
p_5	17.5	100	24.4	23.9	30.4	52.2	25.6	42	65.8	100	50.8	49.9	32.3	68.6	51.2	72.9	100	100	81.1	81.1	85.6	98.7	91	94.9
p_{95}	98.1	100	87	86.3	91.4	100	85.2	94.1	97.3	100	90.2	90.2	99.1	100	87.8	95	100	100	92.3	92.3	97.3	100	95.8	97.8

Table 6.6.: ST measurement errors in the ECG with simulated ST depression (SNR=9 dB). The measured errors are reported for the normal (non-pathological), for the transitional and for the pathological (ST depression) sections. The best results in each section are highlighted in grey. All values are given in [μV]. (Δ_{ST} = average ST amplitude difference between the normal and the pathological segment, μ = mean absolute error, σ = standard deviation of the measurement errors, p_5 = 5th percentile, p_{95} = 95th percentile.)

		Wiener filter									ICA									EKF								
		Normal			Trans			Patho			Normal			Trans			Patho			Normal			Trans			Patho		
Lead	Δ_{ST}	$\mu \pm \sigma$	p_5	p_{95}	$\mu \pm \sigma$	p_5	p_{95}	$\mu \pm \sigma$	p_5	p_{95}	$\mu \pm \sigma$	p_5	p_{95}	$\mu \pm \sigma$	p_5	p_{95}	$\mu \pm \sigma$	p_5	p_{95}	$\mu \pm \sigma$	p_5	p_{95}	$\mu \pm \sigma$	p_5	p_{95}	$\mu \pm \sigma$	p_5	p_{95}
I	50	22 ± 11	3	39	39 ± 27	5	84	58 ± 17	29	84	11 ± 5	5	24	20 ± 10	8	34	28 ± 12	9	43	13 ± 2	10	16	26 ± 13	10	42	42 ± 9	28	54
II	141	43 ± 22	10	86	66 ± 45	3	156	87 ± 28	37	135	20 ± 13	2	51	34 ± 20	4	69	49 ± 24	7	85	2 ± 2	1	7	78 ± 69	1	156	153±23	116	185
III	91	24 ± 19	1	57	41 ± 32	3	96	55 ± 21	21	80	15 ± 10	3	32	17 ± 12	2	41	24 ± 15	1	50	12 ± 2	9	15	62 ± 47	10	113	111±15	88	131
aVR	96	41 ± 15	23	64	68 ± 40	14	140	93 ± 22	63	130	14 ± 10	1	32	26 ± 15	7	49	38 ± 18	7	61	7 ± 2	4	11	52 ± 41	6	99	97 ± 16	72	120
aVL	21	10 ± 7	0	20	23 ± 12	5	43	29 ± 7	16	39	7 ± 6	0	18	7 ± 5	1	16	8 ± 6	2	20	13 ± 1	12	14	24 ± 11	12	36	35 ± 3	30	38
aVF	116	22 ± 17	1	51	21 ± 19	2	49	17 ± 15	1	51	17 ± 11	2	43	24 ± 16	2	55	36 ± 19	6	69	6 ± 2	1	8	68 ± 59	2	135	132±19	102	158
V1	157	54 ± 28	15	103	80 ± 53	7	171	114±26	72	165	52 ± 24	17	98	84 ± 42	14	141	118±21	76	145	15 ± 4	7	22	102±82	10	191	178±30	130	217
V2	146	74 ± 50	7	174	47 ± 34	1	107	40 ± 29	5	95	106±24	64	143	130±34	85	173	166±12	146	188	36 ± 7	23	50	118±77	31	202	184±30	136	218
V3	36	71 ± 59	10	179	72 ± 48	11	157	61 ± 47	2	141	114±28	74	171	116±12	97	137	128±19	100	159	47 ± 8	35	64	70 ± 21	43	95	77 ± 12	54	91
V4	90	39 ± 31	3	107	46 ± 34	2	119	39 ± 30	5	86	81 ± 24	51	125	58 ± 25	21	95	39 ± 27	2	86	35 ± 6	27	46	45 ± 14	20	66	68 ± 14	44	88
V5	143	20 ± 17	1	52	45 ± 42	2	147	60 ± 34	9	130	29 ± 17	3	59	33 ± 13	8	52	38 ± 22	3	69	20 ± 4	14	26	76 ± 53	18	139	136±24	97	170
V6	139	21 ± 14	2	49	47 ± 39	2	132	68 ± 23	39	116	12 ± 7	2	24	44 ± 37	1	87	80 ± 22	45	112	7 ± 2	3	9	76 ± 63	7	149	143±25	103	177
μ		37 ± 24	6	82	50 ± 35	5	117	60 ± 25	25	104	40 ± 15	19	68	49 ± 20	21	79	63 ± 18	34	91	18 ± 4	12	24	66 ± 46	14	119	113±18	83	137
p_5		16 ± 9			22 ± 16			24 ± 11			9 ± 6			13 ± 8			17 ± 9			4 ± 2			25 ± 12			39 ± 6		
p_{95}		72 ± 54			76 ± 50			102±40			110±26			122±39			145±25			41 ± 7			109±79			181±30		

Table 6.7.: ST measurement errors in the ECG with simulated ST depression (SNR=3 dB). The measured errors are reported for the normal (non-pathological), for the transitional and for the pathological (ST depression) sections. The best results in each section are highlighted in grey. All values are given in [μV]. (Δ_{ST} = average ST amplitude difference between the normal and the pathological segment, μ = mean absolute error, σ = standard deviation of the measurement errors, p_5 = 5th percentile, p_{95} = 95th percentile.)

		Wiener filter									ICA									EKF								
		Normal			Trans			Patho			Normal			Trans			Patho			Normal			Trans			Patho		
Lead	Δ_{ST}	$\mu \pm \sigma$	p_5	p_{95}	$\mu \pm \sigma$	p_5	p_{95}	$\mu \pm \sigma$	p_5	p_{95}	$\mu \pm \sigma$	p_5	p_{95}	$\mu \pm \sigma$	p_5	p_{95}	$\mu \pm \sigma$	p_5	p_{95}	$\mu \pm \sigma$	p_5	p_{95}	$\mu \pm \sigma$	p_5	p_{95}	$\mu \pm \sigma$	p_5	p_{95}
I	51	16 ± 10	2	37	37 ± 25	5	73	60 ± 13	37	83	15 ± 6	5	26	14 ± 9	2	29	11 ± 8	1	25	16 ± 2	14	19	26 ± 16	10	50	48 ± 6	37	56
II	145	51 ± 30	7	102	80 ± 46	15	165	116±36	57	182	24 ± 19	4	57	37 ± 31	2	103	51 ± 32	4	103	41 ± 5	35	50	74 ± 44	25	148	125±19	94	150
III	94	25 ± 19	3	62	42 ± 32	2	92	67 ± 30	23	121	17 ± 11	1	34	29 ± 22	1	73	40 ± 24	5	83	25 ± 5	18	33	48 ± 29	15	98	77 ± 14	57	96
aVR	98	45 ± 15	22	66	77 ± 40	16	133	113±18	83	138	18 ± 14	2	41	24 ± 19	3	63	30 ± 20	2	62	28 ± 3	24	33	50 ± 30	20	99	86 ± 12	65	104
aVL	21	13 ± 9	2	33	19 ± 13	2	44	30 ± 10	17	47	9 ± 5	1	16	13 ± 6	3	23	15 ± 9	3	31	4 ± 3	0	9	11 ± 7	3	24	15 ± 4	8	21
aVF	119	28 ± 19	2	62	26 ± 25	1	82	32 ± 26	1	89	20 ± 15	2	46	32 ± 26	3	90	45 ± 28	4	93	33 ± 5	26	41	61 ± 36	17	123	101±16	75	123
V1	162	83 ± 46	16	164	108±65	10	226	149±51	76	246	22 ± 12	5	44	71 ± 45	11	144	111±19	84	142	31 ± 4	25	37	77 ± 54	24	170	131±24	90	166
V2	151	99 ± 77	2	251	114±65	23	232	138±85	15	270	21 ± 16	2	48	62 ± 39	5	120	85 ± 33	40	145	20 ± 5	13	27	69 ± 55	7	162	113±30	57	153
V3	38	79 ± 68	4	220	86 ± 58	8	183	107±64	17	228	112±15	84	133	117±23	78	161	118±11	94	131	11 ± 4	5	18	22 ± 17	0	49	25 ± 11	6	42
V4	92	42 ± 34	3	109	36 ± 26	4	80	40 ± 31	3	92	15 ± 11	1	34	23 ± 20	1	63	41 ± 20	3	71	37 ± 4	32	42	50 ± 27	15	97	92 ± 16	67	120
V5	147	30 ± 16	5	62	62 ± 46	4	136	100±34	55	150	13 ± 9	2	34	37 ± 31	4	98	64 ± 22	27	95	43 ± 3	38	50	75 ± 44	30	147	132±17	100	159
V6	143	31 ± 17	2	63	70 ± 45	4	138	108±24	65	140	16 ± 7	2	25	56 ± 46	3	130	100±18	70	127	37 ± 3	32	42	71 ± 45	24	146	124±17	95	149
μ		45 ± 30	6	103	63 ± 41	8	132	88 ± 35	37	149	25 ± 12	9	45	43 ± 26	10	91	59 ± 20	28	92	27 ± 4	22	33	53 ± 34	16	109	89 ± 16	63	112
p_5		15 ± 10			23 ± 20			31 ± 12			11 ± 6			14 ± 8			13 ± 9			8 ± 3			17 ± 12			21 ± 5		
p_{95}		90 ± 72			111±65			143±73			64 ± 17			92 ± 45			114±32			42 ± 5			76 ± 54			131±27		

Table 6.8.: ST measurement errors in the ECG with simulated ST elevation (SNR=9 dB). The measured errors are reported for the normal (non-pathological), for the transitional and for the pathological (ST elevation) sections. The best results in each section are highlighted in grey. All values are given in [μV]. (Δ_{ST} = average ST amplitude difference between the normal and the pathological segment, μ = mean absolute error, σ = standard deviation of the measurement errors, p_5 = 5th percentile, p_{95} = 95th percentile.)

		Wiener filter									ICA									EKF								
		Normal			Trans			Patho			Normal			Trans			Patho			Normal			Trans			Patho		
Lead	Δ_{ST}	$\mu \pm \sigma$	p_5	p_{95}	$\mu \pm \sigma$	p_5	p_{95}	$\mu \pm \sigma$	p_5	p_{95}	$\mu \pm \sigma$	p_5	p_{95}	$\mu \pm \sigma$	p_5	p_{95}	$\mu \pm \sigma$	p_5	p_{95}	$\mu \pm \sigma$	p_5	p_{95}	$\mu \pm \sigma$	p_5	p_{95}	$\mu \pm \sigma$	p_5	p_{95}
I	79	26 ± 7	14	37	39 ± 19	8	71	53 ± 7	40	63	4 ± 4	0	13	34 ± 27	0	63	61 ± 4	54	67	4 ± 2	2	8	42 ± 36	2	82	81 ± 5	70	86
II	225	46 ± 22	13	90	63 ± 29	17	110	86 ± 14	65	112	33 ± 11	14	47	73 ± 45	17	133	117±21	84	152	30 ± 3	25	34	117±89	19	221	195±19	158	218
III	146	19 ± 15	1	47	71 ± 54	4	142	125±13	105	145	37 ± 9	20	50	44 ± 16	19	70	57 ± 17	30	86	26 ± 3	21	29	75 ± 53	16	140	114±14	88	132
aVR	152	48 ± 12	33	68	59 ± 24	18	92	78 ± 8	62	89	15 ± 7	4	24	51 ± 38	4	98	89 ± 13	69	110	17 ± 2	14	20	80 ± 63	12	151	138±12	114	151
aVL	33	10 ± 6	1	22	14 ± 8	1	29	23 ± 6	13	32	20 ± 4	12	26	11 ± 9	1	26	5 ± 4	1	13	11 ± 2	8	13	16 ± 9	6	29	16 ± 4	9	23
aVF	185	17 ± 13	4	43	17 ± 14	3	42	18 ± 14	1	44	35 ± 10	17	47	58 ± 30	19	101	87 ± 19	57	119	28 ± 2	23	31	96 ± 71	17	181	155±16	123	175
V1	251	74 ± 21	41	105	87 ± 48	18	157	138±25	95	171	69 ± 9	52	85	72 ± 21	25	106	81 ± 31	37	138	59 ± 4	53	66	132±80	35	224	217±20	180	235
V2	234	46 ± 35	2	122	44 ± 32	8	111	47 ± 36	3	113	101±28	54	146	60 ± 40	3	134	39 ± 31	2	89	75 ± 5	67	81	123±59	40	195	187±20	151	205
V3	60	43 ± 36	1	118	54 ± 44	4	131	51 ± 40	4	158	113±45	41	186	91 ± 42	15	166	73 ± 37	19	122	54 ± 4	47	60	33 ± 18	11	57	23 ± 6	12	32
V4	143	27 ± 17	5	54	51 ± 37	3	115	57 ± 32	17	118	72 ± 31	26	123	110±57	29	188	149±28	107	195	7 ± 3	2	11	82 ± 71	2	160	151±11	128	162
V5	227	23 ± 16	2	59	66 ± 47	5	136	99 ± 23	56	136	12 ± 8	2	25	79 ± 65	3	155	144±15	118	170	21 ± 3	17	28	120±96	15	228	216±17	182	233
V6	222	31 ± 14	7	50	64 ± 43	4	125	101±15	79	120	28 ± 8	12	40	71 ± 45	18	128	116±19	83	149	32 ± 3	28	38	117±86	23	214	204±17	171	220
μ		34 ± 18	10	68	52 ± 33	8	105	73 ± 19	45	108	45 ± 15	21	68	63 ± 36	13	114	85 ± 20	55	118	30 ± 3	26	35	86 ± 61	17	157	141±13	116	156
p_5		14 ± 7			16 ± 11			21 ± 7			8 ± 4			24 ± 13			24 ± 4			6 ± 2			25 ± 14			20 ± 5		
p_{95}		60 ± 35			78 ± 51			131±38			106±37			100±61			146±34			66 ± 4			127±92			216±20		

Table 6.9.: ST measurement errors in the ECG with simulated ST elevation (SNR=3 dB). The measured errors are reported for the normal (non-pathological), for the transitional and for the pathological (ST elevation) sections. The best results in each section are highlighted in grey. All values are given in [μV]. (Δ_{ST} = average ST amplitude difference between the normal and the pathological segment, μ = mean absolute error, σ = standard deviation of the measurement errors, p_5 = 5th percentile, p_{95} = 95th percentile.)

		Wiener filter									ICA									EKF								
		Normal			Trans			Patho			Normal			Trans			Patho			Normal			Trans			Patho		
Lead	Δ_{ST}	$\mu \pm \sigma$	p_5	p_{95}	$\mu \pm \sigma$	p_5	p_{95}	$\mu \pm \sigma$	p_5	p_{95}	$\mu \pm \sigma$	p_5	p_{95}	$\mu \pm \sigma$	p_5	p_{95}	$\mu \pm \sigma$	p_5	p_{95}	$\mu \pm \sigma$	p_5	p_{95}	$\mu \pm \sigma$	p_5	p_{95}	$\mu \pm \sigma$	p_5	p_{95}
I	79	26 ± 17	7	59	41 ± 24	4	82	60 ± 14	37	87	5 ± 4	0	12	35 ± 28	1	70	63 ± 4	54	69	2 ± 2	0	5	38 ± 31	4	75	63 ± 9	43	72
II	226	71 ± 40	2	140	61 ± 28	17	120	68 ± 33	7	124	21 ± 18	1	67	75 ± 55	8	170	123±34	62	170	11 ± 3	7	18	116±99	0	230	206±17	175	228
III	146	30 ± 20	0	60	64 ± 47	3	140	104±29	51	144	20 ± 16	1	55	42 ± 29	2	100	61 ± 29	11	100	11 ± 5	6	20	83 ± 67	5	156	143±10	124	156
aVR	153	57 ± 24	22	105	58 ± 23	19	88	72 ± 22	39	114	12 ± 10	2	35	55 ± 42	4	120	93 ± 19	57	119	6 ± 1	4	8	75 ± 69	1	153	135±13	111	150
aVL	33	18 ± 14	1	45	16 ± 11	2	35	19 ± 11	2	39	10 ± 7	1	27	9 ± 7	0	22	10 ± 8	1	31	5 ± 3	1	12	25 ± 15	5	44	40 ± 3	36	44
aVF	186	34 ± 21	3	74	35 ± 30	1	98	40 ± 20	8	76	20 ± 17	1	63	58 ± 42	5	135	92 ± 32	35	135	11 ± 4	7	21	99 ± 85	3	193	175±13	150	192
V1	253	102±52	10	173	89 ± 50	17	178	124±50	14	189	74 ± 19	46	114	69 ± 27	25	125	74 ± 31	23	115	23 ± 4	14	29	128±95	12	249	219±21	179	244
V2	237	122±88	11	276	82 ± 59	7	192	80 ± 52	6	170	132 ± 9	121	146	71 ± 52	6	134	30 ± 20	1	65	35 ± 5	24	44	121±96	9	234	209±25	168	259
V3	62	116±89	8	285	105±68	21	215	81 ± 54	14	168	145±15	117	166	110±26	73	151	86 ± 24	42	128	33 ± 5	24	41	36 ± 24	3	65	61 ± 24	43	135
V4	143	68 ± 47	6	153	69 ± 49	6	144	68 ± 47	6	170	70 ± 23	29	105	104±45	33	169	141±27	93	176	17 ± 4	9	22	68 ± 61	0	139	117±22	55	134
V5	228	43 ± 32	5	108	71 ± 50	4	156	106±43	43	193	21 ± 19	2	52	82 ± 61	4	181	137±31	76	180	5 ± 2	1	9	111±97	5	224	194±21	152	217
V6	223	41 ± 26	4	89	69 ± 42	7	135	100±25	59	149	24 ± 10	8	44	74 ± 51	7	152	124±17	92	148	4 ± 3	0	9	110±94	7	220	192±18	160	214
μ		61 ± 39	7	131	63 ± 40	9	132	77 ± 33	24	135	46 ± 14	27	74	65 ± 39	14	127	86 ± 23	46	120	14 ± 3	8	20	84 ± 70	5	165	146±16	116	170
p_5		22 ± 16			26 ± 18			31 ± 13			8 ± 6			23 ± 17			21 ± 6			3 ± 2			31 ± 20			52 ± 6		
p_{95}		119±88			96 ± 63			114±53			138±21			107±58			139±33			34 ± 5			124±99			214±24		

Table 6.10.: ST measurement errors for the complete ECG with simulated ST depression (SNR=9 dB and SNR=3 dB). The best results in each section are highlighted in grey. All values are given in [μV]. (Δ_{ST} = average ST amplitude difference between the normal and the pathological segment, μ = mean absolute error, σ = standard deviation of the measurement errors, p_5 = 5th percentile, p_{95} = 95th percentile.)

	SNR=9 dB									SNR=3 dB								
	Wiener filter			ICA			EKF			Wiener filter			ICA			EKF		
Lead	$\mu \pm \sigma$	p_5	p_{95}	$\mu \pm \sigma$	p_5	p_{95}	$\mu \pm \sigma$	p_5	p_{95}	$\mu \pm \sigma$	p_5	p_{95}	$\mu \pm \sigma$	p_5	p_{95}	$\mu \pm \sigma$	p_5	p_{95}
I	39 ± 24	5	80	19 ± 11	6	39	26 ± 14	11	49	37 ± 25	3	74	13 ± 8	2	28	29 ± 16	12	54
II	64 ± 39	9	133	33 ± 22	3	75	75 ± 73	1	174	80 ± 46	12	166	36 ± 29	3	100	77 ± 44	31	148
III	39 ± 28	4	89	18 ± 13	2	44	60 ± 49	10	124	44 ± 32	3	93	28 ± 21	2	74	48 ± 28	18	94
aVR	66 ± 35	21	128	26 ± 17	2	56	50 ± 44	5	112	76 ± 39	22	133	24 ± 18	2	62	53 ± 30	21	101
aVL	21 ± 12	2	41	8 ± 5	1	18	23 ± 11	12	38	20 ± 13	2	44	12 ± 7	2	24	10 ± 6	1	21
aVF	20 ± 17	1	51	25 ± 17	3	58	66 ± 62	2	149	28 ± 24	1	83	32 ± 25	2	88	63 ± 36	25	121
V1	81 ± 47	11	164	83 ± 41	19	144	96 ± 83	10	208	110 ± 62	19	228	67 ± 46	10	139	77 ± 53	25	163
V2	53 ± 40	3	116	132 ± 34	84	175	111 ± 77	30	214	115 ± 74	7	252	56 ± 40	4	134	66 ± 53	13	150
V3	69 ± 51	10	165	118 ± 20	88	155	65 ± 20	41	94	90 ± 62	7	214	115 ± 18	84	142	20 ± 14	3	44
V4	42 ± 31	3	110	60 ± 29	13	109	47 ± 17	27	79	39 ± 30	3	99	25 ± 20	1	63	56 ± 29	25	104
V5	41 ± 36	1	120	33 ± 17	5	63	75 ± 57	16	158	62 ± 45	5	138	36 ± 30	2	92	80 ± 45	33	153
V6	44 ± 34	2	105	44 ± 37	2	104	73 ± 67	5	165	68 ± 44	3	136	55 ± 44	3	127	75 ± 45	30	145
μ	48 ± 33	6	109	50 ± 22	19	87	64 ± 48	14	130	64 ± 41	7	138	42 ± 26	10	89	55 ± 33	20	108
p_5	21 ± 15			14 ± 8			25 ± 13			24 ± 19			13 ± 8			16 ± 10		
p_{95}	74 ± 49			124 ± 39			103 ± 80			112 ± 67			89 ± 45			78 ± 53		

Table 6.11.: ST measurement errors for the complete ECG with simulated ST elevation (SNR=9 dB and SNR=3 dB). The best results in each section are highlighted in grey. All values are given in [μV]. (Δ_{ST} = average ST amplitude difference between the normal and the pathological segment, μ = mean absolute error, σ = standard deviation of the measurement errors, p_5 = 5th percentile, p_{95} = 95th percentile.)

	SNR=9 dB									SNR=3 dB								
	Wiener filter			ICA			EKF			Wiener filter			ICA			EKF		
Lead	$\mu \pm \sigma$	p_5	p_{95}	$\mu \pm \sigma$	p_5	p_{95}	$\mu \pm \sigma$	p_5	p_{95}	$\mu \pm \sigma$	p_5	p_{95}	$\mu \pm \sigma$	p_5	p_{95}	$\mu \pm \sigma$	p_5	p_{95}
I	39 ± 17	14	63	32 ± 28	0	66	41 ± 37	2	85	42 ± 23	6	78	34 ± 29	1	69	34 ± 31	0	73
II	63 ± 28	17	107	73 ± 45	16	141	111 ± 86	24	218	66 ± 33	7	124	72 ± 56	3	161	108 ± 100	1	229
III	70 ± 54	2	142	45 ± 17	21	76	70 ± 49	20	137	64 ± 45	3	137	40 ± 29	2	92	77 ± 67	6	155
aVR	60 ± 21	28	90	50 ± 38	5	104	76 ± 62	13	151	62 ± 23	24	102	52 ± 43	3	114	70 ± 67	1	151
aVL	15 ± 9	2	29	12 ± 9	1	25	15 ± 7	6	28	17 ± 12	1	39	10 ± 7	1	27	23 ± 17	3	42
aVF	18 ± 14	2	43	59 ± 30	18	108	91 ± 68	23	178	36 ± 25	2	78	56 ± 42	2	126	93 ± 83	4	192
V1	96 ± 45	26	163	74 ± 22	42	114	132 ± 80	51	232	101 ± 52	14	178	72 ± 26	28	115	120 ± 101	14	245
V2	46 ± 34	3	113	66 ± 42	4	139	125 ± 58	63	202	93 ± 70	7	240	78 ± 53	6	140	118 ± 92	16	235
V3	51 ± 41	2	128	93 ± 44	20	167	36 ± 17	11	59	102 ± 72	9	240	114 ± 31	61	159	41 ± 23	4	66
V4	46 ± 33	5	114	109 ± 53	30	190	78 ± 71	3	160	69 ± 48	6	150	103 ± 44	36	169	66 ± 56	2	136
V5	62 ± 45	5	132	76 ± 66	2	163	116 ± 97	16	231	72 ± 49	6	156	78 ± 62	3	171	101 ± 96	2	219
V6	64 ± 41	7	118	70 ± 46	17	138	114 ± 86	27	219	68 ± 40	7	136	72 ± 51	8	147	100 ± 95	1	217
μ	53 ± 32	9	104	63 ± 37	15	119	84 ± 60	22	158	66 ± 41	8	138	65 ± 39	13	124	79 ± 69	5	163
p_5	17 ± 12			23 ± 13			27 ± 13			27 ± 18			23 ± 17			29 ± 20		
p_{95}	82 ± 49			100 ± 59			128 ± 91			101 ± 71			108 ± 59			119 ± 100		

6.5.2 Real ECG signals

Wiener filter

Exemplary qualitative filtering results of real 3 T ECG records are depicted in Fig. 6.18. It can be seen that the filter output largely depends on the variability of the MHD signal. For both examples shown in Figs. 6.18a and 6.18b, the output of the Wiener filter is still affected by the MHD signal components. Especially smaller peaks, which were present in the MHD signal and were similar to the QRS complex (in the example depicted in Fig. 6.18a approximately in the middle of two adjacent QRS complexes), are still present in the filtered signal. The example depicted in Fig. 6.18b shows a better attenuation of the MHD effect but the QRS complex was also attenuated. Higher variations of the MHD signal were also still visible in the output signal, as can be seen after the first and before the last QRS complex. The morphology of the filtered signals did not correspond to those of the reference signals acquired outside the MR scanner (see Figs. 6.18c and 6.18d). Hence, a reliable analysis of the T-wave or ST-segment does not seem to be possible.

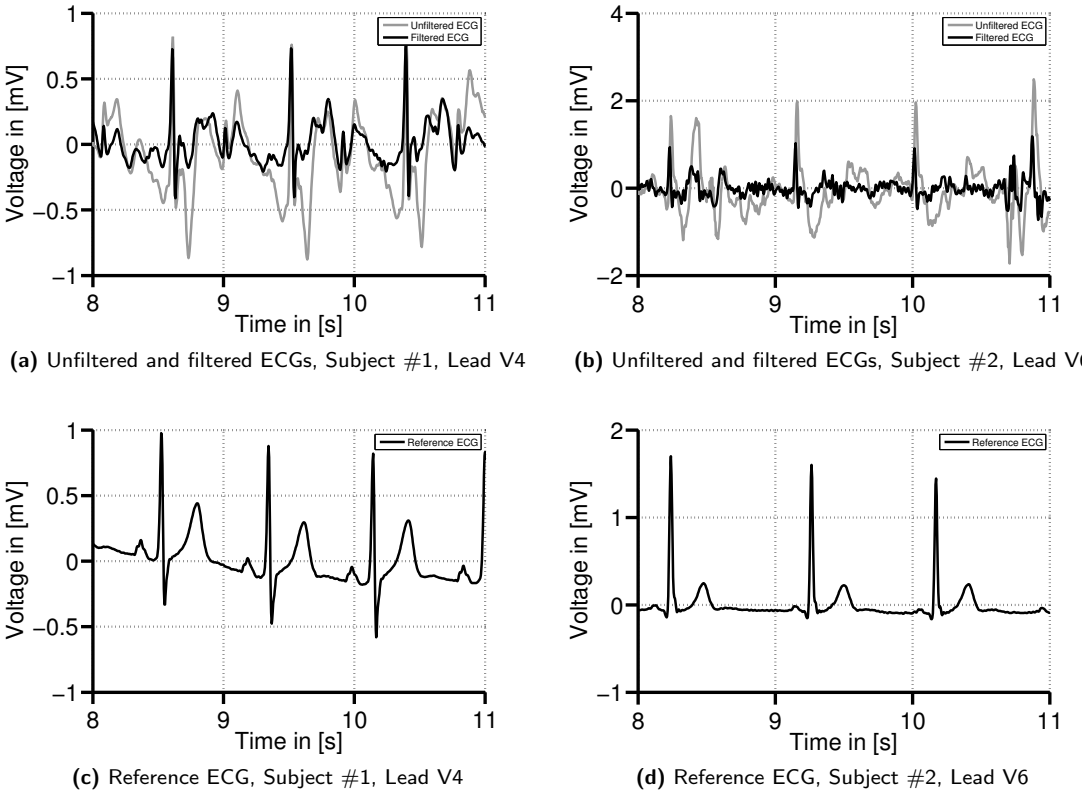

(a) Unfiltered and filtered ECGs, Subject #1, Lead V4

(b) Unfiltered and filtered ECGs, Subject #2, Lead V6

(c) Reference ECG, Subject #1, Lead V4

(d) Reference ECG, Subject #2, Lead V6

Figure 6.18.: Exemplary WF results in real ECG records of two different subjects with the corresponding unfiltered ECGs (a,b). It was difficult or impossible the correctly estimate the end of the T-waves from the unfiltered signals. The filter result still shows high disturbances which do not allow a proper analysis of the T-wave. The filtered signals do not represent the morphology of the reference ECGs acquired outside the MR scanner (c,d).

ICA

Exemplary results of ICA filtered signals are shown in Fig. 6.19. It showed that the quality of the filtered signals largely depended on the subject and on the ECG lead. In general, the influence of the MHD effect can be suppressed by the ICA-filtering technique. The example depicted in Fig. 6.19a shows the reduced MHD effect when compared to the corresponding unfiltered signal. Although the R-peak is clearly visible in this example, the other parts of the ECG – namely the P-wave or the T-wave – cannot be spotted. Figure 6.19b shows an example where the ICA-filtering technique was less successful, i. e. the filtered signal is still dominated by artefacts. These findings are similar to those made in Chapter 5. Using ICA, a detailed diagnostic analysis did not seem to be possible in any of the leads. However, ICA could be used to reduce the MHD effect, which was shown to be helpful for QRS detection purposes.

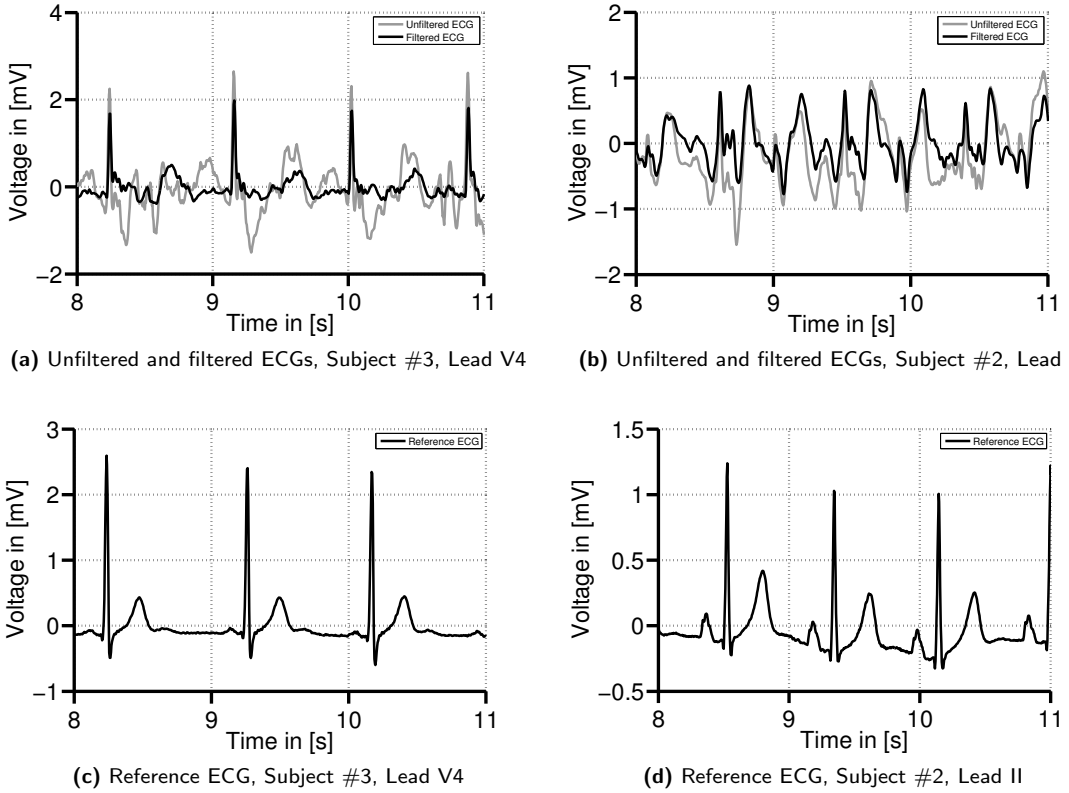

(a) Unfiltered and filtered ECGs, Subject #3, Lead V4

(b) Unfiltered and filtered ECGs, Subject #2, Lead II

(c) Reference ECG, Subject #3, Lead V4

(d) Reference ECG, Subject #2, Lead II

Figure 6.19.: Exemplary ICA filtered ECG records of two different subjects and the corresponding unfiltered ECGs (a,b). In (a), the MHD effect was suppressed in the filtered signal and the QRS complexes are clearly visible. In contrast, the ICA filtered signal shown in (b) is still highly affected by the MHD signal components. The P-wave or T-wave were not preserved in the filtered signals, i. e. it is even not possible to (correctly) identify their locations. The morphology of the reference ECG acquired outside the MR scanner (c,d) was not preserved in the filtered signals.

EKF

Real ECG records filtered by the EKF are depicted in Fig. 6.20. The unfiltered signals depicted in Figs. 6.20a and 6.20b exhibit high beat-to-beat variations of the MHD effect. Using these unfiltered signals, an analysis of the P-wave or T-wave was not possible – it is even not possible to guess their exact locations. In contrast, the filtered ECGs show a smooth and clean estimate of the underlying ECG signal. Besides the T-wave, it was also possible to see the P-wave in the filtered signals.

6.6 Discussion

In this chapter, several filtering methods were applied to simulated and real ECG signals contaminated by the MHD effect. The aim was to improve the diagnostic quality of the ECG signal during MRI which required a suppression or removal of the MHD signal from the ECG. Simulated ECG signals were utilised for a quantitative analysis and comparison of the different filtering methods. Real ECG signals acquired at 3 T were used for a qualitative evaluation. This section discusses the different filtering methods and the simulated signals, which were used during the development and evaluation phase.

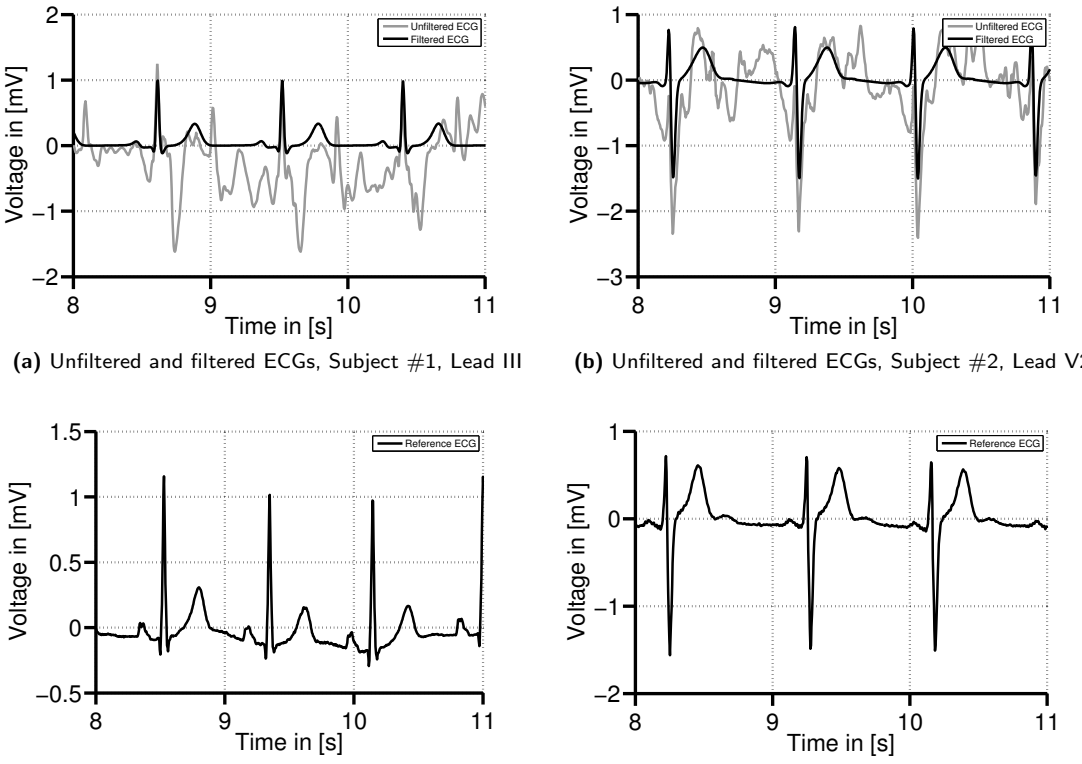

(a) Unfiltered and filtered ECGs, Subject #1, Lead III

(b) Unfiltered and filtered ECGs, Subject #2, Lead V2

(c) Reference ECG, Subject #1, Lead III

(d) Reference ECG, Subject #2, Lead V2

Figure 6.20.: Real ECGs acquired inside the MRI scanner from two different subjects and the corresponding EKF filtered signals (a,b). The reference ECGs acquired outside the MR scanner are depicted in (c,d). The MHD effect and its beat-to-beat variations made it impossible to analyse the P-waves or T-waves in the unfiltered signals (a,b). Despite the high MHD variations, the EKF is able to provide clear traces of the ECG which mostly follow the morphology of the reference ECGs.

Wiener filter

The *Wiener filter coefficients* were computed using PQRST templates. These template were constructed from the normal (i. e. non-pathological) episodes of an ECG record. Once the coefficients were computed, the Wiener filter could be applied in real-time. In the *simulated ECG records*, the Wiener filter did not enable a reliable detection of the QT-interval length or the changes of the T-wave polarity and morphology. As depicted in Fig. 6.6, p. 150, larger signal variations as occurring during an inversion of the T-wave cannot be tracked by the Wiener filter. Even for the normal section of the ECG (where the coefficients were optimised for), larger errors were observed when analysing the T-wave polarity or the QT-interval length. However, the Wiener filter showed a good performance regarding the ST measurements. Especially in the records with simulated ST depression/elevation, the errors made by the Wiener filter in the transitional and pathological sections were lower (in most cases) when compared to the ICA or EKF filtered signals. Nevertheless, the 95$^{\text{th}}$ percentile was $\geq 0.1\,\text{mV}$ in most leads. Hence, the Wiener filter does not seem to be suited to enable a reliable detection of any of the simulated pathologies.

For the *real ECG records*, the same procedure based on PQRST templates was used for the estimation of the WF coefficients. Considering the qualitative comparison of the clean reference ECG and the Wiener filtered signal of the same subject, the results did not satisfy the quality required for a diagnostic analysis, i. e. the measurement of the QT-interval length or the ST amplitude would possibly result in a false clinical diagnosis. As for the simulated signals, PQRST templates of the real ECGs were used for the computation of the filter coefficients. However, the real MHD signals showed higher beat-to-beat variations when compared to the simulated signals. The PQRST templates computed from the real signals could not represent these beat-to-beat variations and hence, these variations were not included in the estimation of the Wiener filter coefficients. This fact can be seen as one reason for the low quality of the filtered signals. In a previous investigation by Krug *et al.* [Krug 12], signal segments only including the ST-segment and the T-wave were concatenated to include the beat-to-beat signal variations and to optimise the results for this segment of the ECG. However, this procedure could not improve the results since errors, especially in the ST-segment, still remained in the filtered output signals. Another method proposed by Tse *et al.* considered the variations in the context of normal and PVC beats in an adaptive filtering filtering approach (but results were not detailed) [Tse 10a, Tse 14]. However, this procedure requires information about the MHD signals during normal and abnormal beats and the corresponding underlying (normal and abnormal or pathological) ECG morphology. Practically, this information is not accessible.

The main limitation was the choice of the input signals (normal, non-pathological ECG signals) used to computed the Wiener filter coefficients. During (the simulated) pathological episodes, the properties of the ECG and MHD signals are subject to changes. The Wiener coefficients do not reflect these changes and hence, an adaption to (pathological) signal variations was not possible.

ICA

ICA was used to separate different signal components. In Chapter 5 it was shown that ICA is not able to completely separate the ECG and MHD signal components, i. e. the computed ICs still contained mixtures of the different signal and noise sources. However, some ICs were dominated by the ECG, whereas other ICs were dominated by the MHD signals. For filtering an ECG using ICA, the challenge was to identify those ICs, which enabled the reconstruction of the underlying ECG morphology by minimising the influence of the MHD effect. The SNR was used to measure the quality of the ICA filtered ECG. An algorithm identified ICs maximising the SNR between a reference ECG and the filtered ECG. This procedure was performed separately for each ECG lead, i. e. one mixing vector was computed for each lead. An optimised mixing matrix was then defined based on the optimised mixing vectors. Once the optimised mixing matrix was computed, ICA-based filtering was applicable in real-time (see the discussion in Section 5.6.2).

In the ICA filtered ECG with *simulated QT prolongation*, the measurement error of the QT-interval length for the records with SNR=9 dB was lower when compared to the results obtained by the Wiener filter. However, a larger error was observed the records with SNR=3 dB. This can be partly explained by the fact that ICA could suppress the MHD signal but not the additional MA noise, i. e. the MA noise was not separated from the other signal components (or was included during the optimisation procedure). When comparing the examples depicted in Figs. 6.6a and 6.7a, it can be seen that the Wiener filter allows a better suppression of the MA noise than the ICA-based method does. The noise was still present since ICA was not able to ideally separate the different signal and noise sources. This could be explained by the fact that there were more sources than observations used in the underlying mixing model.

Considering the analysis of the T-wave morphology, ICA filtered signals achieved good performance ($Se = 88.5\,\%$ and $+P = 95.6\,\%$) in signals with inverted T-waves at SNR=9 dB. For the pathological T-wave inversions and QT prolongation, ICA outperformed the Wiener filter when considering the T-wave detection performance. Moreover, better results were obtained by ICA in the records with simulated QT prolongation (SNR=9dB) and in the normal (non-pathological) ECGs (compare Tables C.5 and C.7, pp. 190).

ICA and Wiener filtered signals achieved a similar performance for the ST measurements, i. e. both methods achieved comparable average errors. For the transitional and pathological sections of ECG signals with ST depression or elevation, lower errors were obtained with ICA than with the EKF technique (see Tables 6.6–6.9). It was already shown in Section 6.5.1.2 that the EKF (with its used parameter configuration) was not able to track the depression or elevation of the ST-segment.

The qualitative results of the *real ECG signals* showed a reduction or attenuation of the MHD effect in the ICA filtered signals (compare Figs. 6.19a and 6.19b, p. 166). From these results, it is obvious that an analysis of the ST-segment or of the T-wave is not possible. Consequently, ICA cannot be used to filter ECG signals during MRI for diagnostic purposes. It was also shown in Chapter 5 that a higher number of ECG leads, especially of the precordial leads, is advantageous for the application of ICA and the separation of ECG and MHD signal components. Typical clinical ECG devices used during MRI are usually limited to two (linearly independent) leads. It would therefore be preferable to have ECG devices with more leads available during MRI. The recent works by Dukkipati *et al.* and Tse *et al.* show that there is a strong interest to make advances in this direction [Dukkipati 08, Tse 10b, Tse 12, Tse 14].

Finally, the divergences of the results for the simulated and real ECG records using the ICA-based

filtering still need to be clarified. As it can be seen in Fig. 6.7, p. 151 and Fig. 6.19, p. 166, a better quality was achieved using the simulated signals (although this finding was not always underpinned by the quantitative results). This can be explained by the model, which was used for the generation of the synthetic ECG and MHD signals (see Section 4.2). Since the simulated 12-lead ECG was derived from the three leads of a VCG model (see Section 4.2.4), all ECG leads are represented by a linear combination of three different source signals (x, y and z components of the VCG; see Section 2.1.3). In contrast, a 'real' 12-lead ECG consists of eight leads (I,II,V1-V6, see Section 2.1.2), which cannot be represented as linear combinations of each other[4]. The sources of the real ECG and MHD signals are spatially distributed and the signals collected by the different ECG electrodes placed on the torso are not linearly related. Because of their spatial distribution, the number of sources is not necessarily limited to the number of sensors since all blood vessels contribute to the MHD effect and the heart itself can be divided into several sources (e. g. the separation of atrial and ventricular activity). Hence, the sources and mixing properties used in the simulation model do not correspond their real counterpart. For future simulation studies using ICA or similar techniques, the existing mixing model could be adjusted such that the number of underlying sources is more realistic, i. e. that the different ECG leads are linearly independent. This could be achieved by using real 12-lead ECG signals superimposed with simulated MHD signals. In general, ICA-based filtering can be applied in real-time by applying the once computed demixing matrix $\mathbf{W}$ to the latest input samples $\mathbf{x}$.

EKF

Overall, the best results for both, the simulated and real ECG records, were achieved by the EKF method. Considering the *simulated ECG records*, the EKF was able to track the simulated inversions of T-waves and the prolonged QT-intervals at different noise levels. The EKF enabled a precise estimation of the QT-interval length in different simulated records. For the classification of the T-wave morphology, the EKF filtered ECG signals showed the best performance. It was observed that the T-wave classification performance slightly dropped in the transitional sections of the ECG with simulated T-wave inversion. This observation was explained by the fact that the EKF parameters were evolving slowly so that the inverted T-waves were detectable with a delay of approximately $10\,\mathrm{s}$ (see Figure 6.13, p. 155). This delay was also observed for the ECGs with simulated prolongation of the QT-interval, where the error of the QT measurement slightly increased in the transitional section (compare Table 6.1).

ST-segment amplitude measurements in the EKF filtered signals showed low errors ($\leq 0.1\,\mathrm{mV}$) for most of the simulated pathologies. However, it turned out that the EKF was not able to adapt to the changes occurring in the records with simulated depression or elevation of the ST-segment (compare Tables 6.6–6.9). This problem was illustrated by an example depicted in Fig. 6.14, p. 156. Although the EKF was able to adapt to changes of the T-wave (T-wave inversion and shift of the T-wave during QT prolongation), changes of the ST-segment were not tracked. It can be assumed that this behaviour was caused by the underlying ECG model used in the EKF (see Section 4.2.2). This model utilised the sum of seven Gaussian functions to simulate the ECG signal (it was previously shown that seven Gaussian are sufficient to represent the fiducials of the ECG: two Gaussians for the P-wave, three Gaussians for the QRS complex and two Gaussian for the T-wave [Sayadi 10]). The placement of the seven Gaussians was optimised by a random search strategy. Since this placement was performed for the clean ECG (no MHD effect, no pathology), it can occur that no Gaussian is placed within the ST-segment. Hence, the EKF could less easily adapt to these variations.

[4] In fact, a VCG can be used to represent a 12-lead ECG (and *vice versa*), but only with a loss of information [Augustyniak 01]

Another important aspect is the training records, which were used to find the optimal parameters for the EKF. The training dataset was composed of ECG records, which were simulated using the information from the real ECG signals (see Section 4.2.3). No pathological episodes were included in the training dataset. Since the EKF parameters were optimised for the non-pathological ECG signals, it is possible that the EKF trusts the model slightly too much and therefore follows the original model. This would be another explanation for the lower performance of the EKF in the pathological section of those records with simulated depression or elevation of the ST-segment.

Although the elevations or depressions of the ST-segment were not directly observable in the EKF-filtered ECG signals, larger variations were observed in the corresponding MHD signals estimated by the EKF. To emphasize these variations, the MHD signal estimated by the EKF (MHD_{ekf}) was compared to a reference MHD signal (MHD_{ref}). MHD_{ref} was computed using the Gaussian wave-based model (see Section 4.2.2). The required Gaussian parameters were estimated from a template of the simulated MHD effect taken from the normal (non-pathological) section of the ECG. The so simulated reference MHD signal MHD_{ref} had the same length and periodicity as MHD_{ekf}. The discrete integral of the absolute difference between MHD_{ref} and MHD_{ekf} was computed on a beat-to-beat basis by

$$\Delta MHD_n = \frac{1}{K} \int_1^K |MHD_{\text{ref,n}}(k) - MHD_{\text{ekf,n}}(k)|\, dk$$

where K is the number of samples per cardiac cycle and n is the n-th cardiac cycle. The discrete integral was solved using the trapezoidal rule. Figure 6.21 depicts the computed ΔMHD values for the ECG signals with ST depression and ST elevation. It can be seen that ΔMHD is increasing with the onset of the pathological episode (starting from $t \approx 80\,\text{s}$). Hence, when considering the changes of the MHD signal estimated by the EKF, inferences about the underlying pathological variations (which could not be recognised in the filtered ECG signal) could be drawn.

The EKF showed a high performance on the *real ECG records*. Compared to the other methods evaluated in this chapter, the results are less affected by the high beat-to-beat variations of the MHD effect. Even the comparatively small P-waves are still visible after filtering. The morphology of the T-waves in the filtered ECG was similar to the one observed in the reference ECG.

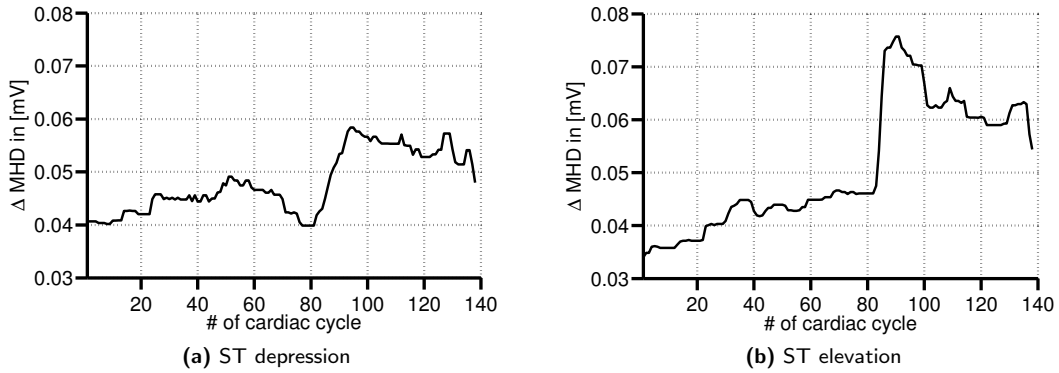

Figure 6.21.: Variations of the MHD signal given as the difference between a reference MHD signal and the MHD signal estimated by the EKF during depression (a) and elevation (b) of the ST-segment (ECG lead II). ΔMHD increases with the onset of the pathological episode ($t \approx 80\,\text{s}$).

Although the EKF gave excellent filtering results (except for the simulated depression or elevation of the ST-segment), there are two limitations, which occur when using the EKF. The *first limitation* involves the input-output relation of the EKF framework. Once a pathological episode starts, the EKF needs several cardiac cycles to adopt its parameters to this new situation. Hence, there is a delay until the simulated pathology is visible at the filter output. This was especially visible for the inversion of the T-waves where there was a delay of $\approx 10\,\mathrm{s}$ before the inversion could be recognised in the filtered output signals. The *second limitation* is caused by the requirement of the phase signal used for the Gaussian wave model (see Section 4.2.2). The computation of the phase signal requires an *a priori* knowledge of QRS complex's location. Hence, filtering of one PQRST or heart cycle can only start once the QRS complex was detected. Currently, this limits the applicability of the EKF for real-time filtering applications such as gating in cardiac MRI (see Chapter 5) but it does not prohibit the use of this technique for monitoring applications. This limitation could be circumvented by a prediction of the next RR interval length or location of the next QRS complex.

Detection of pathological variations - summarising discussion

The Wiener filter, ICA and EKF were applied to simulated ECG signals with three different simulated pathological variations of the ECG morphology: prolongation of the QT-interval length, inversion of the T-waves and depression or elevation of the ST-segment. Considering the overall results, the best results for the detection of the different variations were achieved by the EKF. Only for the ECGs with simulated depression or elevation of the ST-segment, the EKF could not achieve the best results. Hence, the EKF should be further optimised (especially considering the variations in the ST-segment) by considering the aspects discussed above. EKF is the only technique showing promising results for patient monitoring during an MRI examination.

It has to be considered that the (average) results given in Tables 6.1–6.5 and in Tables C.1–C.7 are affected by the number of beats and leads, which were available for the analysis. For the QT and T-wave measurements, only those leads were considered in which a sufficient number of QT-intervals or T-waves were detected in each segment of a record (see descriptions in Section 4.3.2). This means that better average results could occur in certain methods due to fewer analysed leads. Hence, one should also compare the results of the different methods on a beat-to-beat basis for the leads in which the required fiducials were detected in all filtered signals.

Influence of the switched gradient magnetic fields during MR imaging

The influence of the magnetic gradient fields of the MRI scanner was not considered so far. In order to apply the different MHD suppression methods during MRI experiments, filtering of the gradient artefacts (see examples in Fig. 3.1, p. 28) is required. It can be assumed that this additional filtering will alter the characteristics of the ECG signal inside the MRI scanner. Since the Wiener filter as well as the ICA-based filter were not designed to adopt to such signal variations, larger errors within the filtered signals are expected. For the EKF, the additional variations occurring in the gradient filtered signals could be considered by an appropriate adjustment of the $\mathbf{Q}$ and $\mathbf{R}$ matrices. Alternatively, the EKF could be directly used for filtering the gradients. However, since the temporal location of the QRS complex is required for the EKF framework, a preprocessing step including gradient filtering and QRS detection would be required. Future works are required to evaluate the EKF framework during MRI experiments and with different imaging sequences running.

Simulation of the ECG and MHD signals

The real ECG records used for the investigation in this chapter were acquired from young and healthy subjects. Hence, no pathological 12-lead ECG records were available. Additionally, a quantitative analysis was only possible using simulated ECG and MHD signals. In order to investigate if the algorithms enable the detection of cardiac pathologies, which manifest within the ECG, different simulations were performed. Therefore, different ECG signals were modified in order to simulate the variations occurring during pathological episodes. Inversions of the T-wave, prolongations of the QT-interval and ST elevations/depressions were used to study the different algorithms. The morphological modification of the ECG signals considered the typical shapes of a pathological ECG as shown in Figs. 2.11 or 2.13, pp. 16. Additional muscle artefact noise was added to the simulated ECG signals to ensure a more realistic simulation. An existing complex torso model was used to simulate the MHD effect (see Section 3.2.3). Compared to other models, this model provides the most complex MHD signals. During the simulated pathological episodes, the amplitude of the MHD signals was also manipulated in order to better simulate the real scenario. This is the first work which consequently simulated ECG signals with different pathologies and the corresponding MHD signals for the quantitative evaluation of different MHD suppression techniques.

Of course, a simulation cannot reflect the full complexity of a physiological processes and realistic measurement, especially during pathological episodes. Although some possible dynamics of the MHD effect were considered by the simulations, i. e. the beat-to-beat variations depending on the RRI length and a decreased blood flow during pathological episodes, it has to be expected that the variations of the MHD effect are more complex in reality. This can be caused by varying mechanical contractions, varying stroke volume, vasoconstriction or vasodilation, varying blood pressure or ejection fraction leading to different blood flow patterns (see Section 3.2.2).

Besides, information about the blood flow used in the model is limited to the aortic arch. It would be possible to extend the existing model used in this thesis by including additional measurements, e. g. the blood flow at different locations. However, capturing the temporal dynamics of the blood flow by MRI is not possible (at this time), since MRI based blood flow measurements usually require several minutes to obtain information about the blood. Hence, the so estimated signals are averaged over several cardiac cycles so that the individual beat-to-beat dynamics are suppressed. Doppler ultrasound could provide additional information about the beat-to-beat-blood flow dynamics. However, ultrasound has some disadvantages when compared to MRI: access to the blood vessels located in the upper torso and to the heart is limited because of the rip bones, the measured velocity depends on the angle of incidence and velocity is measured in one dimension only. Nevertheless, this method could be considered for the further development of more complex simulation models. Since blood flow dynamics can vary on a beat-to-beat basis, it would be preferable to simultaneously obtain information about the blood flow at several locations within the torso at a high temporal resolution.

7

Summary, conclusions and future work

7.1 Summary and conclusions

During MRI, an ECG signal is required for gating in cardiovascular MRI or for monitoring a patient's vital parameters, e. g. during interventional MRI procedures. Several reasons for preferring the use of the ECG signal over other physiological signals were highlighted in this thesis. However, ECG signals are severely distorted due to the switched gradient magnetic fields and the MHD effect, which are present inside the MRI scanner. This thesis studied the influence of the MHD effect on the ECG signal under different conditions. Several methods were developed and evaluated in order to enable a reliable gating at 7 T and a comprehensive cardiac diagnosis based on the ECG signal at 3 T.

ECG-based gating relies on the detection of the QRS complex. It is known that QRS detection becomes more challenging with an increased magnetic field strength due to the larger MHD effect. This was especially reported for 7 T MR scanners. One state-of-the-art method for QRS detection during MRI (a method based on the VCG) was investigated in further details (see Section 3.3.3) to reveal the reasons for QRS detection problems at 7 T. It was shown that the more complex patterns of the MHD effect at 7 T as well as its intrinsic DC component were responsible for the low QRS detection performances. Based on these findings, two modified approaches of the VCG-based method were developed and evaluated showing an increased performance when compared to the original approach. However, all the VCG-based techniques are based on the definition of a reference vector, which would require an initial QRS detection. To overcome this limitation, a new method based on ICA was developed and evaluated. ICA was used as a preprocessing step prior to QRS detection. Although ICA was not able to ideally separate ECG, MHD and other signal or noise components, it was possible to identify at least one independent component (IC) in each record dominated by the QRS complex. This IC was automatically identified by a template matching technique and was used for QRS detection. Finally, a comparative quantitative analysis of different QRS detection methods (including the ICA-based, the

VCG-based and others) was performed. It was shown that the ICA-based method outperformed the other methods. Additionally, it was found that the usage of one or more precordial ECG leads (in addition to the limb leads) increased the QRS detection quality. The peak detection quality reached with the ICA-based technique was high enough to allow for an accurate triggering for ultra-high field applications.

Patient monitoring during MRI receives more and more attention from the clinical and the research community. A reliable monitoring technique is especially important for EP procedures guided by MRI, for patients receiving anaesthesia or for patients suffering from cardiovascular diseases. However, due to the contaminations of the ECG signal, most of the ECG's information is not accessible while the patient is inside the MRI scanner. This thesis aimed at enhancing the diagnostic ECG quality during MRI by means of different denoising techniques, including the Wiener filter, ICA and an EKF framework. Several simulated ECG signals were used to evaluate the denoising techniques. The simulations were performed using an existing Gaussian wave-based model, which was modified to account for different pathological variations. These variations included the prolongation of the QT-interval, inversions of the T-wave and depression or elevation of the ST-segment. Different levels of muscle artefact noise were added to the simulated ECGs to make them more realistic. The MHD effect was simulated using a torso model and blood flow information in different vessel locations obtained from MRI measurements. Depending on the simulated pathology and the variations of the RRI length, the amplitude of the MHD effect was adjusted accordingly. Compared to previous studies which were limited by their simplified simulation approaches, more extended simulations covering a wider range of pathological episodes were performed in this work. It was shown that the Wiener filter could not adopt the larger variations of the ECG signal, e. g. during an inversion of the T-wave or prolongation of the QT-interval. The ICA-based filter method allowed a reliable detection of the T-wave inversion in most ECG leads with SNR$=9$ dB but the detection performance dropped for the ECGs with SNR$=3$ dB. Larger errors were observed in the analysis of the ST-segment and the QT-interval. The best overall results were obtained by the EKF-based technique, which enabled a reliable detection of the QT prolongation and of the T-wave inversions. Although the EKF showed a high overall performance (low errors) in the ST analysis, it was shown that the current configuration of the EKF did not enable a precise tracking of the variations during a depression or elevation of the ST-segment. Several reasons were discussed to explain this limitation and how it could be overcome in the future. Following the quantitative evaluation using the simulated ECG signals, a qualitative analysis was performed by applying the different filtering techniques to real ECG signals acquired at 3 T. The Wiener filter enabled an attenuation of the MHD effect providing a qualitatively better ECG signal. However, the obtained quality does not seem to provide a good estimate of the underlying ECG morphology and of the relevant clinical parameters. With ICA, it was not possible to obtain similar results as for the simulated signals since the mixing and source model of the real ECGs was more complex. The best results were obtained by the EKF providing a smooth estimate of the underlying ECG morphology. In summary, the best results for both, the simulated and the real ECG signals, were achieved using the EKF technique. The EKF showed great promises and could be used to denoise ECG signals acquired in clinical examinations performed in the MRI environment.

7.2 Future work

During the course of this thesis, several ideas, question and problems arose. Some open questions and possible future research work are given herein.

Extension of ECG hardware: It was shown that additional ECG leads are helpful for gating and monitoring purposes. Especially for patient monitoring during MRI, e. g. during EP examinations, an MRI conditional 12-lead ECG would be advantageous. Dukkipati *et al.* and Tse *et al.* recently addressed this problem by making a conventional 12-lead monitoring device MRI compatible [Dukkipati 08, Tse 10b, Tse 12, Tse 14]. The main challenges during the development of such hardware are the switched gradient magnetic fields and the radio frequency fields of the MR scanner. Besides the distortions of the ECG signals, the electrical currents induced by these fields can cause safety issues due to the heating of the cables and ECG electrodes [Kugel 03, Shellock 04, Niendorf 12].

Evaluation of the ICA-based QRS detection technique: The ICA-based QRS detection technique described in Chapter 5 was evaluated offline since an MRI conditional 12-lead ECG recorder was not available for the experiments conducted within this thesis. However, with the existence of such hardware, it would be interesting to evaluate the developed ICA-based technique in a clinical setting. It would then be also necessary to compare the quality of CMR images acquired using the ICA-based technique to CMR images acquired using other techniques, especially using the phonocardiogram technique (see Section 3.4.2).

Acquisition of pathological/clinical data: So far, no pathological ECG data acquired during MRI are publicly available. Although the ground-truth of the ECG signals acquired during MRI is not known, it would be interesting to further study the changes between normal episodes in the ECG and cardiac arrhythmias. This information obtained from the ECG could be partly correlated with MRI data, e. g. during cardiac stress MRI where wall motion abnormalities are visible during ischemic episodes. Animal studies could provide further information as well, e. g. during an artificial occlusion of coronary arteries or during chest compression for animals in cardiac arrest.

Extension of the existing MHD model: The MHD model used in this work was developed by Oster *et al.* [Oster 15]. It would be of potential interest to extend this model. In the ongoing collaboration between the Universities in Magdeburg and Oxford, it is planned to include further blood flow information in this model, e. g. of the subclavian arteries, the vena cava, the pulmonary arteries and the intracardiac flow. Especially the impact of the intracardiac flow on the MHD effect was not studied so far.

Further improvement of the EKF: Considering the diagnostic ECG during MRI, the best denoising results were achieved using the EKF technique. However, the currently used parameter configuration of the EKF did not enable a precise tracking of pathological depressions or elevations of the ST-segment. Several reasons were discussed to explain this observation. Based on these discussions, the model could be modified, e. g. by the inclusion of pathological episodes in the training data, which was used for the estimation of the EKF parameters. Although the pathological variations of the ST-segment could not be spotted in the filtered ECG signal, larger variations were observed in the MHD signal estimated by the EKF (see Section 6.6). This finding requires further evaluation to show that one can draw inferences about the occurrence of a pathological event based on the observed variations of the estimated MHD signal. For its application in real-time (e. g. for gating purposes), the EKF framework could be extended with an RRI prediction. RRI prediction could be achieved by autoregressive mod-

els, integral pulse frequency modulation (IPFM) [Laguna , Mateo 96, Mateo 00] models or Gaussian processes [Rasmussen 06].

A

VCG-based QRS detection

The following describes the most important steps of the VCG-based QRS detection described by Fischer *et. al* and Chia *et al.* [Fischer 99, Chia 00, Fischer 01]. Firstly, the ECG signal is acquired while the patient is outside the MR scanner. After an automated QRS detection, the reference vector **r** is defined as the vector which points at the position of the R-peak within the VCG space. In the second step, the VCG recorded inside the MR scanner is projected onto a virtual electrode which is parallel to the direction of the R-peak vector **r**

$$A_1(t) = \frac{\mathbf{r}}{|\mathbf{r}|}\mathbf{v}(t) \tag{A.1}$$

The distance between **r** and $\mathbf{v}(t)$ is measured as

$$d(t) = \max(|\mathbf{v}(t) - \mathbf{r}|, 0.01) \tag{A.2}$$

This distance is used the scale the 'optimal' lead which was calculated in Eq. A.1

$$A_2(t) = \frac{A_1(t)}{d(t)^2} \tag{A.3}$$

An additional condition for the occurrence of an QRS complex is the angle between the reference

signal $\mathbf{r}$ and $\mathbf{v}(t)$:

$$A_3(t) = \frac{A_2(t)}{\arccos\left(\frac{\mathbf{r}\cdot\mathbf{v}(t)}{|\mathbf{r}||\mathbf{v}(t)|}\right)} \tag{A.4}$$

A peak detection algorithm can now be applied to the signal $A_3(t)$. Depending on how the threshold is set for the peak detection, each peak should ideally correspond to the position of an R-peak or QRS complex.

B

Jacobian matrices used in the EKF

The two Jacobian matrices of the evoluation function are defined as $\mathbf{A}_k(i,j) = \left.\frac{\partial f_i(\mathbf{x},\mathbf{w},k)}{\partial \mathbf{x}_j}\right|_{\mathbf{x}=\mathbf{x}_k}$ and as $\mathbf{F}_k(i,j) = \left.\frac{\partial f_i(\mathbf{x},\mathbf{w},k)}{\partial \mathbf{w}_j}\right|_{\mathbf{w}=\mathbf{w}_k}$.

The matrix $\mathbf{A}_k(i,j)$ is composed of the following entries

$$\mathbf{A}_k(1,1) = \frac{\partial f_1}{\partial \theta_k} = 1 \tag{B.1}$$

$$
\mathbf{A}_k(2,j) := \begin{cases}
\mathbf{A}_k(2,1) = \dfrac{\partial f_2}{\partial \theta_k} = -\displaystyle\sum_{i=1}^{2} \delta \frac{\omega}{\left(b_{i,k}^E\right)^2} \left(1 - \frac{\left(\Delta\theta_{i,k}^E\right)^2}{\left(b_{i,k}^E\right)^2}\right) \cdot G\left(\alpha_{i,k}^E, \Delta\theta_{i,k}^E, b_{i,k}^E\right) \\
\mathbf{A}_k(2,2) = \dfrac{\partial f_2}{\partial p_k} = 1 \\
\mathbf{A}_k(2,6\ldots7) = \dfrac{\partial f_2}{\partial \alpha_{i,k}^E} = -\delta \dfrac{\omega \Delta\theta_{i,k}^E}{\left(b_{i,k}^E\right)^2} \cdot G\left(1, \Delta\theta_{i,k}^E, b_{i,k}^E\right) \quad i \in \{1,2\} \\
\mathbf{A}_k(2,13\ldots14) = \dfrac{\partial f_2}{\partial b_{i,k}^E} = 2\delta \dfrac{\omega \Delta\theta_{i,k}^E}{\left(b_{i,k}^E\right)^3} \left(1 - \dfrac{\left(\Delta\theta_{i,k}^E\right)^2}{2\left(b_{i,k}^E\right)^2}\right) \\
\qquad\qquad \cdot G\left(\alpha_{i,k}^E, \Delta\theta_{i,k}^E, b_{i,k}^E\right) \quad i \in \{1,2\} \\
\mathbf{A}_k(2,20\ldots21) = \dfrac{\partial f_2}{\partial \xi_k} = \delta \dfrac{\omega}{\left(b_{i,k}^E\right)^2} \left(1 - \dfrac{\left(\Delta\theta_{i,k}^E\right)^2}{\left(b_{i,k}^E\right)^2}\right) \\
\qquad\qquad \cdot G\left(\alpha_{i,k}^E, \Delta\theta_{i,k}^E, b_{i,k}^E\right) \quad i \in \{1,2\}
\end{cases}
\tag{B.2}
$$

$$
\mathbf{A}_k(3,j) := \begin{cases}
\mathbf{A}_k(3,1) = \dfrac{\partial f_3}{\partial \theta_k} = -\displaystyle\sum_{i=3}^{5} \delta \frac{\omega}{\left(b_{i,k}^E\right)^2} \left(1 - \frac{\left(\Delta\theta_{i,k}^E\right)^2}{\left(b_{i,k}^E\right)^2}\right) \cdot G\left(\alpha_{i,k}^E, \Delta\theta_{i,k}^E, b_{i,k}^E\right) \\
\mathbf{A}_k(3,3) = \dfrac{\partial f_3}{\partial q_k} = 1 \\
\mathbf{A}_k(3,8\ldots10) = \dfrac{\partial f_3}{\partial \alpha_{i,k}^E} = -\delta \dfrac{\omega \Delta\theta_{i,k}^E}{\left(b_{i,k}^E\right)^2} \cdot G\left(1, \Delta\theta_{i,k}^E, b_{i,k}^E\right) \quad i \in \{3,4,5\} \\
\mathbf{A}_k(3,15\ldots17) = \dfrac{\partial f_3}{\partial b_{i,k}^E} = 2\delta \dfrac{\omega \Delta\theta_{i,k}^E}{\left(b_{i,k}^E\right)^3} \left(1 - \dfrac{\left(\Delta\theta_{i,k}^E\right)^2}{2\left(b_{i,k}^E\right)^2}\right) \\
\qquad\qquad \cdot G\left(\alpha_{i,k}^E, \Delta\theta_{i,k}^E, b_{i,k}^E\right) \quad i \in \{3,4,5\} \\
\mathbf{A}_k(3,22\ldots24) = \dfrac{\partial f_3}{\partial \xi_k} = \delta \dfrac{\omega}{\left(b_{i,k}^E\right)^2} \left(1 - \dfrac{\left(\Delta\theta_{i,k}^E\right)^2}{\left(b_{i,k}^E\right)^2}\right) \\
\qquad\qquad \cdot G\left(\alpha_{i,k}^E, \Delta\theta_{i,k}^E, b_{i,k}^E\right) \quad i \in \{3,4,5\}
\end{cases}
\tag{B.3}
$$

$$\mathbf{A}_k(4,j) := \begin{cases} \mathbf{A}_k(4,1) = \dfrac{\partial f_4}{\partial \theta_k} = -\displaystyle\sum_{i=6}^{7} \delta \frac{\omega}{\left(b_{i,k}^E\right)^2} \left(1 - \frac{\left(\Delta\theta_{i,k}^E\right)^2}{\left(b_{i,k}^E\right)^2}\right) \cdot G\left(\alpha_{i,k}^E, \Delta\theta_{i,k}^E, b_{i,k}^E\right) \\ \mathbf{A}_k(4,4) = \dfrac{\partial f_4}{\partial t_k} = 1 \\ \mathbf{A}_k(4,11\ldots12) = \dfrac{\partial f_4}{\partial \alpha_{i,k}^E} = -\delta \dfrac{\omega \Delta\theta_{i,k}^E}{\left(b_{i,k}^E\right)^2} \cdot G\left(1, \Delta\theta_{i,k}^E, b_{i,k}^E\right) \quad i \in \{6,7\} \\ \mathbf{A}_k(4,18\ldots19) = \dfrac{\partial f_4}{\partial b_{i,k}^E} = 2\delta \dfrac{\omega \Delta\theta_{i,k}^E}{\left(b_{i,k}^E\right)^3} \left(1 - \dfrac{\left(\Delta\theta_{i,k}^E\right)^2}{2\left(b_{i,k}^E\right)^2}\right) \\ \qquad\qquad \cdot G\left(\alpha_{i,k}^E, \Delta\theta_{i,k}^E, b_{i,k}^E\right) \quad i \in \{6,7\} \\ \mathbf{A}_k(4,25\ldots26) = \dfrac{\partial f_4}{\partial \xi_k} = \delta \dfrac{\omega}{\left(b_{i,k}^E\right)^2} \left(1 - \dfrac{\left(\Delta\theta_{i,k}^E\right)^2}{\left(b_{i,k}^E\right)^2}\right) \\ \qquad\qquad \cdot G\left(\alpha_{i,k}^E, \Delta\theta_{i,k}^E, b_{i,k}^E\right) \quad i \in \{6,7\} \end{cases} \tag{B.4}$$

$$\mathbf{A}_k(5,j) := \begin{cases} \mathbf{A}_k(5,1) = \dfrac{\partial f_5}{\partial \theta_k} = -\displaystyle\sum_{i} \delta \frac{\omega}{\left(b_{i,k}^M\right)^2} \left(1 - \frac{\left(\Delta\theta_{i,k}^M\right)^2}{\left(b_{i,k}^M\right)^2}\right) \cdot G\left(\alpha_{i,k}^M, \Delta\theta_{i,k}^M, b_{i,k}^M\right) \\ \mathbf{A}_k(5,5) = \dfrac{\partial f_5}{\partial m_k} = 1 \end{cases} \tag{B.5}$$

$$\mathbf{A}_k(6\ldots26, 6\ldots26) = \frac{\partial f_6}{\partial \mathbf{x}_k(6\ldots26)} = \mathbf{I}_{21} \tag{B.6}$$

where $\mathbf{I}_{21}$ is a 21×21 identity matrix. The Jacobian matrix $\mathbf{F}_k(i,j)$ is given as

$$
\mathbf{F}_k(i,j) := \begin{cases}
\mathbf{F}_k(1,1) = \dfrac{\partial f_1}{\partial \omega} = 1 \\
\mathbf{F}_k(i,i) = \dfrac{\partial f_i}{\partial \eta_i} = 1 \quad i \in \{2,3,4,5\} \\
\mathbf{F}_k(2,1) = \dfrac{\partial f_2}{\partial \omega} = -\displaystyle\sum_{i=1}^{2} \frac{\delta}{\left(b_{i,k}^E\right)^2} \cdot G\left(\alpha_{i,k}^E, \Delta\theta_{i,k}^E, b_{i,k}^E\right) \\
\mathbf{F}_k(3,1) = \dfrac{\partial f_3}{\partial \omega} = -\displaystyle\sum_{i=3}^{5} \frac{\delta}{\left(b_{i,k}^E\right)^2} \cdot G\left(\alpha_{i,k}^E, \Delta\theta_{i,k}^E, b_{i,k}^E\right) \\
\mathbf{F}_k(4,1) = \dfrac{\partial f_4}{\partial \omega} = -\displaystyle\sum_{i=6}^{7} \frac{\delta}{\left(b_{i,k}^E\right)^2} \cdot G\left(\alpha_{i,k}^E, \Delta\theta_{i,k}^E, b_{i,k}^E\right) \\
\mathbf{F}_k(5,1) = \dfrac{\partial f_5}{\partial \omega} = -\displaystyle\sum_{i} \frac{\delta}{\left(b_{i,k}^M\right)^2} \cdot G\left(\alpha_{i,k}^M, \Delta\theta_{i,k}^M, b_{i,k}^M\right) \\
\mathbf{F}_k(5,27\ldots27+N-1) = \dfrac{\partial f_5}{\partial \alpha_{i,k}^M} = -\delta \dfrac{\omega \Delta\theta_{i,k}^M}{\left(b_{i,k}^M\right)^2} \\
\qquad\qquad \cdot G\left(1, \Delta\theta_{i,k}^M, b_{i,k}^M\right) \quad i \in \{1\ldots N\} \\
\mathbf{F}_k(5,27+N\ldots27+2N-1) = \dfrac{\partial f_5}{\partial b_{i,k}^M} = 2\delta \dfrac{\omega \Delta\theta_{i,k}^M}{\left(b_{i,k}^M\right)^3} \left(1 - \dfrac{\left(\Delta\theta_{i,k}^M\right)^2}{2\left(b_{i,k}^M\right)^2}\right) \\
\qquad\qquad \cdot G\left(\alpha_{i,k}^M, \Delta\theta_{i,k}^M, b_{i,k}^M\right) \quad i \in \{1\ldots N\} \\
\mathbf{F}_k(5,27+2N\ldots27+3N-1) = \dfrac{\partial f_5}{\partial \xi_{i,k}} = \delta \dfrac{\omega}{\left(b_{i,k}^M\right)^2} \left(1 - \dfrac{\left(\Delta\theta_{i,k}^M\right)^2}{\left(b_{i,k}^M\right)^2}\right) \\
\qquad\qquad \cdot G\left(\alpha_{i,k}^M, \Delta\theta_{i,k}^M, b_{i,k}^M\right) \quad i \in \{1\ldots N\}
\end{cases}
\tag{B.7}
$$

where N is the number of Gaussians representing the MHD effect.

The Jacobian matrices of the observation function g are as $\mathbf{C}_k(i,j) = \frac{\partial g_i(\mathbf{x},\mathbf{v},k)}{\partial \mathbf{x}_j}\Big|_{\mathbf{x}=\mathbf{x}_k}$ and as $\mathbf{L}_k(i,j) = \frac{\partial g_i(\mathbf{x},\mathbf{v},k)}{\partial \mathbf{v}_j}\Big|_{\mathbf{v}=\mathbf{v}_k}$. The matrix $\mathbf{C}_k(i,j)$ is given as

$$\mathbf{C}_k(i,j) := \begin{cases} \mathbf{C}_k(1,1) = \dfrac{\partial g_1}{\partial \omega} = 1 \\ \mathbf{C}_k(2,2\ldots5) = \dfrac{\partial g_2}{\partial \mathbf{x}_k(j)} = 1 \\ \mathbf{C}_k(3,5) = \dfrac{\partial g_3}{\partial m_k} = 1 \\ \mathbf{C}_k(3,6\ldots12) = \dfrac{\partial g_3}{\partial \alpha^E_{i,k}} = G\left(1, \Delta\theta^E_{i,k}, b^E_{i,k}\right) \\ \mathbf{C}_k(3,13\ldots19) = \dfrac{\partial g_3}{\partial b^E_{i,k}} = \dfrac{\left(\Delta\theta^E_{i,k}\right)^2}{\left(b^E_{i,k}\right)^3} \cdot G\left(\alpha^E_{i,k}, \Delta\theta^E_{i,k}, b^E_{i,k}\right) \\ \mathbf{C}_k(3,20\ldots26) = \dfrac{\partial g_3}{\partial \xi_{i,k}} = \dfrac{\Delta\theta^E_{i,k}}{\left(b^E_{i,k}\right)^2} \cdot G\left(\alpha^E_{i,k}, \Delta\theta^E_{i,k}, b^E_{i,k}\right) \end{cases} \tag{B.8}$$

and the matrix $\mathbf{L}_k(i,j)$ as

$$\mathbf{L}_k(i,j) = \frac{\partial g_i}{\partial \mathbf{v}_{j,k}} = \mathbf{I}_3 \tag{B.9}$$

where $\mathbf{I}_3$ is a 3×3 identity matrix.

C

Quantitative result tables obtained from simulated ECGs

This appendix extends the results which were presented in Section 6.5.1.2. The results include measurements of the QT-interval lengths (Tables C.1 to C.4), of the T-wave polarity (Tables C.5 to C.7) and of the ST amplitude (Tables C.8 to C.14) using the simulated ECG signals filtered by the Wiener, ICA and EKF techniques.

Table C.1.: QT measurement errors in the ECG with simulated T-wave inversion (SNR=9 dB) using the different filtering methods (Wiener filter, ICA, EKF). The measured errors are reported for the normal (non-pathological), the transitional and the pathological (T-wave inversion) sections of the ECG. All values are given in [ms]. (μ = mean absolute error, σ = standard deviation of the measurement errors, p_5 = 5th percentile, p_{95} = 95th percentile.)

	Wiener filter									ICA									EKF								
	Normal			Trans			Patho			Normal			Trans			Patho			Normal			Trans			Patho		
Lead	$\mu \pm \sigma$	p_5	p_{95}	$\mu \pm \sigma$	p_5	p_{95}	$\mu \pm \sigma$	p_5	p_{95}	$\mu \pm \sigma$	p_5	p_{95}	$\mu \pm \sigma$	p_5	p_{95}	$\mu \pm \sigma$	p_5	p_{95}	$\mu \pm \sigma$	p_5	p_{95}	$\mu \pm \sigma$	p_5	p_{95}	$\mu \pm \sigma$	p_5	p_{95}
I	78 ± 37	51	144	145 ± 71	60	236	223 ± 15	199	249	- ± -	-	-	- ± -	-	-	- ± -	-	-	7 ± 5	0	16	15 ± 42	0	30	7 ± 4	0	16
II	100 ± 32	64	145	73 ± 37	20	132	- ± -	-	-	22 ± 8	4	33	115 ± 110	4	291	152 ± 115	12	300	3 ± 3	0	8	13 ± 9	0	29	12 ± 5	4	20
III	148 ± 90	36	284	187 ± 83	70	292	243 ± 55	90	298	10 ± 4	4	20	124 ± 125	4	306	194 ± 113	29	334	15 ± 8	4	32	11 ± 9	0	32	13 ± 5	4	20
aVR	110 ± 6	99	120	- ± -	-	-	- ± -	-	-	- ± -	-	-	- ± -	-	-	- ± -	-	-	2 ± 3	0	8	12 ± 7	0	20	9 ± 4	4	16
aVL	- ± -	-	-	- ± -	-	-	- ± -	-	-	- ± -	-	-	- ± -	-	-	- ± -	-	-	- ± -	-	-	- ± -	-	-	- ± -	-	-
aVF	74 ± 35	42	127	106 ± 81	2	240	156 ± 76	58	249	8 ± 4	3	13	112 ± 117	1	321	186 ± 110	30	317	7 ± 5	0	20	11 ± 12	0	31	4 ± 4	0	12
V1	27 ± 13	7	48	57 ± 56	0	170	99 ± 50	29	176	132 ± 128	19	352	- ± -	-	-	70 ± 79	4	272	8 ± 9	0	24	20 ± 14	3	37	21 ± 8	4	33
V2	45 ± 73	4	197	131 ± 130	8	388	85 ± 84	4	244	- ± -	-	-	- ± -	-	-	- ± -	-	-	5 ± 4	0	12	12 ± 10	0	34	17 ± 6	4	24
V3	155 ± 122	0	371	166 ± 115	23	397	174 ± 93	24	323	24 ± 14	6	46	134 ± 105	11	305	174 ± 84	22	299	2 ± 3	0	8	12 ± 11	0	29	8 ± 4	4	16
V4	108 ± 85	10	198	- ± -	-	-	86 ± 32	42	160	93 ± 128	8	361	113 ± 117	6	362	152 ± 117	0	332	4 ± 4	0	8	11 ± 8	0	24	6 ± 4	0	12
V5	169 ± 124	17	400	223 ± 104	56	390	220 ± 104	33	394	44 ± 37	18	133	136 ± 111	0	300	157 ± 105	3	315	5 ± 5	0	16	14 ± 17	4	32	7 ± 5	0	16
V6	168 ± 88	36	320	174 ± 113	30	407	144 ± 99	29	330	- ± -	-	-	- ± -	-	-	- ± -	-	-	5 ± 7	0	20	15 ± 11	3	36	10 ± 7	0	20
μ	107 ± 64	33	214	140 ± 88	30	295	159 ± 68	56	269	48 ± 46	9	137	122 ± 114	4	314	155 ± 103	14	310	6 ± 5	0	16	13 ± 14	1	30	10 ± 5	2	19
p_5	36 ± 10			63 ± 45			85 ± 22			9 ± 4			112 ± 106			95 ± 81			2 ± 3			11 ± 8			5 ± 4		
p_{95}	169 ± 123			209 ± 124			235 ± 102			120 ± 128			136 ± 123			192 ± 116			12 ± 9			18 ± 30			19 ± 8		

Table C.2.: QT measurement errors in the ECG with simulated T-wave inversion (SNR=3 dB) using the different filtering methods (Wiener filter, ICA, EKF). The measured errors are reported for the normal (non-pathological), the transitional and the pathological (T-wave inversion) sections of the ECG. All values are given in [ms]. (μ = mean absolute error, σ = standard deviation of the measurement errors, p_5 = 5th percentile, p_{95} = 95th percentile.)

	Wiener filter									ICA									EKF								
	Normal			Trans			Patho			Normal			Trans			Patho			Normal			Trans			Patho		
Lead	$\mu \pm \sigma$	p_5	p_{95}	$\mu \pm \sigma$	p_5	p_{95}	$\mu \pm \sigma$	p_5	p_{95}	$\mu \pm \sigma$	p_5	p_{95}	$\mu \pm \sigma$	p_5	p_{95}	$\mu \pm \sigma$	p_5	p_{95}	$\mu \pm \sigma$	p_5	p_{95}	$\mu \pm \sigma$	p_5	p_{95}	$\mu \pm \sigma$	p_5	p_{95}
I	25 ± 20	0	64	75 ± 86	0	271	90 ± 87	10	278	211 ± 117	25	386	187 ± 116	5	363	167 ± 100	16	354	8 ± 5	0	16	18 ± 16	0	49	18 ± 10	4	36
II	181 ± 157	3	422	184 ± 134	19	356	183 ± 118	28	384	20 ± 18	4	39	113 ± 117	3	357	197 ± 90	11	348	7 ± 4	0	12	28 ± 16	6	58	13 ± 10	0	36
III	212 ± 157	17	476	216 ± 135	33	433	243 ± 140	14	435	17 ± 11	4	41	115 ± 122	8	298	200 ± 82	44	308	- ± -	-	-	- ± -	-	-	13 ± 12	1	41
aVR	196 ± 137	8	384	- ± -	-	-	163 ± 114	37	345	42 ± 85	0	266	114 ± 104	6	310	187 ± 79	53	325	6 ± 3	0	12	24 ± 18	4	68	16 ± 9	4	33
aVL	- ± -	-	-	- ± -	-	-	- ± -	-	-	- ± -	-	-	- ± -	-	-	- ± -	-	-	- ± -	-	-	- ± -	-	-	- ± -	-	-
aVF	230 ± 145	45	425	194 ± 136	30	437	223 ± 118	58	388	12 ± 17	0	34	122 ± 114	0	311	198 ± 74	22	293	8 ± 10	0	36	- ± -	-	-	15 ± 13	0	48
V1	178 ± 105	56	364	185 ± 106	48	371	203 ± 146	8	394	214 ± 127	6	374	211 ± 126	23	394	207 ± 121	11	423	6 ± 4	0	16	16 ± 15	0	45	- ± -	-	-
V2	82 ± 39	9	163	72 ± 48	8	172	- ± -	-	-	22 ± 8	6	35	- ± -	-	-	- ± -	-	-	26 ± 17	4	57	31 ± 24	3	69	43 ± 16	19	72
V3	89 ± 130	3	381	127 ± 122	8	333	189 ± 139	5	394	- ± -	-	-	147 ± 117	8	315	228 ± 79	94	358	6 ± 4	0	12	18 ± 21	0	60	23 ± 6	16	33
V4	126 ± 95	39	355	168 ± 105	40	331	146 ± 120	14	433	150 ± 150	6	399	145 ± 125	16	344	196 ± 103	10	383	5 ± 4	0	12	18 ± 18	0	52	19 ± 8	4	32
V5	201 ± 126	26	395	180 ± 110	14	350	151 ± 121	24	416	116 ± 137	8	387	153 ± 117	16	310	204 ± 112	4	376	6 ± 5	0	16	18 ± 18	0	50	18 ± 8	8	36
V6	- ± -	-	-	- ± -	-	-	- ± -	-	-	- ± -	-	-	208 ± 138	20	441	199 ± 101	19	357	5 ± 3	0	12	16 ± 15	0	42	16 ± 8	0	32
μ	152 ± 111	21	343	156 ± 109	22	339	177 ± 123	22	385	89 ± 74	7	218	152 ± 120	11	344	198 ± 94	28	353	8 ± 6	0	20	21 ± 18	1	55	19 ± 10	6	40
p_5	51 ± 29			73 ± 63			112 ± 98			14 ± 9			113 ± 109			176 ± 76			5 ± 3			16 ± 15			13 ± 7		
p_{95}	222 ± 157			207 ± 136			235 ± 144			213 ± 145			210 ± 133			219 ± 117			18 ± 14			30 ± 23			34 ± 15		

Table C.3.: QT measurement errors in the ECG with simulated T-wave inversion (SNR=9 dB and SNR=3 dB) using the different filtering methods (Wiener filter, ICA, EKF). The measured errors are reported for the complete ECG (covering the normal (non-pathological), the transitional and the pathological (T-wave inversion) sections). All values are given in [ms]. (μ = mean absolute error, σ = standard deviation of the measurement errors, p_5 = 5th percentile, p_{95} = 95th percentile.)

	SNR=9 dB									SNR=3 dB								
	Wiener filter			ICA			EKF			Wiener filter			ICA			EKF		
Lead	$\mu \pm \sigma$	p_5	p_{95}	$\mu \pm \sigma$	p_5	p_{95}	$\mu \pm \sigma$	p_5	p_{95}	$\mu \pm \sigma$	p_5	p_{95}	$\mu \pm \sigma$	p_5	p_{95}	$\mu \pm \sigma$	p_5	p_{95}
I	143 ± 75	52	240	- ± -	-	-	10 ± 28	0	20	68 ± 79	0	247	188 ± 112	15	364	15 ± 12	0	40
II	- ± -	-	-	100 ± 107	4	292	10 ± 8	0	24	183 ± 136	8	360	110 ± 112	6	338	17 ± 15	0	48
III	190 ± 86	49	292	109 ± 122	4	303	13 ± 8	4	28	221 ± 142	21	455	111 ± 115	8	296	- ± -	-	-
aVR	- ± -	-	-	- ± -	-	-	9 ± 6	0	20	- ± -	-	-	121 ± 106	4	311	16 ± 15	4	51
aVL	- ± -	-	-	- ± -	-	-	- ± -	-	-	- ± -	-	-	- ± -	-	-	- ± -	-	-
aVF	107 ± 74	14	238	100 ± 116	4	312	8 ± 9	0	22	210 ± 134	32	424	110 ± 110	2	292	- ± -	-	-
V1	60 ± 53	4	160	- ± -	-	-	16 ± 13	0	36	187 ± 116	36	390	211 ± 124	15	393	- ± -	-	-
V2	93 ± 110	4	324	- ± -	-	-	12 ± 9	0	24	- ± -	-	-	- ± -	-	-	33 ± 21	4	68
V3	164 ± 111	12	368	106 ± 100	8	289	8 ± 9	0	24	131 ± 132	4	364	- ± -	-	-	16 ± 16	0	44
V4	- ± -	-	-	121 ± 121	4	340	8 ± 7	0	21	150 ± 107	38	360	161 ± 127	12	387	14 ± 14	0	42
V5	206 ± 111	26	387	121 ± 105	4	298	10 ± 13	0	28	178 ± 117	16	396	158 ± 124	12	367	15 ± 14	0	44
V6	165 ± 103	30	356	- ± -	-	-	11 ± 10	0	29	- ± -	-	-	- ± -	-	-	13 ± 12	0	40
μ	141 ± 90	24	296	110 ± 112	5	306	10 ± 11	0	25	166 ± 120	19	375	146 ± 116	9	344	17 ± 15	1	47
p_5	72 ± 60			100 ± 101			8 ± 7			90 ± 89			110 ± 107			13 ± 12		
p_{95}	200 ± 111			121 ± 122			15 ± 21			217 ± 140			203 ± 126			27 ± 19		

Table C.4.: QT measurement errors in the ECG without simulated pathologies (normal ECG) (SNR=9 dB and SNR=3 dB) using the different filtering methods (Wiener filter, ICA, EKF). All values are given in [ms]. (μ = mean absolute error, σ = standard deviation of the measurement errors, p_5 = 5th percentile, p_{95} = 95th percentile.)

	SNR=9 dB									SNR=3 dB								
	Wiener filter			ICA			EKF			Wiener filter			ICA			EKF		
Lead	$\mu \pm \sigma$	p_5	p_{95}	$\mu \pm \sigma$	p_5	p_{95}	$\mu \pm \sigma$	p_5	p_{95}	$\mu \pm \sigma$	p_5	p_{95}	$\mu \pm \sigma$	p_5	p_{95}	$\mu \pm \sigma$	p_5	p_{95}
I	82 ± 71	12	208	33 ± 60	4	111	18 ± 11	8	44	150 ± 108	10	351	103 ± 94	4	264	7 ± 5	0	16
II	151 ± 93	7	333	101 ± 79	4	248	14 ± 13	0	40	163 ± 102	15	348	112 ± 98	4	276	12 ± 13	0	37
III	154 ± 80	20	285	40 ± 34	4	127	83 ± 27	36	125	146 ± 85	16	277	111 ± 60	8	204	76 ± 30	20	130
aVR	130 ± 89	8	284	99 ± 80	6	240	13 ± 8	4	32	143 ± 86	16	289	102 ± 95	4	262	6 ± 5	0	16
aVL	- ± -	-	-	- ± -	-	-	- ± -	-	-	- ± -	-	-	- ± -	-	-	- ± -	-	-
aVF	117 ± 111	4	338	98 ± 62	10	211	13 ± 14	0	36	155 ± 120	12	380	114 ± 100	4	295	26 ± 42	0	146
V1	34 ± 48	0	150	37 ± 67	0	172	71 ± 12	52	96	74 ± 93	0	273	61 ± 88	0	271	10 ± 3	4	16
V2	206 ± 118	27	356	19 ± 39	0	134	14 ± 18	0	60	192 ± 128	16	386	39 ± 30	8	74	24 ± 9	16	42
V3	146 ± 118	7	341	72 ± 87	4	244	22 ± 23	0	64	164 ± 123	12	380	144 ± 111	7	324	22 ± 21	4	65
V4	165 ± 102	12	341	139 ± 108	4	334	9 ± 11	0	36	174 ± 123	12	398	123 ± 101	7	290	20 ± 17	0	40
V5	150 ± 97	16	340	111 ± 103	4	277	16 ± 10	4	40	173 ± 105	12	349	104 ± 93	4	287	6 ± 4	0	13
V6	152 ± 84	16	330	83 ± 87	0	261	17 ± 9	4	36	157 ± 96	4	314	87 ± 87	3	255	3 ± 3	0	8
μ	135 ± 92	12	301	76 ± 73	4	214	26 ± 14	10	55	154 ± 106	11	340	100 ± 87	5	255	19 ± 14	4	48
p_5	58 ± 60			26 ± 37			11 ± 9			109 ± 86			50 ± 45			5 ± 3		
p_{95}	186 ± 118			125 ± 106			77 ± 25			183 ± 126			134 ± 106			51 ± 36		

Table C.5.: T-wave detection performance in the ECG records with simulated QT prolongation (SNR=9 dB) filtered using the different methods (Wiener filter, ICA and EKF). The sensitivity Se and the positive predictive value $+P$ (given in [%]) were computed separately for each section (normal, transitional and pathological) and for the complete ECG record. (μ = mean detection performance, p_5 = 5th percentile, p_{95} = 95th percentile.)

	Wiener filter								ICA								EKF							
	Normal		Transition		Pathological		Complete		Normal		Transition		Pathological		Complete		Normal		Transition		Pathological		Complete	
Lead	Se	$+P$	Se	$+P$	Se	$+P$	Se	$+P$	Se	$+P$	Se	$+P$	Se	$+P$	Se	$+P$	Se	$+P$	Se	$+P$	Se	$+P$	Se	$+P$
I	96.7	100.0	95.9	100.0	100.0	100.0	97.2	100.0	100.0	100.0	100.0	100.0	100.0	100.0	100.0	100.0	100.0	100.0	100.0	100.0	100.0	100.0	100.0	100.0
II	100.0	100.0	100.0	100.0	-	-	-	-	100.0	100.0	100.0	100.0	100.0	100.0	100.0	100.0	100.0	100.0	100.0	100.0	100.0	100.0	100.0	100.0
III	63.6	100.0	-	-	-	-	-	-	100.0	100.0	100.0	100.0	100.0	100.0	100.0	100.0	100.0	100.0	94.2	100.0	-	-	-	-
aVR	90.0	100.0	95.7	100.0	100.0	100.0	96.2	100.0	100.0	100.0	100.0	100.0	100.0	100.0	100.0	100.0	100.0	100.0	100.0	100.0	100.0	100.0	100.0	100.0
aVL	89.7	100.0	90.0	100.0	100.0	100.0	92.5	100.0	100.0	100.0	100.0	100.0	100.0	100.0	100.0	100.0	100.0	100.0	100.0	100.0	100.0	100.0	100.0	100.0
aVF	-	-	-	-	-	-	-	-	-	-	-	-	-	-	-	-	100.0	100.0	100.0	100.0	100.0	100.0	100.0	100.0
V1	73.3	100.0	83.8	100.0	87.2	100.0	83.5	100.0	-	-	-	-	-	-	-	-	100.0	100.0	100.0	100.0	100.0	100.0	100.0	100.0
V2	100.0	100.0	98.0	100.0	100.0	100.0	99.1	100.0	100.0	100.0	96.0	100.0	100.0	100.0	98.1	100.0	100.0	100.0	100.0	100.0	100.0	100.0	100.0	100.0
V3	100.0	100.0	100.0	100.0	100.0	100.0	100.0	100.0	100.0	100.0	100.0	100.0	100.0	100.0	100.0	100.0	100.0	100.0	100.0	100.0	100.0	100.0	100.0	100.0
V4	100.0	100.0	100.0	100.0	100.0	100.0	100.0	100.0	100.0	100.0	100.0	100.0	100.0	100.0	100.0	100.0	100.0	100.0	100.0	100.0	100.0	100.0	100.0	100.0
V5	100.0	100.0	100.0	100.0	100.0	100.0	100.0	100.0	100.0	100.0	100.0	100.0	100.0	100.0	100.0	100.0	100.0	100.0	100.0	100.0	100.0	100.0	100.0	100.0
V6	100.0	100.0	100.0	100.0	100.0	100.0	100.0	100.0	100.0	100.0	100.0	100.0	100.0	100.0	100.0	100.0	100.0	100.0	100.0	100.0	100.0	100.0	100.0	100.0
μ	92.1	100	96.3	100	98.6	100	96.5	100	100	100	99.6	100	100	100	99.8	100	100	100	99.5	100	100	100	100	100
p_5	68.5	100	86.6	100	92.3	100	87.1	100	100	100	97.8	100	100	100	99	100	100	100	97.4	100	100	100	100	100
p_{95}	100	100	100	100	100	100	100	100	100	100	100	100	100	100	100	100	100	100	100	100	100	100	100	100

Table C.6.: T-wave detection performance in the ECG records with simulated QT prolongation (SNR=3 dB) filtered using the different methods (Wiener filter, ICA and EKF). The sensitivity Se and the positive predictive value $+P$ (given in [%]) were computed separately for each section (normal, transitional and pathological) and for the complete ECG record. (μ = mean detection performance, p_5 = 5th percentile, p_{95} = 95th percentile.)

	Wiener filter								ICA								EKF							
	Normal		Transition		Pathological		Complete		Normal		Transition		Pathological		Complete		Normal		Transition		Pathological		Complete	
Lead	Se	+P	Se	+P	Se	+P	Se	+P	Se	+P	Se	+P	Se	+P	Se	+P	Se	+P	Se	+P	Se	+P	Se	+P
I	80.0	100.0	94.0	100.0	92.6	100.0	89.7	100.0	100.0	100.0	98.0	100.0	79.3	100.0	93.6	100.0	100.0	100.0	100.0	100.0	100.0	100.0	100.0	100.0
II	77.3	100.0	83.3	100.0	75.0	100.0	79.4	100.0	90.0	100.0	100.0	100.0	96.6	100.0	96.3	100.0	100.0	100.0	100.0	100.0	100.0	100.0	100.0	100.0
III	52.4	100.0	48.1	100.0	57.1	100.0	52.5	100.0	87.5	100.0	91.9	100.0	89.2	100.0	90.1	100.0	100.0	100.0	84.9	100.0	-	-	-	-
aVR	93.1	100.0	95.9	100.0	98.5	100.0	96.5	100.0	100.0	100.0	100.0	100.0	96.2	100.0	98.4	100.0	100.0	100.0	100.0	100.0	100.0	100.0	100.0	100.0
aVL	73.3	100.0	76.7	100.0	91.7	100.0	79.4	100.0	100.0	100.0	98.0	100.0	82.1	100.0	94.4	100.0	100.0	100.0	100.0	100.0	100.0	100.0	100.0	100.0
aVF	72.7	100.0	69.7	100.0	68.4	100.0	70.3	100.0	68.8	100.0	54.3	100.0	40.0	100.0	53.5	100.0	100.0	100.0	-	-	-	-	-	-
V1	50.0	100.0	60.0	100.0	65.8	100.0	60.8	100.0	-	-	-	-	-	-	-	-	100.0	100.0	100.0	100.0	-	-	-	-
V2	83.3	100.0	98.0	100.0	96.6	100.0	93.5	100.0	100.0	100.0	100.0	100.0	100.0	100.0	100.0	100.0	100.0	100.0	100.0	100.0	100.0	100.0	100.0	100.0
V3	93.3	100.0	98.0	100.0	100.0	100.0	97.2	100.0	96.7	100.0	98.0	100.0	96.6	100.0	97.2	100.0	100.0	100.0	100.0	100.0	100.0	100.0	100.0	100.0
V4	100.0	100.0	100.0	100.0	100.0	100.0	100.0	100.0	96.7	100.0	100.0	100.0	82.8	100.0	94.5	100.0	100.0	100.0	100.0	100.0	100.0	100.0	100.0	100.0
V5	100.0	100.0	100.0	100.0	100.0	100.0	100.0	100.0	96.7	100.0	98.0	100.0	79.3	100.0	92.7	100.0	100.0	100.0	100.0	100.0	100.0	100.0	100.0	100.0
V6	100.0	100.0	100.0	100.0	100.0	100.0	100.0	100.0	100.0	100.0	100.0	100.0	89.7	100.0	97.2	100.0	100.0	100.0	100.0	100.0	100.0	100.0	100.0	100.0
μ	81.3	100	85.3	100	87.1	100	84.9	100	94.2	100	94.4	100	84.7	100	91.6	100	100	100	98.6	100	100	100	100	100
p_5	51.3	100	54.6	100	61.9	100	57.1	100	78.2	100	73.1	100	59.7	100	71.8	100	100	100	92.5	100	100	100	100	100
p_{95}	100	100	100	100	100	100	100	100	100	100	100	100	98.3	100	99.2	100	100	100	100	100	100	100	100	100

Table C.7.: T-wave detection performance in the filtered ECG records without simulated pathologies (SNR=9 dB and SNR=3 dB). The sensitivity Se and the positive predictive value $+P$ (given in [%]) were computed for the complete ECG record. (μ = mean detection performance, p_5 = 5th percentile, p_{95} = 95th percentile.)

	SNR=9 dB						SNR=3 dB					
	Wiener filter		ICA		EKF		Wiener filter		ICA		EKF	
Lead	Se	+P	Se	+P	Se	+P	Se	+P	Se	+P	Se	+P
I	90.8	100.0	66.7	100.0	100.0	100.0	80.4	100.0	77.0	100.0	100.0	100.0
II	92.7	100.0	90.8	100.0	100.0	100.0	69.2	100.0	75.2	100.0	100.0	100.0
III	84.9	100.0	88.3	100.0	100.0	100.0	73.8	100.0	66.7	100.0	100.0	100.0
aVR	97.9	100.0	87.6	100.0	100.0	100.0	89.9	100.0	77.2	100.0	100.0	100.0
aVL	-	-	-	-	-	-	-	-	-	-	-	-
aVF	79.2	100.0	90.2	100.0	100.0	100.0	68.9	100.0	73.8	100.0	100.0	100.0
V1	61.7	61.7	51.4	51.4	44.0	44.0	50.0	49.5	50.0	50.0	48.1	48.1
V2	85.2	100.0	14.6	100.0	100.0	100.0	53.8	100.0	72.2	100.0	100.0	100.0
V3	92.6	100.0	78.6	100.0	100.0	100.0	85.2	100.0	76.9	100.0	100.0	100.0
V4	99.1	100.0	85.8	100.0	100.0	100.0	91.7	100.0	72.6	100.0	100.0	100.0
V5	100.0	100.0	80.6	100.0	100.0	100.0	95.4	100.0	86.0	100.0	100.0	100.0
V6	100.0	100.0	85.2	100.0	100.0	100.0	94.4	100.0	83.2	100.0	100.0	100.0
μ	89.5	96.5	74.5	95.6	94.9	94.9	77.5	95.4	73.7	95.5	95.3	95.3
p_5	70.5	80.9	33	75.7	72	72	51.9	74.8	58.4	75	74.1	74.1
p_{95}	100	100	90.5	100	100	100	94.9	100	84.6	100	100	100

Table C.8.: ST measurement errors in the ECG with simulated QT prolongation (SNR=9 dB). The measured errors are reported for the normal (non-pathological), for the transitional and for the pathological (QT prolongation) sections. The best results in each section are highlighted in grey. All values are given in [μV]. (Δ_{ST} = average ST amplitude difference between the normal and the pathological segment, μ = mean absolute error, σ = standard deviation of the measurement errors, p_5 = 5th percentile, p_{95} = 95th percentile.)

		Wiener filter									ICA									EKF								
		Normal			Trans			Patho			Normal			Trans			Patho			Normal			Trans			Patho		
Lead	Δ_{ST}	$\mu \pm \sigma$	p_5	p_{95}	$\mu \pm \sigma$	p_5	p_{95}	$\mu \pm \sigma$	p_5	p_{95}	$\mu \pm \sigma$	p_5	p_{95}	$\mu \pm \sigma$	p_5	p_{95}	$\mu \pm \sigma$	p_5	p_{95}	$\mu \pm \sigma$	p_5	p_{95}	$\mu \pm \sigma$	p_5	p_{95}	$\mu \pm \sigma$	p_5	p_{95}
I	17	52 ± 10	37	72	56 ± 9	41	72	64 ± 11	43	80	20 ± 10	6	39	20 ± 11	4	37	14 ± 9	1	34	2 ± 2	1	5	11 ± 9	0	21	22 ± 3	20	29
II	9	26 ± 9	13	37	31 ± 5	22	38	34 ± 5	25	41	17 ± 5	9	28	17 ± 5	9	25	12 ± 6	1	23	7 ± 5	1	15	8 ± 3	2	13	11 ± 2	9	14
III	9	34 ± 7	22	46	33 ± 6	24	44	37 ± 6	25	47	5 ± 4	0	12	5 ± 4	1	14	4 ± 4	0	12	8 ± 2	4	12	10 ± 2	7	14	11 ± 2	8	15
aVR	13	39 ± 9	27	54	43 ± 7	33	54	49 ± 8	37	60	18 ± 8	6	33	18 ± 8	6	31	13 ± 8	2	28	4 ± 4	0	10	8 ± 6	1	17	17 ± 2	15	21
aVL	13	41 ± 8	29	57	43 ± 8	32	56	50 ± 9	33	61	12 ± 7	2	25	12 ± 8	0	25	9 ± 6	2	23	4 ± 1	2	5	10 ± 5	4	16	17 ± 2	14	22
aVF	0	5 ± 3	0	12	4 ± 3	0	10	4 ± 3	0	9	7 ± 1	6	9	7 ± 1	5	8	6 ± 1	3	7	8 ± 3	3	13	6 ± 4	1	10	1 ± 0	0	2
V1	4	47 ± 9	34	63	47 ± 6	39	56	52 ± 9	38	65	11 ± 4	3	17	11 ± 3	5	15	10 ± 3	4	15	10 ± 4	5	18	8 ± 4	1	13	5 ± 4	0	14
V2	15	8 ± 7	0	23	7 ± 6	0	18	6 ± 4	1	13	25 ± 4	20	34	20 ± 7	10	31	12 ± 6	3	22	15 ± 9	5	32	16 ± 7	2	25	20 ± 4	13	26
V3	36	26 ± 19	4	61	29 ± 20	7	71	38 ± 18	10	71	39 ± 14	22	67	32 ± 18	6	58	19 ± 14	5	44	14 ± 12	1	35	26 ± 15	5	49	47 ± 4	39	52
V4	38	41 ± 21	12	80	44 ± 27	2	90	53 ± 25	12	100	35 ± 15	16	65	29 ± 19	1	56	17 ± 14	1	45	8 ± 9	0	25	24 ± 18	2	48	49 ± 5	44	59
V5	31	48 ± 21	10	81	52 ± 23	15	90	62 ± 23	24	110	27 ± 13	10	52	23 ± 15	0	47	15 ± 11	2	39	4 ± 5	0	14	18 ± 15	0	37	39 ± 5	35	51
V6	20	47 ± 13	23	69	52 ± 13	30	74	61 ± 14	34	89	18 ± 10	5	36	17 ± 11	0	33	11 ± 8	1	29	3 ± 2	0	5	12 ± 9	1	23	25 ± 4	21	35
μ		35 ± 11	18	55	37 ± 11	20	56	43 ± 11	24	62	20 ± 8	9	35	18 ± 9	4	32	12 ± 8	2	27	7 ± 5	2	16	13 ± 8	2	24	22 ± 3	18	28
p_5		7 ± 5			6 ± 4			5 ± 4			6 ± 3			6 ± 2			5 ± 2			3 ± 2			7 ± 3			3 ± 1		
p_{95}		50 ± 21			54 ± 25			63 ± 24			37 ± 14			30 ± 18			18 ± 14			14 ± 10			25 ± 16			48 ± 5		

Table C.9.: ST measurement errors in the ECG with simulated QT prolongation (SNR=3 dB). The measured errors are reported for the normal (non-pathological), for the transitional and for the pathological (QT prolongation) sections. The best results in each section are highlighted in grey. All values are given in [μV]. (Δ_{ST} = average ST amplitude difference between the normal and the pathological segment, μ = mean absolute error, σ = standard deviation of the measurement errors, p_5 = 5th percentile, p_{95} = 95th percentile.)

		Wiener filter									ICA									EKF								
		Normal			Trans			Patho			Normal			Trans			Patho			Normal			Trans			Patho		
Lead	Δ_{ST}	$\mu \pm \sigma$	p_5	p_{95}	$\mu \pm \sigma$	p_5	p_{95}	$\mu \pm \sigma$	p_5	p_{95}	$\mu \pm \sigma$	p_5	p_{95}	$\mu \pm \sigma$	p_5	p_{95}	$\mu \pm \sigma$	p_5	p_{95}	$\mu \pm \sigma$	p_5	p_{95}	$\mu \pm \sigma$	p_5	p_{95}	$\mu \pm \sigma$	p_5	p_{95}
I	17	49 ± 11	33	72	56 ± 15	33	82	59 ± 11	44	76	23 ± 17	1	48	21 ± 15	1	51	17 ± 16	1	54	4 ± 4	0	12	11 ± 9	0	25	15 ± 4	8	20
II	9	24 ± 8	9	36	28 ± 7	14	39	31 ± 7	20	44	18 ± 10	1	35	15 ± 9	4	33	14 ± 9	3	30	6 ± 2	2	9	6 ± 3	2	9	6 ± 2	4	12
III	8	32 ± 10	15	51	33 ± 10	19	51	33 ± 9	13	48	10 ± 8	1	25	11 ± 9	1	30	9 ± 7	0	22	7 ± 5	2	16	11 ± 5	4	19	9 ± 4	3	16
aVR	13	37 ± 9	19	53	42 ± 10	23	61	46 ± 9	34	60	20 ± 12	1	42	18 ± 11	4	36	15 ± 11	1	40	4 ± 1	1	6	7 ± 5	1	17	10 ± 2	8	13
aVL	13	39 ± 10	23	62	43 ± 12	28	64	45 ± 9	28	56	15 ± 12	1	36	16 ± 11	2	43	12 ± 11	2	37	4 ± 4	0	14	10 ± 7	1	21	11 ± 4	3	18
aVF	0	7 ± 5	1	17	8 ± 5	1	16	8 ± 5	1	19	8 ± 6	0	18	7 ± 5	0	15	6 ± 4	1	13	6 ± 2	3	11	6 ± 2	1	9	3 ± 2	0	7
V1	4	46 ± 11	23	62	47 ± 11	27	66	51 ± 13	28	73	12 ± 4	6	18	13 ± 4	5	20	12 ± 4	4	17	6 ± 5	1	15	10 ± 4	3	17	12 ± 3	7	16
V2	15	15 ± 10	2	30	15 ± 12	1	37	13 ± 12	0	38	29 ± 7	18	41	21 ± 10	5	36	17 ± 8	4	31	9 ± 3	4	13	5 ± 4	0	11	0 ± 0	0	1
V3	36	25 ± 22	0	53	33 ± 29	3	100	32 ± 23	3	74	53 ± 24	17	98	41 ± 25	6	82	33 ± 24	7	84	9 ± 3	3	15	17 ± 11	5	38	19 ± 5	12	26
V4	38	31 ± 26	2	60	47 ± 40	1	127	41 ± 33	0	101	49 ± 27	9	97	40 ± 26	2	85	32 ± 26	6	90	8 ± 4	1	13	20 ± 16	1	48	27 ± 6	18	36
V5	30	40 ± 25	6	70	51 ± 36	2	116	48 ± 33	3	108	38 ± 23	6	77	32 ± 22	2	70	26 ± 23	3	76	6 ± 5	0	16	18 ± 15	1	43	25 ± 5	17	34
V6	20	44 ± 16	23	62	53 ± 21	21	87	53 ± 20	26	88	23 ± 15	1	50	20 ± 13	1	43	15 ± 15	1	49	5 ± 4	1	14	13 ± 11	0	31	19 ± 4	13	25
μ		32 ± 14	13	52	38 ± 17	14	71	38 ± 15	17	65	25 ± 14	5	49	21 ± 13	3	45	17 ± 13	3	45	6 ± 4	2	13	11 ± 8	2	24	13 ± 3	8	19
p_5		11 ± 7			12 ± 6			11 ± 6			9 ± 5			9 ± 5			8 ± 4			4 ± 2			6 ± 3			2 ± 1		
p_{95}		47 ± 25			54 ± 38			56 ± 33			51 ± 25			40 ± 25			32 ± 25			9 ± 5			19 ± 15			26 ± 5		

Table C.10.: ST measurement errors in the ECG with simulated T-wave inversion (SNR=9 dB). The measured errors are reported for the normal (non-pathological), for the transitional and for the pathological (T-wave inversion) sections. The best results in each section are highlighted in grey. All values are given in [μV]. (Δ_{ST} = average ST amplitude difference between the normal and the pathological segment, μ = mean absolute error, σ = standard deviation of the measurement errors, p_5 = 5th percentile, p_{95} = 95th percentile.)

		Wiener filter									ICA									EKF								
		Normal			Trans			Patho			Normal			Trans			Patho			Normal			Trans			Patho		
Lead	Δ_{ST}	$\mu \pm \sigma$	p_5	p_{95}	$\mu \pm \sigma$	p_5	p_{95}	$\mu \pm \sigma$	p_5	p_{95}	$\mu \pm \sigma$	p_5	p_{95}	$\mu \pm \sigma$	p_5	p_{95}	$\mu \pm \sigma$	p_5	p_{95}	$\mu \pm \sigma$	p_5	p_{95}	$\mu \pm \sigma$	p_5	p_{95}	$\mu \pm \sigma$	p_5	p_{95}
I	10	4 ± 2	1	8	4 ± 3	0	8	5 ± 4	0	12	9 ± 2	6	11	6 ± 3	1	10	5 ± 3	0	10	2 ± 1	1	3	2 ± 2	0	5	4 ± 1	3	6
II	34	30 ± 10	10	41	29 ± 11	9	45	37 ± 9	24	55	41 ± 6	29	50	25 ± 14	4	47	18 ± 8	6	29	1 ± 1	0	3	7 ± 7	1	21	3 ± 2	0	5
III	24	31 ± 11	10	46	30 ± 12	8	49	35 ± 14	11	58	33 ± 6	23	42	20 ± 11	3	37	13 ± 9	0	25	2 ± 1	0	3	7 ± 6	0	16	6 ± 2	2	9
aVR	22	16 ± 3	11	23	16 ± 7	4	27	23 ± 5	16	33	25 ± 4	17	30	16 ± 8	4	28	11 ± 4	6	18	1 ± 1	0	2	4 ± 4	0	13	2 ± 2	0	5
aVL	7	9 ± 6	1	19	7 ± 5	1	18	8 ± 6	1	21	12 ± 3	8	16	7 ± 4	1	14	6 ± 3	1	11	1 ± 1	0	3	3 ± 2	0	6	5 ± 1	4	6
aVF	29	43 ± 10	23	59	33 ± 12	10	57	36 ± 13	16	59	37 ± 6	26	46	23 ± 12	3	41	16 ± 8	3	27	1 ± 1	0	2	7 ± 6	0	19	4 ± 2	1	7
V1	1	19 ± 4	14	27	15 ± 3	10	20	13 ± 4	8	19	3 ± 1	2	5	2 ± 1	0	5	2 ± 1	0	4	2 ± 1	1	3	2 ± 2	0	6	7 ± 1	5	10
V2	16	7 ± 5	1	15	11 ± 5	1	19	15 ± 2	13	18	6 ± 2	4	10	7 ± 3	3	11	10 ± 1	8	12	2 ± 1	1	3	5 ± 3	1	11	5 ± 1	4	7
V3	33	17 ± 13	2	41	21 ± 16	1	53	19 ± 17	2	56	35 ± 5	30	42	25 ± 9	9	40	23 ± 6	13	36	1 ± 1	0	3	6 ± 6	0	20	2 ± 1	0	4
V4	36	56 ± 10	43	77	41 ± 11	21	56	45 ± 10	32	64	53 ± 11	39	72	35 ± 17	8	67	29 ± 14	7	54	2 ± 2	0	5	6 ± 6	0	20	5 ± 3	1	10
V5	30	28 ± 7	18	39	17 ± 10	2	32	19 ± 10	4	39	44 ± 7	34	56	27 ± 14	3	52	21 ± 9	6	38	2 ± 1	1	5	5 ± 5	0	16	6 ± 3	2	12
V6	19	4 ± 3	0	10	7 ± 4	1	14	8 ± 6	0	18	24 ± 5	16	31	13 ± 10	1	29	7 ± 4	0	14	2 ± 1	1	4	3 ± 3	0	10	6 ± 2	3	10
μ		22 ± 7	11	34	19 ± 8	6	33	22 ± 8	11	38	27 ± 5	20	34	17 ± 9	3	32	13 ± 6	4	23	2 ± 1	0	3	5 ± 4	0	14	5 ± 2	2	8
p_5		4 ± 3			6 ± 3			7 ± 3			5 ± 2			4 ± 2			4 ± 1			1 ± 1			2 ± 2			2 ± 1		
p_{95}		49 ± 12			37 ± 14			41 ± 15			48 ± 9			31 ± 15			26 ± 11			2 ± 1			7 ± 6			6 ± 3		

Table C.11.: ST measurement errors in the ECG with simulated T-wave inversion (SNR=3 dB). The measured errors are reported for the normal (non-pathological), for the transitional and for the pathological (T-wave inversion) sections. The best results in each section are highlighted in grey. All values are given in [μV]. (Δ_{ST} = average ST amplitude difference between the normal and the pathological segment, μ = mean absolute error, σ = standard deviation of the measurement errors, p_5 = 5th percentile, p_{95} = 95th percentile.)

		Wiener filter									ICA									EKF								
		Normal			Trans			Patho			Normal			Trans			Patho			Normal			Trans			Patho		
Lead	Δ_{ST}	$\mu \pm \sigma$	p_5	p_{95}	$\mu \pm \sigma$	p_5	p_{95}	$\mu \pm \sigma$	p_5	p_{95}	$\mu \pm \sigma$	p_5	p_{95}	$\mu \pm \sigma$	p_5	p_{95}	$\mu \pm \sigma$	p_5	p_{95}	$\mu \pm \sigma$	p_5	p_{95}	$\mu \pm \sigma$	p_5	p_{95}	$\mu \pm \sigma$	p_5	p_{95}
I	9	4 ± 4	0	14	4 ± 3	1	9	5 ± 3	1	10	16 ± 7	6	30	12 ± 8	0	29	9 ± 7	2	29	1 ± 1	0	2	3 ± 3	0	8	3 ± 2	0	5
II	33	22 ± 14	5	44	21 ± 12	3	46	25 ± 15	2	49	61 ± 10	48	77	34 ± 23	1	68	14 ± 10	1	30	4 ± 3	0	8	12 ± 11	0	34	14 ± 6	7	25
III	23	28 ± 17	1	66	30 ± 16	4	58	34 ± 17	3	59	46 ± 6	38	54	25 ± 16	4	49	10 ± 5	2	18	5 ± 3	0	9	11 ± 9	1	27	17 ± 6	7	27
aVR	21	14 ± 7	4	26	16 ± 8	5	29	22 ± 8	9	33	38 ± 8	27	53	22 ± 15	3	48	10 ± 9	0	26	2 ± 1	0	4	7 ± 7	1	20	6 ± 3	2	11
aVL	7	10 ± 8	1	28	8 ± 7	1	20	13 ± 9	2	28	16 ± 5	5	22	9 ± 5	1	18	6 ± 5	0	15	3 ± 2	1	5	5 ± 3	1	11	10 ± 3	3	15
aVF	28	35 ± 18	1	69	31 ± 13	6	54	34 ± 17	3	58	53 ± 8	42	68	29 ± 20	3	56	12 ± 7	2	22	5 ± 3	0	8	11 ± 10	1	31	15 ± 6	7	26
V1	1	20 ± 7	8	33	13 ± 7	2	22	11 ± 9	1	29	14 ± 7	3	31	13 ± 8	2	29	12 ± 11	0	41	1 ± 1	0	3	3 ± 2	0	5	2 ± 1	0	4
V2	15	8 ± 4	1	16	11 ± 6	1	19	15 ± 3	11	20	19 ± 2	15	22	11 ± 6	1	20	6 ± 2	1	9	2 ± 1	0	3	4 ± 4	0	10	3 ± 2	1	7
V3	32	8 ± 7	1	20	17 ± 20	2	64	32 ± 24	2	83	35 ± 6	24	47	25 ± 12	5	45	18 ± 9	6	32	2 ± 1	0	4	7 ± 9	0	24	4 ± 3	1	9
V4	35	53 ± 14	27	78	38 ± 17	12	72	39 ± 17	13	67	54 ± 14	32	81	34 ± 22	4	76	18 ± 15	2	47	2 ± 1	0	4	10 ± 10	0	30	4 ± 3	1	8
V5	29	30 ± 13	9	52	20 ± 15	2	58	21 ± 15	2	49	48 ± 13	25	72	30 ± 20	2	71	17 ± 13	1	42	2 ± 1	0	4	9 ± 8	1	25	4 ± 3	0	9
V6	19	7 ± 6	0	18	8 ± 6	0	18	8 ± 6	1	21	23 ± 8	13	38	16 ± 10	3	36	11 ± 8	2	25	1 ± 1	0	3	7 ± 6	1	17	3 ± 3	0	7
μ		20 ± 10	5	39	18 ± 11	3	39	22 ± 12	4	42	35 ± 8	23	50	22 ± 14	2	45	12 ± 8	2	28	3 ± 2	0	5	7 ± 7	1	20	7 ± 3	2	13
p_5		6 ± 4			6 ± 5			7 ± 3			15 ± 4			10 ± 6			6 ± 4			1 ± 1			3 ± 3			3 ± 2		
p_{95}		43 ± 17			34 ± 18			36 ± 20			57 ± 13			34 ± 22			18 ± 14			5 ± 3			11 ± 10			16 ± 6		

Table C.12.: ST measurement errors for the complete ECG with simulated QT prolongation (SNR=9 dB and SNR=3 dB). The best results in each section are highlighted in grey. All values are given in [μV]. (Δ_{ST} = average ST amplitude difference between the normal and the pathological segment, μ = mean absolute error, σ = standard deviation of the measurement errors, p_5 = 5th percentile, p_{95} = 95th percentile.)

	SNR=9 dB									SNR=3 dB								
	Wiener filter			ICA			EKF			Wiener filter			ICA			EKF		
Lead	$\mu \pm \sigma$	p_5	p_{95}	$\mu \pm \sigma$	p_5	p_{95}	$\mu \pm \sigma$	p_5	p_{95}	$\mu \pm \sigma$	p_5	p_{95}	$\mu \pm \sigma$	p_5	p_{95}	$\mu \pm \sigma$	p_5	p_{95}
I	57 ± 11	40	74	19 ± 11	4	37	11 ± 10	0	23	55 ± 14	34	80	20 ± 15	1	50	10 ± 8	0	23
II	30 ± 7	18	39	16 ± 6	6	25	8 ± 4	2	14	28 ± 8	13	39	16 ± 9	2	33	6 ± 2	2	9
III	35 ± 7	24	46	5 ± 4	0	12	10 ± 3	6	14	33 ± 10	16	50	10 ± 8	1	25	9 ± 5	3	18
aVR	43 ± 8	31	56	17 ± 8	4	31	9 ± 7	0	18	41 ± 10	23	58	17 ± 11	2	37	7 ± 5	1	14
aVL	44 ± 9	31	58	11 ± 8	1	25	10 ± 6	3	18	43 ± 11	27	63	14 ± 11	1	36	9 ± 6	1	21
aVF	4 ± 3	0	11	7 ± 1	5	9	5 ± 4	1	12	8 ± 5	1	17	7 ± 5	0	16	5 ± 3	1	10
V1	48 ± 8	36	62	11 ± 3	5	15	8 ± 5	0	16	48 ± 12	26	67	12 ± 4	5	20	9 ± 5	2	17
V2	7 ± 6	0	18	20 ± 8	7	33	17 ± 7	5	27	14 ± 11	1	32	22 ± 10	6	38	5 ± 4	0	12
V3	30 ± 20	5	70	31 ± 17	5	59	28 ± 17	2	51	31 ± 26	2	89	42 ± 25	6	84	15 ± 9	5	32
V4	45 ± 25	9	91	28 ± 18	1	57	26 ± 20	1	51	41 ± 35	1	122	40 ± 26	5	86	18 ± 14	1	42
V5	53 ± 23	15	91	22 ± 15	1	47	19 ± 17	0	40	47 ± 33	5	112	32 ± 22	3	72	16 ± 13	1	37
V6	53 ± 14	32	75	16 ± 10	1	33	12 ± 11	0	26	50 ± 20	23	85	19 ± 14	1	43	12 ± 10	0	27
μ	37 ± 12	20	58	17 ± 9	3	32	14 ± 9	2	26	37 ± 16	14	68	21 ± 13	3	45	10 ± 7	1	22
p_5	6 ± 5			6 ± 2			7 ± 4			11 ± 7			9 ± 5			5 ± 3		
p_{95}	55 ± 24			29 ± 17			27 ± 18			52 ± 34			41 ± 25			17 ± 13		

Table C.13.: ST measurement errors for the complete ECG with simulated T-wave inversion (SNR=9 dB and SNR=3 dB). The best results in each section are highlighted in grey. All values are given in [μV]. (Δ_{ST} = average ST amplitude difference between the normal and the pathological segment, μ = mean absolute error, σ = standard deviation of the measurement errors, p_5 = 5th percentile, p_{95} = 95th percentile.)

	SNR=9 dB									SNR=3 dB								
	Wiener filter			ICA			EKF			Wiener filter			ICA			EKF		
Lead	$\mu \pm \sigma$	p_5	p_{95}	$\mu \pm \sigma$	p_5	p_{95}	$\mu \pm \sigma$	p_5	p_{95}	$\mu \pm \sigma$	p_5	p_{95}	$\mu \pm \sigma$	p_5	p_{95}	$\mu \pm \sigma$	p_5	p_{95}
I	4 ± 3	0	9	6 ± 3	1	11	2 ± 2	0	6	4 ± 3	1	10	12 ± 8	1	29	2 ± 2	0	6
II	31 ± 11	10	46	28 ± 14	5	48	4 ± 6	0	18	22 ± 13	3	47	37 ± 25	2	72	10 ± 9	0	29
III	32 ± 12	10	56	22 ± 12	2	39	5 ± 5	0	15	31 ± 17	3	59	27 ± 18	4	51	11 ± 8	1	26
aVR	18 ± 7	6	28	17 ± 8	5	29	3 ± 3	0	10	17 ± 8	4	32	24 ± 16	2	48	5 ± 5	1	19
aVL	8 ± 6	1	18	8 ± 4	1	15	3 ± 2	0	6	10 ± 8	1	26	10 ± 6	1	20	6 ± 4	1	13
aVF	37 ± 13	17	58	25 ± 13	4	44	5 ± 5	0	16	33 ± 16	5	57	32 ± 21	3	61	11 ± 9	1	27
V1	16 ± 4	9	23	2 ± 1	0	5	4 ± 3	0	8	15 ± 8	2	29	13 ± 9	2	31	2 ± 2	0	5
V2	11 ± 5	1	18	7 ± 3	3	11	4 ± 3	1	10	11 ± 5	1	19	12 ± 7	2	21	3 ± 3	0	8
V3	20 ± 15	2	50	27 ± 9	11	42	4 ± 5	0	16	18 ± 21	1	69	26 ± 12	6	44	5 ± 7	0	21
V4	46 ± 12	25	65	39 ± 18	8	68	5 ± 5	0	16	42 ± 17	14	69	36 ± 23	3	75	6 ± 8	0	26
V5	20 ± 10	3	38	30 ± 14	6	53	5 ± 4	0	13	23 ± 14	2	48	32 ± 20	2	64	6 ± 7	0	23
V6	6 ± 5	0	14	15 ± 10	1	29	4 ± 3	0	10	8 ± 6	0	19	17 ± 10	2	37	4 ± 5	0	15
μ	21 ± 9	7	35	19 ± 9	4	33	4 ± 4	0	12	20 ± 11	3	40	23 ± 15	3	46	6 ± 6	0	18
p_5	5 ± 4			4 ± 2			3 ± 2			6 ± 4			11 ± 7			2 ± 2		
p_{95}	41 ± 14			34 ± 16			5 ± 5			37 ± 19			36 ± 24			11 ± 9		

Table C.14.: ST measurement errors in the ECG without simulated pathologies (normal ECG) (SNR=9 dB and SNR=3 dB). The best results in each section are highlighted in grey. All values are given in [μV]. (Δ_{ST} = average ST amplitude difference between the normal and the pathological segment, μ = mean absolute error, σ = standard deviation of the measurement errors, p_5 = 5th percentile, p_{95} = 95th percentile.)

	SNR=9 dB									SNR=3 dB								
	Wiener filter			ICA			EKF			Wiener filter			ICA			EKF		
Lead	$\mu \pm \sigma$	p_5	p_{95}	$\mu \pm \sigma$	p_5	p_{95}	$\mu \pm \sigma$	p_5	p_{95}	$\mu \pm \sigma$	p_5	p_{95}	$\mu \pm \sigma$	p_5	p_{95}	$\mu \pm \sigma$	p_5	p_{95}
I	86 ± 20	53	123	7 ± 6	0	18	6 ± 4	0	13	72 ± 28	28	119	33 ± 19	5	62	4 ± 3	1	10
II	38 ± 23	6	76	26 ± 13	7	44	10 ± 6	1	20	49 ± 37	5	124	67 ± 33	12	116	6 ± 5	0	16
III	34 ± 19	8	67	22 ± 8	10	34	6 ± 4	0	12	34 ± 20	4	70	35 ± 14	12	57	8 ± 7	0	23
aVR	72 ± 18	42	108	15 ± 9	2	31	7 ± 5	0	15	64 ± 31	12	126	49 ± 26	4	89	3 ± 2	0	7
aVL	13 ± 8	2	26	9 ± 4	2	16	3 ± 2	0	8	7 ± 5	1	16	5 ± 4	0	12	6 ± 5	0	15
aVF	20 ± 15	2	48	24 ± 10	7	40	8 ± 4	0	15	36 ± 25	4	89	51 ± 23	12	86	7 ± 6	1	18
V1	11 ± 8	0	24	43 ± 12	22	68	11 ± 8	1	28	21 ± 18	2	57	51 ± 18	24	82	8 ± 5	1	17
V2	37 ± 24	6	80	79 ± 20	47	122	10 ± 8	1	24	40 ± 30	4	97	110 ± 14	89	133	14 ± 10	1	32
V3	48 ± 39	4	129	88 ± 26	52	135	8 ± 5	1	16	57 ± 40	8	141	130 ± 41	60	194	15 ± 12	1	37
V4	64 ± 48	8	168	62 ± 28	20	113	11 ± 7	1	23	76 ± 61	4	174	97 ± 46	18	170	10 ± 8	1	24
V5	67 ± 43	7	156	38 ± 25	5	87	12 ± 9	0	28	68 ± 54	3	166	49 ± 34	4	118	5 ± 4	0	12
V6	58 ± 27	19	112	15 ± 11	1	37	11 ± 8	1	25	57 ± 38	6	138	26 ± 20	3	69	2 ± 2	0	4
μ	46 ± 24	13	93	36 ± 14	15	62	9 ± 6	1	19	48 ± 32	7	110	59 ± 24	20	99	7 ± 6	1	18
p_5	12 ± 8			8 ± 5			5 ± 3			15 ± 12			17 ± 10			3 ± 2		
p_{95}	78 ± 45			83 ± 27			11 ± 8			74 ± 57			119 ± 43			14 ± 11		

Bibliography

[Abächerli 05] R. Abächerli, C. Pasquier, F. Odille, M. Kraemer, J.J. Schmid & J. Felblinger. *Suppression of MR gradient artefacts on electrophysiological signals based on an adaptive real-time filter with LMS coefficient updates*. MAGMA, vol. 18, no. 1, pages 41–50, 2005. (Cited on pages 25, 28 and 44)

[Abbas 09] A.K. Abbas & R. Bassam. Phonocardiography Signal Processing, volume 4. Morgan & Claypool Publishers, 2009. (Cited on page 52)

[Abi-Abdallah 09a] D. Abi-Abdallah, A. Drochon, V. Robin & O. Fokapu. *Effects of Static Magnetic Field Exposure on Blood Flow*. Eur Phys J-Appl Phys, vol. 45, no. 01, page 11301, 2009. (Cited on page 34)

[Abi-Abdallah 09b] D. Abi-Abdallah, A. Drochon, V. Robin & O. Fokapu. *Pulsed Magnetohydrodynamic blood flow in a rigid vessel under physiological pressure gradient*. Comput Methods Biomech Biomed Engin, vol. 12, no. 4, pages 445–458, 2009. (Cited on page 34)

[Algra 91] A. Algra, J.G. Tijssen, J.R. Roelandt, J. Pool & J. Lubsen. *QTc prolongation measured by standard 12-lead electrocardiography is an independent risk factor for sudden death due to cardiac arrest*. Circulation, vol. 83, no. 6, pages 1888–1894, 1991. (Cited on page 17)

[Allen 02] J. Allen & A. Murray. *Age-related changes in peripheral pulse timing characteristics at the ears, fingers and toes.* J Hum Hypertens, vol. 16, no. 10, pages 711–717, 2002. (Cited on page 54)

[Alpert 00] J.S. Alpert, K. Thygesen, E. Antman, Bassand. J.P.*et al. Myocardial infarction redefined – a consensus document of the Joint European Society of Cardiology/American College of Cardiology committee for the redefinition of myocardial infarction: the Joint European Society of Cardiology/American College of Cardiology Committee*. Eur Heart J, vol. 21, no. 18, pages 1502–1513, 2000. (Cited on page 16)

[Andersen 89] HR Andersen, Erling Falk & Dorthe Nielsen. *Right ventricular infarction: diagnostic accuracy of electrocardiographic right chest leads V3R to V7R investigated prospectively in 43 consecutive fatal cases from a coronary care unit*. Brit Heart J, vol. 61, no. 6, pages 514–520, 1989. (Cited on page 12)

[Andreotti 14] F. Andreotti, M. Riedl, T. Himmelsbach, D. Wedekind, N. Wessel, H. Stepan, C. Schmieder, A. Jank, H. Malberg & S. Zaunseder. *Robust fetal ECG extraction and detection from abdominal leads*. Physiol Meas, vol. 35, no. 8, pages 1551–1567, 2014. (Cited on pages 71 and 134)

[ANSI 98] ANSI. *American National Standrad, EC57:1998/(R)2008, Testing and reporting performance results of cardiac rhythm and ST segment measurement algorithms*, 1998. (Cited on page 79)

[Armstrong 02] B. Armstrong, T. Verron, L. Heppe, J. Reynolds & K. Schmidt. *RGR-3D: simple, cheap detection of 6-DOF pose for teleoperation, and robot programming and calibration*. In Proc Int Conf Robotics and Automation (ICRA), volume 3, pages 2938–2943, Washington DC, 2002. IEEE. (Cited on page 56)

[ASA 11] *Standards for Basic Anesthetic Monitoring*, 2011. (Cited on pages 25 and 26)

[Augustyniak 01] P. Augustyniak. *On the Equivalence of the 12-Lead ECG and the VCG Representations of the Cardiac Electrical Activity*. In Proceedings of 10th International Conference on System-Modelling-Control. Zakopane, pages 51–56, 2001. (Cited on pages 15 and 170)

[Balaji 02] S. Balaji, M. Ellenby, J. McNames & B. Goldstein. *Update on intensive care ECG and cardiac event monitoring*. Card Electrophysiol Rev, vol. 6, no. 3, pages 190–195, 2002. (Cited on page 26)

[Behar 14a] J. Behar, F. Andreotti, S. Zaunseder, Q. Li, J. Oster & G.D. Clifford. *An ECG simulator for generating maternal-foetal activity mixtures on abdominal ECG recordings*. Physiol Meas, vol. 35, no. 8, pages 1537–1550, 2014. (Cited on page 73)

[Behar 14b] J. Behar, J. Oster & G.D. Clifford. *Combining and benchmarking methods of foetal ECG extraction without maternal or scalp electrode data*. Physiol Meas, vol. 35, no. 8, page 1569, 2014. (Cited on page 71)

[Beisteiner 11] R. Beisteiner, S. Robinson, M. Wurnig, M. Hilbert, K. Merksa, J. Rath, I. Höllinger, N. Klinger, C. Marosi, S. Trattnig & A. Geißler. *Clinical fMRI: evidence for a 7T benefit over 3T*. Neuroimage, vol. 57, no. 3, pages 1015–1021, 2011. (Cited on page 26)

[Bergstra 12] J. Bergstra & Y. Bengio. *Random search for hyper-parameter optimization*. J Mach Learn Res, vol. 13, no. 1, pages 281–305, 2012. (Cited on page 144)

[Bhatt 09a] B. Bhatt & M.R. Reddy. *ICA Based Flow Artifact Removal from ECG during MRI*. In Proc Int Conf ACT 09, pages 241–243, 2009. (Cited on page 58)

[Bhatt 09b] B. Bhatt & M.R. Reddy. *Suppression of MHD artifacts on single channel ECG during cardiac MRI*. In Proc IEEE TENCON, pages 1–4. IEEE, 2009. (Cited on page 58)

[Bhatt 09c] B. Bhatt & M.R. Reddy. *Theoretical Analysis of Induced Potentials due to Blood Flow under the Static Magnetic Field of MRI*. Indian Journal of Biomechanics, pages 51–55, 2009. (Cited on pages 33 and 58)

[Blazek 00] V. Blazek, T. Wu & D. Hoelscher. *Near-infrared CCD imaging: possibilities for noninvasive and contactless 2D mapping of dermal venous hemodynamics*. In Proc SPIE, volume 3923, page 2. International Society for Optics and Photonics, 2000. (Cited on page 55)

[Boashash 88] B. Boashash. *Note on the use of the Wigner distribution for time-frequency signal analysis*. IEEE Transactions on Acoustics, Speech and Signal Processing, vol. 36, pages 1518–1521, 1988. (Cited on page 39)

[Boashash 03] B. Boashash. *Discrete Time Frequency Distributions*. In B. Boashash, editeur, Time Frequency Signal Analysis and Processing - A Comprehensive Reference, pages 231–241. Elsevier, 2003. (Cited on page 39)

[Bogaert 04] J. Bogaert, S. Dymarkowski & A.M. Taylor, editeurs. Clinical Cardiac MRI. Springer, 1 edition, 2004. (Cited on page 26)

[Brandts 10] A. Brandts, J.J.M. Westenberg, M.J. Versluis, L.J.M. Kroft, N.B. Smith, A.G. Webb & A. de Roos. *Quantitative Assessment of Left Ventricular Function in Humans at 7 T*. Magnet Reson Med, vol. 64, no. 5, pages 1471–1477, 2010. (Cited on pages 49 and 57)

[Brau 02] A. Brau, C.T. Wheeler, L.W. Hedlund & G.A. Johnson. *Fiber-optic stethoscope: A cardiac monitoring and gating system for magnetic resonance microscopy*. Magnet Reson Med, vol. 47, no. 2, pages 314–321, 2002. (Cited on page 55)

[Carpenter 13] J.-P. Carpenter, A.R. Patel & J.L. Fernandes. *Highlights of the 16th annual scientific sessions of the Cociety for Cardiovascular Magnetic Resonance*. J Cardiovasc Magn Reson, vol. 15, no. Suppl 1, page 60, 2013. (Cited on page 57)

[Castells 05] F. Castells, J. J. Rieta, J. Millet & V. Zarzoso. *Spatiotemporal Blind Source Separation Approach to Atrial Activity Estimation in Atrial Tachyarrhythmias*. IEEE Trans Biomed Eng, vol. 52, no. 2, pages 258–267, 2005. (Cited on pages 93 and 136)

[Chang 10] P.C. Chang, J.C. Hsieh, J.J. Lin & F.M. Yeh. *Atrial Fibrillation Analysis Based on Blind Source Separation in 12-lead ECG*. World Academy of Scinence, Engineering and Technology, pages 599–602, 2010. (Cited on page 136)

[Channer 02] K. Channer & F. Morris. *ABC of clinical electrocardiography: Myocardial ischaemia*. The BMJ, vol. 324, no. 7344, page 1023, 2002. (Cited on pages 16 and 18)

[Chen 89] C. Chen & D.I. Hoult. Biomedical magnetic resonance technology. Institute of Physics Publishing, Bristol, UK, 1989. (Cited on pages 19 and 20)

[Chia 00] J.M. Chia, S.E. Fischer, S.A. Wickline & C.H. Lorenz. *Performance of QRS detection for cardiac magnetic resonance imaging with a novel vectorcardiographic triggering method*. J Magn Reson Imaging, vol. 12, no. 5, pages 678–688, 2000. (Cited on pages 13, 49, 50, 80 and 179)

[Christ 10] A. Christ, W. Kainz, E.G. Hahn, K. Honegger, M. Zefferer, E. Neufeld, W. Rascher, R. Janka, W. Bautz, J. Chen*et al. The Virtual Family - development of surface-based*

anatomical models of two adults and two children for dosimetric simulations. Phys Med Biol, vol. 55, no. 2, pages N23–N38, 2010. (Cited on page 34)

[Clifford 02] G.D. Clifford. *Signal Processing Methods for Heart Rate Variability*. Ph.D. Thesis, St. Cross College, University of Oxford, 2002. (Cited on pages 68, 90, 98, 101, 104, 125 and 126)

[Clifford 05] G.D. Clifford. *Singular Value Decomposition and Independent Component Analysis for Blind Source Separation (Lecture at Massachusetts Institute of Technology*. [Online]. Available: http://www.mit.edu/~gari/teaching/6.222j/ICASVDnotes.pdf, Spring 2005. (Cited on page 103)

[Clifford 06] G.D. Clifford, Francisco A. & P.E. McSharry, editeurs. Advanced Methods and Tools for ECG Data Analysis. Artech House, Inc., Boston, London, 2006. (Cited on pages 17, 73 and 83)

[Clifford 10] G.D. Clifford, S. Nemati & R. Sameni. *An artificial vector model for generating abnormal electrocardiographic rhythms*. Physiol Meas, vol. 31, no. 5, pages 595–609, 2010. (Cited on page 59)

[Clifford 13] G. Clifford, J. Oster, O. Pietquin & M. Geist. *Periodic Artifact Reduction From Biomedical Signals*, April 2013. WO Patent 2,013,052,944. (Cited on page 59)

[Cohen 86] M.M. Cohen, P.G. Duncan, W.D.B. Pope & C. Wolkenstein. *A survey of 112,000 anaesthetics at one teaching hospital (1975–83)*. Can Anaesth Soc J, vol. 33, no. 1, pages 22–31, 1986. (Cited on page 26)

[Commons 09] Wikimedia Commons. *Sinoatrial node*. http://en.wikipedia.org/wiki/Sinoatrial_node, 2009. File: ConductionsystemoftheheartwithouttheHeart-en.svg, last checked: 26.10.2014. (Cited on page 8)

[Comon 10] P. Comon & C. Jutten. Handbook of Blind Source Separation: Independent component analysis and applications. Academic Press, 1 edition, 2010. (Cited on page 96)

[Courneya 11] C.A.M. Courneya & M.J. Parker. Cardiovascular Physiology: A Clinical Approach. Lippincott Williams & Wilkins, 2011. (Cited on page 11)

[Das 10] K. Das & G.C. Saha. *Mathematical Analysis on MHD Pulsatile Flow of Blood through a Rough Thin-Walled Elastic Tube*. Applied Mathematical Sciences, vol. 4, no. 50, pages 2463–2473, 2010. (Cited on page 29)

[Dash 02] PK Dash. *Electrocardiogram Monitoring*. Indian J Anaesth, vol. 46, no. 4, pages 251–260, 2002. (Cited on page 26)

[Davies 88] G.J. Davies, W. Bencivelli, G. Fragasso, S. Chierchia, F. Crea, J. Crow, P.A. Crean, T. Pratt, M. Morgan & A. Maseri. *Sequence and magnitude of ventricular volume changes in painful and painless myocardial ischemia.* Circulation, vol. 78, no. 2, pages 310–319, 1988. (Cited on page 78)

[DeCarlo 97] L.T. DeCarlo. *On the meaning and use of kurtosis*. Psychol Methods, vol. 2, no. 3,

pages 292–307, 1997. (Cited on page 100)

[den Adel 13] B. den Adel, L.M. van der Graaf, G.J. Strijkers, H.J. Lamb, R.E. Poelmann & L. van der Weerd. *Self-Gated CINE MRI for Combined Contrast-Enhanced Imaging and Wall-Stiffness Measurements of Murine Aortic Atherosclerotic Lesions*. PloS one, vol. 8, no. 3, page e57299, 2013. (Cited on page 53)

[Díaz Morales 12] R. Díaz Morales. *Facial segmentation using the Active Shape Model for the contactless monitoring of vital signals*. Master thesis, Technische Universität Dresden, Germany, 2012. (Cited on page 55)

[Dower 80] G.E. Dower, H.B. Machado & J.A. Osborne. *On deriving the electrocardiogram from vectoradiographic leads*. Clin Cardiol, vol. 3, no. 2, pages 87–95, 1980. (Cited on page 14)

[Dower 88] G.E. Dower, A. Yakush, S.B. Nazzal, R.V. Jutzy & C.E. Ruiz. *Deriving the 12-lead electrocardiogram from four (EASI) electrodes*. J Electrocardiol, vol. 21, pages 182–187, 1988. (Cited on page 13)

[Drew 04] B.J. Drew, R.M. Califf, M. Funk, E.S. Kaufman, M.W. Krucoff, M.M. Laks, P.W. Macfarlane, C. Sommargren, S. Swiryn & G.F. Van Hare. *Practice Standards for Electrocardiographic Monitoring in Hospital Settings An American Heart Association Scientific Statement From the Councils on Cardiovascular Nursing, Clinical Cardiology, and Cardiovascular Disease in the Young: Endorsed by the International Society of Computerized Electrocardiology and the American Association of Critical-Care Nurses*. Circulation, vol. 110, no. 17, pages 2721–2746, 2004. (Cited on page 12)

[Drinnan 01] M.J. Drinnan, J. Allen & A. Murray. *Relation between heart rate and pulse transit time during paced respiration*. Physiol Meas, vol. 22, no. 3, pages 425–432, 2001. (Cited on page 54)

[Dukkipati 08] S.R. Dukkipati, R. Mallozzi, E.J. Schmidt, G. Holmvang, A. Avila, R. Guhde, R.D. Darrow, G. Slavin, M. Fung, Z. Malchano*et al.* *Electroanatomic Mapping of the Left Ventricle in a Porcine Model of Chronic Myocardial Infarction With Magnetic Resonance-Based Catheter Tracking*. Circulation, vol. 118, no. 8, pages 853–862, 2008. (Cited on pages 22, 26, 57, 169 and 177)

[Dymarkowski 03] S. Dymarkowski. Characterization of Myocardial Ischemia and Infarction: Experimental MRI-Studies, volume 288. Leuven University Press, 2003. (Cited on page 78)

[Edenbrandt 88] L. Edenbrandt & O.vector Pahlm. *Vectorcardiogram synthesized from a 12-lead ECG: superiority of the inverse Dower matrix*. J Electrocardiol, vol. 21, no. 4, pages 361–367, 1988. (Cited on pages 13 and 15)

[Evans 09] C.H. Evans & R.D. White. Exercise Testing for Primary Care and Sports Medicine Physicians. Springer, 2009. (Cited on page 16)

[Feinberg 10] D.A. Feinberg, D. Giese, D.A. Bongers, S. Ramanna, M. Zaitsev, M. Markl & M. Günther. *Hybrid ultrasound MRI for improved cardiac imaging and real-time*

respiration control. Magnet Reson Med, vol. 63, no. 2, pages 290–296, 2010. (Cited on page 54)

[Felblinger 94] J. Felblinger, C. Lehmann & C. Boesch. *Electrocardiogram acquisition during MR examinations for patient monitoring and sequence triggering*. Magnet Reson Med, vol. 32, no. 4, pages 523–529, 1994. (Cited on page 59)

[Felblinger 95] J. Felblinger, J.F. Debatin, C. Boesch, R. Gruetter & G.C. McKinnon. *Synchronization device for electrocardiography-gated echo-planar imaging*. Radiology, vol. 197, no. 1, pages 311–313, 1995. (Cited on page 59)

[Felblinger 99] J. Felblinger, J. Slotboom, R. Kreis, B. Jung, C. Boesch*et al. Restoration of Electrophysiological Signals Distorted by Inductive Effects of Magnetic Field Gradients During MR Sequences*. Magnet Reson Med, vol. 41, no. 4, pages 715–721, 1999. (Cited on pages 25, 27 and 44)

[Fernandez 10] B. Fernandez, J. Oster, M. Lohézic, D. Mandry, O. Pietquin, P.A. Vuissoz & J. Felblinger. *Adaptive Black Blood Fast Spin Echo for End-Systolic Rest Cardiac Imaging*. Magnet Reson Med, vol. 64, no. 6, pages 1760–1771, 2010. (Cited on pages 23 and 24)

[Ferreira 13] P.F. Ferreira, P.D. Gatehouse, R.H. Mohiaddin & D.N. Firmin. *Cardiovascular magnetic resonance artefacts*. J Cardiovasc Magn Reson, vol. 15, no. 41, pages 1–39, 2013. (Cited on page 43)

[Fischer 99] S.E. Fischer, S.A. Wickline & C.H. Lorenz. *Novel real-time R-wave detection algorithm based on the vectorcardiogram for accurate gated magnetic resonance acquisitions*. Magnet Reson Med, vol. 42, no. 2, pages 361–370, 1999. (Cited on pages 13, 49, 50, 88, 107 and 179)

[Fischer 01] S. Fischer, J. Boef & F. Vugts. *Cardiac Triggering at 3.0 Tesla*. In Proc Intl Soc Mag Reson Med, volume 9, page 1826, 2001. (Cited on pages 13, 49 and 179)

[Fletcher 13] G.F. Fletcher, P.A. Ades, P. Kligfield, R. Arena, G.J. Balady, V.A. Bittner, L.A. Coke, J.L. Fleg, D.E. Forman, T.C. Gerber*et al. Exercise Standards for Testing and Training A Scientific Statement From the American Heart Association*. Circulation, vol. 128, no. 8, pages 873–934, 2013. (Cited on pages 16 and 17)

[Frank 56] E. Frank. *An accurate, clinically practical system for spatial vectorcardiography*. Circulation, vol. 13, no. 5, pages 737–749, 1956. (Cited on page 49)

[Frank 11] M. Frank & J. Rössler. *Method for identifying a characteristic profile of an R-wave in an EKG signal and a computer program product as well as an electronically readable data medium for performing the method*, December 2011. US Patent App. 13/164,968. (Cited on page 51)

[Frank 13] M. Frank, S. Merkel, E. Mustafa & H. Wrobel. *Method for controlling a measurement of a magnetic resonance device on the basis of an electrocardiogram signal*, February 2013. US Patent 8,380,285. (Cited on page 51)

[Fratz 08] S. Fratz, J. Hess, A. Schuhbaeck, C. Buchner, E. Hendrich, S. Martinoff & H. Stern. *Routine clinical cardiovascular magnetic resonance in paediatric and adult congenital heart disease: patients, protocols, questions asked and contributions made*. J Cardiovasc Magn Reson, vol. 10, no. 46, pages 1–6, 2008. (Cited on page 51)

[Frauenrath 08] T. Frauenrath, T. Niendorf & M. Kob. *Acoustic method for synchronization of magnetic resonance imaging (MRI)*. Acta Acustica united with Acustica, vol. 94, no. 1, pages 148–155, 2008. (Cited on pages 52 and 53)

[Frauenrath 09] T. Frauenrath, F. Hezel, U. Heinrichs, S. Kozerke, J.F. Utting, M. Kob, C. Butenweg, P. Boesiger & T. Niendorf. *Feasibility of cardiac gating free of interference with electro-magnetic fields at 1.5 Tesla, 3.0 Tesla and 7.0 Tesla using an MR-stethoscope*. Invest Radiol, vol. 44, no. 9, pages 539–547, 2009. (Cited on pages 49 and 52)

[Frauenrath 10a] T. Frauenrath. *Akustisches Synchronisationsverfahren für die Magnetresonanztomographie*. Ph.d. thesis, RWTH Aachen University, 2010. (Cited on page 24)

[Frauenrath 10b] T. Frauenrath, F. Hezel, W. Renz, T. de Geyer d'Orth, M. Dieringer, F. von Knobelsdorff-Brenkenhoff, M. Prothmann, J. Schulz-Menger & T. Niendorf. *Acoustic cardiac triggering: a practical solution for synchronization and gating of cardiovascular magnetic resonance at 7 Tesla*. J Cardiovasc Magn Reson, vol. 12, no. 67, pages 1–14, 2010. (Cited on pages 49, 52, 54 and 57)

[Frauenrath 10c] T. Frauenrath, W. Renz, F. Patel N. Hezel, M. Dieringer, J. Schulz-Menger & T. Niendorf. *Cardiac imaging at 7.0 T: comparison of pulse oximetry, electrocardiogram and phonocardiogram triggered 2D-CINE for LV-function assessment*. J Cardiovasc Magn Reson, vol. 12, no. Suppl 1, page O15, 2010. (Cited on page 52)

[Friesen 90] G.M. Friesen, T.C. Jannett, M.A. Jadallah, S.L. Yates, S.R. Quint & H.T. Nagle. *A comparison of the noise sensitivity of nine QRS detection algorithms*. IEEE Trans Biomed Eng, vol. 37, no. 1, pages 85–98, 1990. (Cited on page 73)

[Fujioka 00] H. Fujioka & K. Tanishita. Clinical application of computational mechanics to the cardiovascular system, chapitre 3.1: Computational fluid mechanics of the blood flow in an aortic vessel with realistic geometry, pages 99–117. Springer, 2000. (Cited on page 36)

[Gatzoulis 97] Michael A Gatzoulis, Jan A Till & Andrew N Redington. *Depolarization-Repolarization Inhomogeneity After Repair of Tetralogy of Fallot The Substrate for Malignant Ventricular Tachycardia?* Circulation, vol. 95, no. 2, pages 401–404, 1997. (Cited on page 51)

[Gertsch 08] M. Gertsch. Das EKG. Springer, Berlin, 2 edition, 2008. (Cited on pages 11 and 12)

[Gold 62] R.R. Gold. *Magnetohydrodynamic pipe flow. Part 1*. J Fluid Mech, vol. 13, no. 04, pages 505–512, 1962. (Cited on page 33)

[Goldberger 00] A. L. Goldberger, L. A. Amaral, L. Glass, J. M. Hausdorff, P. C. Ivanov, R. G. Mark, J. E. Mietus, G. B. Moody, C. K. Peng & H. E. Stanley. *PhysioBank, PhysioToolkit, and PhysioNet: Components of a New Research Resource for Complex Physiologic*

Signals. Circulation, vol. 101, no. 23, pages 215–220, Jun 2000. (Cited on pages 33, 51, 58, 73 and 82)

[Goldenberg 06] I. Goldenberg, A.J. Moss & W. Zareba. *QT interval: how to measure it and what is normal*. J Cardiovasc Electrophysiol, vol. 17, no. 3, pages 333–336, 2006. (Cited on page 147)

[Gregory 14a] T.S. Gregory, E.J. Schmidt, S.H. Zhang & Z Tse. *Comparing 3DQRS and VCG approaches for ECG QRS detection within 1.5T, 3T and 7T MRI*. J Cardiovasc Magn Reson, vol. 16, no. Suppl 1, page P148, 2014. (Cited on page 49)

[Gregory 14b] T.S. Gregory, E.J. Schmidt, S.H. Zhang & Z.T. Tse. *3DQRS: A method to obtain reliable QRS complex detection within high field MRI using 12-lead electrocardiogram traces*. Magnet Reson Med, 2014. (Cited on page 50)

[Günther 04] M. Günther & D.A. Feinberg. *Ultrasound-guided MRI: Preliminary results using a motion phantom*. Magnet Reson Med, vol. 52, no. 1, pages 27–32, 2004. (Cited on page 54)

[Gupta 08] A. Gupta, A.R. Weeks & S.M. Richie. *Simulation of elevated T-waves of an ECG inside a static magnetic field (MRI)*. IEEE Trans Biomed Eng, vol. 55, no. 7, pages 1890–1896, Jul 2008. (Cited on pages 29 and 33)

[Gupta 12] S. Gupta, A.R. Popescu, R.A. De Freitas, D. Thakrar, J. Puthumana, J. Carr & M. Markl. *Four-Dimensional Magnetic Resonance Flow Analysis Clarifies Paradoxical Symptoms in a Patient With Aortic Bypass and Retrograde Flow Mimicking Subclavian Steal*. Circulation, vol. 125, no. 6, pages e347–e349, 2012. (Cited on page 32)

[Gutberlet 12] M. Gutberlet, M. Grothoff, C. Eitel, C. Lücke, P. Sommer, C. Piorkowski & G. Hindricks. *First clinical experience in man with the IMRICOR-MR-EP system: Electrophysiology study guided by real-time MRI*. J Cardiovasc Magn Reson, vol. 14, no. Suppl 1, page P205, 2012. (Cited on page 26)

[Guyton 06] A.C. Guyton & J. E. Hall. Textbook of Medical Physiology. Elsevier Saunders, 2006. (Cited on page 6)

[Haas 11] N.A. Haas & U. Kleideiter. Kinderkardiologie: Klinik und Praxis der Herzerkrankungen bei Kindern, Jugendlichen und jungen Erwachsenen. Georg Thieme Verlag, 2011. (Cited on page 18)

[Haik 09] J. Haik, S. Daniel, A. Tessone, A. Orenstein & E. Winkler. *MRI induced fourth-degree burn in an extremity, leading to amputation*. Burns, vol. 35, no. 2, pages 294–296, 2009. (Cited on page 22)

[Haykin 01] S. Haykin. Kalman filtering and neural networks, chapitre 1, pages 1–22. Wiley-Interscience, New York, 2001. (Cited on pages 138 and 141)

[He 06] T. He, G. Clifford & L. Tarassenko. *Application of ICA in Removing Artefacts from the ECG*. Neural Comput Appl, vol. 15, no. 2, pages 105–116, 2006. (Cited on page

93)

[Henneberg 92] S. Henneberg, B. Hok, L. Wiklund & G. Sjodin. *Remote auscultatory patient monitoring during magnetic resonance imaging*. Journal Clin Monit, vol. 8, no. 1, pages 37–43, 1992. (Cited on page 52)

[Hick 06] C. Hick & A. Hick, editeurs. Intensivkurs Physiologie. Urban & Fischer Verlag/Elsevier GmbH, 2006. (Cited on pages 7, 10 and 102)

[Hill 02] J. Hill & A. Timmis. *ABC of clinical electrocardiography: Exercise tolerance testing*. Brit Med J, vol. 324, no. 7345, pages 1084–1087, May 2002. (Cited on pages 16 and 26)

[Hyvärinen 99a] A. Hyvärinen. *Fast and Robust Fixed-Point Algorithms for Independent Component Analysis*. IEEE Trans Neural Netw, vol. 10, no. 3, pages 626–634, 1999. (Cited on pages 58 and 96)

[Hyvärinen 99b] A. Hyvärinen. *Survey on Independent Component Analysis*. Neural Comput Surv, vol. 2, no. 4, pages 94–128, 1999. (Cited on page 58)

[Hyvärinen 00] A. Hyvärinen & E. Oja. *Independent Component Analysis: Algorithms and Applications*. Neural Networks, vol. 13, no. 4, pages 411–430, 2000. (Cited on page 95)

[Hyvärinen 01] A. Hyvärinen, J. Karhunen & E. Oja. Independent Component Analysis. Wiley-Interscience, 1 edition, 2001. (Cited on pages 95 and 96)

[Innes 93] J.A. Innes, S.C. De Cort, W. Kox & A. Guz. *Within-breath modulation of left ventricular function during normal breathing and positive-pressure ventilation in man*. J Physiol, vol. 460, no. 1, pages 487–502, 1993. (Cited on page 23)

[Jahnke 06] C. Jahnke, I. Paetsch, S. Achenbach, B. Schnackenburg, R. Gebker, E. Fleck & E. Nagel. *Coronary MR Imaging: Breath-hold Capability and Patterns, Coronary Artery Rest Periods, and β-Blocker Use*. Radiology, vol. 239, no. 1, pages 71–78, 2006. (Cited on page 24)

[Josephson 02] M.E. Josephson. Clinical Cardiac Electrophysiology: Techniques and Interpretations. Lippincott Williams & Wilkins, 3rd edition, 2002. (Cited on pages 15, 18 and 26)

[Kainz 10] W. Kainz, J. Guag, S. Benkler, D. Szczerba, E. Neufeld, V. Krauthamer, J. Myklebust, H. Bassen, I. Chang, N. Chavanne*et al.* *Development and validation of a magneto-hydrodynamic solver for blood flow analysis*. Phys Med Biol, vol. 55, pages 7253–7261, 2010. (Cited on page 34)

[Kastor 75] J. Kastor, B. Goldreyer, M. Josephson, J. Perloff, D.L. Scharf, J.H. Manchester, J.C. Shelburne & J.W. Hirshfeld. *Electrophysiologic characteristics of Ebstein's anomaly of the tricuspid valve*. Circulation, vol. 52, no. 6, pages 987–995, 1975. (Cited on page 51)

[Keltner 90] J.R. Keltner, M.S. Roos, P.R. Brakeman & T.F. Budinger. *Magnetohydrodynamics*

of Blood Flow. Magnet Reson Med, vol. 16, no. 1, pages 139–149, 1990. (Cited on pages 29 and 33)

[Kempen 06] P.M. Kempen. *ICU Patients Need Careful Monitoring in the MRI*. Anesthesia Patient Safety Foundation: Letter to the editor, 2006. (Cited on page 25)

[Kenigsberg 07] D.N. Kenigsberg, S. Khanal, M. Kowalski & S.C. Krishnan. *Prolongation of the QTc interval is seen uniformly during early transmural ischemia*. J Am Coll Cardiol, vol. 49, no. 12, pages 1299–1305, 2007. (Cited on page 18)

[Khurana 06] I. Khurana. Textbook Of Medical Physiology. Elsevier, 2006. (Cited on page 18)

[Kiencke 08] U. Kiencke, M. Schwarz & T. Weickert. Signalverarbeitung. Oldenbourg, 2008. (Cited on pages 39 and 58)

[Kim 11] J. Kim, V. Napadow, B. Kuo & R. Barbieri. *A combined HRV-fMRI approach to assess cortical control of cardiovagal modulation by motion sickness*. In Proc IEEE Eng Med Biol Soc, pages 2825–2828. IEEE, 2011. (Cited on page 26)

[Kinouchi 96] Y. Kinouchi, H. Yamaguchi & T. S. Tenforde. *Theoretical analysis of magnetic field interactions with aortic blood flow.* Bioelectromagnetics, vol. 17, no. 1, pages 21–32, 1996. (Cited on pages 29, 31 and 33)

[Klinge 84] R. Klinge. Das Elektrokardiogramm. Georg Thieme Verlag, Stuttgart - New York, 1984. (Cited on pages 10, 12, 15, 16, 17 and 18)

[Knesewitsch 13] T. Knesewitsch, C. Meierhofer, H. Rieger, J. Rößler, M. Frank, S. Martinoff, J. Hess, H. Stern & S. Fratz. *Demonstration of value of optimizing ECG triggering for cardiovascular magnetic resonance in patients with congenital heart disease*. J Cardiovasc Magn Reson, vol. 15, no. 3, pages 1–7, 2013. (Cited on page 51)

[Koehler 02] B.-U. Koehler, C. Hennig & R. Orglmeister. *The principles of software QRS detection*. IEEE Engineering in Medicine and Biology Magazine, vol. 21, no. 1, pages 42–57, 2002. (Cited on page 39)

[Kohl 11] P. Kohl, F. Sachs & M.R. Franz. Cardiac Mechano-electric Coupling and Arrhythmias. Oxford Univ Pr, 2011. (Cited on page 5)

[Koopmann 13] M. Koopmann & N.F. Marrouche. *Why hesitate introducing real-time magnetic resonance imaging into the electrophysiological labs?* Europace, vol. 15, no. 1, pages 7–8, 2013. (Cited on pages 22 and 26)

[Kording 14] F. Kording, B. Schoennagel, G. Lund, F. Ueberle, C. Jung, G. Adam & J. Yamamura. *Doppler ultrasound compared with electrocardiogram and pulse oximetry cardiac triggering: A pilot study*. Magnet Reson Med, vol. Online, 2014. (Cited on page 54)

[Krug 11] J.W. Krug & G. Rose. *Magnetohydrodynamic Distortions of the ECG in Different MR Scanner Configurations*. In Proc IEEE Comput Cardiol, volume 38, pages 769–772, Hangzhou, China, 2011. (Cited on page 136)

[Krug 12] J.W. Krug, G.D. Clifford, G.H. Rose & J. Oster. *The Limited Applicability of Wiener Filtering to ECG Signals Disturbed by the MHD Effect*. In Proc EUSIPCO, Bucharest, Romania, 2012. (Cited on pages 135 and 168)

[Krug 13a] J.W. Krug, G. Rose, G. Clifford & J. Oster. *Improved ECG based gating in ultra high field cardiac MRI using an independent component analysis approach*. J Cardiovasc Magn Reson, vol. 15, no. Suppl 1, page W33, 2013. (Cited on page 57)

[Krug 13b] J.W. Krug, G. Rose, D. Stucht, G. Clifford & J. Oster. *Limitations of VCG based gating methods in ultra high field cardiac MRI*. J Cardiovasc Magn Reson, vol. 15, no. Suppl 1, page W19, 2013. (Cited on pages 40, 49, 57 and 107)

[Krug 14] J.W. Krug, F. Luesebrink, O. Speck & G. Rose. *Optical Ballistocardiography for Gating and Patient Monitoring during MRI: An Initial Study*. In Proc IEEE Comput Cardiol, Boston, USA, September 2014. (Cited on page 56)

[Kugel 03] H. Kugel, C. Bremer, M. Püschel, R. Fischbach, H. Lenzen, B. Tombach, H. van Aken & W. Heindel. *Hazardous situation in the MR bore: induction in ECG leads causes fire.* Eur Radiol, vol. 13, no. 4, pages 690–694, Apr 2003. (Cited on pages 22, 27 and 177)

[Kwong 07] R.Y. Kwong. Cardiovascular Magnetic Resonance Imaging. Contemporary Cardiology. Humana Press, 2007. (Cited on page 21)

[Kyriakou 12] A. Kyriakou, E. Neufeld, D. Szczerba, W. Kainz, R. Luechinger, S. Kozerke, R. McGregor & N. Kuster. *Patient-specific simulations and measurements of the magneto-hemodynamic effect in human primary vessels*. Physiol Meas, vol. 33, pages 117–130, 2012. (Cited on pages 34, 35 and 37)

[Laguna] P. Laguna & L. Sörnmo. *Modelling Heart Rate Variability*. Rapport technique, Universidad de Zaragoza. (Cited on page 178)

[Laguna 97] P. Laguna, R.G. Mark, A. Goldberg & G.B. Moody. *A database for evaluation of algorithms for measurement of QT and other waveform intervals in the ECG*. In Computers in Cardiology 1997, pages 673–676. IEEE, 1997. (Cited on page 82)

[Lamb 12] H.J. Lamb, L. Van Schinkel, E. Kroner, P.J. van den Boogaard, M.J. Versluis, A. de Roos, A. Webb & H.M.J. Siebelink. *7T clinical cardiovascular MR imaging: initial experience*. J Cardiovasc Magn Reson, vol. 14, no. Suppl 1, page P234, 2012. (Cited on pages 49 and 57)

[Lane 83] James D Lane, Lisa Greenstadt, David Shapiro & Eduardo Rubinstein. *Pulse Transit Time and Blood Pressure: An Intensive Analysis*. Psychophysiology, vol. 20, no. 1, pages 45–49, 1983. (Cited on page 54)

[Leanderson 03] S. Leanderson, P. Laguna & L. Sörnmo. *Estimation of the respiratory frequency using spatial information in the VCG*. Medical Engineering & Physics, vol. 25, no. 6, pages 501–507, 2003. (Cited on page 13)

[Lederman 05] R.J. Lederman. *Cardiovascular Interventional Magnetic Resonance Imaging*. Circu-

lation, vol. 112, no. 19, pages 3009–3017, 2005. (Cited on pages 22 and 26)

[Lempe 13a] G. Lempe, S. Zaunseder, T. Wirthgen, S. Zipser & H. Malberg. *Kamerabasierte Erfassung kardiorespiratorischer Signale*. tm-Technisches Messen Plattform für Methoden, Systeme und Anwendungen der Messtechnik, vol. 80, no. 5, pages 179–184, 2013. (Cited on page 55)

[Lempe 13b] G. Lempe, S. Zaunseder, T. Wirthgen, S. Zipser & H. Malberg. *ROI selection for remote photoplethysmography*. In Bildverarbeitung für die Medizin 2013, pages 99–103. Springer, 2013. (Cited on page 55)

[Lentner 90] Cornelius Lentner. Geigy scientific tables: vol 5. Heart and circulation. CIBA-Geigy AG, 1990. (Cited on page 80)

[Li 06] Y. Li, S.I. Amari, A. Cichocki, D.W.C. Ho & S. Xie. *Underdetermined blind source separation based on sparse representation*. IEEE Trans Sig Proc, vol. 54, no. 2, pages 423–437, 2006. (Cited on page 94)

[Lilliefors 67] Hubert W Lilliefors. *On the Kolmogorov-Smirnov test for normality with mean and variance unknown*. J Am Stat Assoc, vol. 62, no. 318, pages 399–402, 1967. (Cited on pages 104 and 114)

[Ludbrook 05] G.L. Ludbrook, R.K. Webb, M. Currie & L.M. Watterson. *Crisis management during anaesthesia: myocardial ischaemia and infarction*. Qual Saf Health Care, vol. 14, no. e13, pages 1–4, 2005. (Cited on page 26)

[Malmivuo 95] J. Malmivuo & R. Plonsey. Bioelectromagnetism: principles and applications of bioelectric and biomagnetic fields. Oxford University Press, New York, 1995. (Cited on pages 8, 9, 10 and 14)

[Man 09] S. Man, E.W. van Zwet, A.C. Maan, M.J. Schalij & C.A. Swenne. *Individually improved VCG synthesis*. In Proc IEEE Comput Cardiol, pages 277–280. IEEE, 2009. (Cited on page 15)

[Mangano 90] D.T. Mangano, W.S. Browner, M. Hollenberg, M.J. London, J.F. Tubau & I.M. Tateo. *Association of perioperative myocardial ischemia with cardiac morbidity and mortality in men undergoing noncardiac surgery*. New Engl J Med, vol. 323, no. 26, pages 1781–1788, 1990. (Cited on page 26)

[Mark 04] M. Mark & J. Venegas. *Quantitative Physiology: Organ Transport Systems (Lecture at Massachusetts Institute of Technology)*. [Online]. Available: http://ocw.mit.edu/courses/health-sciences-and-technology/hst-542j-quantitative-physiology-organ-transport-systems-spring-2004/readings/, 2004. (Cited on pages 8 and 37)

[Markl 03] M. Markl, F.P. Chan, M.T. Alley, K.L. Wedding, M.T. Draney, C.J. Elkins, D.W. Parker, R. Wicker, C.A. Taylor, R.J. Herfkens*et al.* *Time-resolved three-dimensional phase-contrast MRI*. J Magn Reson Imaging, vol. 17, no. 4, pages 499–506, 2003. (Cited on pages 30 and 36)

[Markl 07] M. Markl, A. Harloff, T.A. Bley, M. Zaitsev, B. Jung, E. Weigang, M. Langer, J. Hennig & A. Frydrychowicz. *Time-resolved 3D MR velocity mapping at 3T: Improved navigator-gated assessment of vascular anatomy and blood flow*. J Magn Reson Imaging, vol. 25, no. 4, pages 824–831, 2007. (Cited on pages 21 and 30)

[Markl 11] M. Markl, P.J. Kilner & T. Ebbers. *Comprehensive 4D velocity mapping of the heart and great vessels by cardiovascular magnetic resonance*. J Cardiovasc Magn Reson, vol. 13, no. 7, pages 1–22, 2011. (Cited on page 31)

[Martin 11a] V. Martin, A. Drochon, O. Fokapu & JF Gerbeau. *MagnetoHemoDynamics Effect on Electrocardiograms*. FIMH, LectNotesComputSc, vol. 6666, pages 325–332, 2011. (Cited on pages 29, 31, 34 and 35)

[Martin 11b] V. Martin, A. Drochon, O. Fokapu, J.F. Gerbeau*et al.* *MagnetoHemoDynamics in Aorta and Electrocardiograms*. INRIA - Rapport de recherche, vol. Version 1, 30 Sep 2011, pages 1–38, 2011. (Cited on page 34)

[Martin 12] V Martin, A Drochon, O Fokapu & J-F Gerbeau. *MagnetoHemoDynamics in the aorta and electrocardiograms*. Phys Med Biol, vol. 57, no. 10, page 3177, 2012. (Cited on pages 34 and 35)

[Mason 66] R.E. Mason & I. Likar. *A new system of multiple-lead exercise electrocardiography*. Am Heart J, vol. 71, no. 2, pages 196–205, 1966. (Cited on page 12)

[Mateo 96] J. Mateo & P. Laguna. *New heart rate variability time-domain signal construction from the beat occurrence time and the IPFM model*. In Proc IEEE Comput Cardiol, pages 185–188, 1996. (Cited on page 178)

[Mateo 00] J. Mateo & P. Laguna. *Improved Heart Rate Variability Signal Analysis from the Beat Occurrence Times According to the IPFM Model*. IEEE Trans Biomed Eng, vol. 47, no. 8, pages 985–996, 2000. (Cited on page 178)

[MATLAB 10] MATLAB. Version 7.10.0 (R2010a). The MathWorks Inc., Natick, Massachusetts, 2010. (Cited on page 71)

[Mattei 08] E. Mattei, M. Triventi, G. Calcagnini, F. Censi, W. Kainz, G. Mendoza, H.I. Bassen & P. Bartolini. *Complexity of MRI induced heating on metallic leads: Experimental measurements of 374 configurations*. Biomedical engineering online, vol. 7, no. 1, page 11, 2008. (Cited on pages 22 and 27)

[Mattern 12] H. Mattern. *Blind Source Separation for Electrocardiography during Magnetic Resonance Imaging*. Bachelor thesis, Otto-von-Guericke University of Magdeburg, Germany, 2012. (Cited on page 137)

[McRobbie 06] D.W. McRobbie, E.A. Moore, M.J. Graves & M.R. Prince. MRI from Picture to Proton. Cambridge University Press, 2006. (Cited on page 21)

[McSharry 03a] P.E. McSharry & G.D Clifford. *ECGSYN - A realistic ECG waveform generator*. [Online]. Available: http://www.physionet.org/physiotools/ecgsyn/, 2003. (Cited on pages 58 and 59)

[McSharry 03b] P.E. McSharry, G.D. Clifford, L. Tarassenko & L.A. Smith. *A Dynamical Model for Generating Synthetic Electrocardiogram Signals*. IEEE Trans Biomed Eng, vol. 50, no. 3, pages 289–294, 2003. (Cited on pages 58, 59, 70 and 73)

[MHRA 07] MHRA. *Safety Guidelines for Magnetic Resonance Imaging Equipment in Clinical Use*, December 2007. (Cited on page 66)

[Misra 07] J.C. Misra & G.C. Shit. *Effect of magnetic field on blood flow through an artery: a numerical model*. Computer Technology (Russian), vol. 12, no. 4, pages 3–16, 2007. (Cited on page 29)

[Nacif 12] M.S. Nacif, A. Zavodni, N. Kawel, E.Y. Choi, J.A.C. Lima & D.A. Bluemke. *Cardiac magnetic resonance imaging and its electrocardiographs (ECG): tips and tricks*. Int J Cardiovasc Imaging, vol. 28, no. 6, pages 1465–1475, 2012. (Cited on pages 23, 24 and 49)

[Nagel 99] E. Nagel, H.B. Lehmkuhl, W. Bocksch, C. Klein, U. Vogel, E. Frantz, A. Ellmer, S. Dreysse & E. Fleck. *Noninvasive diagnosis of ischemia-induced wall motion abnormalities with the use of high-dose dobutamine stress MRI comparison with dobutamine stress echocardiography*. Circulation, vol. 99, no. 6, pages 763–770, 1999. (Cited on page 22)

[Napadow 08] V. Napadow, R. Dhond, G. Conti, N. Makris, E.N. Brown & R. Barbieri. *Brain correlates of autonomic modulation: combining heart rate variability with fMRI*. Neuroimage, vol. 42, no. 1, pages 169–177, 2008. (Cited on page 26)

[Nassenstein 12a] K. Nassenstein, S. Orzada, L. Haering, A. Czylwik, C. Jensen, T. Schlosser, O. Bruder, M.E. Ladd & S. Maderwald. *Cardiac magnetic resonance: is phonocardiogram gating reliable in velocity-encoded phase contrast imaging?* Eur Radiol, vol. 22, no. 12, pages 2679–2687, 2012. (Cited on page 53)

[Nassenstein 12b] K. Nassenstein, S. Orzada, L. Haering, A. Czylwik, M. Zenge, H. Eberle, T. Schlosser, O. Bruder, E. Müller, M.E. Ladd*et al.* *Cardiac MRI: evaluation of phonocardiogram-gated cine imaging for the assessment of global und regional left ventricular function in clinical routine*. Eur Radiol, vol. 22, no. 3, pages 559–568, 2012. (Cited on page 53)

[Natarajan 14] A. Natarajan, E. Gaiser, G. Angarita, R. Malison, D. Ganesan & B. Marlin. *Conditional random fields for morphological analysis of wireless ECG signals*. In Proc 5th ACM Conference on Bioinformatics, Computational Biology, and Health Informatics, pages 370–379. ACM, 2014. (Cited on page 82)

[Nehrke 00] K. Nehrke & D. Manke. *Advanced Navigator Techniques*. International Journal of Bioelectromagnetism, vol. 2, no. 2, 2000. (Cited on page 53)

[Niendorf 12] T. Niendorf, L. Winter & T. Frauenrath. Advances in Electrocardiograms - Methods and Analysis, chapitre Electrocardiogram in an MRI Environment: Clinical Needs, Practical Considerations, Safety Implications, Technical Solutions and Future Directions, pages 309–324. InTech, 2012. (Cited on page 177)

[Nijm 07a] G.M. Nijm, A.V. Sahakian, S. Swiryn & A.C. Larson. *Comparison of signal peak detection algorithms for self-gated cardiac cine MRI*. In Proc IEEE Comput Cardiol, pages 407–410. IEEE, 2007. (Cited on page 80)

[Nijm 07b] G.M. Nijm, S. Swiryn, A.C. Larson & A.V. Sahakian. *A 3D Model of Magnetohydrodynamic Voltages: Comparison with Voltages Observed on the Surface ECG during Cardiac MRI*. In Proc IEEE Comput Cardiol, pages 45–48, 2007. (Cited on page 33)

[Nordbeck 12] P. Nordbeck, F. Fidler, M.T. Friedrich, I. Weiss, M. Warmuth, D. Gensler, V. Herold, W. Geistert, P.M. Jakob, G. Ertl*et al.* *Reducing RF-related heating of cardiac pacemaker leads in MRI: Implementation and experimental verification of practical design changes*. Magnet Reson Med, vol. 68, no. 6, pages 1963–1972, 2012. (Cited on page 22)

[Odille 07] F. Odille, C. Pasquier, R. Abacherli, P.A. Vuissoz, G.P. Zientara & J. Felblinger. *Noise cancellation signal processing method and computer system for improved real-time electrocardiogram artifact correction during MRI data acquisition*. IEEE Trans Biomed Eng, vol. 54, no. 4, pages 630–640, April 2007. (Cited on pages 25 and 28)

[OSC 13] OSC. *OpenStaxCollege: Cardiac Muscle and Electrical Activity*. Lecture notes, Rice University, March 2013. (Cited on page 7)

[Oster 08] J. Oster, O. Pietquin & G. Bosser. *Adaptive RR prediction for cardiac MRI*. In Proc IEEE ICASSP, pages 513–516. IEEE, 2008. (Cited on page 24)

[Oster 09a] J. Oster, O. Pietquin, R. Abacherli, M. Kraemer & J. Felblinger. *A specific QRS detector for electrocardiography during MRI: Using wavelets and local regularity characterization*. In Proc IEEE ICASSP, pages 341–344. IEEE, 2009. (Cited on pages 25, 44 and 50)

[Oster 09b] J. Oster, O. Pietquin, R. Abächerli, M. Kraemer & J. Felblinger. *Independent component analysis-based artefact reduction: application to the electrocardiogram for improved magnetic resonance imaging triggering*. Physiol Meas, vol. 30, pages 1381–1397, 2009. (Cited on pages 25 and 28)

[Oster 10] J. Oster, O. Pietquin, M. Kraemer & J. Felblinger. *Bayesian framework for artifact reduction on ECG IN MRI*. In Proc IEEE ICASSP, pages 489–492, 2010. (Cited on page 28)

[Oster 12] J. Oster, R. Llinares, Z. Tse, Schmidt E.J. & Clifford G. *Realistic MHD Modeling Based on MRI Blood Flow Measurements*. In Proc Intl Soc Mag Reson Med, volume 20, page 912, 2012. (Cited on pages 35 and 59)

[Oster 13] J. Oster, M. Geist, O Pietquin & G.D. Clifford. *Filtering of pathological ventricular rhythms during MRI scanning*. Int J Bioelectromagn, vol. 15, no. 1, pages 54–59, 2013. (Cited on pages 59 and 143)

[Oster 15] J. Oster, R. Llinares, S. Payne, Z.T.H. Tse, E.J. Schmidt & G.D. Clifford. *Comparison of three artificial models of the magnetohydrodynamic effect on the electrocardiogram*. Comput Methods Biomech Biomed Engin, vol. 18, no. 13, pages

1400–1417, 2015. (Cited on pages 35, 36, 38, 64, 73 and 177)

[Pan 85] J. Pan & W.J. Tompkins. *A Real-Time QRS Detection Algorithm*. IEEE Trans Biomed Eng, vol. 32, no. 3, pages 230–236, 1985. (Cited on pages 90, 102, 104, 125 and 126)

[Park 06] H.D. Park, S.P. Cho & K.J. Lee. *A Method for Generating MRI Cardiac and Respiratory Gating Pulse Simultaneously based on Adaptive Real-Time Digital Filters*. In Proc IEEE Comput Cardiol, pages 813–816, 2006. (Cited on page 28)

[Park 09] H. Park, Y. Park, S. Cho, B. Jang & K. Lee. *New Cardiac MRI Gating Method Using Event-Synchronous Adaptive Digital Filter*. Ann Biomed Eng, vol. 37, no. 11, pages 2170–2187, 2009. (Cited on pages 25 and 28)

[Phlypo 07] R. Phlypo, V. Zarzoso, P. Comon, Y. Dasseler & I. Lemahieu. *Extraction of atrial activity from the ECG by spectrally constrained ICA based on kurtosis sign*. Proc 7th Int Conf ICA, pages 641–648, 2007. (Cited on page 136)

[Piorkowski 13] C. Piorkowski, M. Grothoff, T. Gaspar, C. Eitel, P. Sommer, Y. Huo, S. John, M. Gutberlet & G. Hindricks. *Cavotricuspid isthmus ablation guided by real-time magnetic resonance imaging*. Circulation: Arrhythmia and Electrophysiology, vol. 6, no. 1, pages e7–e10, 2013. (Cited on page 26)

[Poh 10] M.-Z. Poh, D.J. McDuff & R.W. Picard. *Non-contact, automated cardiac pulse measurements using video imaging and blind source separation*. Optics Express, vol. 18, no. 10, pages 10762–10774, 2010. (Cited on page 55)

[Poh 11] M.Z. Poh, D.J. McDuff & R.W. Picard. *Advancements in noncontact, multiparameter physiological measurements using a webcam*. IEEE Trans Biomed Eng, vol. 58, no. 1, pages 7–11, 2011. (Cited on page 55)

[Poldermans 99] D. Poldermans, R. Rambaldi, E. Boersma, W. Vletter, S. Carlier, A. Elhendy, J.J. Bax & J. Roelandt. *Stroke volume changes during dobutamine-atropine stress echocardiography: the influence of heart rate and ischaemia*. Int J Cardiovasc Imaging, vol. 15, no. 4, pages 263–269, 1999. (Cited on page 78)

[Rangayyan 87] R.M. Rangayyan & R.J. Lehner. *Phonocardiogram signal analysis: a review.* Critical reviews in biomedical engineering, vol. 15, no. 3, page 211, 1987. (Cited on page 53)

[Ranjan 12] R. Ranjan. *Magnetic Resonance Imaging in Clinical Cardiac Electrophysiology*. Crit Rev Biomed Eng, vol. 40, no. 5, 2012. (Cited on page 26)

[Rasmussen 06] C.E. Rasmussen & C.K.I. Williams. Gaussian Processes for Machine Learning. MIT Press, 2006. (Cited on page 178)

[Ravenswaaij 93] C.M.A. Ravenswaaij, L.A.A. Kollee, J.C.W. Hopman, G. Stoelinga & H.P. van Geijn. *Heart Rate Variability*. Ann Intern Med, vol. 118, no. 6, pages 436–447, 1993. (Cited on page 19)

[Razavi 04] R. Razavi, V. Mutharangu, S.R. Hegde & A.M. Taylor. Clinical Cardiac MRI, chapitre 17: MR-Guided Cardiac Catheterization, pages 513–538. Springer, 2004.

(Cited on page 26)

[Roberts 01] S. Roberts & R. Everson, editeurs. Independent Component Analysis: Principles and Practice. Cambridge University Press, 2001. (Cited on pages 93 and 96)

[Romero 11] D. Romero, M. Ringborn, P. Laguna, O. Pahlm & E. Pueyo. *Depolarization changes during acute myocardial ischemia by evaluation of QRS slopes: standard lead and vectorial approach*. IEEE Trans Biomed Eng, vol. 58, no. 1, pages 110–120, 2011. (Cited on page 13)

[Sameni 06] R. Sameni. *Open Source ECG Toolbox (OSET)*. Online, http://ecg.sharif.ir/, 2006. (Cited on page 70)

[Sameni 07] R. Sameni, M.B. Shamsollahi, C. Jutten & G.D. Clifford. *A Nonlinear Bayesian Filtering Framework for ECG Denoising*. IEEE Trans Biomed Eng, vol. 54, no. 12, pages 2172–2185, 2007. (Cited on page 71)

[Sameni 08] R. Sameni. *Extraction of Fetal Cardiac Signals from an Array of Maternal Abdominal Recordings*. Ph.D. Thesis, Institut Polytechnique de Grenoble, France, 2008. (Cited on pages 70 and 71)

[Sansone 10] M. Sansone, L. Mirarchi & M. Bracale. *Adaptive removal of gradients-induced artefacts on ECG in MRI: a performance analysis of RLS filtering*. Med Biol Eng Comput, vol. 48, no. 5, pages 475–482, 2010. (Cited on pages 25 and 28)

[Sayadi 10] O. Sayadi, M.B. Shamsollahi & G.D. Clifford. *Synthetic ECG generation and Bayesian filtering using a Gaussian wave-based dynamical model*. Physiol Meas, vol. 31, no. 10, pages 1309–1329, 2010. (Cited on pages 70, 142 and 170)

[Schaefer 00] D.J. Schaefer, J.D. Bourland & J.A. Nyenhuis. *Review of Patient Safety in Time-Varying Gradient Fields*. J Magn Reson Imaging, vol. 12, no. 1, pages 20–29, 2000. (Cited on page 27)

[Schmidt 07] R.F. Schmidt & F. Lang, editeurs. Physiologie des Menschen: Mit Pathophysiologie. Springer Medizin Verlag, Heidelberg, 30th edition, 2007. (Cited on pages 5, 6, 7, 9, 29 and 31)

[Schmidt 09] E.J. Schmidt, R.P. Mallozzi, A. Thiagalingam, G. Holmvang, A. Avila, R. Guhde, R. Darrow, G.S. Slavin, M.M. Fung, J. Dando, L. Foley, L. Dumoulin & V.Y. Reddy. *Electroanatomic Mapping and Radiofrequency Ablation of Porcine Left Atria and Atrioventricular Nodes Using Magnetic Resonance Catheter Tracking*. Circulation: Arrhythmia and Electrophysiology, vol. 2, no. 6, pages 695–704, 2009. (Cited on pages 22 and 26)

[Schmidt 14] M. Schmidt, J.W. Krug, A. Gierstorfer & G. Rose. *A Real-time QRS Detector Based on Higher-order Statistics for ECG Gated Cardiac MRI*. In Proc IEEE Comput Cardiol, Boston, USA, September 2014. (Cited on pages 51, 105 and 119)

[Scott 09] A.D. Scott, J. Keegan & D.N. Firmin. *Motion in cardiovascular MR imaging*. Radiology, vol. 250, no. 2, pages 331–351, 2009. (Cited on pages 23 and 24)

[Shechter 05] G. Shechter, J.R. Resar & E.R. McVeigh. *Rest period duration of the coronary arteries: Implications for magnetic resonance coronary angiography*. Medical Physics, vol. 32, no. 1, pages 255–262, 2005. (Cited on page 24)

[Shellock 04] F.G. Shellock & J.V. Crues. *MR Procedures: Biologic Effects, Safety, and Patient Care*. Radiology, vol. 232, no. 3, pages 635–652, 2004. (Cited on page 177)

[Sheppard 11] J.P. Sheppard, T.A. Barker, A.M. Ranasinghe, T.H. Clutton-Brock, M.P. Frenneaux & M.J. Parkes. *Does modifying electrode placement of the 12 lead ECG matter in healthy subjects?* Int J Cardiol, vol. 152, no. 2, pages 184–191, 2011. (Cited on page 12)

[Shetty 88] A.N. Shetty. *Suppression of radiofrequency interference in cardiac gated MRI: a simple design*. Magnet Reson Med, vol. 8, no. 1, pages 84–88, 1988. (Cited on page 27)

[Siemens AG 04] Siemens AG. *Magnets, Flows and Artifacts: Basics, Techniques, and Applications of Magnetic Resonance Tomography*, 2004. (Cited on page 20)

[Silva 14] I. Silva & G. Moody. *An open-source toolbox for analysing and processing PhysioNet databases in MATLAB and Octave*. Journal of Open Research Software, vol. 2, no. 1, page e27, 2014. (Cited on page 82)

[Simonson 63] E. Simonson. *Use of the electrocardiogram in exercise tests*. Am Heart J, vol. 66, no. 4, pages 552–565, 1963. (Cited on pages 12 and 26)

[Slavin 06] G.S. Slavin, G. Holmvang & E. Schmidt. *Systolic-Phase Black-Blood Imaging for Fatty Tissue Detection in Arrhythmogenic Right Ventricular Dysplasia*. In Proc Intl Soc Mag Reson Med, volume 14, page 83, 2006. (Cited on page 24)

[Smith 85] J. Smith, M.K. Cahalan, D.J. Benefiel, B.F. Byrd, F.W. Lurz, W.A. Shapiro, M.F. Roizen, A. Bouchard & N.B. Schiller. *Intraoperative detection of myocardial ischemia in high-risk patients: electrocardiography versus two-dimensional transesophageal echocardiography*. Circulation, vol. 72, no. 5, pages 1015–1021, 1985. (Cited on page 26)

[Sommer 12] P. Sommer. *Bildgebung in der invasiven Elektrophysiologie*. Presentation at 'Kardiologie heute - Symposium am Unfallkrankenhaus Berlin', December 2012. (Cited on page 25)

[Sommer 13] P. Sommer, M. Grothoff, C. Eitel, T. Gaspar, C. Piorkowski, M. Gutberlet & G. Hindricks. *Feasibility of real-time magnetic resonance imaging-guided electrophysiology studies in humans*. Europace, vol. 15, no. 1, pages 101–108, 2013. (Cited on page 26)

[Stein 94] P.K. Stein, M.S. Bosner, R.E. Kleiger & B.M. Conger. *Heart rate variability: a measure of cardiac autonomic tone*. Am Heart J, vol. 127, no. 5, pages 1376–1381, 1994. (Cited on page 19)

[Steinberg 09] J.S. Steinberg & S. Mittal. Electrophysiology: A Companion Guide for the Cardi-

ology Fellow During the EP Rotation. LWW medical book collection. Lippincott Williams & Wilkins, 2009. (Cited on page 17)

[Stone 04] James V. Stone. Independent Component Analysis - A Turorial Introduction. The MIT Press, 2004. (Cited on page 96)

[Strohm 06] Oliver Strohm, Peter Bernhardt & Thoralf Niendorf. Kardiovaskuläre MRT in der Praxis: Anleitungen und Fallbeispiele, volume 1. Elsevier, Urban&FischerVerlag, 2006. (Cited on pages 22, 23 and 24)

[Stucht 12] D. Stucht, P. Schulze, K.A. Danishad, I.Y. Kadashevich, M. Zaitsev, B.S.R. Armstrong & O. Speck. *Accuracy of prospective motion correction in MRI using tracking markers on repositionable dental impressions*. In Medical Image Understanding and Analysis, Swansea, UK, 2012. (Cited on page 56)

[Sundnes 06] J. Sundnes, G.T. Lines, X. Cai, B.F. Nielsen, K.A. Mardal & A. Tveito. Computing the electrical activity in the heart, volume 1. Springer, Berlin Heidelberg, 2006. (Cited on page 34)

[Suttie 12] J.J. Suttie, L. Delabarre, A. Pitcher, P.F. van de Moortele, S. Dass, C.J. Snyder, J.M. Francis, G.J. Metzger, P. Weale, K. Ugurbil, S. Neubauer, M. Robson & T. Vaughan. *7 Tesla (T) human cardiovascular magnetic resonance imaging using FLASH and SSFP to assess cardiac function: validation against 1.5 T and 3 T*. NMR Biomed, vol. 25, no. 1, pages 27–34, 2012. (Cited on page 57)

[Taleb 99] A. Taleb & C. Jutten. *On underdetermined source separation*. In Proc IEEE ICASSP, volume 3, pages 1445–1448. IEEE, 1999. (Cited on page 94)

[Tarassenko 14] L. Tarassenko, M. Villarroel, A. Guazzi, J. Jorge, D.A. Clifton & C. Pugh. *Non-contact video-based vital sign monitoring using ambient light and auto-regressive models*. Physiol Meas, vol. 35, no. 5, page 807, 2014. (Cited on page 55)

[Thompson 04] R. Thompson & E. McVeigh. *Flow-Gated Phase-Contrast MRI Using Radial Acquisitions*. Magnet Reson Med, vol. 52, no. 3, pages 598–604, 2004. (Cited on pages 25 and 80)

[Thompson 06] R.B. Thompson & E.R. McVeigh. *Cardiorespiratory-resolved magnetic resonance imaging: Measuring respiratory modulation of cardiac function*. Magnet Reson Med, vol. 56, no. 6, pages 1301–1310, 2006. (Cited on page 23)

[Tse 10a] Z. Tse, C. Dumoulin, G. Clifford, M. Jerosch-Herald, D. Kacher, R. Kwong, W. Stevenson & E. Schmidt. *MRI-compatible 12-lead ECGs with MHD separation: application to cardiac MRI gating, physiological monitoring and noninvasive cardiac-output estimation*. In Proc Intl Soc Mag Reson Med, page 286, Stockholm, 2010. (Cited on pages 49, 57, 125 and 168)

[Tse 10b] Z. Tse, C.L. Dumoulin, G. Clifford, M. Jerosch-Herold, D. Kacher, R. Kwong, W.G. Stevenson & E.J. Schmidt. *12-lead ECG in a 1.5 Tesla MRI: Separation of real ECG and MHD voltages with adaptive filtering for gating and non-invasive cardiac output*. J Cardiovasc Magn Reson, vol. 12, no. Suppl 1, page O95, 2010. (Cited on

pages 169 and 177)

[Tse 11a] Z.T.H. Tse, C.L. Dumoulin, G. Clifford, M. Jerosch-Herold, D. Kacher, R. Kwong, W.G. Stevenson & E.J. Schmidt. *Improved R-wave detection for enhanced cardiac Gating using an MRI-compatible 12-lead ECG and multi-channel analysis*. J Cardiovasc Magn Reson, vol. 13, no. Suppl 1, page P3, 2011. (Cited on pages 49, 105 and 120)

[Tse 11b] Z.T.H. Tse, C.L. Dumoulin, G. Clifford, M. Jerosch-Herold, D. Kacher, R. Kwong, W.G. Stevenson & E.J. Schmidt. *System for real-time cardiac MRI gating, 12-lead ECG monitoring, and non-invasive stroke volume estimationanalysis*. In Proc Intl Soc Mag Reson Med, volume 13, pages 1–3. Springer, 2011. (Cited on page 57)

[Tse 12] Z. Tse, C. Dumoulin, G. Clifford, J. Oster, M. Jerosch-Herold, R. Kwong, W. Stevenson & E. J. Schmidt. *Cardiac MRI with concurrent physiological monitoring using MRI-compatible 12-lead ECG*. J Cardiovasc Magn Reson, vol. 14, no. Suppl 1, page P231, 2012. (Cited on pages 49, 105, 169 and 177)

[Tse 13] Z. Tse, C. Dumoulin, R. Watkins, K.B. Pauly, R.Y. Kwong, G.F. Michaud, W. Stevenson, F. Jolesz & E.J. Schmidt. *Improved cardiac gating at 3T with the 3D-QRS method utilizing MRI-compatible 12-lead ECGs*. J Cardiovasc Magn Reson, vol. 15, no. Suppl 1, page W20, 2013. (Cited on pages 49, 57 and 105)

[Tse 14] Z. Tse, C. Dumoulin, G.D. Clifford, J. Schweitzer, L. Qin, J. Oster, M. Jerosch-Herold, R. Kwong, G. Michaud, W. Stevenson & E. Schmidt. *A 1.5T MRI-Conditional 12-Lead Electrocardiogram for MRI and Intra-MR Intervention*. Magnet Reson Med, vol. 71, no. 3, pages 1336–1347, 2014. (Cited on pages 49, 57, 58, 125, 168, 169 and 177)

[Tsitlik 93] J.E. Tsitlik, H. Levin, H. Halperin & M. Weisfeldt. *ECG amplifier and cardiac pacemaker for use during magnetic resonance imaging*, June 8 1993. US Patent 5,217,010. (Cited on page 27)

[Tung 10] N.G. Tung R.and Boyle & K. Shivkumar. *Catheter Ablation of Ventricular Tachycardia*. Circ, vol. 122, pages e389–e391, 2010. (Cited on page 18)

[van Gorselen 07] E.O.F. van Gorselen, F.W.A. Verheugt, B.T.J. Meursing & A.J.M. Oude Ophuis. *Posterior myocardial infarction: the dark side of the moon*. Neth Heart J, vol. 15, no. 1, page 16, 2007. (Cited on page 12)

[van Oosterom 04] A. van Oosterom & T.F. Oostendorp. *ECGSIM: an interactive tool for studying the genesis of QRST waveforms*. Heart, vol. 90, no. 2, pages 165–168, 2004. (Cited on page 35)

[Vaseghi 09] S.V. Vaseghi. Advanced digital signal processing and noise reduction. Wiley, Chichester, West Sussex, 4th edition, 2009. (Cited on pages 96, 130, 131, 132 and 141)

[Vergara 11] G.R. Vergara, S. Vijayakumar, E.G. Kholmovski, J.J.E. Blauer, M.A. Guttman, C. Gloschat, G. Payne, K. Vij, N.W. Akoum, M. Daccarett*et al.* *Real-time magnetic resonance imaging–guided radiofrequency atrial ablation and visualization of*

lesion formation at 3 Tesla. Heart Rhythm, vol. 8, no. 2, pages 295–303, 2011. (Cited on page 44)

[Villarroel 14] M. Villarroel, A. Guazzi, J. Jorge, S. Davis, P. Watkinson, G. Green, A. Shenvi, K. McCormick & L. Tarassenko. *Continuous non-contact vital sign monitoring in neonatal intensive care unit*. Healthcare Technology Letters, vol. 1, no. 3, pages 87–91, 2014. (Cited on page 55)

[Webster 92] J.G. Webster, editeur. Medical Instrumentation : Application and Design. Houghton Mifflin Company, 1992. (Cited on page 30)

[Weiss 11] S. Weiss, D. Wirtz, B. David, S. Krueger, O. Lips, D. Caulfield, S.F. Pedersen, J. Bostock, R. Razavi & T. Schaeffter. *In vivo evaluation and proof of radiofrequency safety of a novel diagnostic MR-electrophysiology catheter*. Magnetic Resonance in Medicine, 2011. (Cited on page 27)

[Weissler 73] A.M. Weissler. Noninvasive cardiology. Clinical cardiology monographs. Grune & Stratton, 1973. (Cited on page 56)

[Welch 04] G. Welch & G. Bishop. *An introduction to the Kalman filter*, 2004. (Cited on page 139)

[Werner 05] J. Werner. Kooperative und autonome systeme der medizintechnik. Oldenbourg Verlag, 2005. (Cited on page 102)

[Wilson 34] F.N. Wilson, F.D. Johnston, A.G. Macleod & P.S. Barker. *Electrocardiograms that represent the potential variations of a single electrode*. Am Heart J, vol. 9, no. 4, pages 447–458, 1934. (Cited on page 12)

[Wilson 44] F.N. Wilson, F.D. Johnston, F.F. Rosenbaum, H. Erlanger, C.E. Kossmann, H. Hecht, N. Cotrim, R.M. de Oliveira, R. Scarsi & P.S. Barker. *The precordial electrocardiogram*. Am Heart J, vol. 27, no. 1, pages 19–85, 1944. (Cited on page 12)

[Wu 11] V. Wu, I.M. Barbash, K. Ratnayaka, C.E. Saikus, M. Sonmez, O. Kocaturk, R.J. Lederman & A.Z. Faranesh. *Adaptive Noise Cancellation to Suppress Electrocardiography Artifacts During Real-Time Interventional MRI*. J Magn Reson Imaging, vol. 33, pages 1184–93, 2011. (Cited on pages 25 and 28)

[Zapatero 14] J.P.R. Zapatero, I. Morchio, R. Cui & J. Vicente. *Mathematics for Economics - Linear Systems (Lecture at Universidad Carlos III de Madrid)*. [Online]. Available: http://www.eco.uc3m.es/docencia/matematicasfico/english/index.html, October 2014. (Cited on page 131)

[Zaunseder 14] S. Zaunseder, A. Heinke, A. Trumpp & H. Malberg. *Heart beat detection and analysis from videos*. In Proc IEEE 34th International Conference on Electronics and Nanotechnology (ELNANO), pages 286–290. IEEE, 2014. (Cited on page 55)

Journal publications

[1] J.W. Krug, G. Rose, G. Clifford, and J. Oster. ECG-Based Gating in Ultra High Field Cardiac MRI using an Independent Component Analysis Approach. *J Cardiovasc Magn Reson*, 15(104):1–13, 2013.

Conference publications

[1] J.W. Krug, F. Luesebrink, O. Speck, and G. Rose. Optical Ballistocardiography for Gating and Patient Monitoring during MRI: An Initial Study. In *Proc IEEE Comput Cardiol*, Boston, USA, September 2014. *(Poster presentation)*.

[2] R. Schulte, J.W. Krug, and G. Rose. Identification of a signal for an optimal heart beat detection in multimodal physiological datasets. In *Proc IEEE Comput Cardiol*, Boston, USA, September 2014. *(Oral presentation)*.

[3] M. Schmidt, J.W. Krug, A. Gierstorfer, and G. Rose. A Real-time QRS Detector Based on Higher-order Statistics for ECG Gated Cardiac MRI. In *Proc IEEE Comput Cardiol*, Boston, USA, September 2014. *(Oral presentation)*.

[4] F. Luesebrink, J.W. Krug, G. Rose, and O. Speck. Contact-free measurement of physiological parameters by means of an optical tracking system. In *Proc BMT*, Hannover, Germany, October 2014. *(Oral presentation)*.

[5] M. Schmidt, J.W. Krug, and G. Rose. QRS detection using 5th order cumulants for ECG gated cardiac MRI. In *Proc BMT*, Hannover, Germany, October 2014. *(Oral presentation)*.

[6] J.W. Krug, G. Rose, G. Clifford, and J. Oster. Improved ECG based gating in ultra high field cardiac MRI using an independent component analysis approach. *J Cardiovasc Magn Reson*, 15(Suppl

1):W33, January 2013. *(Poster presentation)*.

[7] J.W. Krug, G. Rose, D. Stucht, G. Clifford, and J. Oster. Limitations of VCG based gating methods in ultra high field cardiac MRI. *J Cardiovasc Magn Reson*, 15(Suppl 1):W19, January 2013. *(Oral presentation)*.

[8] J.W. Krug, G. Rose, G. Clifford, and J. Oster. Real-time gating for 7T cardiac MRI using a 6D vector space method based on the precordial electrocardiogram signals. In *European Society for Magnetic Resonance in Medicine and Biology (ESMRMB)*, volume 26, page 74, Toulouse, France, October 2013. Springer. *(Oral presentation)*.

[9] J.W. Krug, G. Rose, G. Clifford, and J. Oster. EKG-basierte Triggerung für die kardiale Ultrahochfeld-Magnetresonanztomographie. In S.Zaunseder H. Malberg, M.G. Abreu, editor, *AUTOMED - Automatisierungsverfahren für die Medizin*, Dresden, 2013. Steinbeiss. *(Oral presentation)*.

[10] J.W. Krug, K. Jungnickel, M. Kaiser, J. Ricke, G. Rose, and A. Boese. Investigating the Artifacts of Different Rapid Prototyping Materials under MRI. In *Proc Interventional MRI Symposium*, Boston, USA, September 2012. *(Poster presentation)*.

[11] J.W. Krug, K. Jungnickel, N. Thuermer, M. Kaiser, J. Ricke, and G. Rose. RF Induced Heating during an Interventional Scenario in a 1T Open MRI Scanner. In *Proc Interventional MRI Symposium*, Boston, USA, September 2012. *(Poster presentation)*.

[12] J. Krug, K. Jungnickel, J. Ricke, F. Fischbach, and G. Rose. Heating of conductive wires in an open high field MRI environment: Effect of different wire positions in the MR scanner room. In *Proc BMT*, Jena, Germany, September 2012. *(Poster presentation)*.

[13] J.W. Krug, G.D. Clifford, G.H. Rose, and J. Oster. The Limited Applicability of Wiener Filtering to ECG Signals Disturbed by the MHD Effect. In *Proc European Signal Processing Conference (EUSIPCO)*, Bucharest, Romania, August 2012. *(Oral presentation)*.

[14] J.W. Krug, G.H. Rose, D. Stucht, G.D. Clifford, and J. Oster. Filtering the Magnetohydrodynamic Effect from 12-lead ECG Signals using Independent Component Analysis. In *Proc IEEE Comput Cardiol*, Krakow, Poland, September 2012. *(Poster presentation)*.

[15] K. Jungnickel, N. Thürmer, J. Krug, U. Wonneberger, J. Ricke, and F. Fischbach. HF-Erwärmung von Führungsdrähten bei MR-gestützten Interventionen? In *RöFo-Fortschritte auf dem Gebiet der Röntgenstrahlen und der bildgebenden Verfahren*, volume 184, page VO205_3, 2012. *(Oral presentation)*.

[16] C. Kühnel, J. Krug, Z. Salah, K. Jungnickel, U. Wonneberger, K. Toennies, and G. Rose. Bildbasiertes Tracking im MRT unter Verwendung von Resonanzmarkern. In *Proc CURAC*, Magdeburg, Germany, September 2011. *(Oral presentation)*.

[17] J.W. Krug and G. Rose. Magnetohydrodynamic Distortions of the ECG in Different MR Scanner Configurations. In *Proc IEEE Comput Cardiol*, volume 38, pages 769–772, Hangzhou, China, September 2011. *(Poster presentation)*.

[18] M. Kaiser, J. Krug, and J. Rose. Minimal-invasive Surgery under MR guidance. In *Proc IEEE*

MTT-S, Baltimore, USA, June 2011. *(Oral presentation)*.

[19] K. Will, J. Krug, K. Jungnickel, F. Fischbach, J. Ricke, G. Rose, and A. Omar. MR-compatible RF ablation system for online treatment monitoring using MR thermometry. In *Proc IEEE Eng Med Biol Soc*, Buenos Aires, Argentina, August 2010. *(Oral presentation)*.

[20] J. Krug, K. Will, and G. Rose. Simulation and experimental validation of resonant electric markers used for medical device tracking in magnetic resonance imaging. In *Proc IEEE Eng Med Biol Soc*, volume 2010, pages 1878–1881, Buenos Aires, Argentina, August 2010. *(Oral presentation)*.

[21] J. Krug, K. Will, and G. Rose. Catheter tracking in MRI guided interventions using resonant circuits in an open high field MR environment: Simulations and experimental measurements. In *Proc Interventional MRI Symposium*, Leipzig, Germany, September 2010. *(Poster presentation)*.

[22] J. Krug, S. Zaunseder, M. Rabenau, R. Poll, and H. Sager. Comparative Analysis of different Wigner-Ville Distribution Implementations for the ECG-based Detection of Obstructive Sleep Apnea. In *Proc IFMBE - WC2009*, Munich, Germany, September 2009. *(Oral presentation)*.

Invited talks

[1] J. Krug. Electrocardiogram in the MRI: Only Artefacts? In *IIIOS Training Event*, Luebeck, Germany, October 2011.

(Conference papers [4-8,12] were published as journal supplements.)

Nomenclature

Acronyms

AV	Atrioventricular
BCG	Ballistocardiogram
BSS	Blind source separation
CHD	Congenital heart disease
CMR	Cardiac magnetic Resonance (Imaging)
ECG	Electrocardiogram
EEG	Electroencephalography
EKF	Extended Kalman filter
EP	Electrophysiological
Ff	Feet first (position in the MR scanner)
FIR	Finite Impulse Response
fMRI	functional magnetic resonance imaging
Hf	Head first (position in the MR scanner)
HF	High frequency (here: frequency range in the HRV spectrum)
HR	Heart Rate
HRV	Heart rate variability
ICA	Independent Component Analysis
ICU	Intensive care unit
IIR	Infinite impulse response
iMRI	Interventional magnetic resonance imaging
IVC	Inferior vena cava
KF	Kalman filter
LF	Low frequency (here: frequency range in the HRV spectrum)
LMS	Least mean square
LSE	Least squared error
MA	Muscle artefacts
MHD	Magnetohydrodynamic
MMSE	Minimum mean square error
MRI	Magnetic resonance imaging
PAC	Premature atrial contractions
PCA	Principal component analysis
PCG	Phonocardiogram
PPG	Photoplethysmography
PTT	Pulse transit time
PVC	Premature ventricular contractions

RF	Radio frequency
rPPG	Remote PPG
RRI	RR interval (distance between two adjacent R-peaks)
RSA	Respiratory sinus arrhythmia
SA	Sinoatrial
SPWVD	Smoothed pseudo Wigner-Ville distribution
STFT	Short-time Fourier transform
SVC	Superior vena cava
SVD	Singular value decomposition
TFED	Time frequency energy distribution
UHF	Ultra-high field
VCG	Vectorcardiogram

Danksagung

Diese Arbeit entstand während meiner Tätigkeit als wissenschaftlicher Mitarbeiter am Lehrstuhl für medizinische Telematik und Medizintechnik der Otto-von-Guericke Universität Magdeburg. Meinem Doktorvater Prof. Dr. Georg Rose möchte ich dafür danken, dass er es mir ermöglicht hat, dieses Thema zu bearbeiten und mich bei meiner Tätigkeit stets beratend unterstützt hat. Die Zusammenarbeit mit der University of Oxford wäre nicht ohne die Unterstützung und das Vertrauen von Dr. Gari Clifford (jetzt Emory University) zustande gekommen. Besonders möchte ich mich bei Dr. Julien Oster (University of Oxford) für die intensiven Diskussionen, für umfangreiches Feedback beim Schreiben von Veröffentlichungen und die gute Betreuung während meiner Forschungsaufenthalte in Oxford bedanken. Ich freue mich auch sehr über das Interesse von Prof. Jacques Felblinger (Université de Lorraine) an dieser Arbeit und für seine Bereitschaft zur Übernahme des Zweitgutachtens.

Den Mitarbeitern des Lehrstuhls, insbesondere der INKA-Forschungsgruppe unter der Leitung von Dipl.-Ing. Axel Boese, möchte ich für das angenehme und produktive Klima sowie den Einblick in die vielen verschiedenen und spannenden Forschungsthemen danken. Dipl.-Ing. Daniel Stucht (Abteilung biomedizinische Magnetresonanz) und Dr. Kerstin Jungnickel (Klinik für Radiologie und Nuklearmedizin) haben mich stets bei meinen Messungen am Universitätsklinikum unterstützt. Bedanken möchte ich mich auch bei meinen Studenten, die sich durch ihre Abschlussarbeiten und Forschungsprojekte mit eingebracht haben. Für mein Interesse am EKG und den Biosignalen ist nicht zuletzt Dr. Sebastian Zaunseder (TU Dresden) mit verantwortlich.

Besonderer Dank gilt natürlich meinem persönlichen Umfeld. Für die Unterstützung sowohl vor als auch während der Dissertation möchte ich meiner gesamten Familie danken. Auch mein Freundeskreis hat seinen Teil zum Gelingen der Arbeit beigetragen. Meine Freundin gab mir immer den für die Arbeit nötigen Rückhalt. In den letzten Monaten der Dissertation hat mir aber ganz besonders unsere Tochter Laura immer wieder Momente des Ausgleichs gewährt.